Studies of Nucleation and Surface Kinetics in

Molecular Beam Expitaxy of GaN

PhD Thesis

by

Gregor Koblmüller

DISSERTATION

Studies of Nucleation and Surface Kinetics in
Molecular Beam Epitaxy of GaN

ausgeführt zum Zwecke der Erlangung des akademischen Grades eines Doktors
der technischen Wissenschaften/der Naturwissenschaften unter der Leitung von

Professor Dr. Peter Pongratz
E138
Institut für Festkörperphysik

eingereicht an der Technischen Universität Wien
Fakultät für Physik

von

DI Gregor Koblmüller
9226273
Otto –Hahn–Ring 6, D–81730 München

Wien, am 10.12.2004

KURZFASSUNG

In der vorliegenden Arbeit wurden die Nukleation und Oberflächenkinetik während der Molekularstrahlepitaxie (MBE) von GaN untersucht. Um diese Phänomene direkt und vollkommen quantitativ zu bestimmen, wurde ein Verfahren der Massenspektrometrie entwickelt, bei dem ein Quadrupol Massenspektrometer in direkter Ausrichtung auf die wachsende GaN Schicht die Desorption von Ga Atomen misst. Damit konnten Aussagen über atomistische Oberflächenprozesse wie Adsorption, Desorption, Inkorporation aber auch direkte Wachstumsratenbestimmungen realisiert werden.

Mit diesem Verfahren konnten zum ersten Mal die theoretischen Vorhersagen direkt experimentell nachgewiesen werden, dass die polaren Oberflächen der Wurtztit GaN Kristallstruktur mit unterschiedlichen thermodynamisch stabilen metallischen Ga Gleich-gewichtsbedeckungen terminiert sind, anders als bei allen anderen konventionellen III–V Halbleitern. Im Falle der N–polaren (000-1) GaN Oberfläche, bildet sich ein ~1 ML dicke Ga Gleichgewichtsbedeckung, während an der Ga–polaren (0001) Oberfläche sich eine lateral kontrahierte Ga Doppelschicht von ~ 2.4 ML stabilisiert. Konkrete temperaturabhängige Untersuchungen der Verweildauer der Ga Adatome in diesen Ga Bedeckungen deuten darauf hin, dass die Adatome stärker auf einer N–polaren GaN Oberfläche gebunden sind als auf einer Ga–polaren Oberfläche. Darüberhinaus konnte ein Phasenzustand gefunden werden, bei dem sich auf diesen Gleichgewichtsbedeckungen zusätzliche metallische Ga Tropfen ausbilden, in denen die Ga Adatome sehr schwach gebunden sind.

Besonderes Augenmerk wurde weiters auf das MBE Wachstum der technologisch relevanteren Ga–polaren Oberfläche gelegt, indem die Entwicklung der Ga Bedeckung als Funktion der Wachstumsparameter Temperatur und Ga/N Flussverhältnis studiert wurde. Es zeigte sich, dass die Ga Bedeckung *kontinuierlich* mit steigendem Ga Fluss von 0 ML an der Stöchiometriegrenze (wo Ga und N Flüsse ident sind) bis 2.4 ML an der Ga Tropfengrenze steigt. Dieses Verhalten spiegelt sich direkt in den Oberflächenmorphologien von dicken GaN Schichten wider, wobei bei geringen Ga Bedeckungen nahe der Stöchiometriegrenze eine grosse Anzahl von Oberflächendefekten (sog. Pits) auftreten, während die besten Morpho-logien mit verschwindend kleiner Pitdichte direkt an der Tropfengrenze erzielt wurden. Daraus konnte ein direkter Zusammenhang von Oberflächenmorphologie, Ga Bedeckung und der damit verbundenen Oberflächendiffusion der N Adatome abgeleitet werden.

In einer weiteren Studie wurde die Nukleation von GaN auf verschiedensten Substraten (Saphir, SiC und AlN) untersucht. Die Nukleationsphase ist entscheidend für den sich ausprägenden Wachstumsmodus und wird als kritisches Stadium für die Generation von Kristalldefekten angesehen. Im Falle der heteroepitaktischen Nukleation von GaN auf Saphir und SiC wurde ein bemerkenswertes Nukleationsproblem gefunden, was sich in anfänglichem Schichtdickenverlust und nichtlinearem Wachstum widerspiegelt. Insbesondere prägt sich in diesen Fällen ein charkateristisches 3D–Inselwachstum (Volmer Weber Wachstum) aus, welches durch eine quadratisch ansteigenden Wachstumrate beschrieben werden kann, wobei nach der Koaleszenz der Inseln lineares Wachstum dominiert.

Ein komplett anderer Nukleationsmechanismus konnte beim GaN Wachstum auf AlN festgestellt werden, wobei sich hier anfänglich eine rund 2ML dicke stark verspannte 2D

Schicht bildet, die bei weiterem Wachstum elastisch relaxiert und 3D Inseln bildet. Dieses Wachstumsphänomen, das häufig bei kompressiv verspannten Materialien auftritt, wird auch als Stranski Krastanow Wachstum bezeichnet und es konnte mittels Massenspektrometrie gezeigt werden, dass beim 2D–3D Übergang die Wachstumsrate einem Übergang von linearem zu exponentiellem Wachstum entspricht. Die damit reduzierte Wachstumsrate von 3D Inseln wurde durch eine verminderte Inkorporation von Atomen durch das Spannungsfeld an verspannten und teils relaxierten Inseln beschrieben. Weiters wurde gezeigt, dass bei Ga Gleichgewichtsbedeckungen grösser als 1 ML der Stranski Krastanow Modus unterdrückt werden kann und vollständig 2D Wachstum bevorzugt wird. Hier wirkt die Ga Bedeckung als Surfactant und ermöglicht die Relaxation der wachsenden GaN Schicht nur durch die Generierung von Misfit Versetzungen.

Je nachdem, ob 2D Wachstum von GaN unter hohen Ga Bedeckungen bevorzugt wird oder ob ein Stranski Krastanow Übergang unter geringen Ga Bedeckungen stattfindet, ermöglicht daher das gezielte Wachstum von GaN quantum wells oder GaN quantum dots auf AlN.

Table of Contents

1. Introduction and Objective

The increasing demand of novel applications in the fields of microelectronics, opto-electronics and chemical sensors has driven many researchers to explore the suitability of a variety of material systems, particularly that of new–generation semiconductor materials. Microelectronic devices such as power transistors and monolithic microwave integrated circuits (MMICs) for their use in high performance radar units and wireless broadband communication links, as well as ultra–high power (> 1MW) switches for distribution control on electricity grid networks require the capability of operation at high power levels, high temperatures and caustic environments. Unfortunately, existing device technologies of elemental semiconductors (Si, Ge) and conventional III–V semiconductors (GaAs, GaP, InP, etc.) cannot tolerate greatly elevated temperatures or chemically hostile environments due to the uncontrolled generation of intrinsic carriers and their low resistance to caustic chemicals.

Separately, there is a strong need for optical devices, especially emitters that are active in the blue and ultraviolet (UV) wavelength region. Currently, light–emiting diodes (LEDs) are increasingly applied to full color displays, traffic lights and automobile and aircraft lighting. Shorter–wavelength semiconductor laser technologies are desired for denser optical storage media, where the storage density can be enhanced quadratically with decreasing laser wavelength. Besides, UV optical sources could be used for airborne chemical and biological sensing systems, allowing direct multi–wavelength spectroscopic identification and monitoring of UV–induced reactions.

The material system of choice offering the possibility to fullfill the majority of all these newer application areas was found to be the group–III nitride semiconductor system, with GaN as its most potential candidate. With a wide direct band gap of 3.4 eV and unique mechanical, electrical and thermal properties, such as high thermal conductivity, a large breakdown field, high electron saturation velocities and a strong bond strength, GaN is an extremely robust material, similar to silicon carbide or diamond. It also forms continuous alloys with other group–III nitrides, that allows tuning of the band gaps and emission wavelengths from ~ 0.7 eV (InN) to 6.2 eV (AlN). Besides, the group–III nitrides exhibit exceptionally high spontaneous and piezoelectric polarization coefficients, which has some attractive applications due to the resulting large built–in electric fields in nitide–based heterostructures.

Early reasearch pinpointed a number of problems with the nitrides which hindered efforts to grow high quality material and fabrication into devices. Since – even to date – there are no commercial bulk GaN crystals available, initially GaN films were grown heteroepitaxially on highly lattice– and thermally mismatched substrates such as GaAs, Si and sapphire by several conventional crystal growth techniques. The resulting films consisted of invariably high defect densities with ~10^{10} dislocations/cm^{-2} and shallow donors, due to crystal defects or impurities. Both the poor crystal quality and the difficulties in p–type doping of GaN have obstructed researchers from fabricating usefull devices for more than twenty years. Over the past decade, great improvements began to appear, particularly with the metal organic chemical vapor deposition (MOCVD) technique along with the use of optimized GaN growth para-

meters and the implementation of low–temperature GaN or AlN nucleation layers. Another breakthrough was achieved by the successful p–type doping of GaN using low–energy beam irradiation and subsequent thermal annealing. These ground–breaking achievements paved the way for the commercialization of high–brightness blue and green LEDs in 1994, though the state–of–the–art GaN devices exhibited dislocation densities still in the 10^8 cm^{-2} range, much higher compared to more mature semiconductor systems such as Si or GaAs.

In addition to the strong device–oriented researches in the nitride field, fundamental studies are currently ongoing to understand the GaN growth mechanisms and further develop the growth technology in an attempt to reduce defect generation and impurity incorporation. Under the non–vacuum conditions of MOCVD generally high growth temperatures are employed, which are beneficial in that they allow growth closer to thermodynamic equilibrium, but pose the disadvantage that upon postgrowth cooling the thermal mismatch with the underlying substrate yields significant amounts of strain and defects in the GaN film. As an alternative, molecular beam epitaxy (MBE) was introduced recently for the nitride system as a comparatively low–temperature growth method, that allows also accurate composition and dopant control on an atomic scale. Moreover, the ultra–high vacuum MBE environment is particularly well suited for studies of growth mechanims thanks to a variety of standard *in situ* analysis tools such as reflection high–energy electron diffraction (RHEED) or laser reflectivity. Even though the MBE growth technique seems more sophisticated, in many application areas the performance of MBE grown heterostructures is still below that obtained by MOCVD. This has raised the question, if the inferior material quality was an inherent limitation of MBE, or whether the conditions for MBE growth of GaN have not been fully optimized. Lately, strong theoretical and experimental efforts were therefore directed towards the optimization of the MBE growth conditions for GaN, in an attempt to improve the typically poor surface morphologies and huge concentrations of extended defects of the films. As an important step in that direction, a detailed understanding of the surface structure and the effect on the atomic–scale growth processes and surface adatom kinetics is essential.

Prior to this research work, extensive theoretical investigations were performed to determine the surface atomic geometries and their reconstructions of the most relevant GaN growth orientations and relate these surface structures to the MBE growth conditions. To prove the theoretical surface concepts, a variety of experimental attempts were suggested by many research groups, but which were either non-direct, i.e. not performed during GaN growth (as by scanning tunneling microscopy, Auger electron spectroscopy) or merely qualitatively (as by RHEED). This leaves the critical interplay between surface structure and the basic dynamic processes during MBE growth of GaN rather speculative. To overcome these experimental limits, in this work a direct and fully quantitative method was developed, that facilitates studies of the relevant atomic–scale surface adatom processes. By means of a quadrupole mass spectrometer (QMS) directed in line–of–sight to the growth surface, the desorbing Ga atoms during growth can be recorded, which gives detailed insights into adsorption/desorption equilibria, surface reactivities, incorporation mechanisms and allows even precise growth rate determinations in GaN growth. In particular, it will be shown that unlike in any other III–V semiconductor material, the equilibrium GaN surface is always terminated by a metal Ga layer, with its thickness changing substantially between different surface orien-

tations. The typical surface lifetimes of the Ga adatoms within this Ga adlayer are determined, which generates a good understanding of the representative Ga adsorbate–substrate binding energetics. Also, to date it was strongly anticipated that the Ga adlayer acts as a surface acting species (*surfactant*) that governs the GaN growth kinetics, especially the diffusion and incorporation of N adatoms. No clear assertion was gained so far and controversies remain of how the Ga adlayer evolves as a function of the MBE growth conditions and to what extent it influences the final GaN surface morphologies. This issue will be resolved in a detailed study, where the Ga adlayer coverages are directly correlated with surface morphologies and surface–mediated defects of the technologically most relevant wurtzite (0001) GaN surface.

While these primary investigations determine the key features of surface and growth kinetics on GaN surfaces during *homoepitaxial growth*, a second focus of this work will deal with the *heteroepitaxial* nucleation kinetics of GaN on different substrates. As known for many other heteroepitaxial systems, the nucleation stage is a crucial determinant for the subsequent layer properties, since the majority of deterious crystal defects, mainly dislocations, are generated during this phase. In general, GaN growth on conventional substrates such as sapphire or SiC follows a typical three–dimensionsal (3D) island (i.e. Volmer Weber) growth mode, leading to high amounts of threading dislocations (TDs) upon coalescence of these islands. To understand the tendency for island formation and to propose the possibility for precise control of the island growth rate and the coalescence stage, further useful insights will be delivered by the QMS technique as it facilitates an exact determination of the initial "wetting problem" and the current growth rate.

Furthermore and in view of the fast development of GaN–based nanostructures, such as quantum dot (QD) structures, the heteroepitaxial nucleation and the island growth kinetics are also extended to GaN growth on AlN substrates. Such GaN–based QD structures are lately heavily pursued as they are expected to lead to improved properties in optoelectronic devices, such as higher gains, lower threshold currents and enhanced temperature characteristics due to quantum confinement effects. To date, the most successful fabrication of GaN QDs is realized by their self–assembled growth via the Stranski–Krastanow (SK) growth mode, that occurs not only during GaN heteroepitaxy on AlN, but also during growth of many other semiconductor epilayers under compressive strain (i.e. SiGe on Si, InAs on GaAs, CdSe on ZnSe, etc). Within the SK mode, an initially deposited highly strained two–dimensional (2D) wetting layer is known to relax through the free surfaces of 3D–islands (QDs), instead of generating misfit dislocations. As a major research topic at present, these dislocation–free islands are sought to be controlled in a way to obtain homogenous size distributions as well as well–defined sizes, densities and positions. However, these tasks underlie considerable limitations, since in GaN QD formation the complex dependency of growth conditions (GaN coverage, temperature and Ga/N flux ratio) and the statistical nature of nucleation yield nonuniformities in size and uncontrolled positions. Ambitious efforts of investigating the effect of the growth kinetics on the strain relaxation and QD formation during GaN heteroepitaxy on AlN have been done so far, but none were strictly concerned with understanding the influence of the atomic–scale adatom processes on the island growth mechanisms. Special emphasis will be directed to these latter issues in the final part of this work, where extensive Ga desorption studies will demonstrate that the GaN island formation is intimately linked to the AlN substrate surface

structure, the strain relaxation mechanism and particularly the Ga surface and incorporation kinetics. Also, the role of the Ga adlayer coverage on the growth and relaxation of the GaN/AlN structure will highlight its impact on the details of the SK growth mode. With these fully quantitative experiments, moreover the exact growth rate during the entire SK–island growth can be gained. This allows not only a more accurate determination of the actual critical thickness for strain relaxation, but also opens the gateway for precise size and density control of GaN QDs.

2. Crystal Properties of Group–III (Ga, Al, In, B) Nitrides

2.1. Common Crystal Structures

Among the family of the group–III nitrides typically three main crystal structures are shared: the wurtzite (α-phase), zincblende (β-phase) and rocksalt (NaCl) structures. While the rocksalt structure (a cubic modification) is synthesized only at very high pressures, the thermodynamically stable phases under ambient conditions are wurtzite for bulk GaN, AlN and InN, and zincblende for BN. All other structures and their modifications (polymorphs) for any given nitride are either less common or metastable. For BN the hexagonal or graphite–like (sp^2 hybridized) crystal structure is only rarely produced (under high temperatures and low pressures) and the wurtzite structure occurs as a metastable phase during shock compression, with typically a high degree of defects, impurities and contamination with other crystal modifications. On the other hand, zincblende GaN, AlN and InN have been successfully stabilized by epitaxial growth on cubic substrates such as Si [1], 3C–SiC [2], GaAs [3] and MgO [4].

In the wurtzite structure the group–III and nitrogen atoms arrange in two hexagonal close packed (hcp) sublattices, that are displaced along the c–axis ((0001) direction) by 5/8 of

wurtzite   **zincblende**

[0001] a_{cub} [111]

c_{hex}
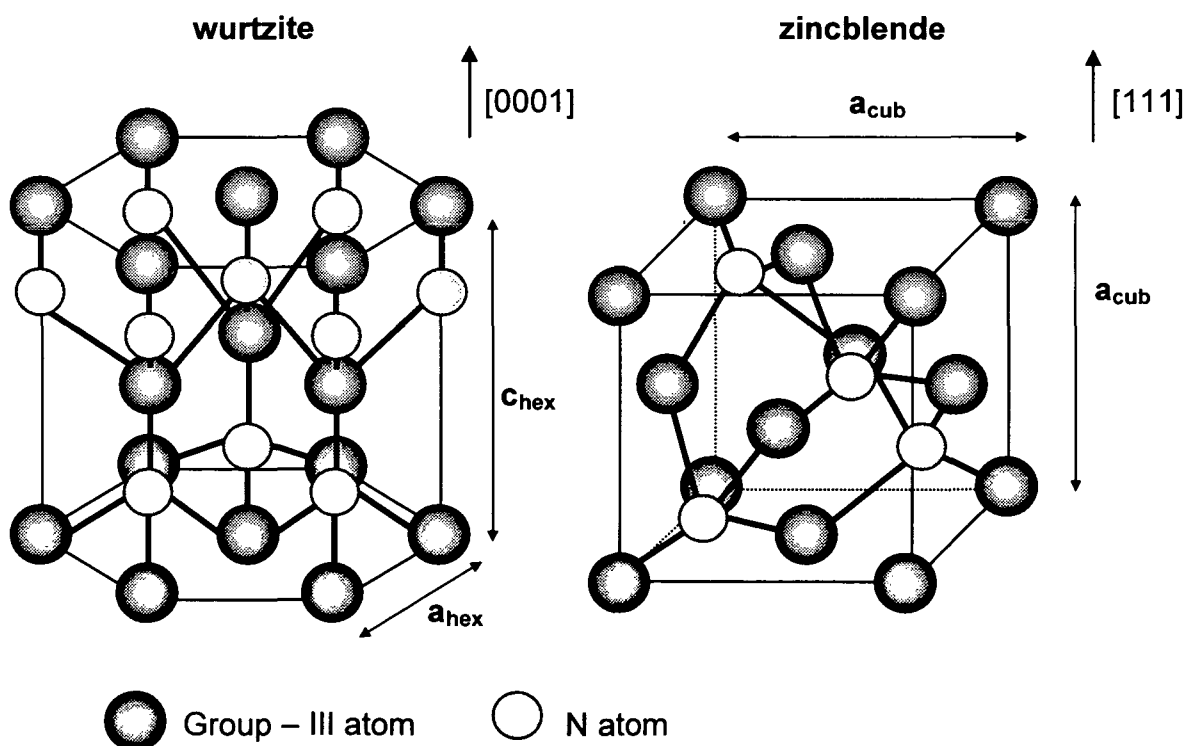
a_{cub}

a_{hex}

● Group – III atom   ○ N atom

Fig. 2.1. The wurtzite structure along the [0001] direction (left) and zincblende structure along the [111] direction (right) with their respective lattice constants a_{hex}, c_{hex} and a_{cub}.

the cell height. Similar to the diamond crystal structure, the zincblende structure consists of two face centered cubic (fcc) sublattices (with four atoms of each type) shifted by 1/4 of the distance along the body diagonal (Fig. 2.1). In both structures, each atom (group–III and N atom) is bound by four sp^3–hybridized atomic orbitals to its nearest neighbor, which results in a tetrahedral coordination with coordination number 4. The basic difference between the two can be seen merely in the stacking sequence of the closest packed (cp) diatomic planes. Whereas the wurtzite structure is defined by a stacking sequence of ABABAB for the (0001) planes along the [0001] direction, an ABCABC sequence for the (111) planes along the [111] direction is characteristic for the zincblende structure. Another difference appears when viewing the respective bond lengths in both structures. The group–III – nitrogen bond lengths are all the same in the zincblende structure, but two deviating bond lengths are found in the wurtzite structure. While one bond length equals uc, the other three bonds have a length described by

$$a\left[\tfrac{1}{3} + \left(\tfrac{1}{2} - u\right)^2 \left(\tfrac{c}{a}\right)^2\right]^{\frac{1}{2}}$$

(2.1.)

where u is a dimensionless internal cell structure parameter defining the cation – anion bond length. Ideally, this parameter has a value of $u = 8/3$ and the ratio between c- and a- lattice

Physical property	α-AlN	α(β)-GaN	α-InN	β-BN
band gap E_g [eV]	6.2	3.4 (3.2)	~0.7 - 0.9	6.1 - 6.4
lattice constant a [Å]	3.112	3.189 (4.52)	3.533	3.615
lattice constant c [Å]	4.982	5.186	5.693	
binding energy E_b [eV/atom pair]	11.67	9.06	7.97	8.15
density ρ [g/cm³]	3.23	6.15	6.81	3.45
Debye temperature Θ_D [K]	1150	600	660	1700
static dielectric constant ε	8.5	8.9 (9.7)	15.3	7.1
thermal conductivity k [W/mK]	285	130	80	416 - 742
thermal expansion coefficients α_a [10⁻⁶/K]	4.2	5.59	3.8	1.2
α_c [10⁻⁶/K]	5.3	3.17	2.9	
melting temperature T_m [K]	2773	3023	1373	3246

Tab. 2.1. Relevant crystal and physical parameters of the predominant phases of binary group–III nitrides (all data emanate from Ref. [6], except for the controversial band gap of InN with an energy of 1.9 eV for nano–crystalline [7] and the recently experimentally determined energy of 0.7 eV for wurtzite single–crystalline material [8]; the binding energies are taken from Refs. [9,10]).

constant should be given by c/a = $(8/3)^{1/2}$. However, in real crystals (applying also for the group–III nitrides) u and c/a are slightly different. For AlN, GaN and InN $c/a < (8/3)^{1/2}$ holds true, while for BN $c/a > (8/3)^{1/2}$ was found. These observations correlate with the fundamental conception that wurtzite materials with a c/a ratio less then the ideal value are stable, and such with a greater value are unstable [5].

As a consequence of the large difference in the electronegativities the bonds between the group–III and the nitrogen atoms have a significant ionic component to the overall covalent bond nature. Among all III–V semiconductors the nitrogen based materials offer exceptionally strong covalent bonds, because nitrogen has the smallest covalent atomic radius of 0.7 Å of all group–V elements (comparatively: P: 1.1 Å, As: 1.18 Å, Sb: 1.3 Å). The consequentially short bond lengths and high binding energies explain the outstanding mechanical, thermal and chemical stability of the group–III nitride family. For a general overview, some of the most relevant crystal and physical properties for the predominant phases of GaN, AlN, InN and BN are displayed in Table 2.1.

2.2. Polarities of Wurtzite Nitrides

Although cubic nitrides pose some potentially interesting features, to date nearly all technological applications of the (Ga, Al, In)N system are based on their most stable form, the wurtzite phase. For this phase, the prime growth direction is along the hexagonal {0001} basal plane, where the atoms are stacked in bilayers with one side consisting of anions and the other of cations. As the wurtzite structure is not centrosymmentric, there needs to be clearly distinguished between two possible atomic arrangements for each side of the bilayers and also which atom (group–III metal or N) exists on the final {0001} plane of each surface. This conception is referred to polarity, defining two inequivalent growth orientations for the group––III nitrides: the [0001] or metal–face orientation with group–III atoms in the top position of the bilayer and the [000$\overline{1}$] or N–face orientation with N atoms in the top

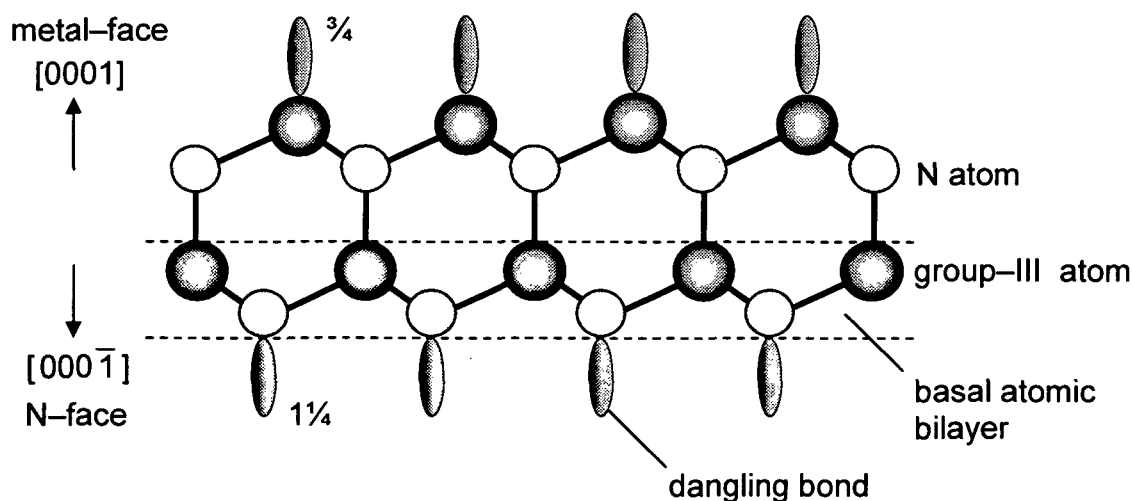
Fig. 2.2. Side view ($\langle 11\overline{2}0 \rangle$ projection) of the polar wurtzite orientations ([0001] or metal–face and [000$\overline{1}$] or N–face) for the group–III nitrides indicating also the number of electrons per dangling bond.

position (Fig. 2.2). Also, the two polar surfaces differ slightly in the number of electrons per dangling bond, which amount to ¾ for metal–face surfaces and 1¼ for N–face surfaces. At this point it is also important to note that surface polarity must not be mistaken with surface termination, i. e. a metal–face surface does not simultaneously mean metal terminated. Termination is a surface property that is correlated with surface reconstructions of the top atomic layer.

The realization of different surface polarities is especially sensitive to the applied growth technique, as has been demonstrated to great extent for the case of GaN. Holding true for any technique, however, polarity remains a bulk property and is fixed once the first bilayer of GaN is grown. Growing GaN by metalorganic chemical vapor deposition (MOCVD) on a sapphire substrate results typically in high–quality Ga–face (0001) surfaces [11,12], while MBE growth on the same substrate yields commonly N–face ($000\bar{1}$) surfaces [13,14]. On the other hand and independent of the growth technique, GaN grown on Si (111) [15,16] and 6H-SiC [17,18] was found to always induce Ga–face surfaces.

The differences of the two polar surfaces are further reflected in the growth kinetics, such as adatom surface diffusion, incorporation and doping mechanisms which in turn determine the overall structural and electrical properties of the grown material. For instance, for a N–face surface adatoms experience a much higher diffusion barrier [19,20], p-type doping is aggravated [21] and residual impurities such as carbon and oxygen are more likely to incorporate compared to growth along the Ga–face surface [22]. These observations can be ascribed to specific surface atomic structures along with the possible surface reconstructions, as will be discussed in detail for both relevant orientations in section 5. In addition, the formation of extendend defects was found to also rely strongly on the chosen growth orientation: generally, higher dislocation densities [23] and elevated levels of point defects [24] with consequently inferior electrical transport properties are observed more in GaN films grown along N–face orientations than along Ga–face orientations [25,26].

Finding out which type of polarity is predominant for a grown GaN film cannot be simply deduced from any of the above empiricisms, but requires mostly refined electron microscopic techniques such as high–resolution image matching of electron micrographs [17] or convergent beam electron diffraction (CBED) [11]. However, the first attempts using CBED to determine the polarity of identical GaN films have led to contradictory results [11,27]. Meanwhile, Seelmann–Eggebert *et al.* developed a very straightforward method to directly identify the respective surface polarities by exploiting their different chemical etch reactivities [28]. Using hydroxide solutions (NaOH, KOH), N–face GaN surfaces were found to be reduced to atomically flat surfaces, while Ga–face surfaces were basically inert to etching, as determined from subsequent roughness analysis by atomic force microscopy (AFM). Recently, a novel scanning probe microscopy (SPM) technique was employed to map the polarity distribution of GaN heterostructures by taking advantage of the pronounced piezoelectric character of the group-III nitrides. Originally developed to visualize the domain structure in ferroelectric thin films, this so-called piezoresponse force microscopy (PFM) method is based on the sign dependence of the piezoelectric coefficient on the polarization direction, which leads to an opposite phase contrast between Ga- and N-face polar regions and further allows to resolve the inversion domain boundary (IDB) structure on a nanometer scale [29].

The latter method is particularly suitable for the group-III nitride system which benefits from exceptionally huge polarization coefficients. In their wurtzite phase, the group-III nitrides are piezoelectric as a result of strain, with piezoelectric coefficients about one order of magnitude higher than in other III-V semiconductors [30]. Consequently, large ($\approx$ MV/cm) built-in electrostatic fields are induced, which affect dramatically the optical and electrical properties of nitride heterostructures. For instance, new and unexpected effects as a significant reduction of the effective band gap were observed due to the quantum-confined Stark [31] and Franz Keldysh [32] effects that cause a red shift in optical absorption and emission spectra [33]. Moreover, theoretical and experimental investigations on piezoelectric-induced effects led to the realization of high-density low-dimensional charge gases, e.g. at high electron mobility transistor (HEMT) heterointerfaces [34].

To give an understanding of the relationship between strain and piezoelectric polarization, the piezoelectric tensor along the c-axis of wurtzite group-III nitrides is defined by

$$P_{PE} = 2\frac{a - a_0}{a_0}\left(e_{31} - e_{33}\frac{C_{13}}{C_{33}}\right) \qquad (2.2.)$$

where e_{31} and e_{33} are the piezoelectric coefficients, C_{13} and C_{33} the elastic constants and a, a_0 the basal lattice parameters for strained and relaxed crystals. In addition to the strain-induced piezoelectric polarization, Bernardini *et al.* predicted that a significant spontaneous polarization along the hexagonal c-axis is present in wurtzite nitrides due to their non-centrosymmetry and large ionicity factor of the covalent metal-nitrogen bonds. Experimental results revealed that even in unstrained GaN heterostructures there exist very large electric fields [34-36].

The orientation of both piezoelectric and spontaneous polarization is defined by convention such that the positive direction goes from the metal atom (cation) to the nearest neighbor nitrogen atom (anion) along the crystallographic [0001] axis. Since the sign of the spontaneous polarization is predicted to be negative, the orientation then always points from the metal-face to the N-face side of the crystal (i.e. [$000\bar{1}$] direction) [29]. On the other hand, from (e_{31} - $e_{33}(C_{13}/C_{33})$) < 0 follows that the piezoelectric polarization is negative for tensile and positive for compressive strained nitride crystals. As a consequence, the orientation of the piezoelectric and spontaneous polarization is parallel in the case of tensile strain, and anti-

material	P_{SP}	e_{31}	e_{33}
AlN	-0.1	-0.64	1.8
GaN	-0.032	-0.44	0.86
InN	-0.041	-0.52	1.09
ZnO	-0.057	-0.02	-0.02
GaAs		0.06	-0.12

Tab. 2.2. Spontaneous polarization and piezoelectric coefficients all in units of C/m^2 for the wurtzite group-III nitrides compared with other semiconductor materials, as obtained from first principles local density approximation (LDA) calculations [30].

parallel in the case of compressive strain. Thus, the absolute value of the total polarization is defined by the sum of spontaneous and piezoelectric polarization. To picture the contribution of each polarization component, theoretical values calculated from first principles density-functional theory are presented in Table 2.2 for the group-III nitrides in comparison with other semiconductor materials. It is obvious that the value for the spontaneous polarization increases from GaN to InN and further to AlN. This relation can be understood easily when considering the nonideality of these wurtzite structures, with the internal structure parameter u getting larger and the c/a ratio smaller when going from GaN over InN to AlN.

2.3. Substrates for Nitride Heteroepitaxy

One of the final objectives of nitride-based technologies is the commercial production of dislocation–free devices, since dislocations act as non-radiative recombination centers and traps for charge carriers that impair the performance of both optoelectronic and microelectronic devices severely. The most simple scenario to reduce dislocation densities by at least the amount of the strain induced contribution by misfit dislocations can be pursued by performing homoepitaxial growth on nitride bulk material. At present, this approach, however, is limited by extreme difficulties in the synthesis of single-crystalline bulk nitride wafers mainly due to thermodynamic reasons. As for the case of GaN, an extremely high melting temperature ($\approx$ 2500 °C) and an enormous equilibrium nitrogen pressure of $\approx$ 45 kbar make conventional liquid crystal growth techniques from stoichiometric melts (such as the Czochralski- and Bridgman methods as typically used for other semiconductors) basically impossible. Such conditions resemble rather the high-pressure synthesis of diamond and can be easily understood in the context of the very strong bond strengths for the three participating phases of gas (N_2), metallic liquid (Ga) and semiconductor solid (GaN). Molecular nitrogen is the strongest bonded diatomic molecule in nature with a dissociation energy of 9.76 eV, whereas liquid Ga has a very high enthalpy for evaporization (2.81 eV/atom) that is also reflected in its very high boiling point of 4000 K [37]. Likewise, solid GaN is strongly bonded with an energy of 9.12 eV/atomic pair, explaining the high melting temperature as noted above [38]. Although limited to fundamental research, the most promising results in this direction were achieved by nitrogen dissolution in a Ga melt at reduced temperatures between 1400 - 1600 °C and a lower nitrogen gas pressure of $\approx$ 20 kbar [39]. Wurtzite GaN crystals were then stabilized through a layer-by-layer growth mode by controlled cooling of the supersaturated melt, leading to wide defect-free areas of negligible dislocation densities between 10 - 100 cm^{-2}. However, the limited lateral size of < 0.5 inches and the slow growth rate of below 0.1 mm/h, yielding an enormous process duration of typically 120 - 150 hours, have restricted the availability of such high-quality GaN substrates for commercial uses.

Due to this unfortunate situation, the whole technological development of nitride-based devices relies inevitably on heteroepitaxial growth on foreign substrates. Consequently, researchers have to put up with much higher dislocation densities, but to achieve yet improved nitride film quality, selecting the most appropriate substrate has proven to be of great importance for nitride heteroepitaxy. There are several criteria required for such a proper selection:

First, the high growth temperatures typical for the heteroepitaxial growth of group-III nitrides demand temperature-stable substrate materials that do not melt, decompose, undergo any phase transitions and that also are chemically non-reactive in the temperature range of interest. Along with these high temperatures, thermal expansion mismatch is regarded as a significant factor that could cause distortion, cracking and even layer detachment. Therefore, the thermal expansion coefficients of the substrate should be as close as possible to those of the nitrides in order to avoid such thermally-induced drawbacks during cooling from the elevated growth temperatures. Another prerequisite is a generally high substrate crystal quality with low defect density and low surface roughness, which can not only be influenced by the respective growth technique but which are also strongly dependent on mechanical and chemical treatments like polishing, etching and cleaning. Besides, aiming at minimized misfit dislocation densities in the epitaxial layer, a low lattice mismatch between substrate and nitride is usually desirable. However, early investigations, especially in metal epitaxy, have pointed out that good epitaxy can also occur when lattice mismatches are not that small [40]. The converse is also true, and excellent lattice match is no guarantee of good oriented epitaxy. In particular, Green *et al.* were unable to observe oriented growth of metals on LiF, even for lattice misfits of less than 0.4% [41]. For epitaxial growth of nitrides, the lattice mismatch actually does not play such an important role as does thermal mismatch, because the nitrides mostly crystallize in either the wurtzite or zincblende structures on several substrates even with quite different lattice constants [42], as also summarized in Table 2.3.. Finally, of all criteria considered here, availability and low-cost production are undoubtedly the most significant, as they dictate what kind of substrates are suitable for high-grade technological applications.

With respect to the realization of particular devices there are often additional demands necessitated for the substrate material. For instance, the presence of appropriate substrate cleavage planes perpendicular to the grown epilayer surface are especially useful for edge–emitting lasers. Microelectronic devices (such as high-power transistors) require typically a high thermal conductivity and favor also good electrical conductivity of the substrate material in order to realize backside contacting.

The major difficulties in group-III nitride heteroepitaxy are mainly given by the lack of an adequate substrate material that fulfills the majority of these requirements. However, to comply with the respective application one needs to make compromises and select between a variety of possible substrates.

Sapphire

To date, basal c-plane sapphire (Al_2O_3) presents the most preferred substrate material for growth of wurtzite nitrides, due to a variety of advantages: Sapphire offers a wide availability, low-cost and large area production of excellent crystal quality and is mechanically very stable at the elevated temperatures in nitride heteroepitaxy. Because of the high energy gap of 8.8 eV it is transparent in the spectral region of the nitrides (which e.g. is quite beneficial for the fabrication of light emitting diodes) and also insulating (which on the other hand impairs the contact preparation of laser structures). The lattice and thermal mismatches between sapphire and the group-III nitrides are rather large and result in considerable strain

after postgrowth cooling. Represented by a rhombohedral crystal structure, Al_2O_3 can also be described by a larger unit cell of hexagonal symmetry in $\{0001\}$ projection, where two hexagonal oxygen sublattices are rotated by $30°$. Consequently, the group-III nitrides grow with a $30°$ in-plane rotation with respect to the sapphire substrate. The atomic arrangement on the (0001) basal plane for both c-plane sapphire and group-III nitride is shown schematically in Fig. 2.3., with an epitaxial relationship as follows: $(0001)_{III-N} \parallel (0001)_{sapphire}$, $[01\bar{1}0]_{III-}$ $_N \parallel [\bar{1}2\bar{1}0]_{sapphire}$, and $[\bar{1}2\bar{1}0]_{III-N} \parallel [\bar{1}100]_{sapphire}$. According to this concept, the large lattice mismatch (-13.9 % for GaN and -10.9 % for AlN on sapphire) is accommodated by domain matching where integral multiples of lattice constants or major lattice planes match across the film/substrate interface [43]. In the case of (0001) AlN, it was found that for a complete domain match every eight $[01\bar{1}0]$ atomic planes of AlN correspond to nine $[\bar{1}2\bar{1}0]$ atomic planes of sapphire [44]. This relation of domain matched atomic planes corresponds to a 6/7 ratio between (0001) GaN and sapphire, as verified by high-resolution electron microscopy [45].

O-plane of sapphire

III-plane of III-N

$[\bar{1}100]$

a_{III-N}

axes of sapphire

$[11\bar{2}0]$
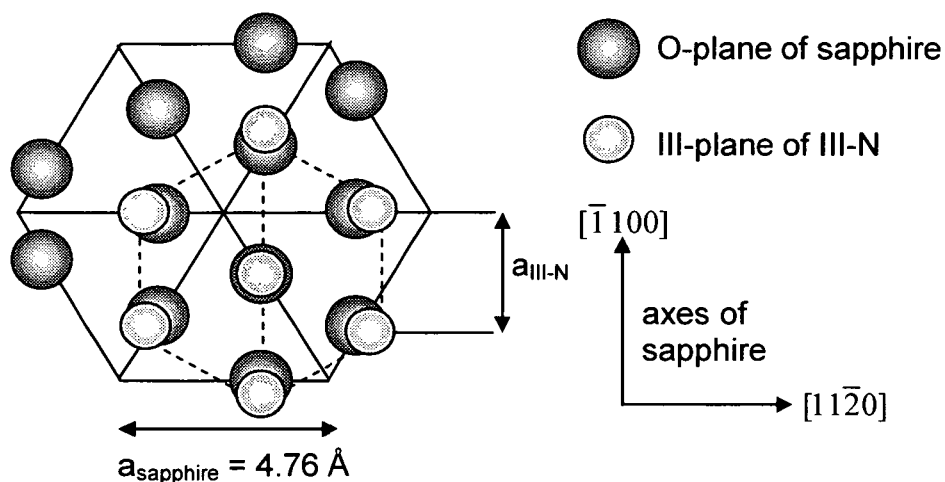
$a_{sapphire} = 4.76\ \text{Å}$

Fig. 2.3. Schematic representation of the in-plane atomic arrangement for (0001) group-III nitride growth on c-plane sapphire.

When group-III nitrides are grown on c-plane sapphire, the predominant polar $\{0001\}$ set of orientations give rise to pronounced polarization fields that are generally advantageous for particular microelectronic applications as for the two-dimensional electron gas formation in HEMT structures [34]. For short-wavelength optoelectronic devices these polarization fields need to be avoided since they cause increased charge separation within quantum wells that decrease electron–hole recombination rates and redshift the emission wavelengths [31, 46-48]. The most promising approach to eliminate such polarization effects is through growth of nitride structures along nonpolar directions, i.e. perpendicular to the c-axis. Satisfactory internal field-free GaN structures were recently demonstrated on particular Al_2O_3 orientations, such as r-plane $[1\bar{1}02]$ [49], a-plane $[11\bar{2}0]$ [50], and m-plane $[01\bar{1}0]$ Al_2O_3 [51]. Although GaN grown on a-plane sapphire has a lattice mismatch of less than 2% [52], the a-plane does not coincide well with the crystallographic symmetry of GaN and mixed orientations were observed [53]. A similarly small lattice mismatch is present when GaN is grown on m-plane

sapphire with the additional benefit that complete crystallographic symmetry between the two orientations exists. Optimizing the tilt angle of the *m*-plane sapphire substrate around the *c*-axis was proposed as a proper means to achieve near lattice–match and reduce the commonly high dislocation densities typical for GaN grown directly on *c*-plane sapphire ($10^8 - 10^{11}$ cm^{-2}). However, the best reported dislocation densities in GaN films grown on *m*-plane sapphire with MOCVD and non-optimized tilt angles are 2×10^9 cm^{-2} [51]. Stronger efforts in dislocation reduction were made for nonpolar GaN grown on *r*-plane sapphire, especially by using the epitaxial lateral overgrowth (ELO) technique. Also applicable to GaN on *c*-plane sapphire or any other substrate, this technique (achievable in MOVCD and hydride vapor phase epitaxy (HVPE)) eliminates defects partially by implementing adequate dielectric masks that hinder the propagation of threading dislocations (TDs) of the initially highly dislocated GaN into its overlayer. That way, for the non-polar case (i.e. on *r*-plane sapphire), TD densities could be reduced from 10^9 cm^{-2} in non-ELO GaN to basically defectfree areas in the overgrown regions and 5×10^6 cm^{-2} in the unmasked wing regions of the ELO material [54,55]. It is therefore conceivable that group-III nitride based optoelectronic technologies will increasingly benefit from a combination of device structure growth along non-polar planes (i.e. substrate orientations perpendicular to the *c*-axis) and the unique ELO technology.

Silicon Carbide

Besides the use of sapphire, silicon carbide (SiC) is gaining more significance as a base material for group-III nitride epitaxy, as SiC itself shows outstanding properties for the realization of unique microelectronic applications. The high electron saturation velocity and thermal conductivity as well as the large breakdown electric field allow the operation of high–power and high–frequency microelectronic devices in regions that are typically out of reach for Si or GaAs based devices. Also, its extreme mechanical hardness and chemical and radiative stability give this wide band gap semiconductor a commanding position where device performance in hazardous environments is needed, even above 1000 K. Besides the band gap energy of 2.4 – 3.3 eV for the different polytypes and its good electrical conductivity along with the availability of both n- and p-type doped material, SiC has an additional advantage over sapphire in that it offers a much smaller thermal and lattice mismatch with the group-III nitrides (see also Table 2.3. for comparison). Although much progress has been made in the fabrication of SiC–based technologies, the serious SiC growth problems accompanied by the very high costs (10 times more expensive than sapphire production) limit some large scale industrial applications. In conventional SiC growth, where single crystals grow on a cooled seed by sublimation, the interface produces high densities of defects, such as dislocations, inclusions and also micropipes which are the most severe ones [56–58]. Micropipes are proposed to be generated in the presence of screw dislocations and by the involvement of liquid silicon droplets [59]. These linear voids pass through the whole length of the crystal and even replicate into the epitaxial film. For device manufacture, micropipe densities of less than 10 cm^{-2} are required, otherwise these defects destroy p-n junctions and have deleterious effects on power devices [60].

Similar to the diamond crystal structure, SiC consists of a tetrahedral coordination where each atom is covalently bonded to four atoms of the other species. These Si–C bonds are structured in hexagonal bilayers of alternating silicon and carbon atoms, where different stacking and orientation sequences of the bilayers determine different crystal modifications, so called polytypes. According to two possibilities to continue the tetrahedral arrangement of Si–C bonds, eihter by a 60 ° or 180° rotation, two ways exist for the mutual orientation of adjacent bilayers, being either of zincblende or wurtzite nature. Zincblende bonds are rotated 60 ° with respect to nearest neighbors while the hexagonal bonds in the wurtzite structure represent mirror images (Fig. 2.4).
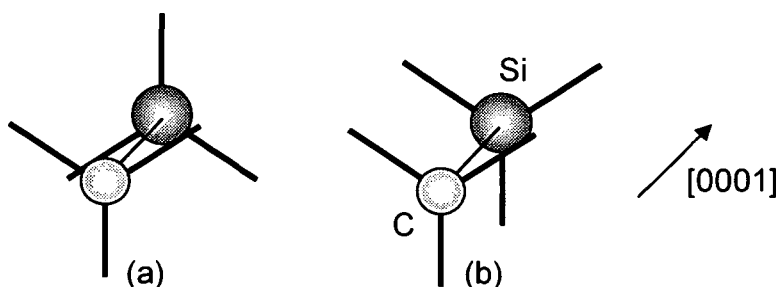

Fig. 2.4. Zincblende (a) and wurtzite (b) bonding between Si and C atoms in adjacent planes. The three tretrahedral bonds are 60 ° rotated in the cubic case and mirror images in the wurtzite case.

Zincblende SiC is also referred to as 3C–SiC (or β – SiC), whereby the number 3 indicates the number of bilayers per unit cell along the [0001] direction and the letter C emphasizes the overall cubic symmetry of the crystal. In this case, the stacking of the Si–C bilayers obeys an ABC(ABC)...sequence, as illustrated in Fig. 2.5 (a). The purely wurtzite ABAB...stacking sequence is denoted as 2H–SiC, meaning that the bilayer arrangement is repeated every two bilayers. However, the 2H polytype has not been observed to be stable in nature. The 3C–SiC and 2H–SiC polytypes are the only pure ones, meaning they have either totally cubic or completely hexagonal bonds only. A combination of cubic and hexagonal stacking sequences is the most common and stable arrangement in SiC and about 170 such polytypes have been identified experimentally, that consist of sometimes quite large cubic/hexagonal periodicities along the [0001] direction [61]. Among these polytypes, 4H– and 6H–SiC are the predominant candidates used for group-III nitride based device applications. While 4H–SiC is composed equally of cubic and hexagonal bonds, i.e. two bilayers of identical orientation are followed by two bilayers of opposite orientation, the 6H–SiC polytype is found to be two-thirds cubic, yielding stacking sequences as presented in Figs. 2.5 (b) and (c). Both these polytypes are based upon hexagonal unit cells of a height of 4 bilayers (10.05 Å) and 6 bilayers (15.12 Å), respectively. Because of this overall hexagonal symmetry, the family of hexagonal polytypes is collectively referred to as α–SiC, despite the partially cubic bond nature. Unlike growth on c-plane sapphire, there is a parallel epitaxial order between the group-III nitrides and the α–SiC polytypes, i.e. $(0001)_{III-N} \| (0001)_{\alpha\text{-SiC}}$ and $[2\bar{1}\bar{1}0]_{\alpha\text{-SiC}}$

$[2\bar{1}\bar{1}0]_{\text{III-N}} \parallel [2\bar{1}\bar{1}0]_{\alpha\text{-SiC}}$. It is also important to note, that a single polytype might exhibit different surface truncations, depending on the position of the topmost bilayer. In the case of 6H–SiC there exist six possible surface truncations, given by three different bilayer depths (that cause stacking faults) and three possible surface terminations constituted through a 60 ° rotation. As for any wurtzite crystal, one needs to also distinguish between two possible polarities, where in the ideal case of a bulk truncation with intact bilayers the (0001) 6H–SiC surface would be Si–terminated and the ($000\bar{1}$) surface C–terminated.
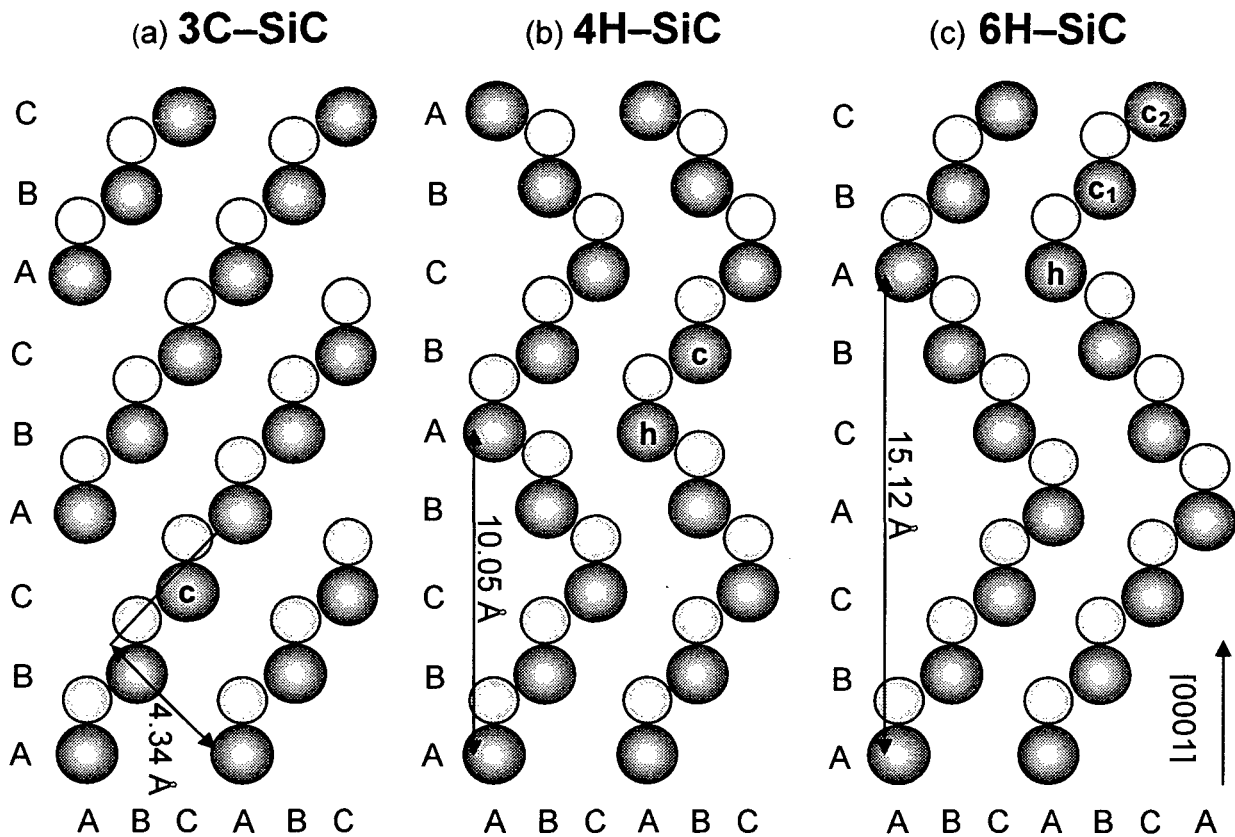

Fig. 2.5. Crystal structures in side view, i.e. $\langle 11\bar{2}0 \rangle$*, projection of (a) the purely cubic 3C–SiC polytype, (b) the 4H–SiC polytype where half of the atomic sites are hexagonally bonded (h) while the other half are cubic (c) and (c) the 6H–SiC polytype where two-thirds of the atomic sites are cubic. Note the different lattice constants for the various polytypes.*

One of the most crucial issues for nitride epitaxy is the requirement of a high quality substrate surface, that is atomically flat and free of any surface impurities and imperfections. Compared with the high perfection of Si, GaAs and even sapphire wafers, commercially available SiC substrates exhibit a poor surface morphology with large amounts of damage from cutting and polishing processes. Since SiC is quite inert, it is difficult to remove the contaminated and disordered surface layer by conventional chemical methods (e.g. molten hydroxides and peroxides) and gain atomically flat surfaces [62,63]. Reactive ion etching (RIE) does also not apply well to SiC surface preparation because of usually high levels of

plasma induced surface damage. On the other hand, prolonged heating in oxygen at atmospheric pressures and temperatures around 1000 °C produces well ordered SiC surfaces but also leaves some polishing scratches behind [64] and causes an unwanted oxide layer, that in turn could be removed by hydrofluoric acid [65,66]. Nevertheless, the SiC surface will in any case be contaminated with spurious and very stable oxides when exposed to ambient atmosphere. Therefore, pregrowth ultrahigh vacuum (UHV) procedures are further required for complete oxide removal; e.g. annealing at temperatures above 1000 °C does successfully remove oxides and contaminants, but leads to Si depletion and graphitization [66,67]. To bypass this problem, Kaplan and Parrill suggested to treat the SiC surface by a Si or Ga beam to remove oxides as volatile SiO and Ga_2O at temperatures low enough (850 °C) to prevent Si depletion [65]. In order to achieve SiC surfaces free of polishing scratches, hydrogen etching has proved as the most appropriate method. Performed at temperatures above 1400 °C this technique yields typically atomically flat terraces of more than 1000 Å width (for low miscut angles) which are separated by integral multiples of the SiC unit cell [68–72].

Even on such perfectly prepared SiC substrates there exists still a variety of implications that makes nitride growth on this substrate not necessarily more favorable than on sapphire. Several studies pointed to the poor wetting behavior of GaN when directly deposited on 6H-SiC [73,74] along with the difficulty of performing two–dimensional growth; instead typically three-dimensional islands occur [75,76], which upon their coalescence lead to GaN films with high defect densities and similar defects as those observed in GaN grown on c-plane sapphire [77,78].

Other Substrates

Several other substrate materials for nitride heteroepitaxy have been tried, some of which are starting to show quite good suitability. Early studies focussed on the readily available cubic GaAs (100) and (111) substrates, where according to the large thermal and lattice mismatch between GaAs and GaN and the lack of thermal stability of GaAs [79] at the high temperatures required for optimum GaN growth, generally very poor quality GaN material was produced [80,81]. Attempts to grow cubic GaN on MgO with a lattice mismatch of 7.5 % have also resulted in material with electrical and optical quality much inferior to that grown on sapphire [82].

As a low–cost alternative with large–size availability, Si (111) is gaining some interest, even though the large lattice and thermal mismatches to GaN (0001) seem at first unfavorable. Especially, the large tensile strain introduced by the difference in thermal expansion coefficients is responsible for cracking of thick GaN films appears. But, with the implementation of AlN nucleation layers crack–free epilayers of GaN could be achieved [83] and with a systematic insertion of Si interlayers (Si δ–doping) dislocation densities were significantly reduced [84], therefore even on Si (111) the fabrication of light emitters was facilitated [85].

As another candidate, spinel or cubic $MgAl_2O_4$ (111) offers not only a smaller lattice mismatch to GaN (~ 9%) as compared with sapphire (~14 %), but also shares a common cleavage plane with GaN, allowing the fabrication of cleaved cavities required for edge emitting lasers.

In this case, the wurtzite GaN material was reported to show physical properties equivalent or even superior to those grown on basal c-plane sapphire substrates [86–88].

The fabrication of nitride based optoelectronic devices free of polarization induced fields can be facilitated by performing growth along nonpolar directions, as has been discussed for the various orientations perpendicular to c-plane sapphire substrate. Additionally, ZnO $(1\bar{1}00)$ and γ-LiAlO$_2$ are substrates appropriate to produce similar nonpolar m-plane $(1\bar{1}00)$ GaN surfaces with an anisotropic lattice mismatch of only between 0.5–2 % [89–91]. In constrast to sapphire or SiC, γ-LiAlO$_2$ can also be selectively etched with respect to GaN, and the epitaxial structure could thus be bonded to an integrated reflector, that would enable the production of on-chip LEDs. In this context, improved quantum efficiency has recently been demonstrated for nonpolar GaN/(Al,Ga)N quantum wells by direct growth on γ-LiAlO$_2$ [92].

The most novel substrate that has come into play only recently is zirconium di–boride (ZrB$_2$), a semi-metal with a primitive hexagonal lattice structure that has been proposed as a closely lattice and thermally matched substrate for GaN epitaxy (0.6 % and 5 % mismatch, respectively) [93,94]. First attempts to grow high–quality GaN on this substrate resulted in threading dislocation densities about two orders of magnitude lower than on c-plane sapphire $(10^8\,\mathrm{cm}^{-2}$ versus $10^{10}\,\mathrm{cm}^{-2}$, respectively), but also generated an intermediate cubic–phase layer of ZrBN as a consequence of interdiffusion of nitrogen and boron atoms [95].

For an overview, Fig. 2.6. displays the basal lattice parameters and thermal expansion coefficients for a variety of substrates which ideally should be matched as close as possible to the group-III nitrides.
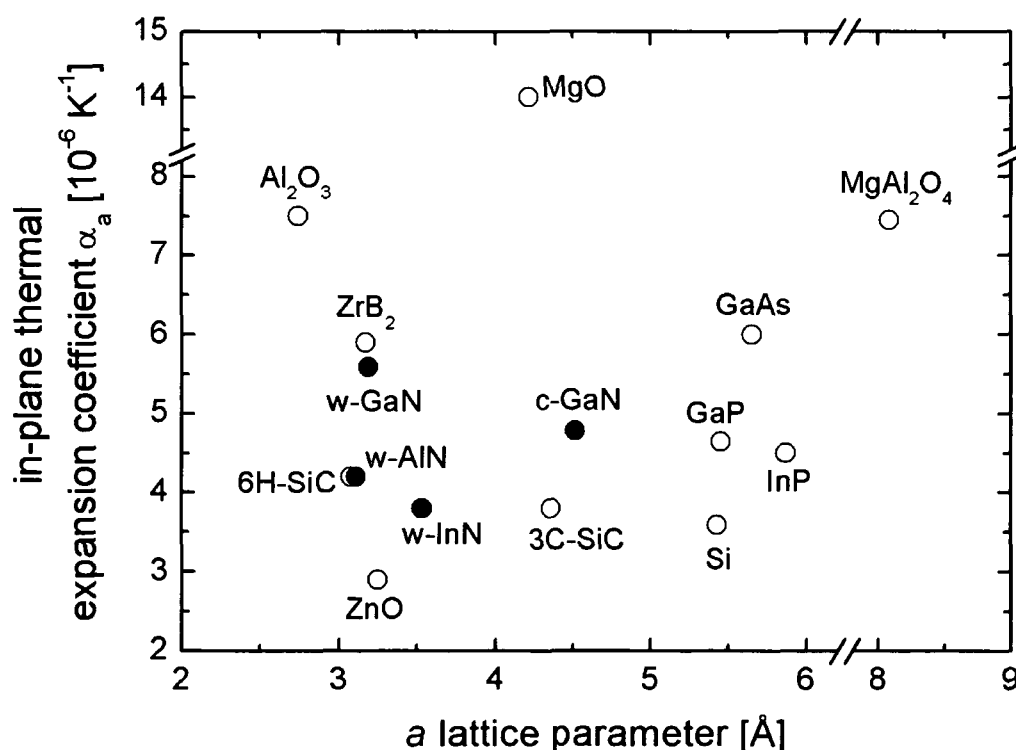

Fig. 2.6. In-plane lattice parameter and thermal expansion coefficient at 300 K for various different substrates (open symbols) and the predominant phases of the binary group-III nitrides (closed symbols).

3. Plasma–Assisted Molecular Beam Epitaxy (PAMBE)

3.1. Description and Schematics of MBE

Molecular beam epitaxy (MBE), an epitaxial growth method developed in the late 1960's, has over the years enabled the fabrication of advanced semiconductor heterostructure materials. With enormous progress in the control of MBE growth and the development of more sophisticated equipment, MBE was gradually transformed from a research tool into a large–scale industrial production facility, as demonstrated especially for the group–III arsenide and also group–III phosphide based semiconductor devices. For the epitaxial growth of group–III nitrides, however, the main commercialized nitride components, such as InGaN LEDs and laser diodes, are primarily produced by metalorganic chemical vapor deposition (MOCVD) [96]. This is mainly due to the fact that in MOCVD the higher growth temperatures and non–vacuum conditions are nearer to thermodynamic equilibrium which has long led to superior material quality, and it was not clear whether problems with material quality were an inherent limitation of MBE, or whether conditions for MBE growth were not fully optimized. Within the last few years though the performance of MBE–grown nitrides has begun to approach that of state–of–the–art material grown by MOCVD [97–102] thanks to strong efforts directed towards the optimization of growth conditions [25,26,103], that finally gave MBE an equal position regarding its suitability for device fabrication.

The basic principle of MBE relies on the crystallization of a thin film via reactions between thermal–energy molecular or atomic beams of the constituent elements at a substrate surface, which is maintained at an elevated temperature in ultra–high vacuum (UHV). The molecular beams are generated from solid source elements kept in conventional Knudsen effusion cells by heating them to very high temperatures. The MBE system used in the present work is a V80H type designed by VG Semicon that is equipped with two Ga, one Al, one Si and two high–temperature boron cells (see Fig. 3.1.). For any of these elements the evaporation rate depends directly on the respective vapor pressure, which in turn determines the arrival rate of the constituent atoms and hence the composition and doping level of the grown film.

In a Knudsen cell, the total evaporation or flux rate (i.e. the total number of molecules or atoms evaporating into vacuum per time) is given by the Knudsen effusion equation

$$\Gamma_e = \frac{dN}{dt} = A_e \left(p_{eq} - p_v \right) \sqrt{\frac{N_A}{2\pi M k_B T}} \quad \text{[molecules per sec].} \qquad (3.1.)$$

In this idealized case, where no evaporated atoms are reflected (i.e. evaporation coefficient = 1), A_e defines the orifice area of the evaporating surface with equilibrium evaporant pressure p_{eq}. The pressure p_v in the vacuum reservoir is negligible for evaporation into a UHV environment. The other relevant parameters are the molar mass of the evaporating species M, the

Boltzmann constant k_B, the temperature T and the Avogadro constant N_A. In order to guarantee very good flux stabilities, the temperature of the effusion cell must be controlled very accurately. This is achieved by high performance proportional–integral–derivative (PID) controllers and thermocouple feedback, consisting typically of a W/Re alloy. The conventional Knudsen cells in use are cylindrically shaped with conical crucibles containing the source elements. The preferred crucible material now is pyrolytic boron nitride (pBN), which allows cell heating well up to ~ 1200 °C and only at around 1400 °C dissociation of this material sets in. Care needs to be taken that the stand–by temperatures of the cells are kept well above the melting point of the source elements (29.8 °C for Ga and 660.4 °C for Al), because solidification of these materials would lead to expansion and cracks in the pBN crucibles. Regarding the high–temperature cells for boron operating up to 2000°C, typical crucible materials such as W, glass–like carbon or pyrolytic graphite are used. The growth of group–III nitrides requires also a nitrogen source that is installed in a standard port for effusion cells and more details about the characteristics of this source are given in the following section.

One very advantageous feature of MBE is that the composition and doping levels can be controlled on an atomic scale with the use of mechanical shutters in front of the beam sources allowing very rapid interruptions of the molecular beams. The uniformity in thickness and in composition of the grown films depends on the uniformities of the molecular fluxes and also on the geometrical configuration between the sources and the substrate. Conventional configurations give a flux distribution over the substrate area that follows a characteristic $\cos^2$–law, which results generally in quite inhomogenous films. To manage better thickness and composition homogeneities, the substrate is usually rotated with a constant angular velocity around
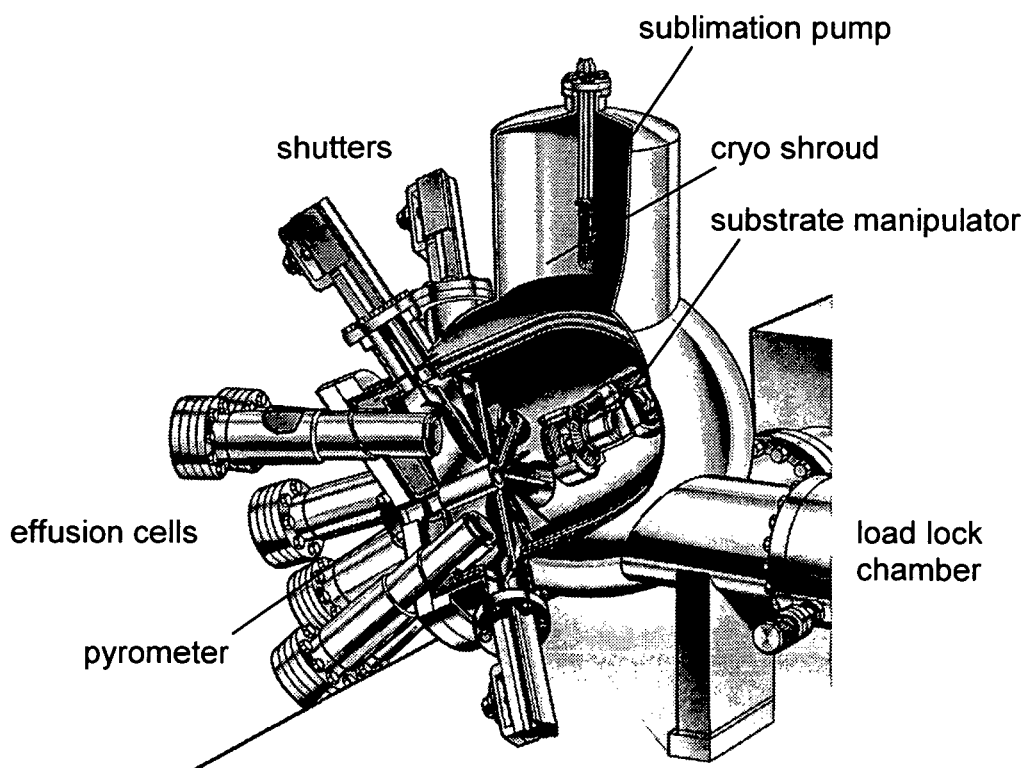

Fig. 3.1. Cutaway illustration of the V80H MBE chamber as designed by VG Semicon showing its most basic components.

the axis perpendicular to its surface. In the present configuration, the substrate is fixed on a heatable horizontal axis manipulator, which is positioned slightly before the intersection point of the molecular beams. To facilitate the radiation–induced heating of the substrate, the backsides of the substrates are sputter coated with TiW, a refractory metal, and that way temperatures up to ~ 850 °C can be reached. The substrate temperature is measured by a pyrometer with a maximum sensitivity at 940 nm, positioned in direct line of sight with the substrate sample. Also sited on the substrate manipulator is a movable ion gauge, which can be moved towards the sample growth position that serves not only for an accurate measurement of the beam fluxes but also for vacuum control.

Providing ultra–high vacuum conditions for MBE growth is indispensable for two reasons: First, it has to be ensured that the molecular mass transport has a beam nature, meaning that the mean free path of the evaporated molecules is large enough so that no scattering processes with residual gas molecules occur. This would aggravate the control of both composition and doping severely. Secondly, for very high film quality it has to be guaranteed that no or infinitesimal levels of residual gas impurities are incorporated. Considering a base pressure of only 10^{-6} mbar, the residual gas molecules would form an adsorbate monolayer (ML) on the sample surface in only one second under the assumption of a sticking coefficient of 1 [104]. Such a fast accumulation of residual gas coverage coincides roughly with the typical MBE film growth rates [1 μm/h $\approx$ 1 ML/s] and would lead to enormously high impurity levels. For these reasons, the base pressure in the growth chamber needs to be as low as possible, and values between 10^{-11} – 10^{-10} mbar are necessary, which can easily be achieved by providing high speed pumping facilities. This is mainly reached by the employment of an ionic and cryogenic pump along with coating the interior of the growth chamber completely with a cryo shroud that is permanently filled with liquid nitrogen to trap impurities. The load lock or preparation chamber is evacuated by a turbomolecular pump and a titanium sublimation pump, in order to facilitate the high–vacuum transfer into the growth chamber.

In contrast to other epitaxial methods, the UHV environment in MBE offers an additional advantage, namely that *in situ* growth control is rendered possible by using special surface diagnostic methods. Reflection high energy electron diffraction (RHEED) is the most common *in situ* technique being used in basically any MBE, but additionally in this work also quadrupole mass spectrometry (QMS) in line–of–sight operation was developed as a novel method to measure the desorbing species during growth and determine the current growth rate (see further details in section 3.3. and 3.4.).

3.2. The Nitrogen Plasma Source

Because of the inert nature of nitrogen, the MBE growth of group–III nitrides requires the use of reactive nitrogen species which can be produced by compact plasma sources. To date, among all available plasma sources merely two are suited for the growth of group–III nitrides, the electron cyclotron resonance (ECR) microwave source and the radio frequency (RF) source. Here, an Epi Unibulb RF source is used, which has several advantages over an ECR source: it provides higher growth rates (~ 1μm/h versus 0.15 μm/h [105]), operates at higher

vacuum and produces lower molecular ion content. Several studies pointed out that especially high ion contents were made responsible for the inferior GaN material quality in ECR-MBE growth, with typically high point defect densities as a result from the plasma–induced ion implantation-like damage [106,107]. Neutral atomic nitrogen is therefore needed, which is generally believed to represent the only reactive species participating in GaN growth by PAMBE. Although ionized molecules (N_2^+) and ionized atoms (N^+) are also present in an RF source, their concentration is much smaller and the predominant nitrogen species are made up mainly by atoms (N) and excited neutral molecules (N_2^*) [105,108].

A schematic representation of an RF plasma source is illustrated in Fig. 3.2., which operates by means of an electrical discharge created from the inductive coupling of an RF excitation coil. The objective is to deliver all available power from a RF generator (with a maximum power of 600 W and an operating frequency of 13.56 MHz) to the discharge tube (cylindrical pBN cavity) without losses and without reflecting power. As these losses appear as an extra heat load on the chamber, the entire source is designed with integral water cooling. Avoiding reflected power by impedance mismatches can be achieved by varying the matching capacitances in an external matching unit so that the power load appears purely resistive. However, upon discharge the plasma sheath confines ions and electrons within the tube and primarily low–energy (<10 eV) neutral species escape. The ion content of the created plasma was able to be minimized by two approaches: first, by keeping the temperature of the discharge tube walls above room temperature [109], and secondly by a reduction of the size of the holes in the aperture plate [110] that is mounted on the exit zone of the discharge tube. Additional reduction of ion concentration can be achieved by means of ion deflection plates fitted to the source, so that the electric field across the aperture deflects any escaping ions away from the sample. Finally, controlling the composition of the nitrogen plasma beam has
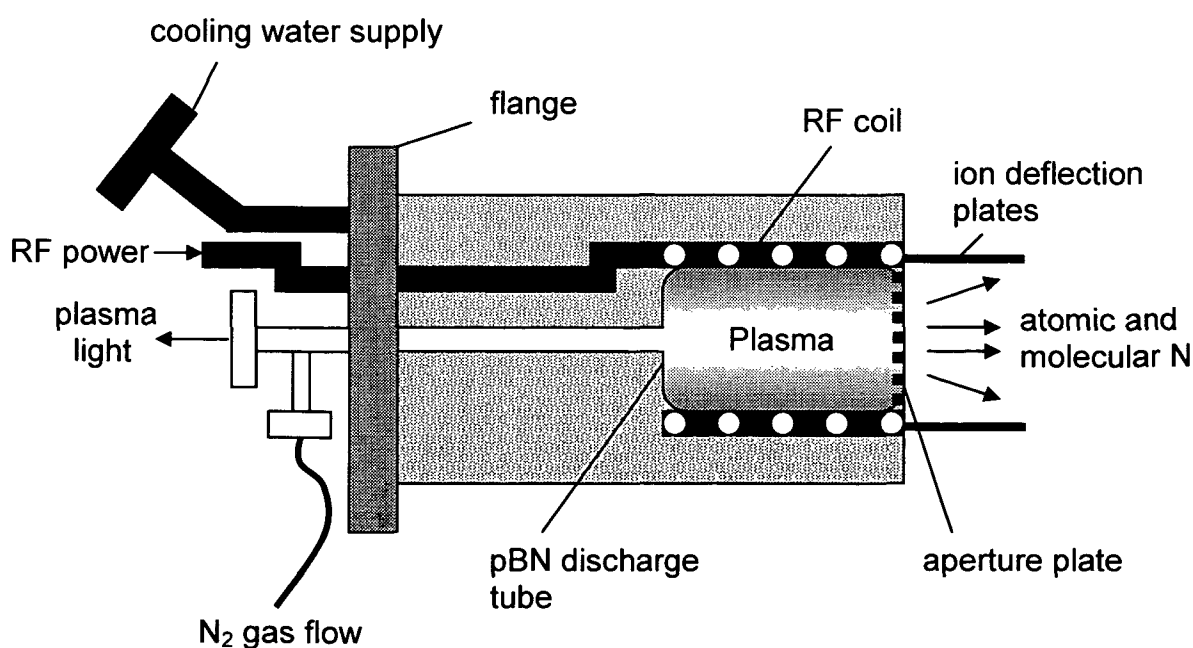

Fig. 3.2. Schematic illustration of a conventional radio frequency (RF) plasma source for the supply of reactive nitrogen species.

been also found to be very sensitive to the input power and the N_2 gas flow, i.e. the atomic nitrogen content increases with increasing power and decreasing gas flow [111]. To regulate the gas flow, conventional mass flow controllers from MKS Inc. are used and N_2 of 5N (99.999%) purity is supplied. In addition, the present setup enables one to fully control the plasma stability by observing the emission intensity of the plasma light coming through a view port.

3.3. In situ Growth Characterization Techniques

3.3.1. Reflection High Energy Electron Diffraction (RHEED)

The employment of reflection high energy electron diffraction (RHEED) offers the capability to investigate the crystallography and microstructure of surfaces and very thin films in MBE. In this case, the diffraction does not give a local picture but rather a statistical view of the surface disorder for the many processes occuring at surfaces, such as growth, phase transformations, the formation of steps and other processes that involve deviations from perfect order. Technically, a RHEED experiment is realized by directing a relatively high electron beam (5 – 40 keV) to the surface at a very grazing angle of incidence (1 – 3°), so that the penetration of the beam into the surface is low and is restricted only to the outermost few
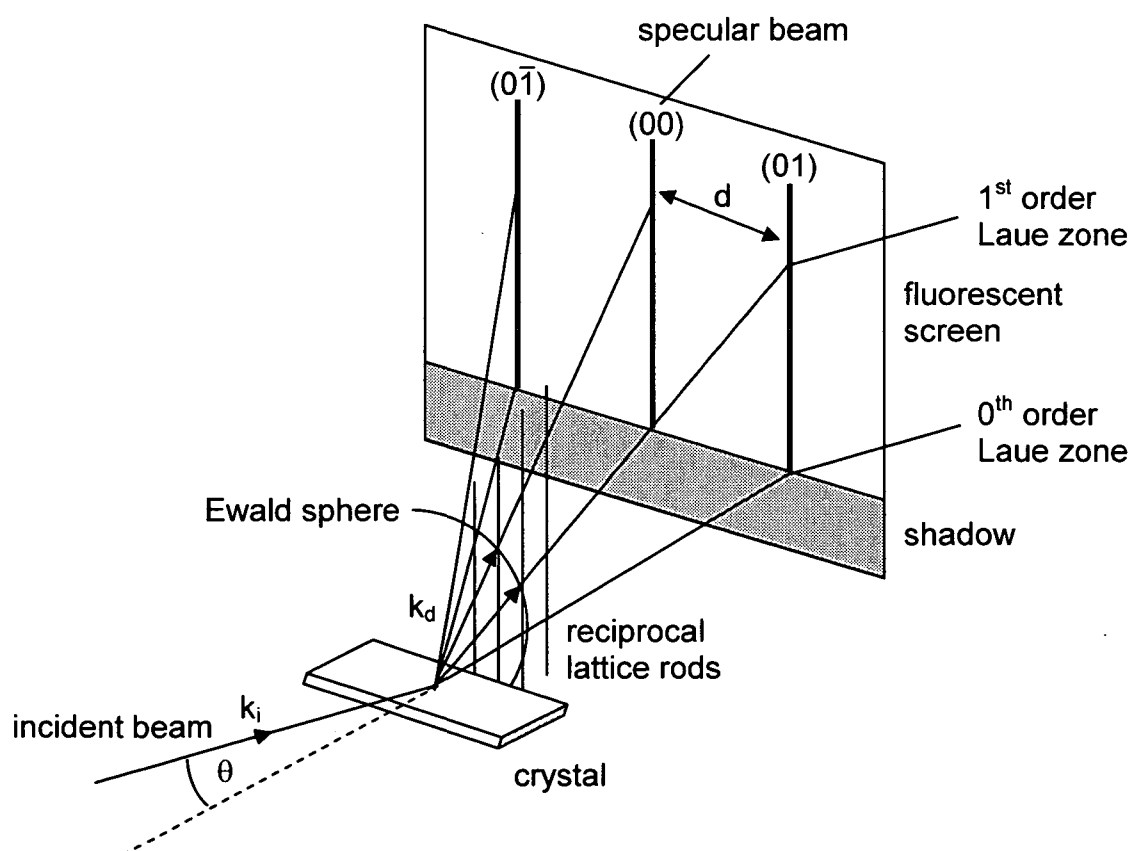

Fig. 3.3. Experimental geometry of RHEED showing also the Ewald sphere construction that explains the formation of streaks; the wave vector k_i is very large compared to the reciprocal interrod spacing.

atomic layers (see Fig. 3.3). To describe the conditions for the constructive interference of the scattered electrons it is appropriate to use the Ewald construction in the reciprocal lattice. In the case of a smooth surface, where the interaction of the electron beam is essentially with a two–dimensional atomic net, the third dimension in real space is missing, and therefore the third dimension in reciprocal space is also not defined. As a consequence, the surface layer is represented in reciprocal space by rods in a direction perpendicular to the real surface. Due to the high energy electrons (small wavelength, large wave vector $|k_i|$) of the incident beam, the Ewald sphere appears very large compared to the reciprocal interrod spacing. This means that the Ewald sphere cuts the specular beam, i.e. (00) rod, almost along its length which gives rise to a long streak, as displayed on a fluorescent screen. Other reciprocal lattice rods which intersect the Ewald sphere will also result in streaks but in practice the sphere is so large that these are very few. For the case of reconstructed surfaces, additional rods appear, i.e. if the surface reconstruction is e.g. 2×2, the lattice vector of the surface in real space is twice as long as the bulk lattice vector while the corresponding reciprocal lattice vector is only one half, respectively. Therefore, one additional streak would appear inbetween the specular and first diffracted beam. As a consequence of the finite energy spread of the incident beam and its angular divergence, the RHEED beam has a limited coherence length at the surface, that is typically of the order of 2000 Å. Disorder occuring on the surface on larger scales than this may therefore be difficult to detect. Because of the grazing incidence used in the experiment, RHEED is also extremely sensitive to surface roughness on scales smaller than the coherence length. In some cases it may be difficult to obtain a surface which is sufficiently flat to give a clear pattern of streaks, as shown in Fig. 3.4 (a). If the surface is rough, the RHEED beam may pass also through any protuberances on the surface, resulting in bulk diffraction and spots, rather than streaks in the RHEED pattern (Fig. 3.4 (b)).
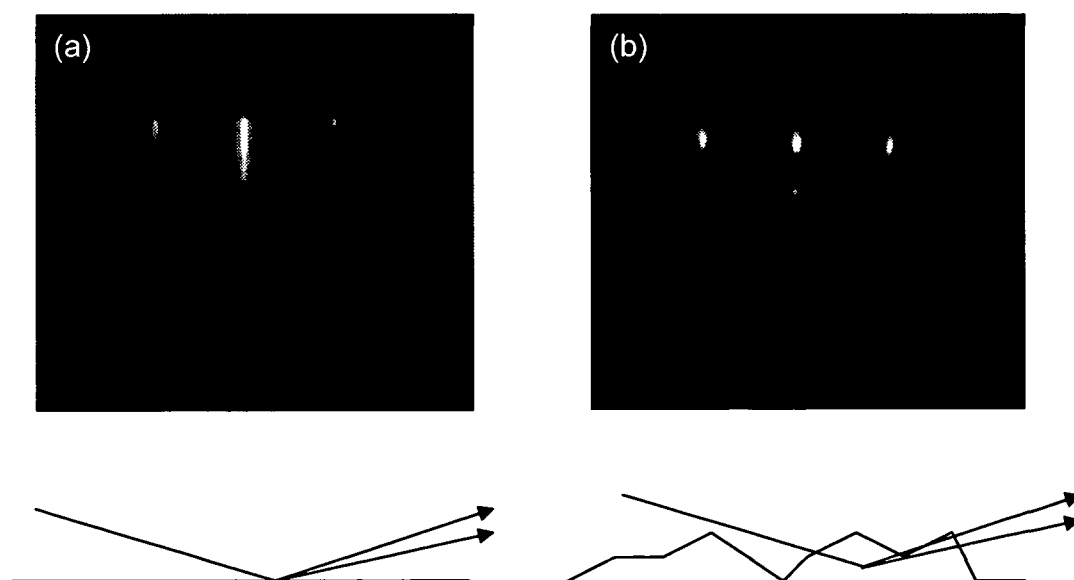

Fig. 3.4. Modes of grazing incidence electron diffraction: (a) true reflection on a flat surface with streaky features, (b) a combination of transmission and reflection diffraction on a rough surface resulting in many spotty features.

In order to realize the evolution of RHEED patterns in real–time, a 10–bit digital high–sensitivity charge–coupled device (CCD) camera and a frame grabber with full software control by k–Space Associates Inc. was used to monitor the RHEED images on the fluorescent screen with a time resolution of 30 frames/sec. Such real–time acquisition allows the determination of streak spacings, strain evolution, surface reconstructions as well as of growth rates by means of intensity oscillations. Evaluating the strain state differences at het-erointerfaces, changes in the spacing between specular and higher–order diffracted beams are directly correlated with changes of the in–plane a lattice parameter in the top layer of the crystal. Beyond this, the most important application of RHEED, however, is its use to monitor the layer–by–layer growth by measuring the intensity of the specular diffracted beam as a function of time. In this case, the intensity typically exhibits very regular oscillations, with their period corresponding exactly to the growth rate of one monolayer (ML) of the deposited material in its preferred growth orientation. The maxima in the reflectivity correspond to atomically flat surfaces, i.e. before the deposition of a layer, and when deposition of integral
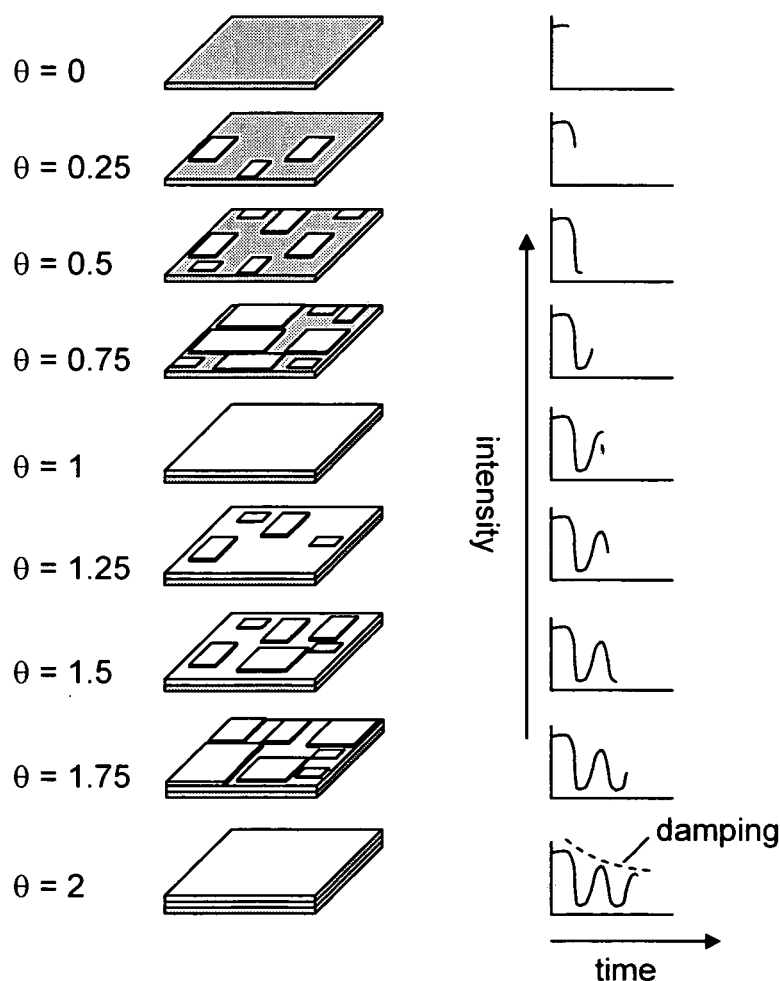

Fig. 3.5. Intensity oscillations of the specular beam in the RHEED pattern during MBE layer–by–layer growth as a function of time (and layer coverage); intensity maxima correspond to atomically flat surfaces occurring for integer layer coverages, whereas minima are due to completely disordered surfaces or fractional coverages. The period of the oscillations corresponds exactly to the growth rate of a single monolayer.

layer coverages is complete (θ = 0,1,2,...).The reflectivity minima correspond to the most disordered surfaces, i.e. for fractional layer coverages of θ = 0.5,1.5,...as shown in Fig. 3.5. It is important to note that layer–by–layer growth is not restricted to the consecutive build–up of integral monolayers, but can recommence in a new layer before the preceding layer is complete. In the early stages, however, one layer is likely to be almost complete before the next layer starts, resulting in a reflectivity increase as the surface becomes smooth. But, with increasing layer thickness the intensity of the oscillations decreases progressively (i.e. oscillation damping), as the surface becomes statistically distributed over several incomplete atomic layers and the different surface domains are out of phase with respect to the electron beam. In general, such RHEED intensity profiles can cause some errors in interpretation as they consist of both elastically and diffusively scattered electrons. It is therefore important to select diffraction conditions, where the elastic contribution prevails, as can be achieved for instance under "off–azimuth" conditions for the directly reflected electron beam.

3.3.2. Line–of–Sight Quadrupole Mass Spectrometry (QMS)

In conventional crystal growth such as MBE, the condensation of a thin epitaxial film can be described by several surface atomic processes that a vapor atom is usually subjected to. In a simplified view, an adsorbed vapor atom (or adatom) may move over the surface by diffusion processes until it interacts with other adatoms to form a stable or critical cluster or it reevaporates (or desorbs) again into the vapor phase (see Fig. 3.6). In such an atomistic picture, condensation and film growth are therefore the net result of an equilibrium between adsorption and desorption processes.
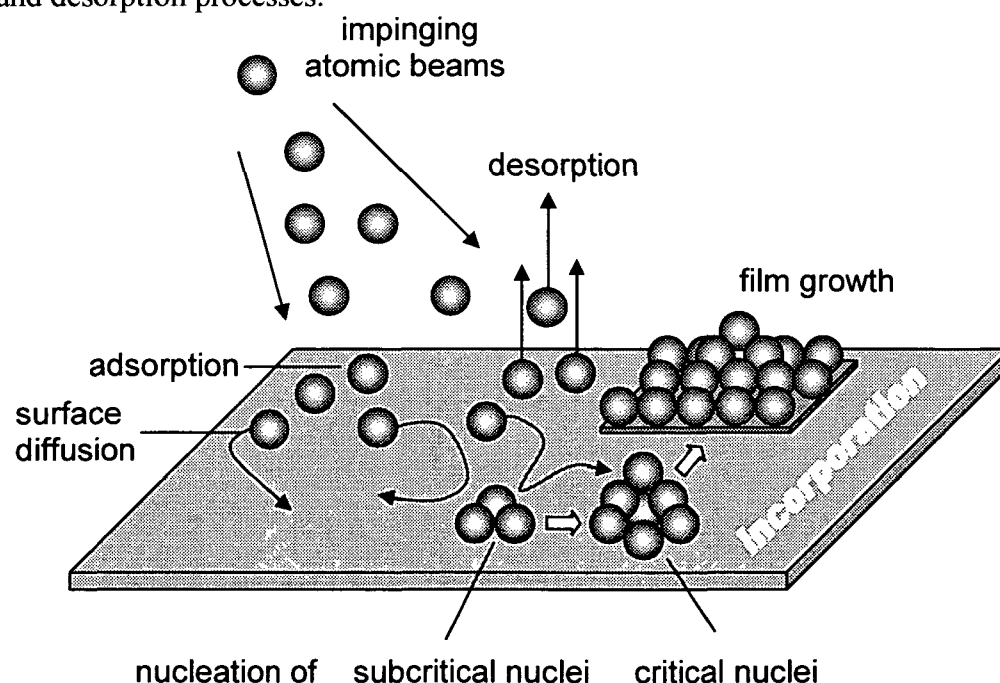

Fig. 3.6. Schematics of the surface processes occurring during film growth by MBE.

To acquire such fundamental knowledge of the growth and surface kinetic processes, quadrupole mass spectrometry (QMS) was developed primarily for this work as a novel *in situ* meth-

od to quantitatively determine the desorbing species during growth. Technically, this unique technique was achieved by selecting a specific geometrical configuration between sample and mass spectrometer, such that the ionizer of the mass spectrometer is directed in direct line–of–sight to the sample wafer. Such a configuration allows mass spectrometry even on a local basis since the mean free path of the desorbing species is very long under the given UHV conditions and any scattering effects do not occur. In its principal operation, the quadrupole mass spectrometer transforms the desorbing species into mass separated ions by a number of steps. First, the desorbed neutral atoms or molecules are ionized to positive ions and further injected into the electric field of the four electrode configuration as typical for any standard QMS. Here, the mass separation of the ions with a specific m/Z (mass–to–charge) ratio takes place where they describe different mass–dependent trajectories. At their exit an ion detector measures either the ion current directly (in a Faraday Cup) or the electron current proportional to the ion current (by means of a continuous dynode electron multiplier, CDEM), with both these currents given directly as equivalent partial pressure.
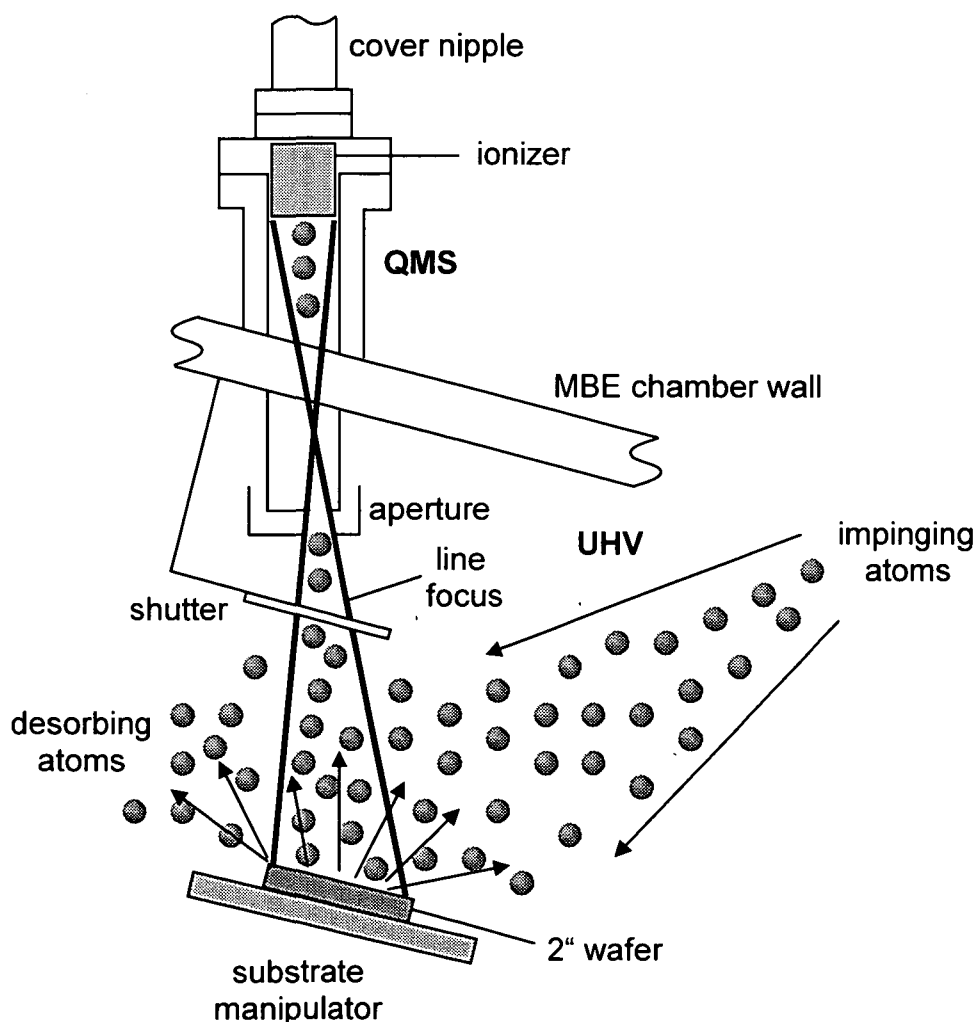

Fig. 3.7. Schematic setup of a quadrupole mass spectrometer (QMS) in line–of–sight operation for monitoring the desorbing atoms; most important feature is an appropriate aperture plate that limits the angle of acceptance ideally to the size of the sample wafer.

As for the setup, a conventional state–of–the–art quadrupole mass spectrometer (Residual Gas Analyzer AccuQuad 300D by K. J. Lesker) was installed on a flange designated for beam sources and collimated with an appropriate aperture. This aperture restricts the acceptance angle to the desorbing species originating merely from a center area of the sample wafer, and completely suppresses any background signals from the substrate manipulator or chamber walls (see Fig. 3.7.). However, collimation reduced the signal relative to background and shot noise, but ellaborate geometrical considerations on QMS–to–sample distance and aperture plate design were done to achieve optimum sampling conditions [112]. Detection of ions in a mass range of 1 to 300 atomic mass units (amus) with a resolution better than 0.5 amu (at 10 % peak height) is typical for this mass spectrometer. This QMS is also equipped with a continuous dynode electron multiplier (CDEM) that enables partial pressures to be detected as low as 5×10^{-14} mbar. In the CDEM operation mode a time resolution of better than 2 sec was made possible. Protection from unwanted coating when the QMS is not in use is guaranteed by a mechanical shutter, similar to those placed in front of the other beam sources.

In the case of GaN and AlN growth as presented in this work, the desorbing species of interest are mainly given by the two Ga isotopes ^{69}Ga (60.1 %) and ^{71}Ga (39.9 %), ^{27}Al (100%) and ^{28}N$_2$. Since the bulk of these growth studies is performed under metal–rich conditions, it is mainly the excess metallic atoms that desorb from the growing surface (while all N is incorporated) and for this reason one can restrict the QMS experiments to recording merely the metal atoms. For GaN growth then, the QMS is set to measure the partial pressure of the
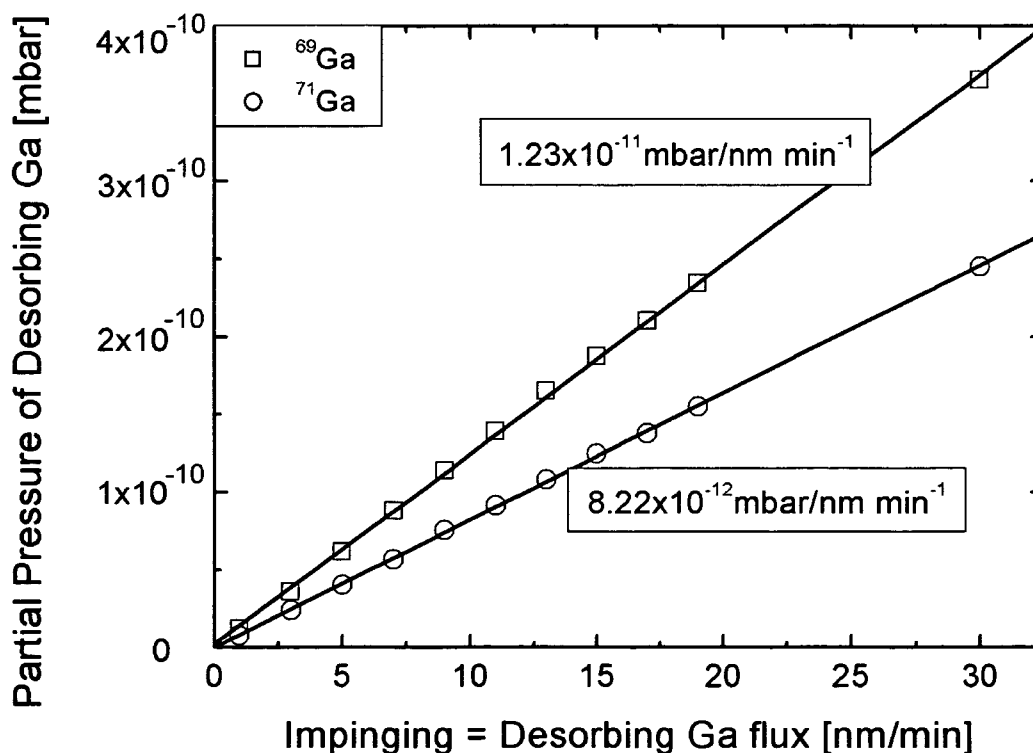

Fig. 3.8. Calibration of the partial pressure as a function of desorbing Ga flux for a sequence of incident Ga fluxes impinging on a sapphire wafer heated to 800 °C, where all impinging Ga atoms desorb completely. The results give a linear relationship that enables the quantification of desorbing fluxes in relation to supplied fluxes (so–called mass balancing).

desorbing isotopes ^{69}Ga and ^{71}Ga. To correlate the partial pressure to a desorbing flux in units of nm/min or ML/sec, along with the prospect of quanitifying the desorbing species as equivalent surface coverage or film thickness, it is important to evaluate the relationship between partial pressure and desorbing Ga flux. This can be done by measuring the partial pressure of both isotopes for a sequence of known incident Ga fluxes evaporated onto e.g. a sapphire substrate at such a high temperature (~ 800 °C), so that all impinging Ga desorbs completely. The results in Fig. 3.8. evidence that the partial pressure rises linearly as a function of the desorbing Ga flux with a proportional constant of 1.23×10^{-11} mbar/nm min^{-1} for the ^{69}Ga isotope and with 8.22×10^{-12} mbar/nm min^{-1} for the ^{71}Ga isotope, respectively. The different slopes are due to their relative natural occurrence, that are given by the 60.1 % : 39.9 % ratio. As the sensitivity of the QMS ionizer changes slightly during extensive use, this calibration routine has to be repeated occasionally with progressing operation time. Furthermore, by evaluating the difference between the known incident Ga flux and the desorbing Ga flux (which is later also referred to as *mass balancing*), this novel method proves further appropriate to determine the growth rate at any stage during GaN growth.

At this point it should be also noted, that similar desorption measurements cannot be applied for AlN growth, because Al desorption at the typical AlN growth temperatures is extremely low, but more so because of the disadvantageous mass unit of Al. With no other isotope, ^{27}Al lies in the immediate vicinity of ^{28}N$_2$, where N$_2$ typically prevails by orders of magnitude over Al in the residual gas spectrum during AlN growth. Due to the limited mass resolution of the QMS, there appears then a significant overlap between the two masses that rules out any reasonable measurement of Al desorption.

4. GaN Growth Phase Diagram

4.1. Introduction

Unlike other III–V semiconductors which are grown under conditions (temperature, pressure) where the III–V compound and its vapor are thermodynamically stable, the growth of GaN occurs typically under conditions far from thermodynamic equilibrium. In order to overcome kinetic barriers of epitaxy, the optimum growth temperature for high–quality single crystals was empirically determined to ~1/2 to 2/3 of the melting temperature. For GaN growth by MBE, it has been demonstrated that single–crystalline material needs to be grown at temperatures significantly below ~1/2 of the theoretically predicted GaN melt temperature (3023 K), meaning roughly below 850 °C [114]. Under these conditions, the MBE growth of GaN can be understood as a metastable process in the sense that there exists a strong competition between the forward reaction (GaN formation), which depends on the arrival rate of the nitrogen species on the surface, and the reverse reaction, given by GaN thermal decomposition. In general though, at these comparably low temperatures sufficient GaN formation can be expected as the rate of GaN thermal decomposition is supposed to be rather low due to the strong Ga–N bonds at the surface. This limit to such relatively low growth temperatures (< 850 °C) in PAMBE creates concerns for the GaN material quality, much more than in other higher–temperatures growth techniques such as MOCVD.

In the following a calibration routine for the metal and nitrogen material fluxes and their influence on the GaN growth rate will be given. As a consequence of this, certain growth regimes will be outlined and an empirical growth phase diagram as a function of Ga flux and growth temperature will be presented. On the basis of this GaN growth diagram a calibration method for the substrate temperature will be introduced that benefits from Ga desorption measurements using the QMS technique. To further clarify the mechanisms of forward and reverse growth reactions, the rates of thermal decomposition of the technologically more relevant GaN (0001) surface will also be determined.

4.2. Determination of Metal and Nitrogen Fluxes

To give a measure of the material fluxes, they are typically calibrated in units of potential growth rate, which is achieved by performing GaN growth under either group V– or group III–rich conditions. Under group V–rich conditions (N–rich regime), all excess N was found to desorb as N_2 from the growing surface yielding stoichiometric GaN films with a growth rate that is limited by the amount of available Ga atoms (Fig. 4.1(a)). This means that the growth rate rises monotonically with increasing Ga flux (ϕ_{Ga}) up to a limit where the Ga flux matches the supplied active N flux ($\phi_{Ga} = \phi_N$), as also found in an earlier investigation in our group [115]. Thus, under the assumption of a sticking coefficient equal to 1, the metal flux can be easily determined by subsequent thickness measurements from GaN cross sections

(for instance by scanning electron microscopy, SEM). Under group III–rich conditions (Ga–rich regime), the GaN growth rate is limited by the amount of available reactive nitrogen and for the typical growth temperatures all excess Ga can be desorbed from the surface (Fig. 4.1(b)). Likewise, the growth rate increases monotonically with rising N flux, which can be determined also from thickness measurements of GaN layers grown under the Ga–rich conditions.
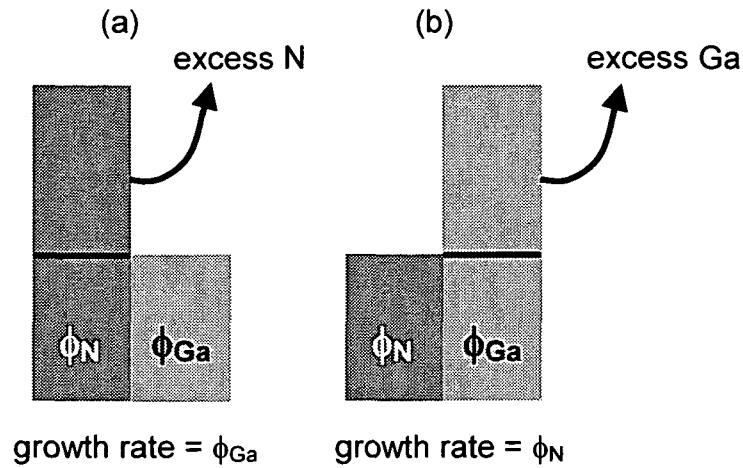

Fig. 4.1. (a) N–rich and (b) Ga–rich growth conditions of GaN with its growth rate being determined by the smaller one of the two fluxes, as all material in excess desorbs.

4.3. GaN Growth Phase Diagram

The core of all following GaN growth studies is an empirical PAMBE growth phase diagram that was developed in our group [116]. To introduce briefly the main features of this diagram, it relies on a thorough investigation not only of the role of the III/V flux ratio but also of the substrate temperature, where the latter results in a split–up of the Ga–rich regime into two distinct ones (Fig. 4.2.). These are termed "Ga–droplet" and "intermediate" regimes, which are separated by a sharp boundary line apparently due to a temperature–dependent desorption behavior of the excess Ga atoms. This boundary line was determined by growing thick GaN films under various Ga fluxes and temperatures, but constant N flux (2.5 nm/min) and observing by subsequent optical microscopy (OM) whether macroscopic metallic Ga droplets have formed on the surface during growth. GaN films grown at low temperatures and/or high Ga fluxes exhibit droplets which cannot be desorbed thermally, while at higher temperatures and intermediate Ga fluxes no droplets occur. The boundary has an exponential nature and obeys an Arrhenius dependence with growth temperature, yielding an activation energy of ~2.8 eV for the maximum desorbable Ga flux, as described by the following equation [116]:

$$\phi_{Ga}^* - \phi_N = \left(2.2 \times 10^{15}\,nm/min\right) \times \exp\left(\frac{-2.83eV}{kT}\right) \tag{4.1.}$$

Here, ϕ_{Ga}^{*} is the Ga flux at the boundary, ϕ_N the supplied N flux, k the Boltzmann constant and T the substrate temperature in degrees Kelvin. The value of this activation energy agrees well with the evaporation energy of Ga over liquid Ga ($E_A = 2.9$ eV), as derived from equilibrium Ga evaporation data [117]. Besides the two Ga–rich regimes, this empirical growth diagram for GaN shows also the N–rich regime that appears for low Ga fluxes ($\phi_{Ga}/\phi_N < 1$) and which is independent of the substrate temperature (at least up to the onset of GaN thermal decomposition, as described later). In a basic view, a regime within such a diagram defines a set of growth conditions that produce similar surface properties (i.e. RHEED reconstruction, surface roughness and type of surface morphology): whereas growth in the N–rich regime results in typically spotty RHEED patterns and rough, highly facetted surface morphologies, Ga–rich conditions are characterized by streaky RHEED patterns and generally much smoother surfaces, except for the occurrence of droplets under extremely Ga–rich conditions [116].
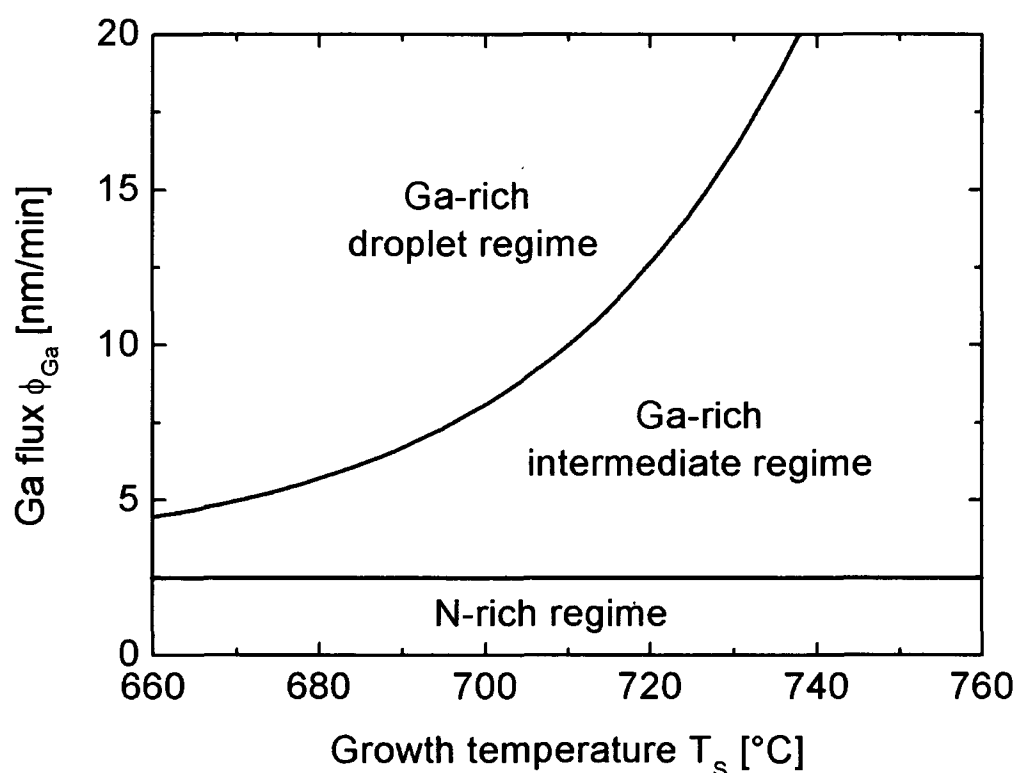

Fig. 4.2. Growth phase diagram for PAMBE of GaN as determined for an active N flux of 2.5 nm/min; the Ga flux and growth temperature conditions define three distinct growth regimes, namely one N–rich regime and two Ga–rich (intermediate and Ga droplet) regimes. The latter two are separated by an exponential boundary line that is equivalent to the maximum desorbing Ga flux with an activation energy of 2.8 eV [116].

Needless to say, the use of such a growth phase diagram is therefore essential to identify optimum growth contitions in order to produce device quality GaN films. After our group has established this diagram, several studies pointed out that the best physical properties were achieved marginally below the border for Ga droplet formation [26,102,116,118,119].

Throughout this work, all growth studies are referred to the present GaN growth diagram, which will be even further refined by the following direct QMS measurements of the Ga desorption (as presented in Sect. 6 & 7). It will then allow a clearer assertion why the growth conditions must be chosen in close vicinity of the droplet border.

4.4. Substrate Temperature Calibration

A direct comparison of absolute substrate temperatures among different MBE systems is known to be quite a challenging task. But, as the growth phase diagram is universal in nature and therefore applicable to any MBE system, substrate temperatures between different MBE systems can be correlated, if they are calibrated with respect to this diagram. Besides, the substrate temperature also within one system can change over time due to many reasons. In PAMBE systems, especially, where substrate temperature control is often facilitated by means of a pyrometer, the primarily metal–rich growth conditions can cause severe and undesired metal coating of the optical window of the pyrometer. This can lead to changes in its optical transmission and therefore large deviations in the actual temperature reading over extended periods of growth time. This problem entails in general an opening of the system and a thorough cleaning process of the optical window which is accompanied with a long period of a non–operative MBE stand-by mode.
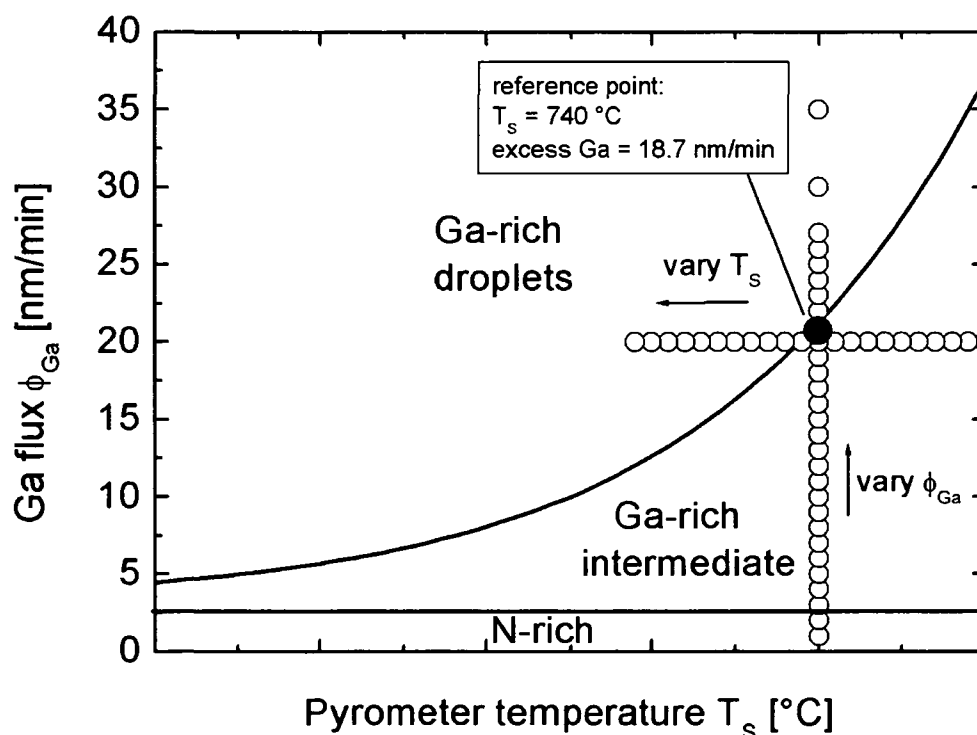

Fig. 4.3. Schematic illustration of two GaN growth series along the GaN growth phase diagram for the calibration of the substrate temperature. The first series will explore the Ga desorption characteristics for constant T_S and N flux, but variable Ga flux, while the second series will focus on variable T_S, respectively.

To bypass such costly drawbacks, the offset between nominal and actual substrate temperature can be determined *in situ* from evaluating the Ga desorption characteristics along the GaN growth diagram by employing the QMS technique.

Starting from an uncoated pyrometer window (where the offset between nominal and real temperature reading is zero), the growth diagram (as determined for instance *ex situ* by optical microscopy) enables one to define an arbitrary reference point for the substrate temperature, namely directly on the border for Ga droplet formation. According to equation (4.1.), for instance a temperature of 740 °C corresponds then to a maximum excess Ga flux of 18.7 nm/min that still desorbs completely from the growing GaN surface, while for any higher Ga flux Ga droplets accumulate on the surface. Using this reference point, two GaN growth series were performed by varying first only the Ga flux (at constant N flux and temperature) and secondly only the substrate temperature (at constant III/V flux ratio) along the GaN growth diagram (see Fig. 4.3.). With simultaneous monitoring of the Ga desorption it is possible to clearly differentiate between the three GaN growth regimes and particularly identify the point of Ga droplet formation.

4.4.1. GaN Growth with variable Ga Fluxes

The Ga desorption measurements of the first GaN growth series including both Ga isotopes are displayed in Fig. 4.4. The Ga flux was varied gradually from 1 nm/min (N–rich
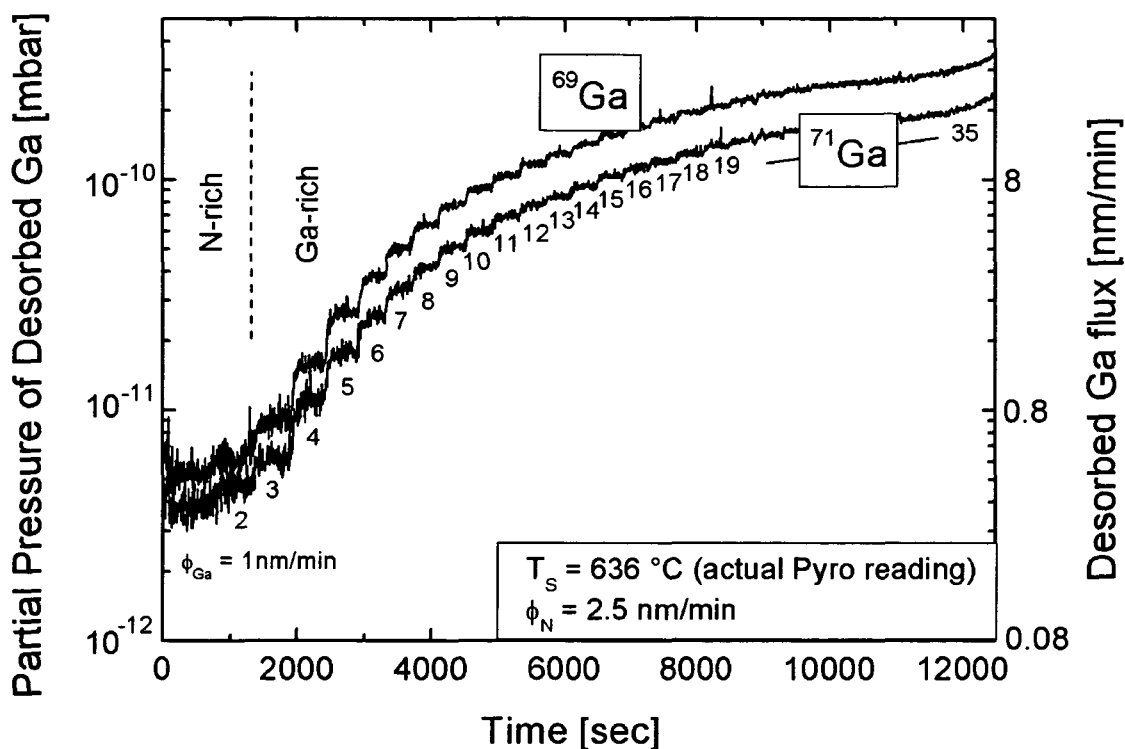

Fig. 4.4. Ga desorption including both isotopes during continuous GaN growth at different incident Ga fluxes, but constant N flux (2.5 nm/min) and $T_S = 636$ °C actual temperature of the metal–coated pyrometer. Note, that increased Ga desorption above the background detection limit occurs only under Ga–rich conditions.

regime) up to 35 nm/min (Ga–droplet regime) without any growth interruptions and with a fast ramp rate from one to the next Ga flux of approximately 20 sec. After each flux ramp, the GaN growth duration was set to 400 – 600 sec, sufficiently long for the Ga desorption signal to reach an equilibrium level for each single Ga flux. During this series the N flux was constant at 2.5 nm/min and the substrate temperature was set to 636 °C actual temperature as measured under non-ideal conditions by the metal–coated pyrometer. It was found that basically no Ga atoms desorb under N–rich conditions and only the background partial pressure signal is detected. But with increasing incident Ga flux, the desorbing Ga flux rises also continuously under Ga–rich conditions. From this data, the mean value of the equilibrium Ga desorption for each Ga flux can then be plotted as a function of incident Ga flux, as shown in Fig. 4.5. There is clear evidence of the three proposed growth regimes. For Ga fluxes below 3 nm/min (N–rich regime) the amount of desorbing Ga is zero. For Ga fluxes exceeding flux stoichiometry ($\phi_{Ga} > 3$ nm/min), the desorbing Ga flux rises linearly, proving that all excess Ga desorbs from the growing surface. At very high Ga fluxes ($\phi_{Ga} > 22$ nm/min), however, there is a distinct bend from the linear data curve and proportionally less Ga seems to desorb. This effect is attributed to the accumulation of Ga droplets as the selected substrate temperature poses an upper thermal limit to Ga desorption (above the Ga droplet border). Under the assumption of a purely thermal limit to Ga desorption, one would however expect that the curve would level out for all incident Ga fluxes beyond the droplet border, meaning that independent of the accumulated amount of Ga in droplets no further Ga desorp-
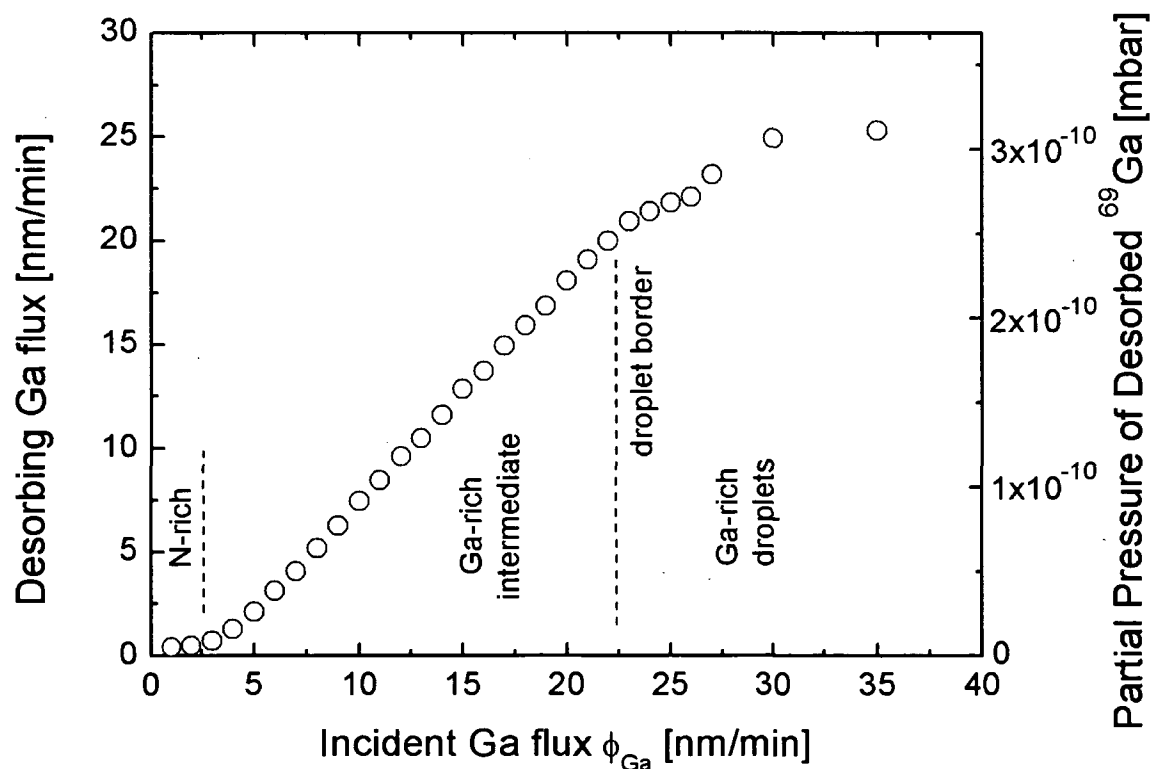

Fig. 4.5. Desorbing Ga flux as a function of incident flux measured from short GaN growth pulses under conditions of constant N flux (2.5 nm/min) and T_S = 636 °C (actual pyrometer temperature) evidencing three growth regimes (N–rich, Ga–rich intermediate and droplet regimes).

tion would occur. Instead, there is an apparently slight increase of the desorbed Ga flux even above the droplet border. It can be suggested that Ga droplets cause additional desorption, also due to the increased surface area, which becomes larger with increased Ga droplet coverage and size.

In order to finally determine the nominal substrate temperature for this growth experiment, one needs to compare the point of droplet accumulation (i.e. excess desorbing Ga flux = 18.7 nm/min) relative to the reference point defined by the standard growth diagram of Fig. 4.2 and equation (4.1.). For an excess Ga flux of 18.7 nm/min the equivalent nominal substrate temperature is then 742 °C. This yields an offset of 106 °C between nominal and actual (metal–coated) pyrometer temperature, meaning that one needs to add this offset to the measured temperature to quote subtrate temperature in real terms.

4.4.2. GaN Growth with variable Substrate Temperature

Alternatively, calibrating the substrate temperature with respect to the GaN growth diagram can also be achieved by varying the substrate temperature and keeping both Ga and N fluxes constant, as illustrated schematically in Fig. 4.3.. For this reason, roughly 100 short (50 sec long) GaN growth pulses were performed interrupted by 20 sec vacuum desorption phases (i.e. N, Ga shutters closed). The substrate temperature was gradually decreased with a rate of -0.5 °C/growth pulse from 666 to 614 °C, actual pyrometer reading. The Ga flux was set to 22.5 nm/min, while the N flux remained unaltered at 2.5 nm/min, yielding 20 nm/min excess Ga. Fig. 4.6 (a) depicts the first two GaN pulses that are referred to the Ga–rich intermediate growth regime. As expected, upon opening of the shutters the Ga partial pressure signal rises instantly to a level corresponding to the desorption of all excess Ga atoms. When the growth pulse is terminated, there is a subsequent fast drop of the Ga desorption back to its background level. This characteristic desorption behavior also holds for several additional growth pulses performed at the gradually lowered growth temperatures (see Fig. 4.6 (b)). This means that the desorbing Ga flux during growth displays always the same partial pressure level, which is followed by a sharp drop of the desorption signal during vacuum desorption. A significant change in the desorption behavior occurs at around 640 °C, where with decreasing temperature the Ga desorption level during growth decreases continually. Simultaneously, the 20 sec vacuum desorption time does not seem long enough to desorb all adsorbed Ga and to reach the background level. Both these features are related again to the accumulation of metallic Ga droplets on the surface and the point of this crossover can be defined as the Ga droplet border. Deriving the desorbing Ga flux during the GaN growth phase for each pulse at the various different pyrometer temperatures leads to the data in Fig. 4.7.. The same desorption characteristics as in Sect. 4.4.1. are revealed again, namely that within the intermediate regime all excess Ga desorbs and beyond the transition to the droplet regime the desorption is continually lowered. To evaluate the offset between nominal and actually measured pyrometer temperature, the point of droplet formation with respect to the reference point defined by Equ. (4.1.) provides the essential information. As a result of this equation, the droplet border at an excess Ga flux of 20 nm/min corresponds to a nominal temperature of
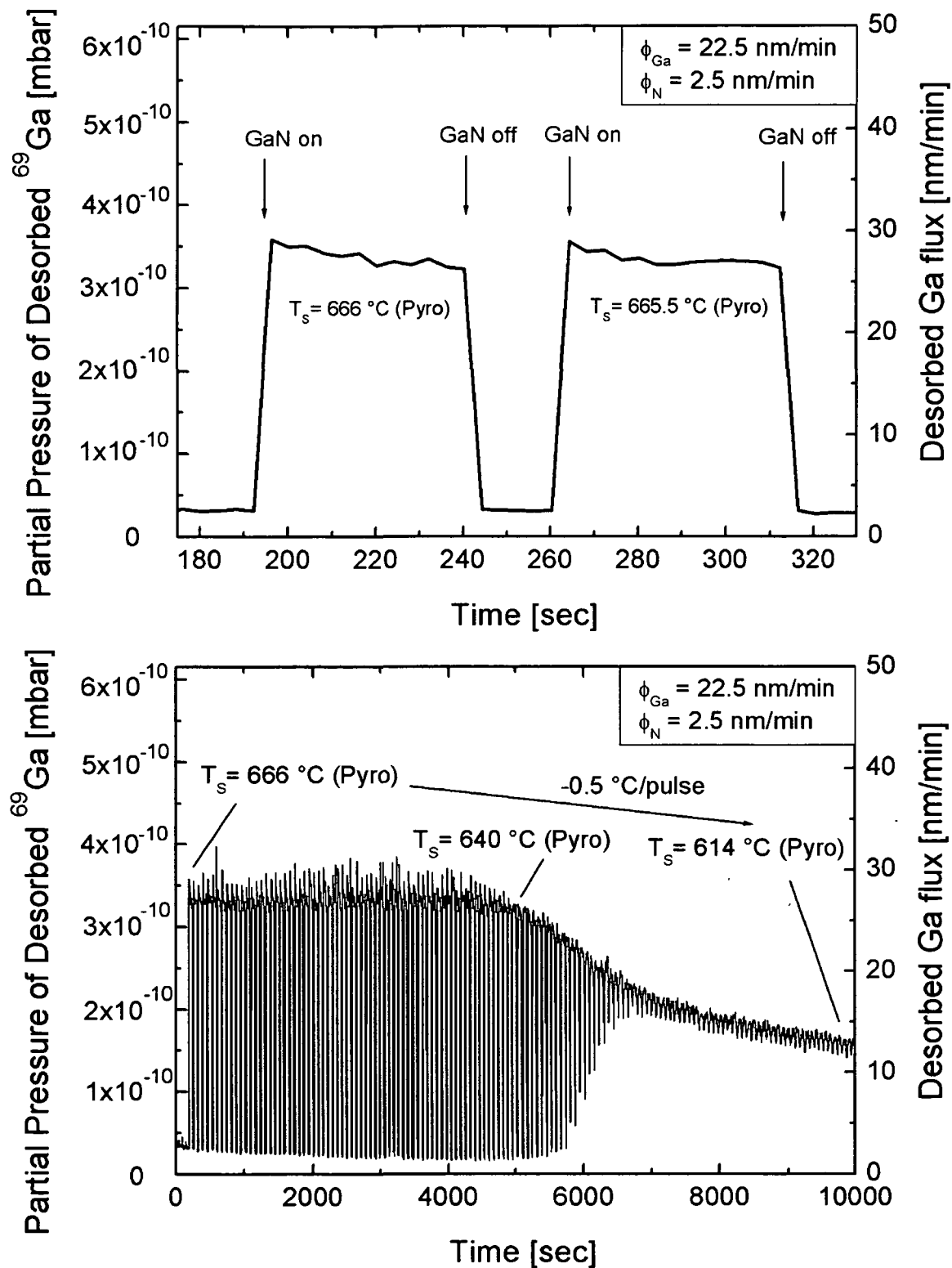
Fig. 4.6. (a) Closeup view of the Ga desorption of two 50 sec long GaN growth pulses in the Ga–rich intermediate regime at constant III/V ratio but slightly different temperatures; (b) Ga desorption of 100 identical growth pulses with the substrate temperature decreasing gradually from 666 to 614 °C (actual pyrometer reading); note that a distinct change occurs for temperatures below 640 °C, which is attributed to the accumulation of Ga droplets (droplet regime). window leads to an offset of 104 °C, which is in very close match with the value determined from the constant temperature growth series (Sect. 4.4.1.).

744 °C. The difference between this temperature and the temperature measured with a metal–coated pyrometer Substrate temperatures given in all following sections will be corrected by the determined offsets, yielding thus the nominal temperatures. To consider the temporal variations in temperature with increasing metal coating of the pyrometer window, both these calibration routines are applied to our system every now and then.
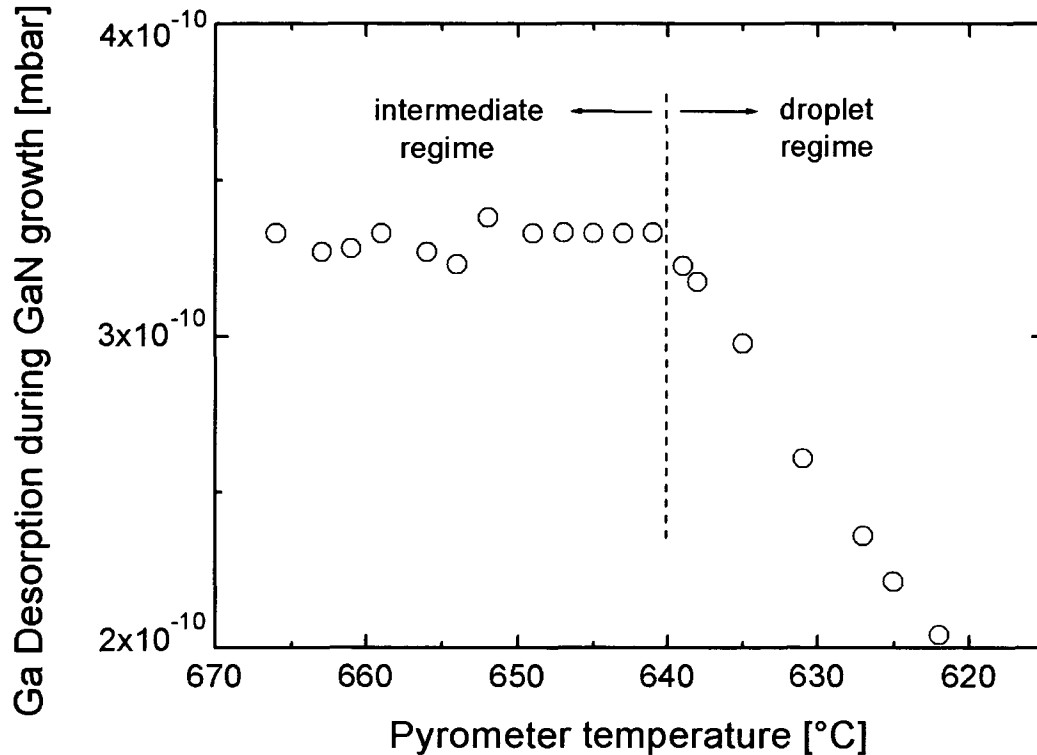

Fig. 4.7. Ga desorption during the 50 sec long GaN growth pulses as a function of substrate temperature at a constant III/V ratio as deduced from Fig. 4.6.; the break–off in the desorption is equivalent to the borderline for Ga droplet formation allowing the determination of the offset between nominal and actually measured substrate temperature.

4.5. Thermal Decomposition of GaN

A crucial aspect regarding the stability of GaN–based devices is the knowledge of the thermal stability and its consequences for the several processing steps performed at the commonly high temperatures. For instance, high–temperature annealing as one such step is typically employed for the activation of Mg dopants to achieve p–type doping [120], for the removal of processing–induced damage [121] and for the alloying of ohmic contacts to both n–type and p– type GaN [122]. At these elevated temperatures there occurs often a preferential loss of N_2 [123] resulting in undesired decomposition and coarsening of the GaN surfaces. The onset temperature for thermal decomposition gives therefore an upper limit for the unrestricted processing and operation of such GaN devices. Understanding the decomposition kinetics is further important for GaN growth itself, as they not only influence the actual growth rate but also determine the surface morphology. In particular, high–quality GaN growth con-

sists often of a two–stage growth procedure, initiated with a low–temperature GaN nucleation layer that proves generally beneficial for the crystallinity of the consecutively grown high–temperature GaN layer [124-126]. The involved temperature ramp or annealing procedure of such a low–T nucleation layer is then a key determinant of the resultant defect densities in the subsequently grown high–T GaN epilayers [127], mainly as a consequence of the degree of coarsening from thermal decomposition.

To quantify the rate of decomposition for the technologically most relevant GaN (0001) surface, the QMS technique was applied to directly measure the desorbing Ga species during the high temperature evaporation of the GaN surface into the MBE vacuum environment. As a starting basis, a ~ 2μm thick GaN template grown on sapphire by MOCVD (yielding the Ga–polar (0001) surface) was heated up to 705 °C and a 5 nm thin GaN buffer layer was grown on top by MBE under Ga–droplet conditions (ϕ_{Ga} = 15 nm/min, ϕ_N = 2.5 nm/min fixed). This should ensure the prevention of any possible surface contaminantion effects and the very Ga–rich conditions provide for a smooth GaN growth front [116]. The buffer layer growth was followed by a ~ 200 sec long vacuum evaporation phase, where the predominant Ga desorption is used to give a direct measure of the decomposition rate. During this vacuum desorption stage the background pressure was in the low 10^{-6} mbar range, given by residual nitrogen from the previous buffer layer growth. The GaN buffer layer growth and vacuum

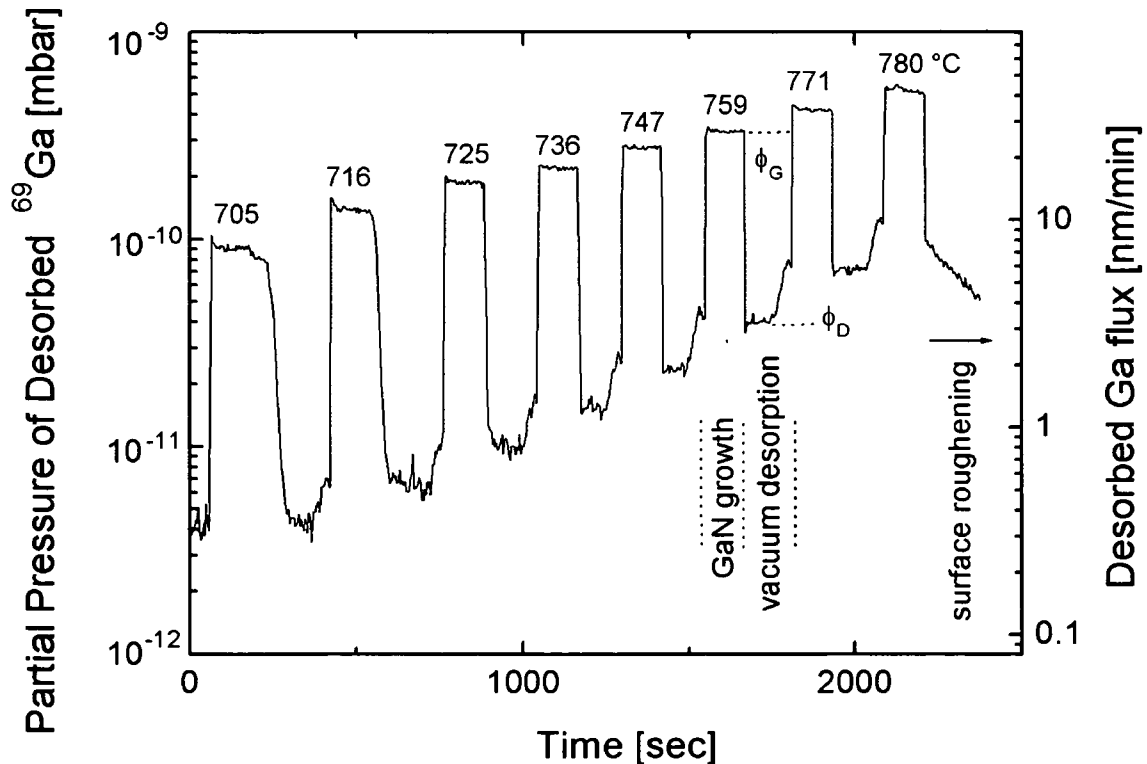*Fig. 4.8. Series of GaN growth and vaccum evaporation cycles at various different temperatures (705–780 °C) and their respective Ga desorption characteristics. As a measure for GaN thermal decomposition the level ϕ_D (as indicated exemplarily for 759 °C) for Ga vacuum evaporation rises continuously with increasing temperature up to 780 °C, but drops beyond due to surface roughening and faceting.*

desorption cycle was then repeated for higher temperatures. Each growth cycle was performed under identical Ga–droplet conditions, achieved by adapting the Ga flux for each temperature in such a way that the excess Ga flux above the droplet border was always 2 nm/min. The Ga desorption measurements for both growth and vacuum desorption processes are displayed in Fig. 4.8 for a sequence of temperatures ranging from 705 to 780 °C. It is obvious that the GaN growth phase is characteristic of an increased Ga desorption, which after the growth stop, i.e. during vacuum evaporation, decreases to a level that is roughly one order of magnitude lower. Before each growth cycle there is a slow shoulder–like increase in the Ga desorption arising from the ramp from one temperature to the next. Most significant for this experiment is the continuous rise in the absolute level of the Ga desorption with increasing temperature for both growth (ϕ_G) and vacuum desorption (ϕ_D), respectively. The rise during the growth phase is due to the increased amount of excess Ga being able to desorb thermally according to the exponentially increasing border for Ga droplet formation (see for comparison also Fig. 4.2.). On the other hand, the rise in Ga desorption during the vacuum evaporation phase can only be attributed to an increased rate of thermal decomposition of the bare GaN surface. Note, that this level ϕ_D rises continually up to temperatures of about 780 °C, but beyond it decreases again. Simultaneous RHEED observations also indicated a transition at this point from a streaky to a spotty pattern, suggesting a coarsening and faceting of the GaN surface. To prove the proposed surface coarsening effect by decomposition, the surface morphology was investigated after 200 sec of vacuum annealing at three different temperatures. The 1×1 μm^2 atomic force microscopy (AFM) images in Fig. 4.9 display GaN (0001) surfaces annealed at (a) 705 °C, (b) 750 °C and (c) 790 °C, respectively. It is remarkable that for the two lower temperatures (a) and (b) the GaN surface morphology remains rather uneffected from thermal decomposition, resulting in overall very smooth surfaces showing a pronounced step–flow growth character, i.e. a terracelike surface structure with monolayer (2 – 3 Å) high steps. However, the surface in Fig. 4.9 (a) is also disrupted by occasionally large pits and shallower surface depressions along the steps. The mean surface roughness (rms) over the whole 1×1 μm^2 area is as low as 0.83 nm for the GaN surface annealed at 705 °C and 0.34 nm for the one annealed at 750 °C, respectively. On the other hand, GaN annealed at 790 °C evidences a significant degree of decomposition resulting in a very cratered surface with an rms roughness as high as 12.5 nm.

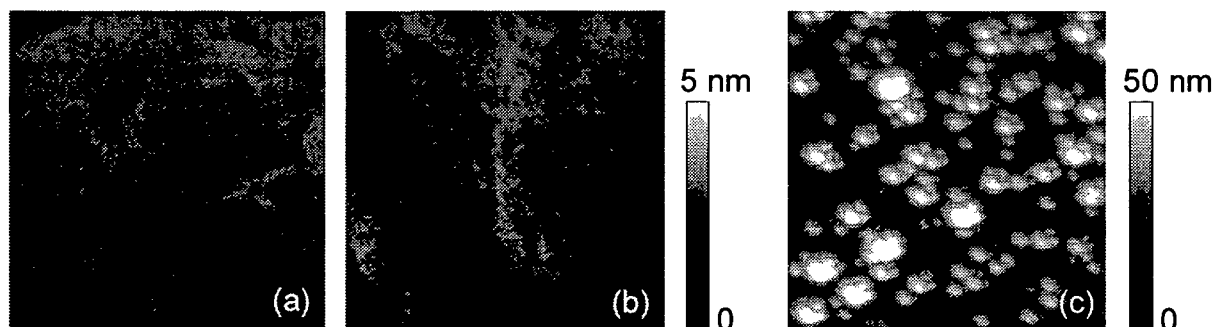*Fig. 4.9. 1×1 μm^2 atomic force microscopy images of GaN (0001) surfaces annealed in vacuum for 200 sec at (a) 705 °C, (b) 750 °C and (c) 790 °C. Note the severe roughening in (c) due to an enhanced degree of thermal decomposition.*

In order to explain the continuous drop in Ga desorption (ϕ_D) during vacuum evaporation at temperatures beyond 780 °C, it can be assumed that this is generated by the formation of a certain facet being preferentially stable against thermal decomposition while the surrounding matrix material is more prone to decomposition (see also discussion).
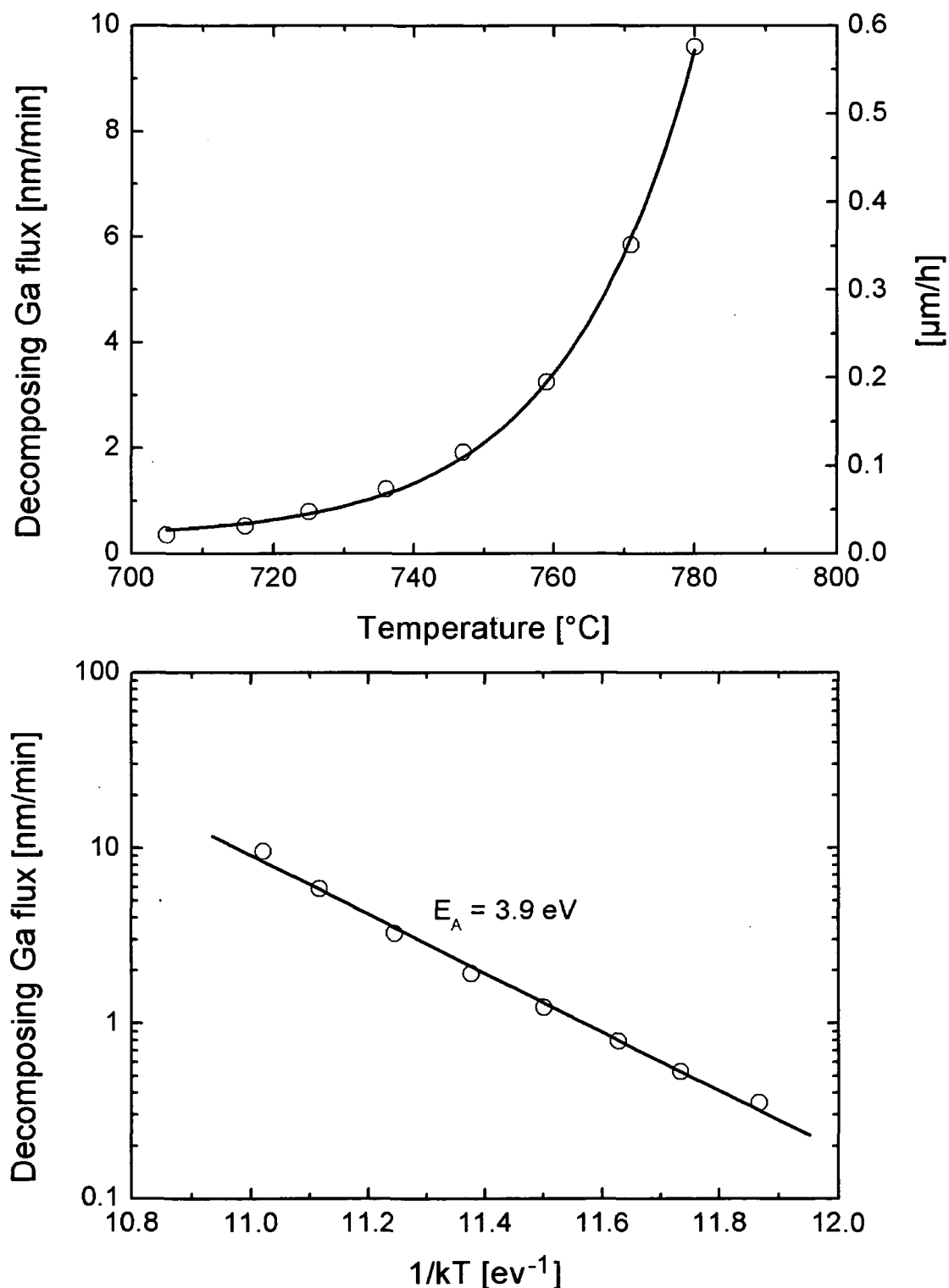

Fig. 4.10. Decomposition rate of the GaN (0001) surface under vacuum conditions (a) as a function of annealing temperature derived from plotting the values for ϕ_D of Fig. 4.8. and (b) in Arrhenius presentation yielding an activation energy of 3.9 eV.

When plotting the absolute level of the Ga desorption during vacuum evaporation (ϕ_D) as a function of the annealing temperature, the resulting data in Fig. 4.10 (a) shows an exponential increase of the decomposing Ga flux with temperature. Extrapolating the experimental data to higher temperatures yields then an easily memorized decomposition rate of 1 μm/h at a temperature of ~ 800 °C. Furthermore, from the Arrhenius–like behavior of the decomposition rate (Fig. 4.10 (b)) one can deduce an activation energy for the decomposition process which was determined to 3.9 eV by a linear fit to the experimental data.

Discussion

The acquired thermal decomposition rates of the GaN (0001) surface under vacuum conditions are based on the widely used assumption that the reverse reaction of decompostion is limited by the formation and desorption of N_2 [128,129]. Under such conditions the driving force for the decomposition of GaN into the MBE vacuum can be described by the chemical reaction [130]

$$2GaN(\text{solid}) \rightarrow 2Ga(\text{solid}/\text{gas}) + N_2(\text{gas}).$$ (4.2.)
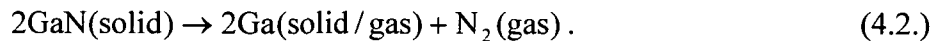
As a product of this reaction Ga may remain on the GaN surface as metallic Ga droplets, as has been observed for the case where the GaN decomposition rate exceeds the Ga desorption rate [127], or it may be desorbed as gaseous species immediately after decomposition [128]. Because of the much lower decomposition rates compared to the Ga desorption rates at any given temperature (evident when comparing Fig. 2 and Fig. 4.10 (a)), no Ga droplets on the surface are observed, as confirmed by subsequent optical microscopy and AFM. Therefore, according to the stoichiometric reaction in Equ. (4.2.) it is valid to take the desorbing Ga flux as an absolute measure for the GaN decomposition rate. However, in a rare case only the formation and desorption of GaN clusters has also been observed [131].

Much more diverse decomposition reactions occur when GaN growth is carried out by MBE with an ammonia source (NH_3) or even more so in an MOCVD environment, where the decomposition rate is substantially dependent on the characteristically near atmospheric pressures and the ambient gases N_2 or H_2 [129,132]. In a systematic gravimetric study by Koleske and coworkers it was found that the GaN decomposition rate can be enhanced in flowing H_2 when increasing the pressure. These results were explained by suggesting a pronounced involvement of hydrogen in the decomposition reactions, i.e. mainly the chemical dissociation of H_2 on the GaN surface which then increases the Ga or Ga hydride surface mobility and further aggravates N_2 desorption [127]. This is also reflected in the relatively low activation energies for decomposition which are 2.96 eV measured in H_2 at 76 Torr and even lower for pressures above 100 Torr. When N_2 was substituted for H_2, however, the activation energy for decomposition was independent of the pressure and increased to 3.62 eV because the chemical pathways for forming hydrogenated N and Ga species are absent, leading to a much larger kinetic barrier to GaN decomposition [133]. Slightly lower activation energies (3.2–3.6 eV) for the (0001) surface orientation were derived from the the various different techniques of investigating the GaN evaporation processes in ammonia–assisted

MBE growth [134–138]. To explain these miniscule differences, Grandjean *et al.* argued that the NH_3 flux influences the overall GaN decomposition rate through a nitrogen–controlled blocking effect of the top GaN adsorption layer [137]. Also, the surface polarity and morphology are found to play an important role in that the decomposition rate is lower and consequently the activation energy is higher from a GaN surface that lacks of any inversion domains [137]. In this context, the polarity–dependent study of the thermal stability of GaN films grown on various different substrates by C. J. Sun et al. [139] pointed out that the N–polar ($000\bar{1}$) GaN surface appeared to be the most stable surface, followed by the nonpolar ($11\bar{2}0$) surface, while the Ga–polar (0001) surface is the least stable one. The present decomposition measurements by QMS yielded one of the highest ever reported activation energies of 3.9 eV, close to the $E_A = 3.93$ eV deduced by a similar QMS method of GaN samples annealed in an evacuated quartz tube by O. Ambacher et. al. [140]. These exceptionally high activation energies can be attributed to a much larger kinetic barrier for thermal decomposition, in accordance with the absence of any surface activated hydrogen (in contrast to MBE and MOCVD with NH_3 sources) which would usually yield much lower activation energies. Besides this interpretation, the influence of a high threading and line defect density on the overall decomposition rate cannot be ruled out. Epitaxial GaN on sapphire, the base material also in the present work, has a large number of such defects propagating to the surface, which are expected to yield much higher decomposition rates in the vicinity of the defects compared to less disordered regions between defects [141]. As the RHEED pattern and the AFM image in Fig. 4.9 (c) indicated a strong roughening and faceting of the surface at a temperature above 780 °C, the issue of an enhanced defect–dependent decomposition behavior becomes very likely. One possible type of defect that could be associated with this facet stability is an inversion domain boundary (IDB), that would cause N–polar inclusions in the predominantly Ga–polar matrix. However, thermal decomposition of GaN generates several additional defects, typically microscopic defects such as vacancies and vacancy complexes which evolve into macroscopic lattice disorder (pitting) with increasing annealing temperature, as found from defect analysis of Raman spectra [142] and by channeling experiments in Rutherford backscattering spectroscopy [128]. In order to increase the thermal stability of GaN surfaces, chemical passivation layers can be used for stabilization but also for diffusion barriers on these surfaces. A surprisingly successful step in this direction was recently achieved by adsorbing 1 ML of a C_{60} molecule complex, which upon its complete desorption leaves the underlying GaN surface entirely undecomposed even at a temperature above 1000 °C [143].

5. Ga Adsorption and Desorption on Polar GaN {0001} Surfaces

5.1. Introduction

One of the primary obstacles regarding the optimization of GaN–based devices is the generally poor morphology of the MBE grown layers. Compared to traditional semiconductors like GaAs or Si, where low impurity and dislocation densities are standard, for GaN even device–quality material contains huge concentrations of extended defects [144]. As an important step to improve the GaN surface morphology and control dopant incorporation in a systematic way it is essential to understand the surface structure and the underlying growth processes on an atomic scale. In particular, the kinetic processes of adsorption, desorption and adatom diffusion on the surface are considered as key parameters that govern the surface morphology, incorporation kinetics and consecutively the overall material quality. So far, extensive studies have tried to evalute the relationship between surface structure and their accompanying surface reconstructions to understand GaN epitaxial growth. The range of possible reconstructions that may appear on each GaN {0001} surface were recently determined by RHEED, low energy electron diffraction (LEED), and scanning tunneling microscopy (STM) and the chemical composition of these surfaces was estimated from Auger electron spectroscopy (AES) after growth and theoretical first–principles total–energy calculations [12,13,145-150]. As a stunning result, the driving mechanisms for surface reconstructions are fundamentally different to those in other (arsenic– or phosphorous–based) III–V semiconductors, in that the GaN {0001} surfaces appear always metal–rich and nitrogen on and in the surface layer is thermodynamically unstable and therefore absent. In this context, adatom diffusion calculations revealed that the metal–rich surface facilitates high adatom mobilities, particularly fostering adatom transport between subsurface sites (which is also often understood as surfactant effect) [19,20]. For both polar {0001} GaN surfaces, the N–polar [000$\bar{1}$] and the Ga–polar [0001] orientations, there are ongoing attempts to study the chemical composition of the metal–rich surface layer (i.e. Ga adlayer) and explore the adatom mobility by dynamic Ga adsorption and desorption experiments. The only *in situ* studies, so far, have been based upon determining the desorption time of the Ga adlayer from measurements of specular beam intensities in RHEED patterns, yielding merely a semi–quantitative description of the Ga adlayer composition for the different polarities [118,151,152].

To give a fully quantitative determination of the Ga adlayer composition and its dynamic processes involved such as adsorption, surface reactivity and desorption, the following Ga wetting experiments make use of the direct of line–of–sight QMS method, allowing detailed insights into the GaN surface structure for both N– and Ga–polar surfaces. Consistent with theoretical predictions, it will be shown that the Ga adlayer forms an equilibrium coverage that differs substantially between the two surface polarities. Additional temperature–depend-

ent measurements of the surface lifetime of Ga adatoms will further generate a good under-standing of the representative Ga adsorbate–substrate binding energetics and for discussion purposes the Ga adsorbate desorption kinetics will be modelled by differential rate equations and compared to experimental data. The results of this Ga adsorption/desorption study will be the fundamental basis for further investigating the role of the Ga adlayer during PAMBE growth of GaN.

5.2. Ga Wetting Experiments

A set of Ga wetting experiments was performed to identify the adsorption and desorption behavior on both N–polar and Ga–polar GaN surfaces and to determine their pos-sible surface structures. Prior to the experiments, the different surface polarities needed to be prepared by two different growth techiques: The N-polar [$000\bar{1}$] surface was produced by nucleating and growing $\approx 1 \mu m$ GaN directly on c-plane sapphire in our MBE system with active nitrogen supplied by the Epi Unibulb rf plasma source. Under growth conditions of Ga/N=4 and a temperature of 730°C the RHEED pattern resulted in a streaky 1×1 phase, which transformed to a 3×3 surface reconstruction upon cooling below 300°C. Such a reconstruction is a direct evidence of the obtained N-polar GaN surface [12]. The Ga-polar surface, on the other hand, was prepared by growing ≈ 2 μm GaN on sapphire by MOCVD (done by the University of Gent, Belgium). In order to guarantee a surface free of any contamination, this template has been overgrown homoepitaxially with ≈ 0.5 μm GaN, using the same conditions as for the growth of N-polar GaN. The final RHEED pattern showed a smooth 1×1 surface with no additional reconstruction.

Each of these two polar GaN surfaces have now been subjected to a set of Ga wetting experi-ments in the absence of incident nitrogen. This was realized by evaporating short pulses of Ga onto the GaN surfaces by opening and closing the shutter of the Ga effusion cell. The shutter sequences ranged from 1–20 sec and the substrate temperature was kept constant at 650°C. The Ga flux was set to 0.25 ML/sec, thus the shutter sequences corresponded to an amount of deposited Ga between 0.25 and 5 MLs. Then, the QMS setup was used to monitor the desorb-ing Ga signal from the sample surface.

5.2.1. Critical Ga Adlayer Coverage on N–Polar GaN ($000\bar{1}$)

The Ga desorption measurements of the first series of wetting experiments are illust-rated in Fig. 5.1. for the N–polar GaN surface. To explain the main features emphasis is first placed on a closeup view of the typical Ga desorption behavior [Fig. 5.1(a)]. Initializing the very first Ga pulse, the shutter of the Ga effusion cell is opened for only 1 sec and a nominal amount of θ = 0.25 ML Ga is deposited onto the surface. During this shutter sequence Ga starts desorbing, evidenced by a rise of the partial pressure signal of the [69]Ga isotope to a certain peak level. Upon closure of the Ga shutter, the Ga desorption signal then decays exponentially to zero. For the second Ga pulse (shutter sequence = 2 sec, i.e. Ga coverage θ = 0.5 ML), an identical desorption behavior is observed, but notice that the desorption peak has
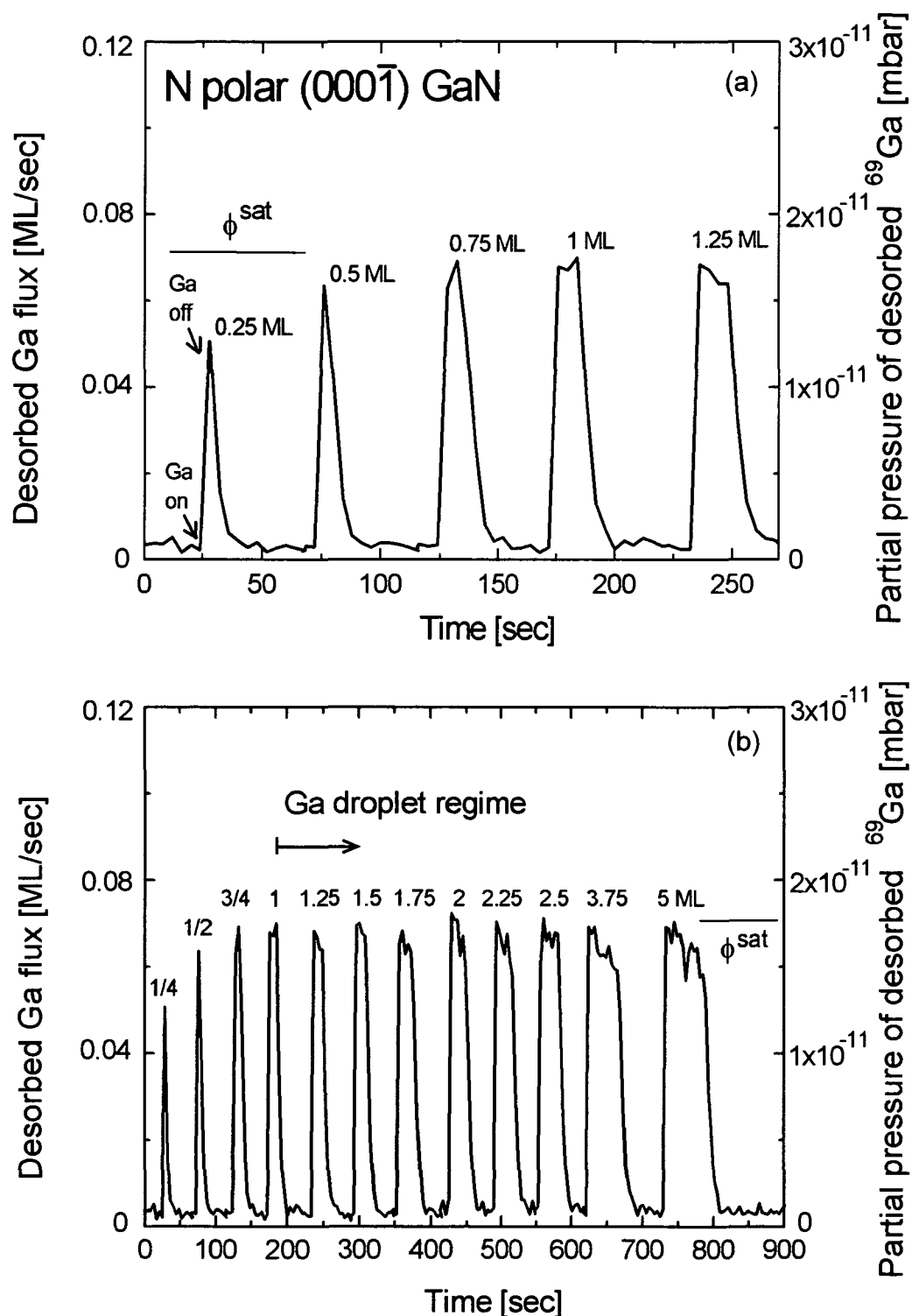
Fig. 5.1. Ga desorption versus time for a series of Ga pulses deposited on a GaN (000$\bar{1}$) surface at constant 650°C. The measurements in (a) illustrate a closeup view of the first few Ga pulses, while (b) shows also longer pulses. The Ga pulses correspond to shutter sequences ranging from 1-20 sec (and coverages of θ = 0.25-5 MLs). The level ϕ^{sat}, at which the peak of the desorption signal saturates and steady-state desorption sets in, indicates the accumulation of excess Ga on the surface (i.e. Ga droplet regime).

increased. As it becomes obvious from the following Ga pulses, this peak rises continuously with surface coverage until it saturates at a Ga coverage of $\theta \approx 1$ ML. Concurrent with the peak saturation, the desorption signal changes in shape for Ga coverages exceeding 1ML, since there is no immediate decay after shuttering. Instead, an equilibrium plateau along with steady-state desorption appears. This situation becomes even more evident when the Ga pulses are extended to higher Ga coverages [see Fig. 5.1(b)]. As a clear trend, it is found that with increasing Ga coverages the duration of the steady-state desorption is getting longer. By integrating the area below each single desorption signal, exactly the same amount of Ga is obtained as has been deposited nominally. This proves that over time all adsorbed Ga atoms desorb completely and no Ga remains on the surface, giving convincingly the direct relation between the Ga desorption signal and the adsorbed Ga surface coverage.

These first-hand results clearly point out that depending on the Ga surface coverage two distinct desorption regimes exist, a monoexponential and a steady-state regime. The transition between the two occurs at a critical Ga coverage $\theta^{crit} \approx 1$ ML. The exponential regime features a decreasing desorption rate with time, while the steady-state regime represents an overall very high desorption rate. These differences imply that Ga on a ($000\bar{1}$) GaN surface must be adsorbed in two different states: (a) as a Ga adlayer up to a maximum coverage of ≈ 1ML and (b) as excess Ga in a rather weakly adsorbed state on top of the adlayer.

To evaluate the nature of the excess Ga, the time evolution of the steady-state behavior was investigated for various Ga coverages. For this purpose, a characteristic steady-state desorption time t^D was defined as the duration between the closure of the shutter and the drop-off in steady-state desorption.
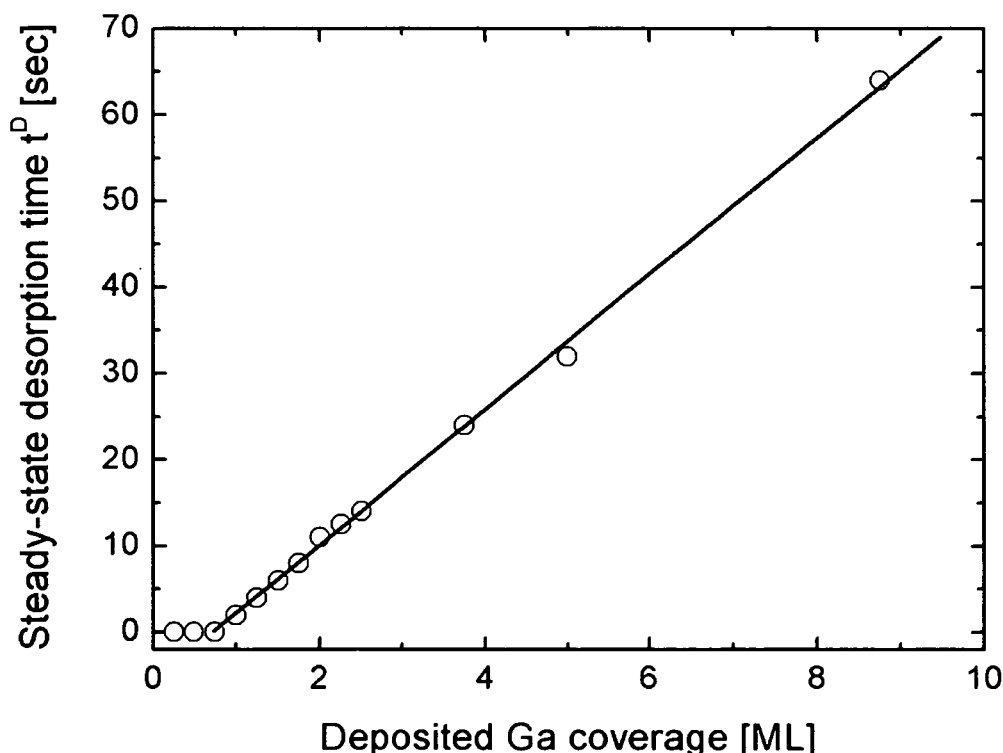

Fig. 5.2. Steady–state desorption time t^P as a function of deposited Ga coverage showing a linear increase of t^P above a coverage of 1ML, which is attributed to Ga droplet accumulation.

When plotting the desorption time t^D as a function of deposited Ga coverage, as displayed in Fig. 5.2., the desorption time was found to scale linearly with the Ga coverage for coverages above the critical coverage of 1ML. This indicates that the weakly adsorbed Ga is accumulated on the surface as some excess Ga reservoir, which might eventually develop macroscopic Ga droplets by a ripening process [118,153]. Simultaneous RHEED intensity observations support this evolution in desorption qualitatively. They exhibited a low-contrast streaked pattern during steady-state desorption that converted to a higher contrast 1 × 1 phase at the final drop-off. A particular RHEED Bragg spot intensity profile for a Ga pulse of 5 ML deposited onto the GaN ($000\overline{1}$) surface at 650 °C is shown in Fig. 5.3. This profile is exactly inverted to the QMS signal and shows low intensity during deposition and desorption of Ga droplets, while the final monotonic increase to higher intensity corrsponds to the desorption of the remaining Ga adlayer. To explain the low intensity contrast of the RHEED patterns during droplet desorption it was recently assumed that droplets cause a severe shadowing effect during very metal-rich conditions in GaN [118] and even in AlN [155] growth. For the low excess Ga coverages in this study though, it can be asumed that the accumulated Ga resembles more or less a continuous metallic Ga film with possibly very small–sized droplets. In fact, the desorption of macroscopic Ga droplets deviates from the steady-state behavior in that they give rise to additional desorption, as will be shown in Sect. 7. However, for simplicity the accumulated excess Ga is from now on referred to Ga droplets.
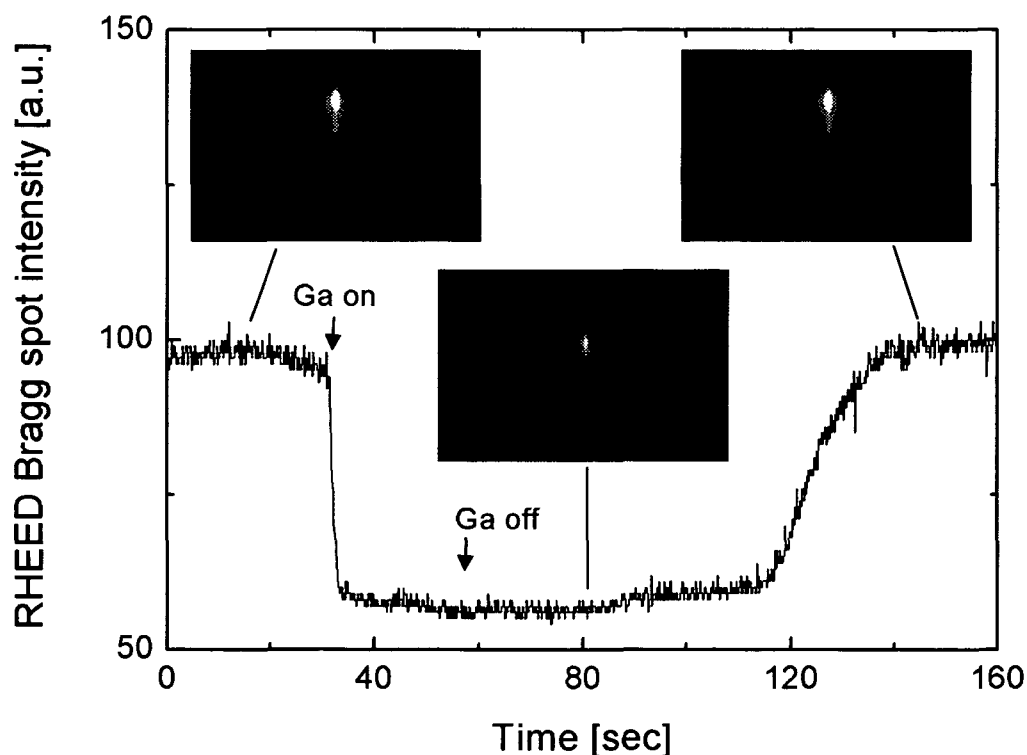

Fig. 5.3. Exemplary RHEED Bragg spot intensity profile as a function of time for the deposition of 5 ML (i.e. 20 sec) Ga on GaN ($000\overline{1}$*) at 650 °C. The RHEED intensity drops during deposition and remains unaltered during Ga droplet desorption, while it increases again for the desorption of the Ga adlayer.*

5.2.2. Critical Ga Adlayer Coverage on Ga–Polar GaN (0001)

Quite different desorption features (desorption times and coverages) occur when Ga pulses are adsorbed on a Ga-polar GaN surface (Fig. 5.4). Depending on the Ga surface coverage, it can basically be differentiated between three essential desorption regimes:

(a) for submonolayer coverages (θ < 1ML) again a fast rise followed by a monoexponential decay of the Ga desorption signal is observed, similar to the N-polar case. The decay, however, proceeds by a much slower rate on Ga-polar GaN (note the difference in the time scale for the two cases).

(b) For Ga coverages above 1ML, the desorption peak rises continuously with surface coverage, until it saturates at $\theta^{crit} \approx 2.7$ MLs. In this range (1ML < θ < 2.7 MLs), the decay of the desorption signal deviates substantially from the typical monoexponential behavior by indicating a rather complicated looking process, which will be investigated later.

(c) Exceeding the critical Ga coverage (θ > 2.7 MLs) yields again a steady-state desorption due to the accumulation of excess Ga on the surface (i.e. Ga droplet regime).
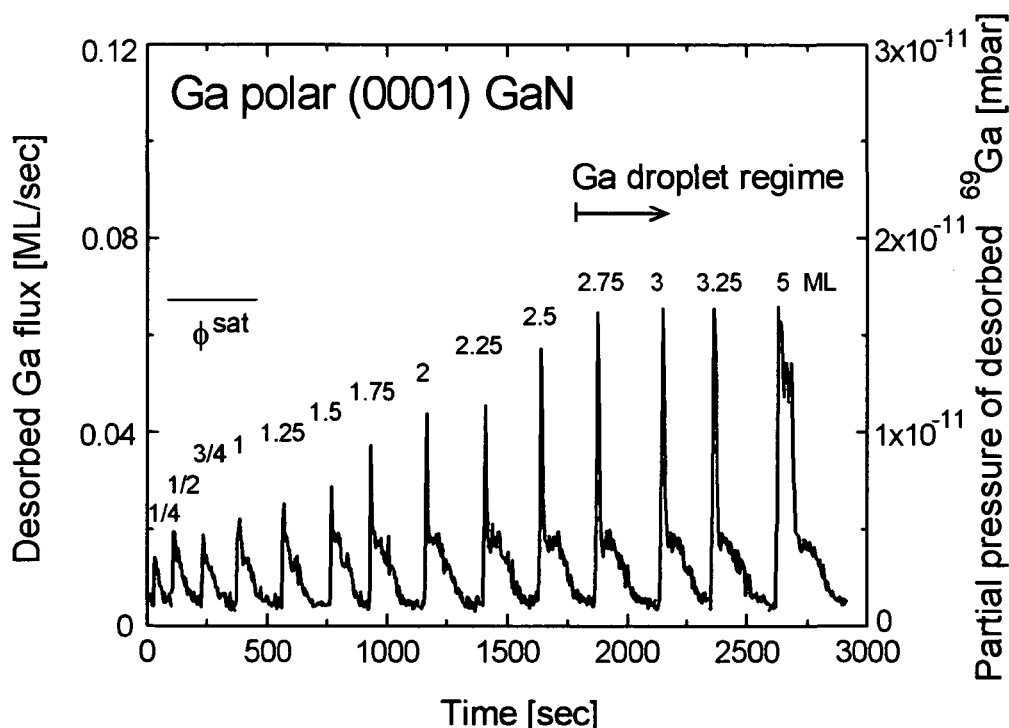

Fig. 5.4. Ga desorption for a series of Ga pulses deposited on a GaN (0001) surface at 650°C. Shutter sequences and Ga coverages are the same as in Fig.5.1. The saturation of the desorption peak at ϕ^{sat} and the onset of steady-state desorption give again the transition to the Ga droplet regime.

In accordance to the N-polar case, the transition between the subcritical and the steady-state regime allows one also to discriminate between a Ga adlayer and excess Ga as droplets on top. Strikingly, the maximum Ga adlayer coverage on Ga-polar GaN has thus a thickness of ≈ 2.7

MLs (corresponding to a laterally contracted Ga bilayer [150]) which is by far higher than the ≈ 1 ML thick analogon on N-polar GaN.

The existence of Ga bilayer and droplets on Ga–polar GaN has also been clearly identified by simultaneous RHEED intensity measurements. In Fig. 5.5 a RHEED Bragg spot intensity profile is shown for the deposition and desorption of ≈10 ML of Ga at 650 °C. The Ga adsorption occurs by a pseudooscillatory transient followed by a low steady-state intensity. The oscillatory behavior can be attributed to the formation of a Ga bilayer, similar to the completion of 2MLs observed from typical growth rate oscillations during layer–by–layer growth as previously shown in the schematics of Fig. 3.5. The subsequent low intensity contrast, however, is again due to the formation of Ga droplets. When the deposition of Ga is terminated, all adsorbed Ga gets desorbed, which follows a behavior inverse to that in the case of adsorption. This means that first the Ga droplets desorb until the bare Ga bilayer remains on the surface. The Ga bilayer desorbs then, as expected, by two oscillations: first approaching a minimum intensity at 1.5 ML, followed by a maximum at 1 ML (evidencing a smooth surface), then again going through a minimum at 0.5 ML and finally reaching the original intensity level at 0 ML, that corresponds to the bare GaN surface.
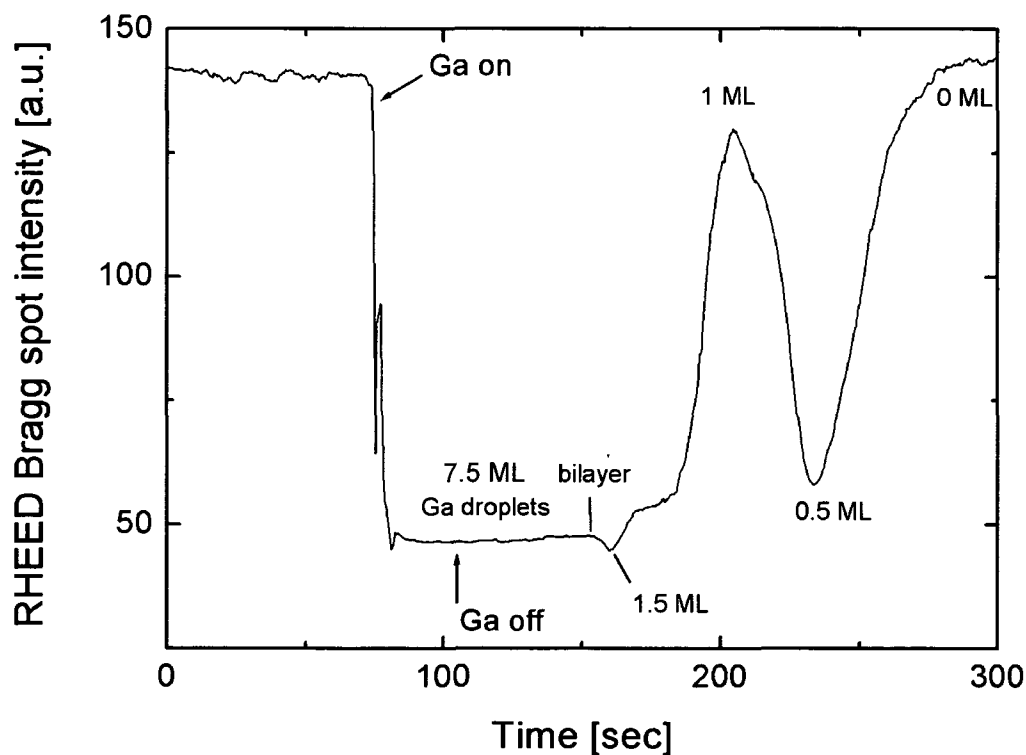

Fig. 5.5. RHEED Bragg spot intensity profile as a function of time for the deposition of 10 ML (i.e. 30 sec) Ga on a GaN (0001) surface at 650 °C. The RHEED intensity drops during deposition (showing a pseudooscillatory feature) and remains unaltered during Ga droplet desorption. After desorption of the Ga droplets the RHEED intensity undergoes a bioscillatory behavior, that can be attributed to the desorption of the remaining Ga bilayer (compare also Fig. 3.5).

5.2.3. Ga Adlayer in Dynamic Equilibrium

In the following, special emphasis is placed on the final stage of the steady-state desorption. The details of this study are exemplified in Fig. 5.6. for a total amount of 14 MLs of Ga deposited on a N-polar and a Ga-polar GaN surface at 650°C.
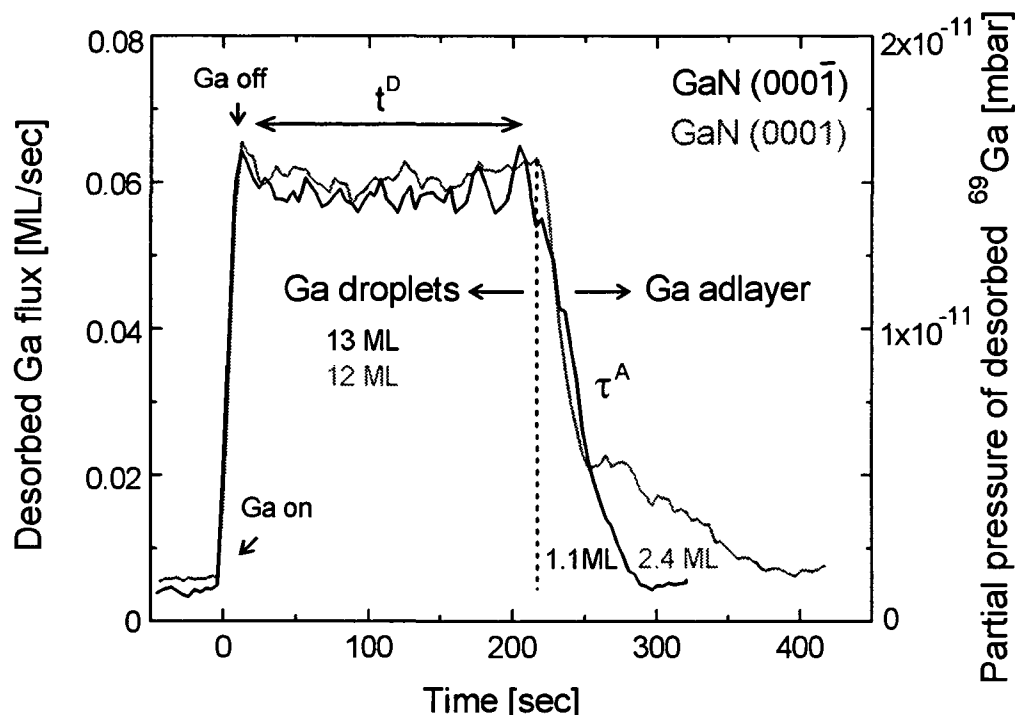
Fig. 5.6. Ga desorption of 14 MLs of Ga deposited on a GaN ($000\overline{1}$) (black curve) and a GaN (0001) surface (grey curve) at constant 650°C. Integrating the areas below the desorption signals facilitates a precise deconvolution of Ga contained in both Ga droplets and the residual adlayer: Ga adlayer coverages are 1.1 MLs on a GaN ($000\overline{1}$) and 2.4 MLs on a GaN (0001) surface, respectively (t^D denotes the steady-state desorption time and τ^A is the characteristic adlayer decay time).

Due to the high amount of excess Ga, there is first a very long period of steady-state desorption t^D, which is of the same order for both polar surfaces. However, when the excess Ga droplets are depleted and the steady-state desorption ceases, subsequently either a monoexponential decay (on N-polar GaN) or the complicated "taillike" decay (on Ga-polar GaN) is observed. Integrating the area below these two types of decaying signals (i.e. the right hand side of the dashed line) gives the remaining Ga coverage. From this and several other extended Ga pulses the residual Ga coverage was found to be independent of the initially adsorbed Ga coverage and amounts to $\theta = 1.1 \pm 0.1$ ML for N-polar GaN, while it equals to $\theta = 2.4 \pm 0.2$ ML on Ga-polar GaN.

Moreover, these values are also independent of the substrate temperature within the experimental error as shown in Fig. 5.7 for a temperature range between 670 – 720 °C.
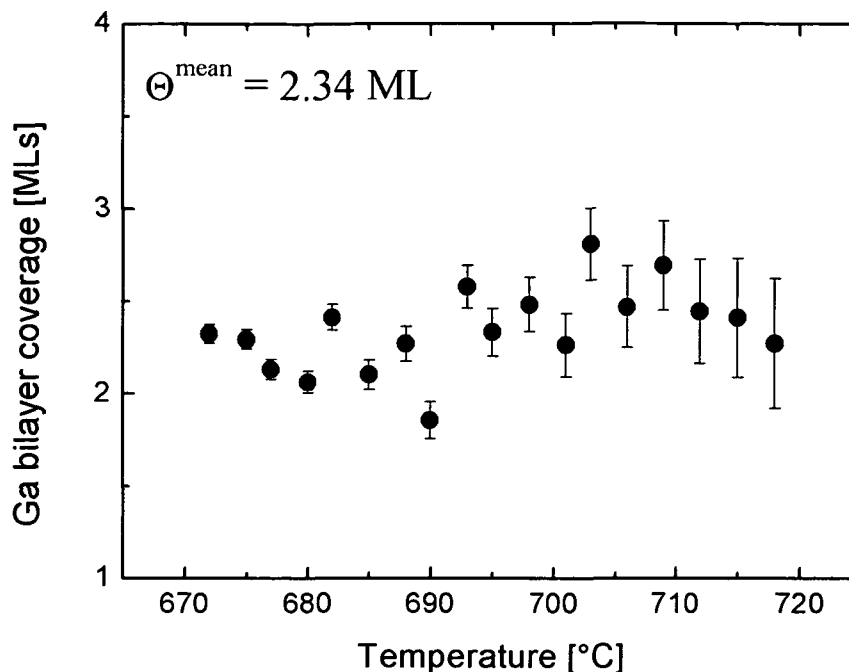
Fig. 5.7. Ga bilayer coverage as a function of substrate temperature as evaluated from pure Ga adsorption (without incident N); the coverage is independent of temperature and has a mean value of 2.34 ML, being in excellent agreement with the theoretical value of 2.33 ML [118].

Note, that these residual Ga coverages reflect exactly the maximum Ga adlayer coverages as evaluated from Figs. 5.1. and 5.4. This means that during the steady-state desorption of excess Ga the whole Ga adlayer is kept fully in dynamic equilibrium and is depleted only afterwards. Most remarkable, these measured Ga adlayer coverages are in sound agreement with recent theoretical predictions: the energetically most favorable Ga adlayer coverages have been determined to 1 ML on GaN ($000\overline{1}$) and to a 2.33 ML laterally contracted Ga bilayer on GaN (0001) [13,150].

The $\approx$2.4 ML thick Ga bilayer on a Ga-polar GaN surface was found to desorb in a complicated fashion. First, there is a quick exponential decay (similar to the $\approx$1ML adlayer decay in the N-polar case), which is followed by a much slower desorption term. It can be assumed that these two terms are associated to the desorption of two individual monolayers adding up to the whole bilayer decay: the quick decay refers to a top ML and the subsequent slow decay corresponds to a bottom ML. Based on this concept, the typical decay times τ^A of the individual monolayers differ severely. Consequently, drastically different interaction strengths between the respective monolayer and the underlying GaN surface are expected.

Indeed, evidence for such a bilayer split-up into single monolayers is further endorsed in the next section, where the representative adsorbate–substrate binding energetics will be given at every desorption stage. Also, a model is presented in the discussion, which resolves the decay of a laterally contracted Ga bilayer structure on the basis of simple differential rate equations.

5.3. Mean Surface Lifetime of Ga Adatoms

In a second series of Ga wetting experiments the previous findings will be extended by a temperature-dependent study of the desorption from Ga adlayer and droplets. Particularly, the mean surface residence lifetime of the Ga adatoms in adlayer and droplets will be determined as a function of substrate temperature. For this investigation, an equal amount of 14 MLs of Ga (with a Ga flux of 1.75 ML/sec) is deposited onto the respective GaN surface for a wide set of substrate temperatures ranging from 620 to 700 °C and, as before, the desorbing Ga atoms are monitored. Care has been taken that this temperature range was well below the onset for thermal decomposition of GaN (see Sect. 4.5), in order to exclude additional desorption from GaN and changes in surface structure due to thermally induced roughening.

5.3.1.   Ga Lifetime on GaN ($000\bar{1}$)

An exemplary extract of these measurements is given in Fig. 5.8(a) for the case of N-polar GaN. There is clear evidence that with increasing temperature the overall desorption time becomes shorter. Consequently, this leads to an elevated Ga desorption signal, since the total amount of deposited Ga is constant throughout the entire study.

Based on these features, one of the key measures in adsorption theory can be determined, namely the mean surface lifetime of adatoms. Such measurements of Ga adatom lifetimes have been studied already quite early for submonolayer coverages on GaAs [156] and GaN [141]. In the present case though, another evaluation scheme has to be applied that considers adatom lifetimes in both Ga droplets and adlayer. If t^D is – as earlier introduced – the desorption time during steady-state desorption of Ga droplets, and θ_D the amount of Ga contained in droplets, then the mean Ga adatom lifetime in droplets is simply expressed by $\tau^D = t^D/\theta_D$. To assess the characteristic Ga adatom lifetime in the remaining adlayer, the monoexponential decay of the Ga desorption signal provides useful information. Since the Ga surface population n decays in first order kinetics by $n \propto \exp(-t/\tau^A)$, where t is the time, the mean adatom lifetime in the adlayer is then equivalent to the decay time τ^A. Using these expressions, the Ga adatom lifetime in droplets and adlayer varies by approximately $\tau^D = 3 - 85$ sec and $\tau^A = 4 - 170$ sec in the 620 – 700°C temperature range (the superscripts D and A refer to droplets and adlayer). As intuitionally expected, adatoms remain longer in the adlayer, due to a stronger bonding mechanism to the GaN surface compared to the weakly adsorbed excess Ga in the droplets For further proof, the determination of the activation energies for these desorption processes can give more proper insight. Applying the Frenkel equation for the adatom lifetime [157]

$$\tau = \frac{1}{v_0} \exp\left(\frac{E}{kT}\right),$$ (5.1.)

where ν_0 is the adatom-surface vibrational frequency, T the substrate temperature and k the Boltzmann constant, the adatoms face an activation process for desorption with a characterist
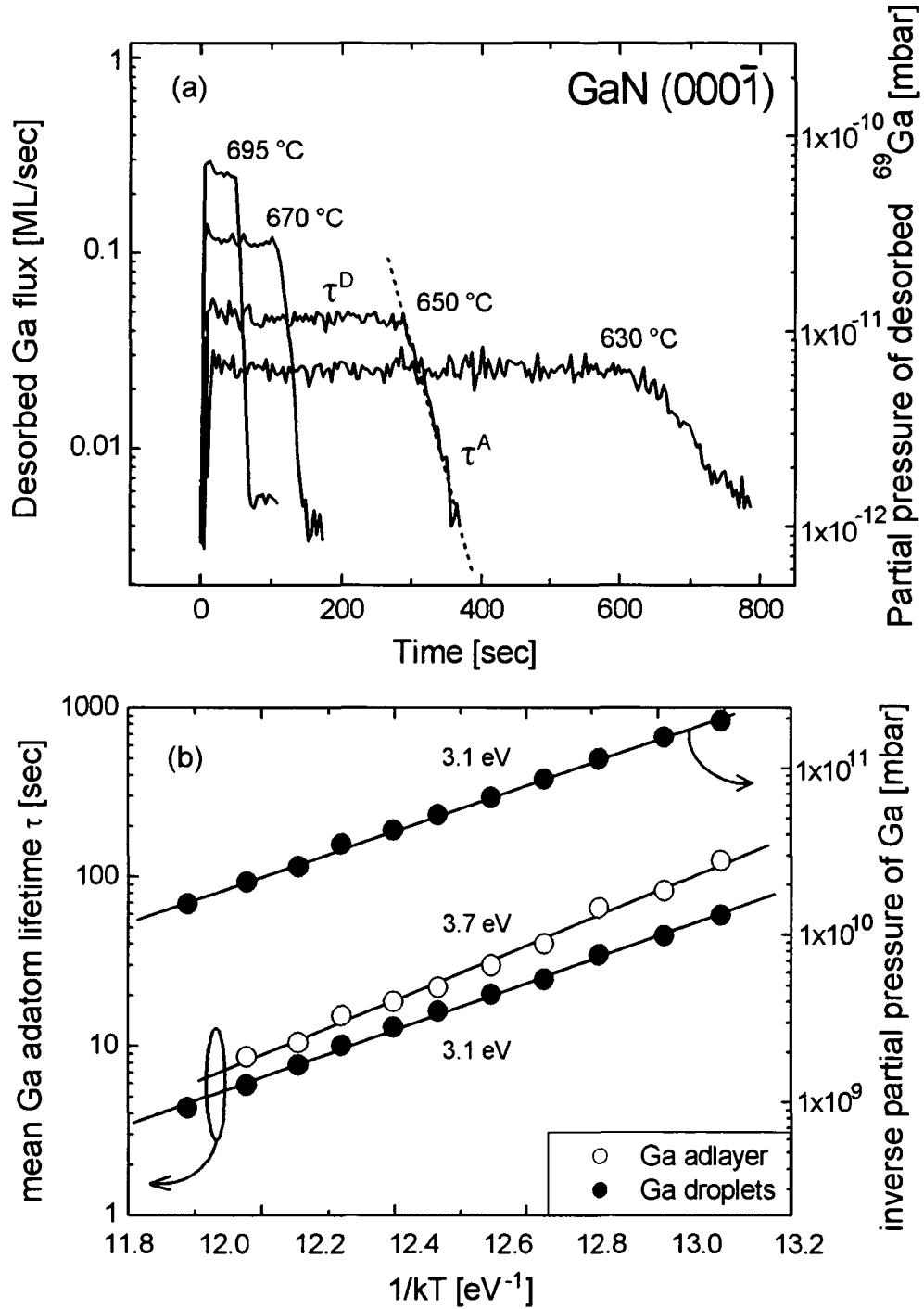

Fig. 5.8. *(a) Temperature-dependent Ga desorption versus time for 14 MLs of Ga adsorbed on a GaN (000$\bar{1}$) surface; the duration of the steady-state desorption and the decay time of the adlayer yield (b) the mean Ga adatom lifetime τ in Ga droplets and adlayer as a function of 1/kT. The gradients of the curves give the activation energies for desorption from droplets (E^D = 3.1 eV) and adlayer (E^A = 3.7 eV). Alternatively, plotting the the Ga partial pressure level during steady-state desorption of Ga droplets yields an identical activation energy.*

ic energy E. An Arrhenius-type fit to the data [Fig. 5.8(b)] results in activation energies for Ga desorption from droplets and adlayer equal to $E^D = 3.1$ eV and $E^A = 3.7$ eV, respectively. The activation energy for Ga desorption from droplets can even be evaluated by a more simple routine. Plotting the inverse of the Ga partial pressure signal (1/desorption rate = lifetime) during steady-state desorption as a function of 1/kT yields also $E^D = 3.1$ eV (see upper curve in Fig. 5.8(b)).

5.3.2. Ga Lifetime on GaN (0001)

A similar, but more complex picture emerges when deriving Ga adatom lifetimes on Ga-polar GaN surfaces. Akin to the N-polar case, both the overall desorption time and the partial pressure level of the Ga desorption signal scale with substrate temperature [Fig. 5.9(a)]. The only difference though arises from the complicated desorption process of the Ga bilayer structure. In detail, it is proposed that this characteristic bilayer decay represents a superposition of separate terms which correspond to the depletion of a top and a bottom monolayer (see also discussion). According to this, Ga adatom lifetimes in the individual monolayers can be deconvolved by fitting the initial and the final part of the decaying Ga signal to two exponential functions (i.e. dashed lines denoted by τ^T and τ^B) and using the same expressions as introduced above. The intermediate part of the bilayer decay can be neglected for this evalutaion, but will be explained as a central feature in the discussion. The resulting lifetimes plotted as a function of inverse substrate temperature are shown in Fig. 5.9(b).

Due to the different degrees of bond strengths in the respective layers, Ga adatom lifetimes are the shortest in droplets, a little longer in the top layer and very long in the bottom layer of the Ga bilayer. This is further reflected by the activation energies for desorption from Ga droplets and the single monolayers, which were determined to $E^D = 3.2$ eV, $E^T = 3.7$ eV and $E^B = 4.9$ eV, respectively (the superscripts D, T and B refer to droplets, top ML and bottom ML). To give an overview, all the key parameters describing the Ga desorption energetics (E, v_0, τ) are summarized in Table 5.1. for both polar GaN surfaces. Previous indirect techniques have highlighted a wide scatter in the activation energy for Ga desorption from droplets, ranging from 2.4 to 5.1 eV [116,118,151,157,158]. For statistical reasons, additional Ga wetting experiments were performed to identify the accuracy of this specific activation energy. Altogether, four such experiments on each of the two GaN surface orientations were carried out, including also one set of rough GaN surfaces which has been grown under N-rich conditions. The activation energies have then been derived by the two equivalent techniques as described in Sect. 5.3.1. (i.e. desorption time t^D and steady-state partial pressure level). The average activation energy for desorption from Ga droplets results thus to $\overline{E}^D = 3.1 \pm 0.2$ eV, independent of the underlying GaN surface orientation and surface roughness.
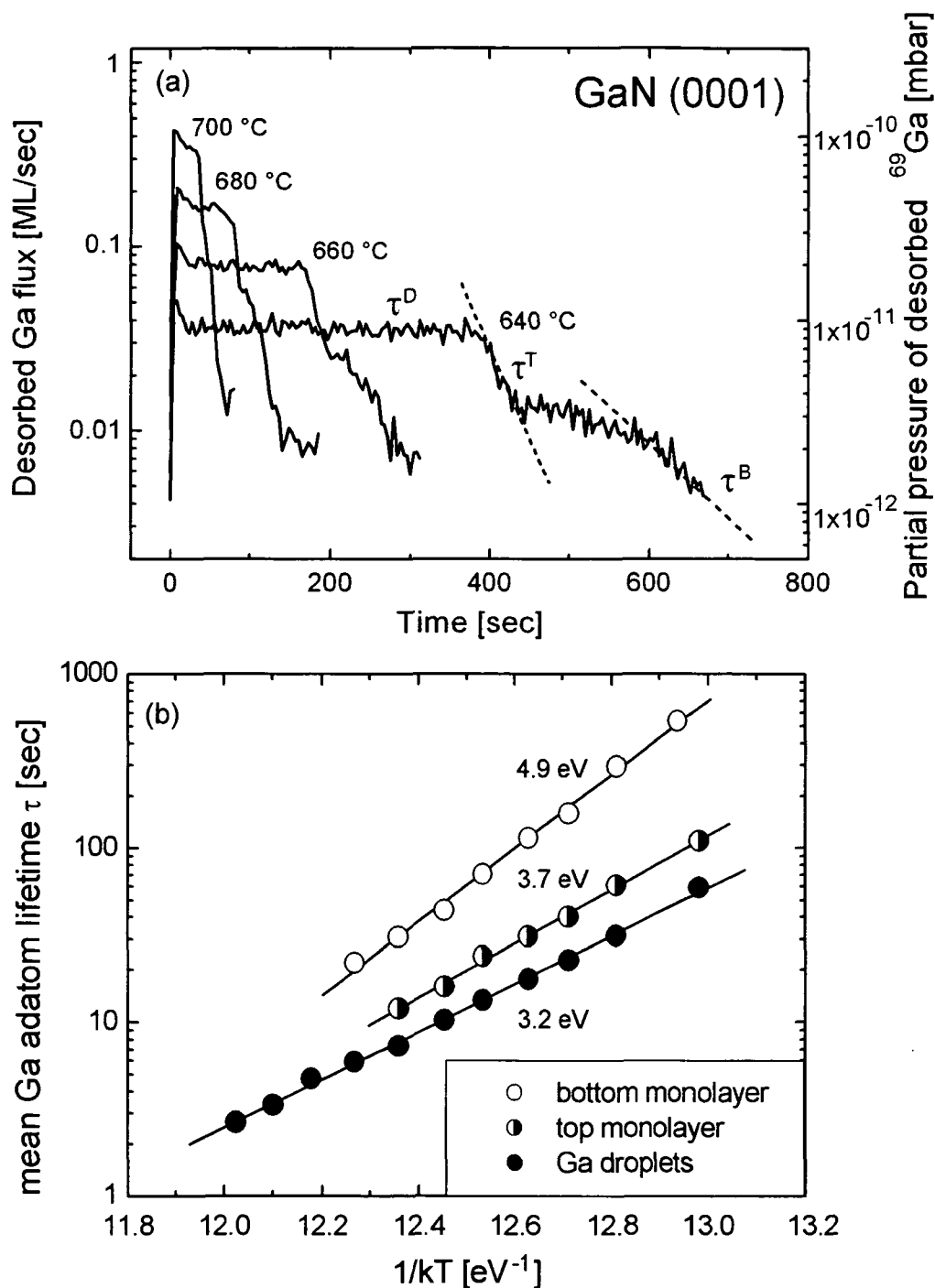
Fig. 5.9. (a) Temperature-dependent Ga desorption versus time for 14 MLs of Ga adsorbed on a GaN (0001) surface yielding (b) the mean Ga adatom lifetime τ in Ga droplets and both single monolayers of the Ga bilayer structure as a function of 1/kT. The activation energies for desorption from droplets and monolayers are $E^D = 3.2$ eV, $E^T = 3.7$ eV and $E^B = 4.9$ eV.

GaN surface	Layer	E [eV]	ν_0 [Hz]	τ [sec]
	bottom ML	4.9	6.6×10^{24}	5 - 750
(0001)	top ML	3.7	6.2×10^{18}	3.3 - 125
	droplets	3.2	1.9×10^{16}	2.5 - 60
(000$\bar{1}$)	adlayer	3.7	4.5×10^{18}	4.3 - 170
	droplets	3.1	4.1×10^{15}	3.5 - 85

Tab. 5.1. Characteristic parameters for Ga desorption from both (0001) and (000$\bar{1}$) GaN surfaces; E denotes the activation energy, ν_0 the adatom-surface vibrational frequency and τ is the mean Ga adatom surface lifetime (the values for the lifetime given below are restricted to a temperature range from 620 – 700°C).

5.4. Differential Rate Equations and Model for Ga Bilayer Decay

As obvious from Fig. 5.6 – 5.8, the ≈ 1.1 ML Ga adlayer coverage on the N-polar GaN surface is prone to decay by a simple monoexponential law. The ≈ 2.4 ML thick Ga bilayer on Ga-polar GaN follows, however, a more complicated desorption process. To understand the latter process, a basic model is offered that involves the decay of two single monolayers adding up to the observed bilayer desorption. For this reason, it is assumed that the Ga bilayer structure can be split up into ≈ 1ML of Ga above the last Ga-terminated GaN layer (i.e. bottom monolayer) and a Ga toplayer containing ≈ 1.4 MLs in terms of GaN atomic density (1ML = 1.14×10^{15} atoms/cm^2). Such an arrangement has actually been validated from some of the previous experiments [in Fig. 5.9(a)] by simply integrating the area below each single desorption term. Independent of substrate temperature, the amount of Ga referring to the initial fast decay yielded 1.4 ± 0.2 MLs (i.e. top ML), while the subsequent taillike decay gave exactly the remaining ≈ 1 ML (bottom ML). According to first-principles total energy calulations by Northrup et al. [150], this bilayer split-up represents the energetically most favorable surface structure under Ga-rich conditions. In this case, the Ga bottom ML matches the underlying substrate and therefore features a Ga–Ga in-plane separation corresponding to the 1×1 GaN surface (≈ 3.2 Å). The Ga toplayer on the other hand faces lateral contraction with respect to the substrate, allowing ≈ 1.4 ML of Ga atoms being squeezed into its plane. This benefits from a reduction in the surface free energy along with the Ga–Ga in-plane spacing having almost values typical for liquid Ga (≈ 2.7 Å) [150]. This situation is schematically drawn in Fig. 5.10.

Applying these concepts, a qualitatively and quantitatively correct description of the entire bilayer desorption process relies on the implementation of three essential desorption

stages. In the following, each stage is modeled by a set of differential rate equations which describe the time evolution of the individual layer coverages θ and give exactly the desorbing Ga fluxes ϕ.

(A) *Relaxation stage*: During this very first stage, it is proposed that only the laterally contracted ≈ 1.4 ML top layer desorbs, which fosters a simultaneous self–relaxation process. Formally speaking, with Ga atoms desorbing from the strained top layer, the Ga–Ga in-plane spacing becomes gradually larger. When the top layer coverage θ^T decreases to 1 ML (i.e. total bilayer coverage = 2 ML), full relaxation is finally accomplished and the Ga–Ga separation complies with the underlying bottom ML as well as the GaN surface (see also Fig. 5.10). Ideally, during relaxation the Ga atoms in the top layer keep the bottom ML completely covered, so that no atoms from the bottom ML can escape. The following differential equations describe this situation for both top and bottom monolayer in the effective range of $1.0 < \theta^T(t) < 1.4$ ML:

$$\phi^T(t) = -\frac{d\theta^T(t)}{dt} = \theta^T(t) \cdot a \qquad (5.2.)$$

$$\phi^B(t) = -\frac{d\theta^B(t)}{dt} = 0. \qquad (5.3.)$$

Subjected to the initial conditions of $\theta_0^T = 1.4$ ML and $\theta_0^B = 1.0$ ML, the bottom monolayer remains entirely unaffected, while the coverage of the top layer decreases by a simple exponential law. With $a = v_0^T \exp(-E^T/kT)$, denoted as the desorption probability from the top layer, this term depends only on the substrate temperature T, the activation energy for desorption E^T and the adatom-surface vibrational frequency v_0^T (similar to the Frenkel Equ. 5.1).

$\theta^T = 1.4$ ML
$\theta^B = 1.0$ ML
$a^T_\parallel = 2.7$ Å
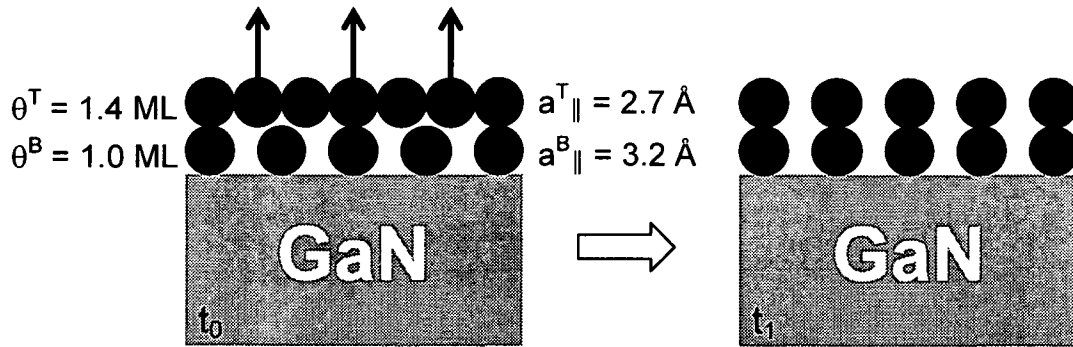$a^B_\parallel = 3.2$ Å

Fig. 5.10. Schematic illustration of the relaxation of the top part of the Ga bilayer at the initial condition t_0 ($\theta^T(t_0) = 1.4$ ML) (left) and at its final stage t_1 ($\theta^T(t_1) = 1ML$) (right).

(B) *Transfer stage*: Starting from a fully relaxed top layer ($\theta^T = 1$ML), Ga atoms keep desorbing as in the relaxation stage. But, with the gradual decrease in θ^T over time ($0 < \theta^T(t) < 1.0$ ML), the surface of the bottom ML becomes increasingly bare, allowing atoms from the bottom part to desorb as well. While this occurs, it is assumed that subsequently Ga atoms from the top layer hop down and nourish the bottom ML, in order to keep it fully populated

(as illustrated in Fig. 5.11.). From an energetical point of view, this transfer process is reasonable, since Ga atoms are more strongly bound in the bottom layer and do not face an activation barrier for downhill transport [159]. Under these assumptions, the overall coverage of the bottom layer remains constant at $\theta^B = 1.0$ ML, while the top layer follows a rather fast depletion given by both its characteristic desorption and the transfer mechanism. With the desorption probability $b = v_0^B \exp(-E^B/kT)$ for the bottom layer, this stage is then characterized by the following equations:

$$-\frac{d\theta^T(t)}{dt} = \phi^T(t) + \text{Transfer} = \theta^T(t) \cdot a + \text{Transfer} \qquad (5.4.)$$

$$-\frac{d\theta^B(t)}{dt} = \phi^B(t) - \text{Transfer} = \left(\theta_0^B - \theta^T(t)\right) \cdot b - \text{Transfer} = 0 . \qquad (5.5.)$$

$\theta^T = 1.0$ ML

$\theta^B = 1.0$ ML

$a^T_{\parallel} = 3.2$ Å
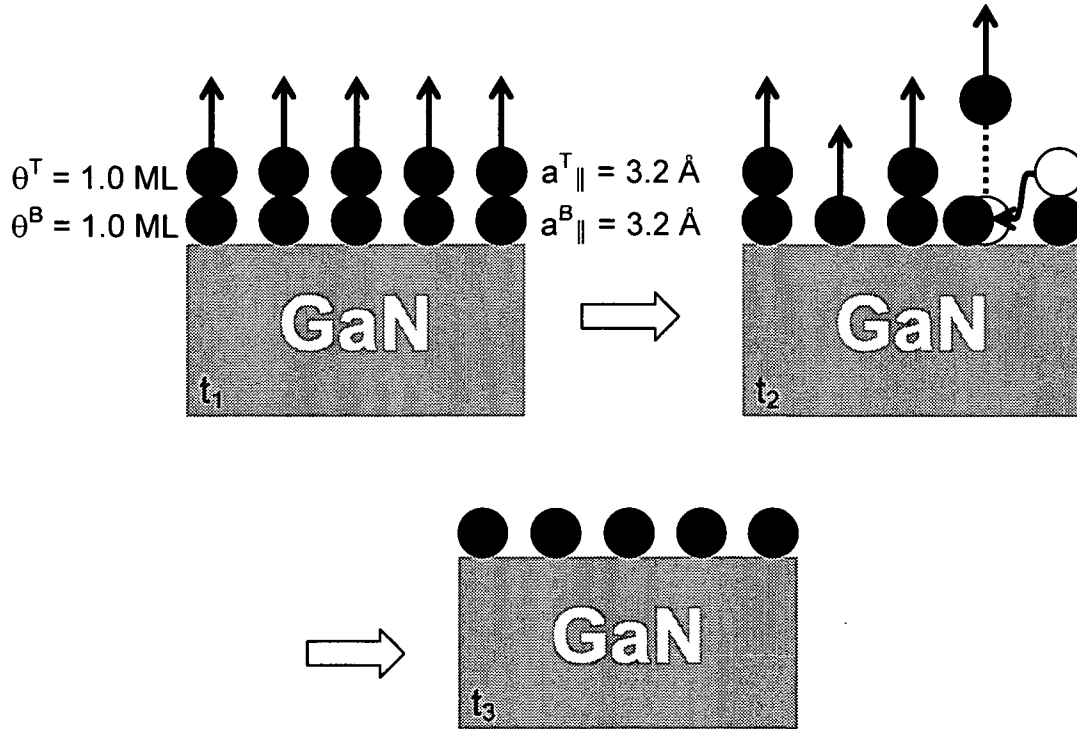
$a^B_{\parallel} = 3.2$ Å

Fig. 5.11. Representation of the adatom transfer stage: with continuous desorption of the top ML starting at t_1, the bottom ML becomes bare and also prone to desorption, resulting in an energetically favorable adatom transfer from the top to the bottom layer (t_2) to keep the latter fully populated. When the top layer Ga coverage is reduced to $\theta^T(t_3) = 0$ ML, this feeding mechanism ceases and the entire bottom ML $(\theta^B(t_3) = 1.0$ ML) remains.

(C) *Bottom ML decay stage*: When finally the top layer is completely depleted ($\theta^T = 0$), the coverage of the bottom ML starts to decrease by a simple exponential law, similar to the relaxation of the top layer in stage (A). The desorption of the remaining bottom layer is illustrated schematically in Fig. 5.12. For this stage the equations can therefore set up by

$$\phi^T(t) = -\frac{d\Theta^T(t)}{dt} = 0$$

(5.6.)

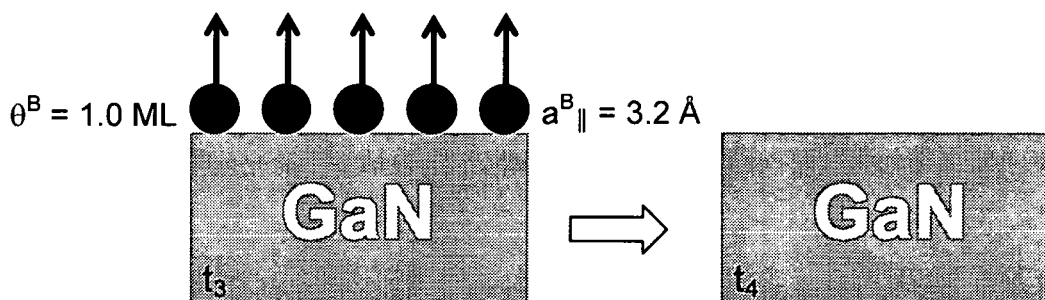$$\phi^B(t) = -\frac{d\Theta^B(t)}{dt} = \Theta^B(t) \cdot b.$$

(5.7.)

Fig. 5.12. Schematics for the desorption of the remaining Ga bottom ML starting at t_3 where the coverage is still fully populated ($\Theta^B(t_3)$ = 1.0 ML) and its approach to where all Ga is desorbed at the final stage t_4.

While initially the experimental data was modeled by simple biexponential models and by the relaxation models, they could not provide a close fit to the data. Thus including the transfer stage was necessary to explain the experimentally observed bilayer decay. By analytically integrating the expressions (5.2.) – (5.7.), the evolution of the individual layer coverages Θ and desorbing Ga fluxes ϕ is obtained easily. The results and the experimental data for a substrate temperature of 640 °C are illustrated in Fig. 5.13., with the contributions of the single layers marked by dashed lines. Taking the activation energies $E^{(T,B)}$ as derived in Sect. 5.3.2 and by adapting only the prefactors $v_0^{(T,B)}$, the proposed model achieves reasonable consistence with the experimental desorption data [see Fig. 5.13(b)], even explaining the two pronounced kinks. To further confirm this model, the bilayer decay has also been calculated for higher temperatures. In close match with the experimental data, it was found that with increasing temperature the desorption probabilities a and b become larger, which consequently leads to a much faster decay. Associated with this, the transfer stage gets gradually shorter and almost disappears for very high temperatures of ≈ 700 °C, in full consistence with the experimental data. Note, that for all these fits no additional fitting parameters were used other than the activation energies and desorption probabilities.
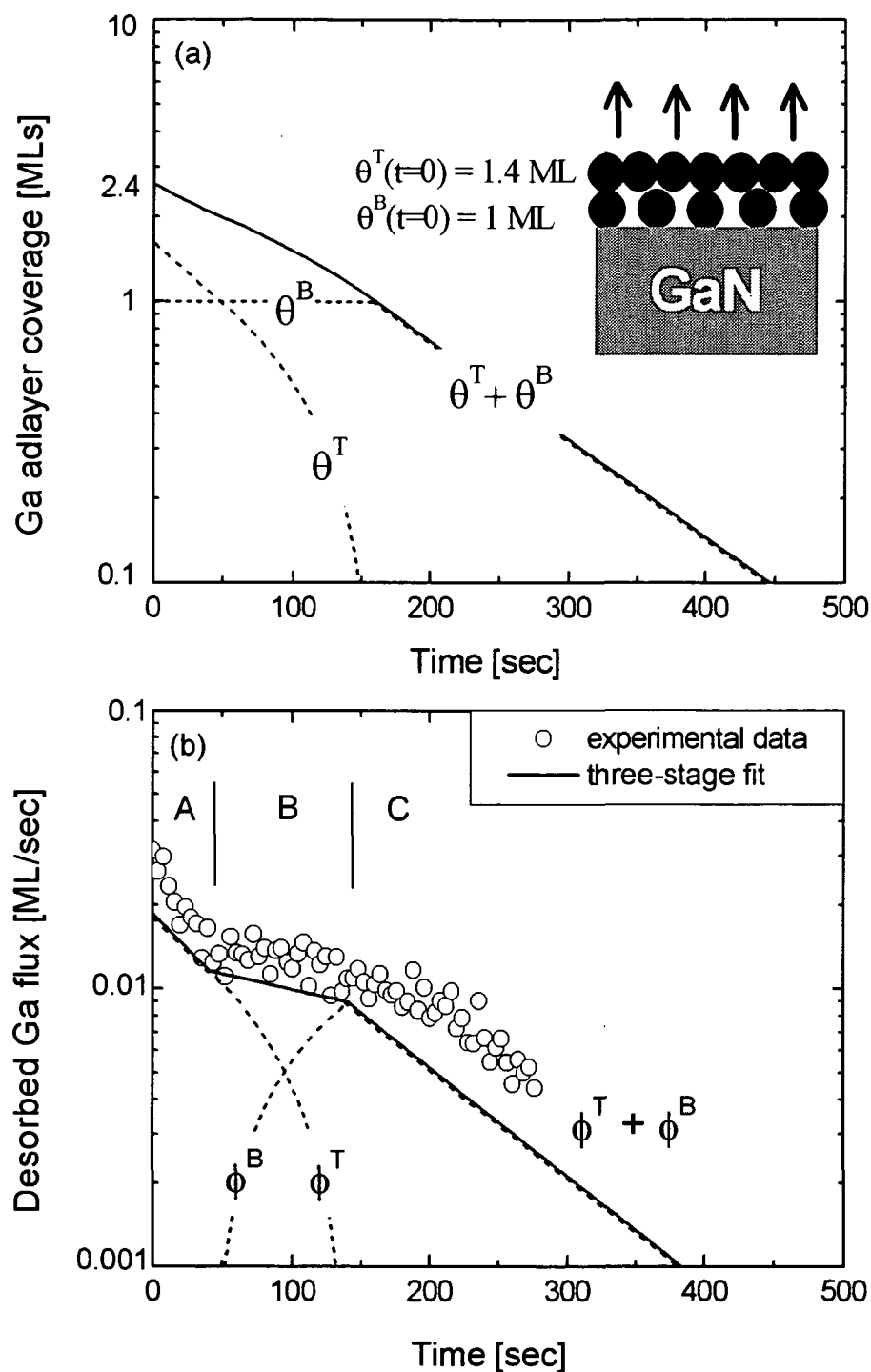
Fig. 5.13. Modeled evolution of (a) the Ga coverage θ and (b) the desorbing Ga flux φ from a decaying laterally contracted 2.4 ML Ga bilayer on a Ga-polar GaN surface at 640°C. Splitting up the bilayer into single monolayers proves important to resolve the complicated three-stage decay featuring (A) the relaxation stage, (B) the transfer stage and (C) the bottom ML decay stage. The contribution of each individual layer (T...top, B... bottom) is represented by dashed lines. Note, the reasonable agreement with experimental datapoints (open circles), using a = 0.0115 Hz, b = 0.009 Hz and the activation energies derived from Fig. 5.9.

5.5. Discussion on Ga Bond Strenghts

As a consequence of polarity, the (0001) and ($000\bar{1}$) GaN surfaces differ crucially in the atomic geometry of the surface terminating atoms. In the N-polar ($000\bar{1}$) case each Ga surface atom has ideally three dangling bonds, in contrast to only one in the Ga-polar (0001) case [19]. This causes the Ga-polar surface to produce strongly directed sp_z orbitals, while the N-polar surface is characterized by delocalized metallic bonds between the surface atoms [25]. The latter leads therefore to a substantially weaker adsorbate–substrate interaction. Based on these considerations, it is comprehensible why in dynamic equilibrium only ≈ 1.1 ML of Ga can be stabilized on a ($000\bar{1}$) GaN surface, compared to a ≈ 2.4 ML stable Ga bilayer on a (0001) surface.

The polarity-related differences in adsorbate–substrate bonding are further reflected by the mean Ga lifetimes and activation energies for Ga desorption from the adlayer. Ga adatoms interacting directly with the GaN substrate (i.e. monolayer coverages) face a much lower activation energy for desorption from a N-polar surface (3.7 eV), as compared to a Ga-polar surface (4.9 eV). On the other hand, the laterally contracted top part of the Ga bilayer on Ga-polar GaN exhibits desorption properties comparable to the Ga adlayer on N-polar GaN ($E^T \approx E^A \approx 3.7$eV). Backed by theoretical, STM and Auger electron spectroscopical studies, [13,148,150] these results suggest an overall stronger bonded Ga adlayer on Ga-polar GaN than on a N-polar surface. The different metallic adlayer configurations also cast a severe influence on surface diffusion mechanisms of N adatoms, in letting them experience a much lower diffusion barrier on a Ga-polar compared to a N-polar GaN surface [19,20]. Furthermore, it is reckoned that these broadly differing bonding and diffusion properties might pose a strong effect on both impurity incorporation and defect formation during GaN growth. Some studies pointed out that GaN grown along the (0001) orientation exhibits smoother surfaces [28,160,161] and alleviates p-type doping by Mg, whereas residual impurities such as C and O are more likely to incorporate on a ($000\bar{1}$) polar surface [162,163].

While the present Ga adatom lifetimes and activation energies are the first ever reported *direct* measures for the binding energetics on a N-polar GaN surface, various other groups have paid more attention towards the Ga-polar surface. In an early work, Guha *et al.* [141] employed also the mass spectrometry technique to determine Ga adatoms lifetimes on a (0001) GaN surface, but restricted themselves only to submonolayer coverages and a high temperature range of 680 – 750 °C. While the lifetimes in the low end of this interval coincide with the results in this work (i.e. τ^B (690 °C) $\approx$ 5 sec), their activation energy for desorption with 2.2 eV is much lower (compared to the present value of 4.9 eV). Adelmann *et al.* deduced the Ga coverage indirectly from measurements of the variation in the RHEED Bragg spot intensity in a similarly high temperature range [118,151]. For the RHEED transition between mono- and bilayer desorption they have reported two different activation energies, i.e. 3.7 eV [118] versus 5.2 eV [151]. Moreover, Ga desorption studies by mass spectrometry have also been carried out in the presence of NH_3 [164,165]. The obtained activation energies for the desorption of submonolayer coverages were considerably lower, i.e. 1.4 eV in the 625

– 740 °C range and 0.4 eV in the 740 – 825 °C range [164]. The low activation energies were speculated to arise from complex surface bonding mechanisms involving hydrogen.

As demonstrated, excess Ga accumulates on the adlayer-stable GaN surface, when depositing Ga fluxes that exceed the critical adlayer coverage (i.e. 1.1 ML on N-polar and 2.4 ML on Ga-polar GaN). This accumulation of excess Ga was earlier referred to a regime where Ga droplets might eventually evolve after a certain time (i.e. droplet regime). As a key point, it is important to note that during the steady-state desorption of these Ga droplets the adlayer is sustained in full dynamic equilibrium. This implies that during the desorption an adatom transfer mechanism must be active, similar to what has been proposed for the bilayer decay (Sect. 5.4.). In other words, if Ga atoms from the adlayer happen to desorb, subsequently atoms from the excess Ga reservoir will nourish the adlayer. We can easily understand this situation, when considering the evaluated relations for the activation energies, where $E^D < E^A$ and $E^D < E^T < E^B$ hold true. Furthermore, due to the stronger bond strength for Ga adatoms in the adlayer, the adlayer represents a system of lower energy as compared to the Ga droplet reservoir. Along with this concept, the surface free energy of the whole Ga adlayer-droplet assembly can thus be minimized [166].

These energetical considerations also suit the model for the laterally contracted Ga bilayer [150]. While the bottom ML of Ga matches the in-plane lattice parameter of the underlying GaN and hence faces the highest bond strength, the top ≈ 1.4 ML exhibits a weaker substrate interaction and a Ga–Ga in-plane spacing approching a value typical for liquid Ga. Excess Ga atoms accumulated in droplets on top experience the weakest interaction, given that they are completely out of registry with the substrate lattice.

The previous *ex situ* investigation [116] on the boundary condition between the Ga adlayer and droplet regime as well as results from RHEED reconstructions by Hacke *et al.* [157] yielded an activation energy of ≈ 2.8 eV for this transition. So far, this is the closest ever reported value to the present directly determined activation energy for Ga desorption from droplets (i.e. $\overline{E}^D = 3.1 \pm 0.2$ eV). All these separately acquired values agree convincingly with the activation energy for Ga evaporation from bulk Ga, which equals to 2.9 eV [117]. Much higher activation energies for Ga desorption from droplets have been unveiled from RHEED intensity variations by Adelmann *et al.* on GaN (0001) surfaces, being 4.8 eV [118] with incident N and 5.1 eV [151] without N. The differences in their activation energies were speculated to rely on an interplay between N flux and the nucleation of Ga droplets.

Thus by the finding of a complicated three–stage bilayer decay this contradiction could be clearly resolved in this work.

6. Evolution of the Ga Adlayer during PAMBE Growth of GaN (0001)

6.1. Introduction

In the previous section a direct demonstration of the existence of a thermodynamically stable Ga adlayer on both polar wurtzite GaN surfaces was given. Now these findings will be extended to the PAMBE growth of the technologically more relevant (0001) orientation of GaN in an effort to resolve the evolution of the Ga adlayer as a function of the growth conditions, i.e. in the presence of incident nitrogen. As already earlier pointed out, the Ga adlayer coverage, as defined by the Ga/N flux ratio, determines the N adatom surface diffusion [19,20], which in turn has a direct influence on the GaN growth mode, the surface structure and the structural, electrical and optical properties of the grown material [25,26,103, 116,118,167,168,169]. Specifically, GaN grown with low Ga/N ratios (N–rich growth) was found to procede by a threedimensional growth mode and results typically in heavily pitted surfaces, a tilted columnar structure with a high density of stacking faults [25] and insulating material [26]. High Ga/N ratios (Ga–rich growth) prove necessary to acquire device quality GaN through a two–dimensional growth mode [167]. The best GaN surface morphologies were achieved under such high Ga/N flux ratios that matched the borderline where Ga droplet formation occurred. In a further systematic study, the electron mobility in (0001) GaN [26] and two-dimensional electron gas (2DEG) AlGaN/GaN structures [170] was found to increase with rising Ga/N ratio and reaches its highest values at a Ga/N ratio marginally below the border for Ga droplet formation. Restrictions for such device applications, however, were shown to arise for very high Ga/N ratios or low temperatures, as these lead inevitably to the accumulation of metallic Ga droplets on the surface [116].

To explore the crucial impact between adatom mobility and the resulting GaN material properties, to date only few efforts have been made to quantify the Ga adlayer coverage as a function of the growth conditions. The only *in situ* studies were based upon determining the desorption time of the Ga adlayer from measurements of specular beam intensities in reflection high energy electron diffraction (RHEED) patterns [118,151]. With the assumption of a constant desorption rate, i.e. a linear relationship between desorption time and Ga adlayer coverage, the latter was then proposed to evolve *discontinuously* with changing Ga flux and to form a stable ≈ 2.5 ML thick bilayer for a wide range of Ga fluxes. Such self-regulated discrete Ga adlayer coverages would then be expected to produce constant material properties despite small fluctuations in substrate temperature or Ga flux.

The following direct and quantitative QMS measurements of the Ga adlayer during PAMBE growth will demonstrate though that the adlayer coverage evolves *continuously* with changing growth conditions. Therefore, no evidence of a self-regulating Ga coverage is found which means that precise control of Ga/N ratio and growth temperature is required to stabilize the growth conditions for optimum material properties. The immediate effect of this continuous

evolution in Ga adlayer coverage with respect to the GaN surface structure is finally also endorsed in a systematic GaN morphology study.

6.2. GaN Growth Pulses along the GaN Growth Phase Diagram

To evaluate the Ga adlayer coverage on GaN (0001) under different growth conditions, a series of GaN growths was performed with a fixed nitrogen flux of 0.23 ML/sec. The Ga flux was varied from 0.06–2.25 ML/sec for five different temperatures in a range from 669 to 734 °C. For each temperature, the GaN growth pulses started at high Ga fluxes in the Ga droplet regime and by gradually decreasing the Ga flux finally N-rich conditions were reached (see also GaN growth diagram (Fig. 4.2.)). Inbetween each growth cycle, sufficient time was given for the adsorbed Ga species to desorb completely. Such a GaN growth sequence, where high Ga fluxes are followed by gradually lower Ga fluxes, seemed necessary in order to maintain a smooth non–disrupted GaN growth front by the effect of Ga acting as an autosurfactant [171].

In Fig. 6.1(a) Ga desorption measurements by QMS are presented for a series of 90 sec GaN growth pulses under the variable Ga fluxes at a constant temperature of 722 °C. It is evident that each GaN growth pulse provides two phases in the desorbed Ga signal, one during growth itself (later referred to as the maximum desorption level) and the other as desorption of an adsorbed Ga surface coverage after growth into vacuum [also detailed in the closeup views of Fig. 6.1(b) and (c) for two different Ga fluxes]. According to the maximum desorption level in the growth phase, one can differentiate – as in the previous study done by our group [116] – between three distinct regimes of growth: for high Ga fluxes between 1.93 and 1.22 ML/sec (A) the maximum desorption is constant at a rate around 1 ML/sec. This rate is limited by the temperature and any excess Ga flux accumulates as weakly–bonded metallic droplets on the surface (Ga droplet regime). When the Ga flux is lowered to a range between 1.22 – 0.23 ML/sec (B) the maximum desorption level decreases monotonically. This is referred to the Ga–rich intermediate regime, where the excess Ga flux desorbs from the growing surface (independent of the supplied flux). And third, GaN growth with Ga fluxes below 0.23 ML/sec (C) results in virtually no Ga desorption, since the arriving Ga flux limits the growth rate and is consumed completely by the nitrogen atoms (N-rich regime).

6.3. Ga Surface Coverage and Desorption Time

To evaluate the Ga surface coverage prevalent in the different regimes, the area below the desorbing Ga flux during the vacuum desorption of each pulse was integrated [i.e. hatched area as exemplified in Fig. 6.1(b) and (c); similar to the evaluation scheme in Sect. 5.3.2.]. The integrated Ga coverages are plotted in Fig. 6.2 as a function of the impinging Ga flux (full circles), which demonstrate a *continuous* increase of the Ga surface coverage with increasing Ga flux. For N–rich growth, no excess Ga is accumulated on the surface, but Ga–
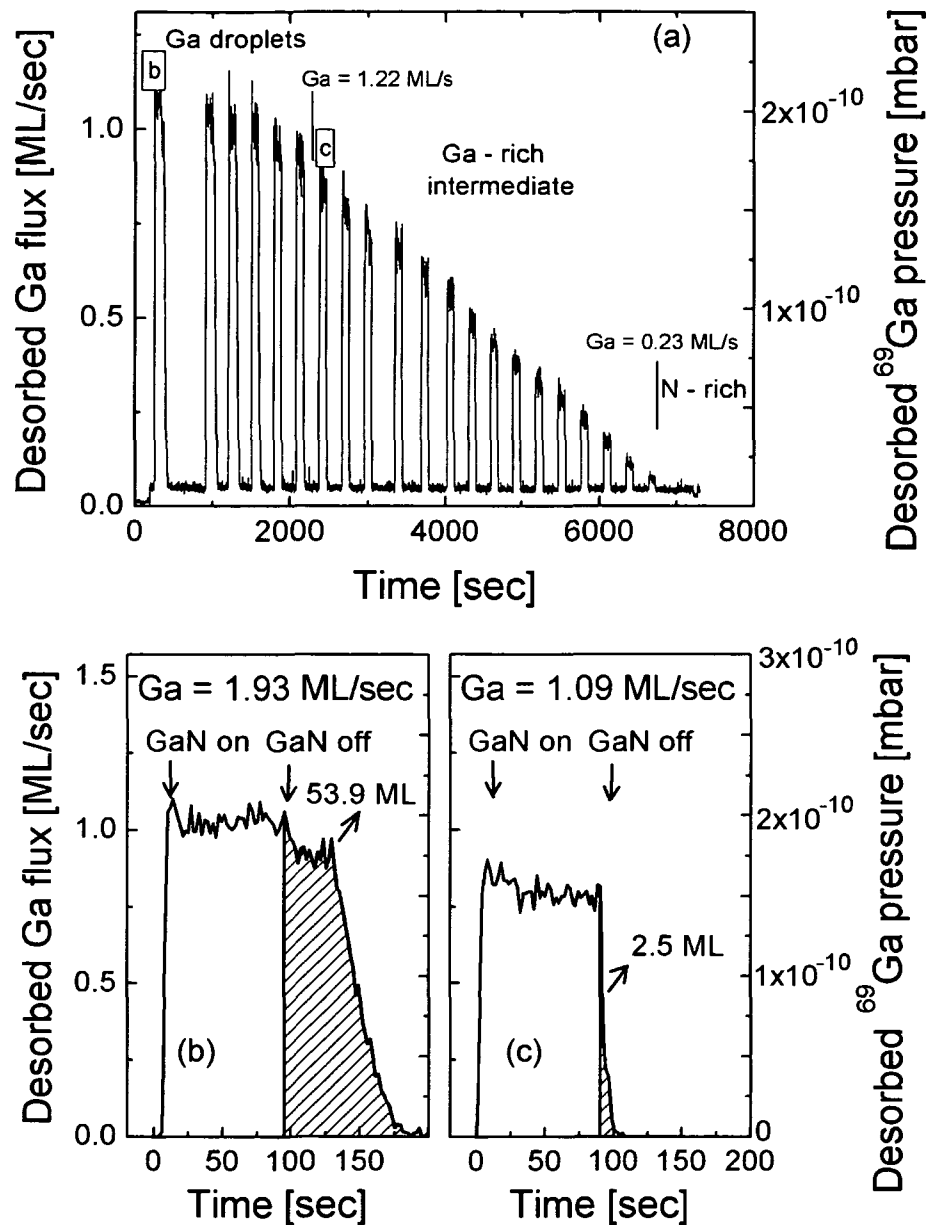
Fig. 6.1. (a) Ga desorption for a series of 90 sec GaN pulses with gradually decreasing Ga fluxes from 1.93 – 0.06 ML/sec at constant 722°C. The Ga fluxes in the (b) droplet and (c) intermediate regimes illustrate the determination of the Ga surface coverage (equal to the hatched areas) from its vacuum desorption after growth.

rich intermediate conditions yield Ga adlayer coverages between 0 and 2.5 ML. Within the intermediate regime error bars are on the order of ± 0.3 ML, resulting mainly from the 2 sec time resolution of the mass spectrometer. However, for the lower investigated temperatures of 669 °C and 686 °C (as follows in the next section) the respective error is only ± 0.1 ML, due to the greater duration of the Ga adlayer desorption process. From additional growth experiments with growth times of up to 2 hours it was observed that these adlayer coverages did not vary more than ± 0.2 ML for any given Ga flux, hence being completely independent of the previous growth time. Thus, for each Ga flux a certain steady–state coverage is stabilized

within the intermediate regime. The maximum Ga adlayer coverage of 2.5 ML measured in this work is in good agreement with the laterally–contracted bilayer model (i.e. 2.33 ML of Ga in terms of GaN atomic density) [150], as also found for the pure adsorption case in Sect.5. For very high Ga fluxes, the slope in Ga surface coverage changes drastically, which is attributed to an increasing accumulation of Ga droplets on top of the bilayer, as also observed by Adelmann et al. [118,151]. For comparison, the desorption time of the Ga surface coverage has also been evaluated, as given by the duration between the closure of both Ga and N shutters and the drop to zero desorption (open circles in Fig. 6.2). The desorption time evolves in contrast to the Ga surface coverage; it shows two constant plateaus for Ga fluxes in the range between 0.4 – 1.22 ML/sec (error bars are from ± 2 sec time resolution). This stepwise evolution can be understood by the *non-constant desorption rate*, which was determined for Ga adlayer coverages between 1–2.4 ML in the previous Sect. 5.4. To recollect, the decay of the Ga bilayer was found to consist of a complicated three-stage desorption process, and only submonolayer coverages desorb in a monoexponential fashion. At this stage it becomes clear why here a continuous increase in the Ga adlayer coverage with rising Ga flux is observed, in constrast to apparent regimes of constant coverages as evaluated from changes in RHEED intensity by Adelmann et al. [118,151]. The continuous evolution in Ga adlayer coverage has also been strongly anticipated in recent electron mobility studies of thick GaN [26] and AlGaN [170] films, and will be directly confirmed in the following GaN morphology study in Sect. 6.5.
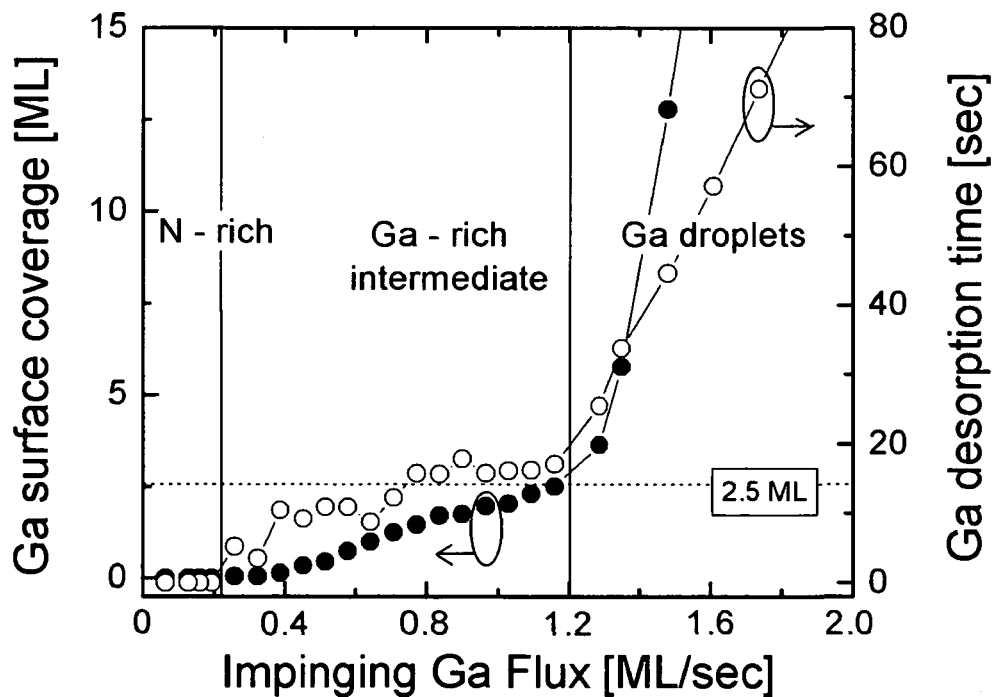

Fig. 6.2. Evolution of the Ga surface coverage and its characteristic desorption time as a function of the impinging Ga flux for (0001) GaN growth at constant N flux (0.23 ML/sec) and T = 722 °C. Error bars for the surface coverage are ± 0.3 ML and ± 2 sec for the desorption time, respectively.

6.4. Temperature–dependent Ga Surface Coverage

The explicit relationship between impinging Ga flux and steady–state Ga surface coverage has also been verified for different temperatures in the range between 669 – 734 °C [Fig. 6.3(a)]. It is obvious that for higher growth temperatures the transition between Ga adlayer and Ga droplet coverages is shifted to higher Ga fluxes, whereas the stoichiometry border (where Ga and N fluxes are equal) is independent of the temperature. Note, that for all temperatures the continuous behavior in Ga surface coverage as a function of impinging Ga flux holds true.
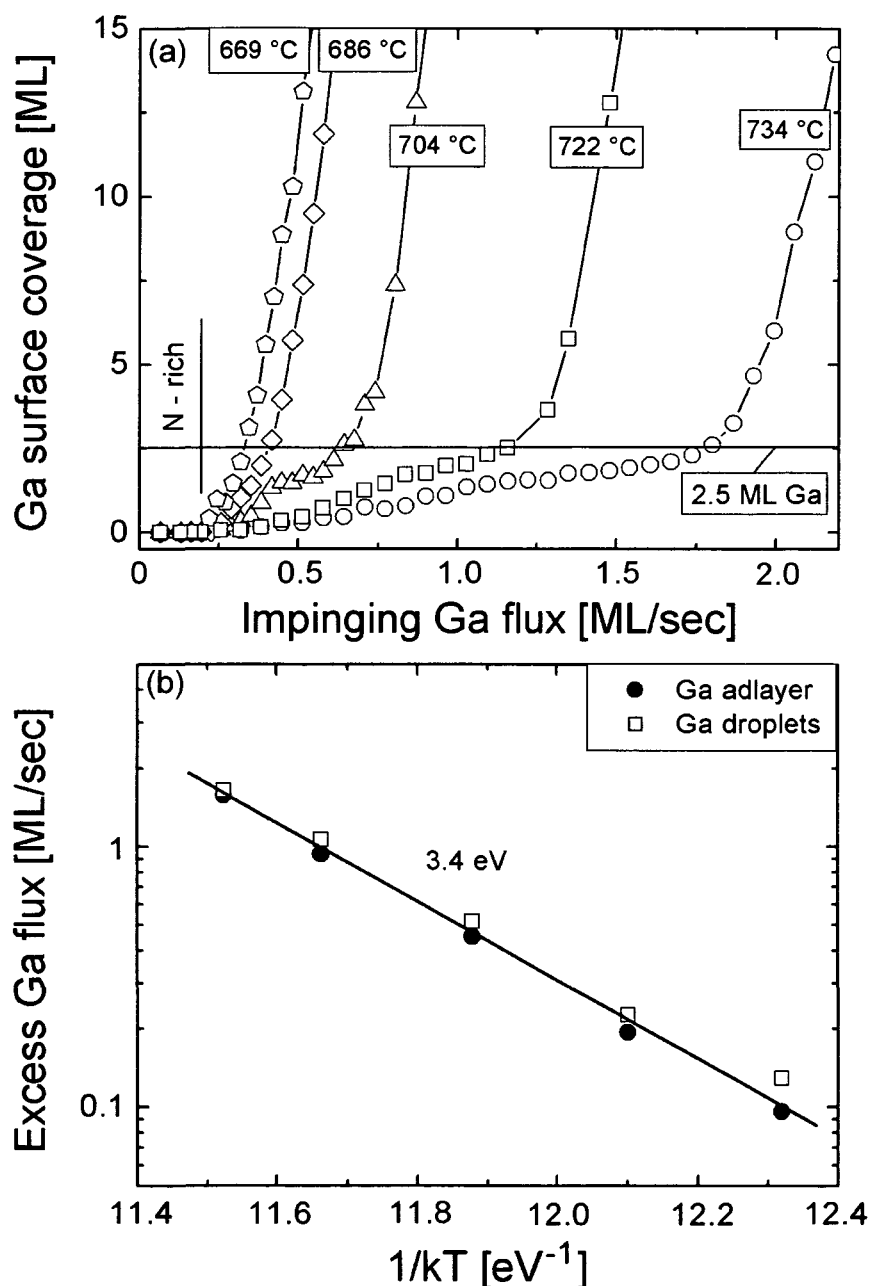

Fig. 6.3. (a) Temperature–dependent Ga surface coverages as a function of the impinging Ga flux, yielding (b) a transition between Ga adlayer and droplet fluxes with an Arrhenius nature and an activation energy of 3.4 ± 0.1 eV.

Moreover, plotting the transition fluxes between the intermediate and droplet regime (given by the intersection at 2.5 ML) as a function of temperature yields an Arrhenius dependence with an apparent activation energy that is determined to be 3.4 ± 0.1 eV [Fig. 6.3 (b)]. The Ga desorption measurements without N (as in Sect. 5) yielded activation energies of 3.1 and 3.7 eV for the desorption of Ga droplets and the top part of the bilayer, respectively. Hence, the value of 3.4 eV for the current phase transition fits favorably within the two and supports therefore also the pure Ga adsorption study. Much higher activation energies for this particular transition have been reported from RHEED intensity measurements, being 4.8 eV [118] with incident N and 5.1 eV [151] without N. Lower values of around 2.8 eV resulted from our earlier investigation [116] as well as from RHEED transitions between 2×2 and 1×1 reconstructed surfaces [157]. In both of these latter studies the supplied N fluxes were substantially higher (> 0.28 ML/sec), which could be responsible for the different outcomes in the activation energies. On the basis of first–principles total energy calculations it was proposed that there might be a strong interdependence between N flux and a temperature–dependent Ga bilayer coverage that in turn could influence the activation energy for the nucleation of Ga droplets [151]. However, the bilayer coverages under the different temperatures as plotted in Fig. 5.7. reveal that independent of the growth temperature (at least in the investigated range) the coverage is at constant 2.34 ± 0.2 ML within the experimental limits.

On the other hand, when investigating the desorption of very high Ga surface coverages (adlayer + droplets), there are several obvious differences in the desorption features between pure Ga adsorption (without N) and GaN growth (with N). For this reason, a relatively high Ga flux and low substrate temperature ($T_S = 650 - 670$ °C) was chosen in order to accumulate a fair amount of Ga droplets on top of the bilayer for both the adsorption case [Fig. 6.4 (a)] and the growth case [Fig. 6.4(b)]. The differences in the absolute desorbing Ga flux is due to the fact that that the temperature was slightly different between the two experiments. The major difference between the two cases arises especially at the point where the desorption signal starts to decay to zero. When active N is absent [Fig. 6.4(a)], the characteristic three–stage decay is observed and the integrated area under the desorption signal to the right of the dashed line yields exactly the proposed Ga bilayer coverage of 2.7 ML. Not so in the case where N is involved [Fig. 6.4(b)], which evidences a rather monoexponential decay at the final drop–off. The area under the decaying signal does also not correspond to the Ga bilayer coverage and is much higher, namely $\theta = 11$ ML in equivalent thickness. This increased amount of Ga at the final decay must mean that at least some residual droplets seem to contribute to the desorbing Ga signal.

To prove this, another 90 sec long GaN growth pulse under Ga droplet conditions was performed at 720 °C and kept at this temperature for the entire desorption after the growth stop. As obvious in Fig. 6.6(a), the decaying Ga desorption follows again a monoexponential behavior and the total desorbing Ga amounts to 64 ML. The same GaN growth pulse was then repeated, with the distinction that the sample was cooled down very fast once the Ga desorption started to decay (indicated by the full circle in Fig. 6.6(a)), in anticipation to inhibit the desorption of the entire Ga surface coverage and therefore detect some residual Ga droplets. Indeed, the SEM image in Fig. 6.6(b) evidences the existence of a few large Ga droplets with a radius of approximately 2 μm and an average height of 550 nm. Taking these

droplet size data and their ratio to the total surface area ($\approx 10^{-2}$) it is possible to calculate the equivalent thickness of the metallic Ga surface coverage.
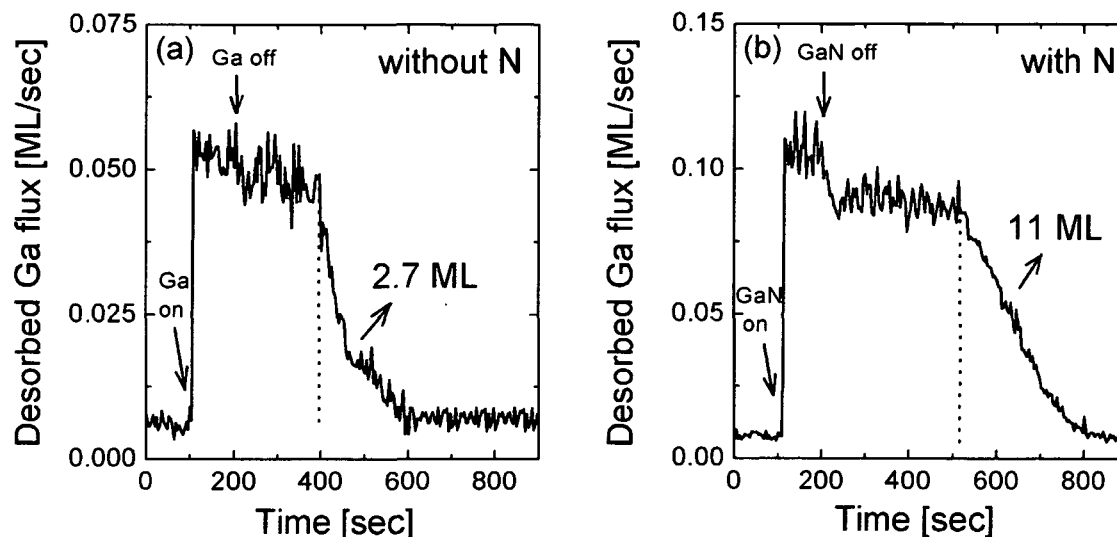

Fig. 6.4. Ga desorption from high Ga surface coverages (droplets + adlayer) on GaN (0001) for cases of (a) pure Ga adsorption (no incident N) at T_S = 650 °C and (b) GaN growth (with incident N) at T_S = 670 °C; note the strong deviation in desorption features during the final decay between the two cases.
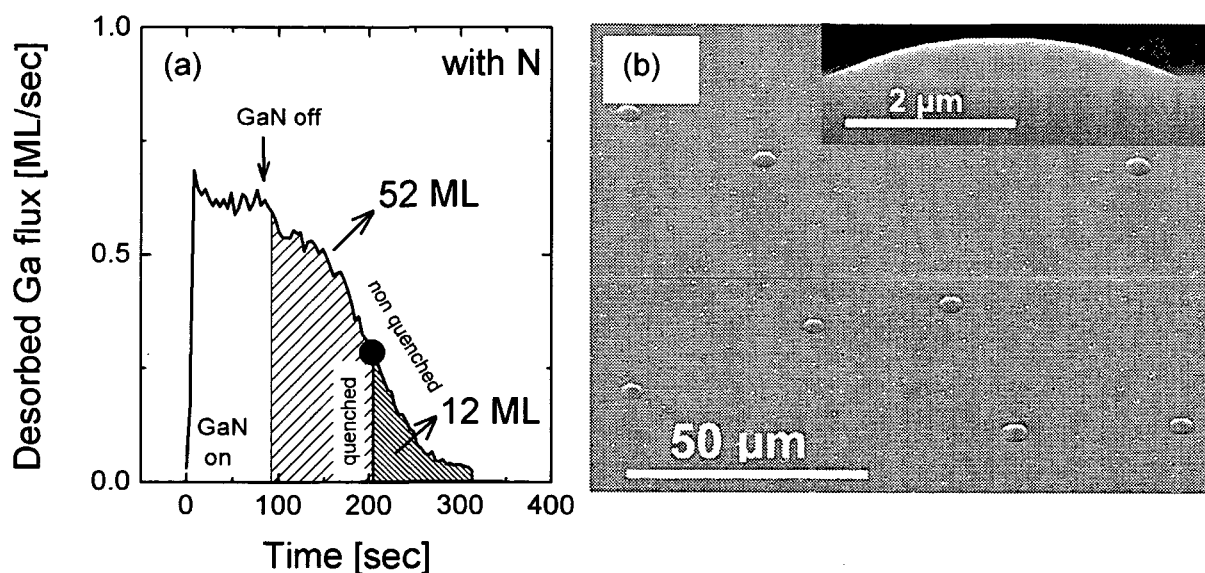

Fig. 6.5. (a) Ga desorption spectrum of a GaN growth pulse in the Ga droplet regime and subsequent vacuum desorption, showing a characteristic monoexponential decay. In a repeated growth pulse the sample was quenched instantly once the monoexponential desorption stage was reached (full circle), with the corresponding SEM surface morphology shown in (b). The surface exhibits an overall smooth topology with a few Ga droplets with a radius of typically 2 μm and a height of 0.55 μm.

Assuming that the droplets were spread out as a thin film covering the entire surface area, the equivalent thickness would be 11.1 ML. When comparing the QMS spectra between the quenched (cooled down) and non quenched case [Fig. 6.5(a)], the difference between the two hatched areas should correspond to the amount of residual Ga in droplets. This mass balanced amount results in 12 ML which is in sound agreement with the droplet coverage as determined from the postgrowth SEM analysis.

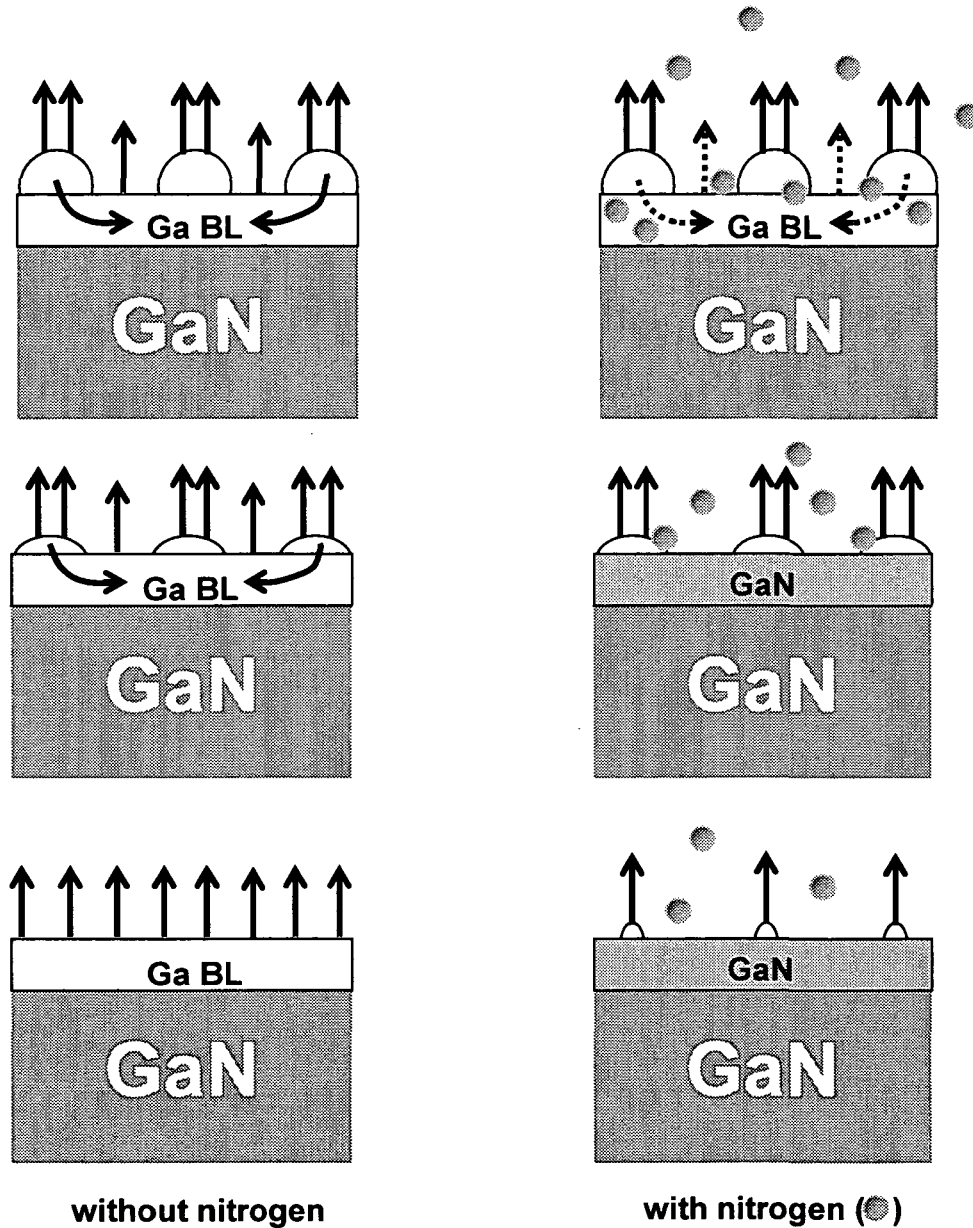without nitrogen   with nitrogen (○)

Fig. 6.6. Model of Ga droplet desorption after growth stop into vacuum for (a) pure Ga adsorption (no background N) and (b) GaN growth (with residual N even after growth). In case (a) Ga droplets get depleted also by an adatom transfer to the bilayer (BL) underneath, keeping the 2.7 ML bilayer fully populated until the Ga droplet reservoir is entirely gone. The background N atoms in case (b) consume the Ga bilayer by forming additional GaN and only Ga droplets contribute to the final desorption.

The existence of such Ga droplets, even during the final decay of the desorption signal, indicates that the desorption mechanism needs to be very different between the growth case (with incident N) and the pure adsorption case (no incident N), where no such droplets remain in the final stage of desorption. To explain these discrepancies, it is assumed that even after GaN growth is terminated there is a residual amount of N in the growth chamber that interacts instantly with the adsorbed Ga surface coverage to form small quantities of additional GaN. Especially, it can be anticipated that upon growth stop the Ga bilayer beneath the droplets is entirely consumed by the residual N atoms to form GaN, therefore blocking the transfer of atoms from Ga droplets to bilayer, as proposed in Sect. 5.5 for the case of pure Ga adsorption. As this "feeding mechanism" is suppressed, the entire desorption after GaN growth consists then basically of the decay of Ga droplets. A schematic comparison of the desorption of Ga droplets and bilayer between the adsorption case and the GaN growth case is represented in Fig. 6.6.

6.5. Consequences for GaN Material Properties: A Surface Morphology Study

To investigate the impact of the *continually* rising Ga adlayer coverage on the resulting GaN material properties, a systematic study on surface morphology was undertaken. Specifically, a growth series of 0.5 μm thick GaN layers was performed on low threading dislocation (TD) density ($\approx 5 \times 10^8$ cm^{-2}) MOCVD–GaN templates grown by LUMILOG. Selecting such GaN templates was necessary not only to achieve the required Ga–polar GaN growth, but also to evaluate dislocation induced surface pit density variations additionally arising due to differing growth kinetics during MBE growth. The MBE GaN layers were grown at constant temperature T_S = 710 °C and a fixed N flux of 0.17 ML/s, but with a variable Ga flux between 0.19 – 0.77 ML/s. For each individual Ga flux the Ga surface coverage was determined from the postgrowth vacuum desorption of 90 sec GaN growth pulses by QMS, identical to the scheme applied in Sect. 6.3. This growth series along with the resulting Ga surface coverages (from the 90 sec growth pulses) is presented in the GaN growth diagram of Fig. 6.7. Consistent with the previous results, the Ga surface coverage evolves continuously with rising Ga flux (from 0.02 – 2.44 ML) and coverages higher than the laterally contracted bilayer emerge when droplets accumulate on the surface.

The typical surface morphologies observed by AFM of the 0.5 μm GaN layers grown under the various Ga fluxes and consequently different Ga surface coverages are presented in Fig. 6.9. Comparatively, in Fig. 6.8 (a) also the morphology of a model as–received MOCVD LUMILOG GaN template is shown, evidencing a very smooth surface with an array of terraces separated by GaN monolayer high steps of 2–3 Å. The terraces are rather well aligned in a straight manner with only a slight curvature and no surface depressions are observed. A similarly smooth surface with steps and terraces appears when GaN is grown by MBE under Ga droplet conditions at a Ga flux of ϕ_{Ga} = 0.64 ML/s [Fig. 6.8 (b)].
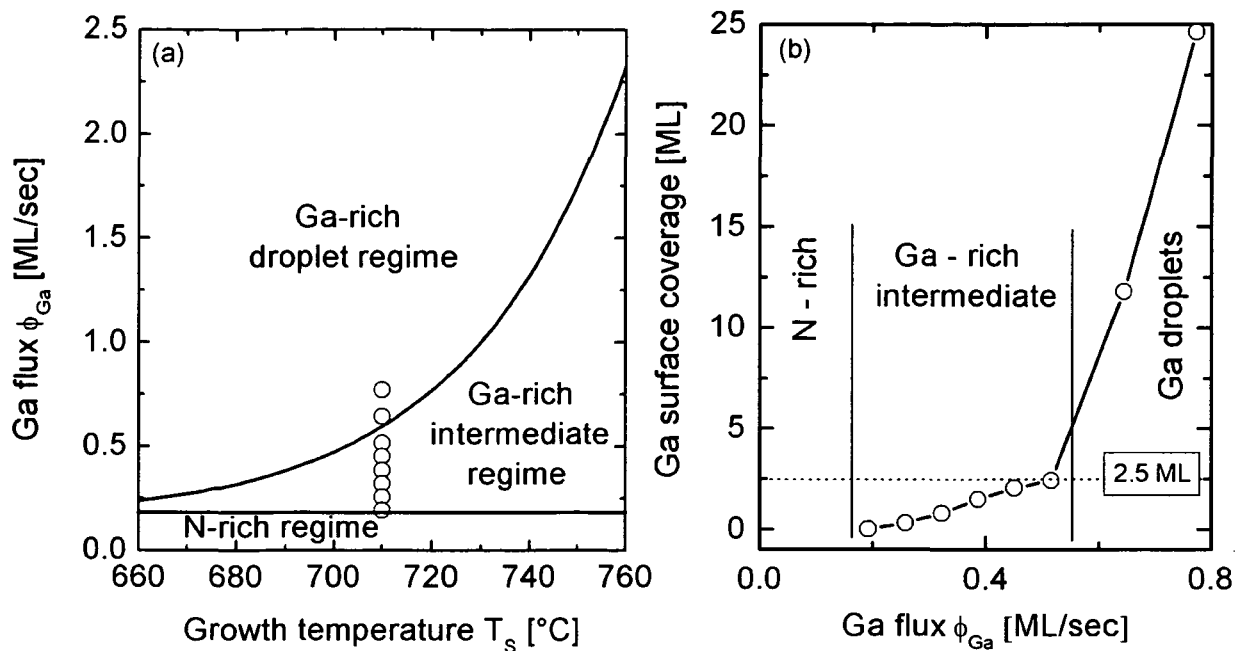
Fig. 6.7. (a) GaN growth series along the growth phase diagram yielding (b) the respective Ga surface coverages as a function of impinging Ga flux, as determined by QMS for 90 sec long GaN growth pulses at T_S = 710 °C and N = 0.17 ML/s. Note again the continuous rise in Ga adlayer coverage up to 2.5 ML and the break-off beyond, indicative of the formation of Ga droplets.

In contrast to the MOCVD GaN, the terraces here are organized in the shape of spiral growth hillocks, a typical MBE growth mechanism around mixed–type dislocations [103]. The driving force of the spiral hillocks is associated with the step–flow growth conditions given at such high Ga fluxes, where the pinned steps grow outward and around the dislocations. Also, some nanoislands are observed on the surface which may be attributed to Ga clusters acting as precursors for Ga droplets. When growth is performed in the intermediate regime, the GaN surfaces show a continuous degradation when lowering the Ga flux to almost N–rich conditions [Fig. 6.8(c)–(h)], also accompanied by a vanishing degree in spiral hillock formation. Whereas under near–droplet conditions [Fig. 6.8(c)] the smoothest surfaces with spiral hillocks and no surface depressions appear, gradually surface depressions (predominantly as nanopipes, also referred to as hexagonal inverted pyramids (HIPs) or "V" defects [116]) come into existence, leading to heavily pitted and rough surface morphologies under near–stoichiometric conditions [Fig. 6.8(h)]. The density of the hexagonal nanopipe defects (with diameters of typically 200 nm) are plotted in Fig. 6.9. Their density is highest under low excess Ga (in the order of $\approx 2 \times 10^9$ cm^{-2}) and decreases continually to zero as the excess Ga approaches the droplet border where a complete Ga bilayer covers the surface. Besides these nanopipe defects other surface depressions with much lower depth of ~ 8 – 14 Å were observed, especially visible in the GaN layer in Fig. 6.9(d). Such surface depressions form exactly at the surface termination of dislocations due to the high strain energy density in the vicinity of these dislocations [172]. According to B. Heying et al. [103] these shallow depressions in the MBE grown GaN layers
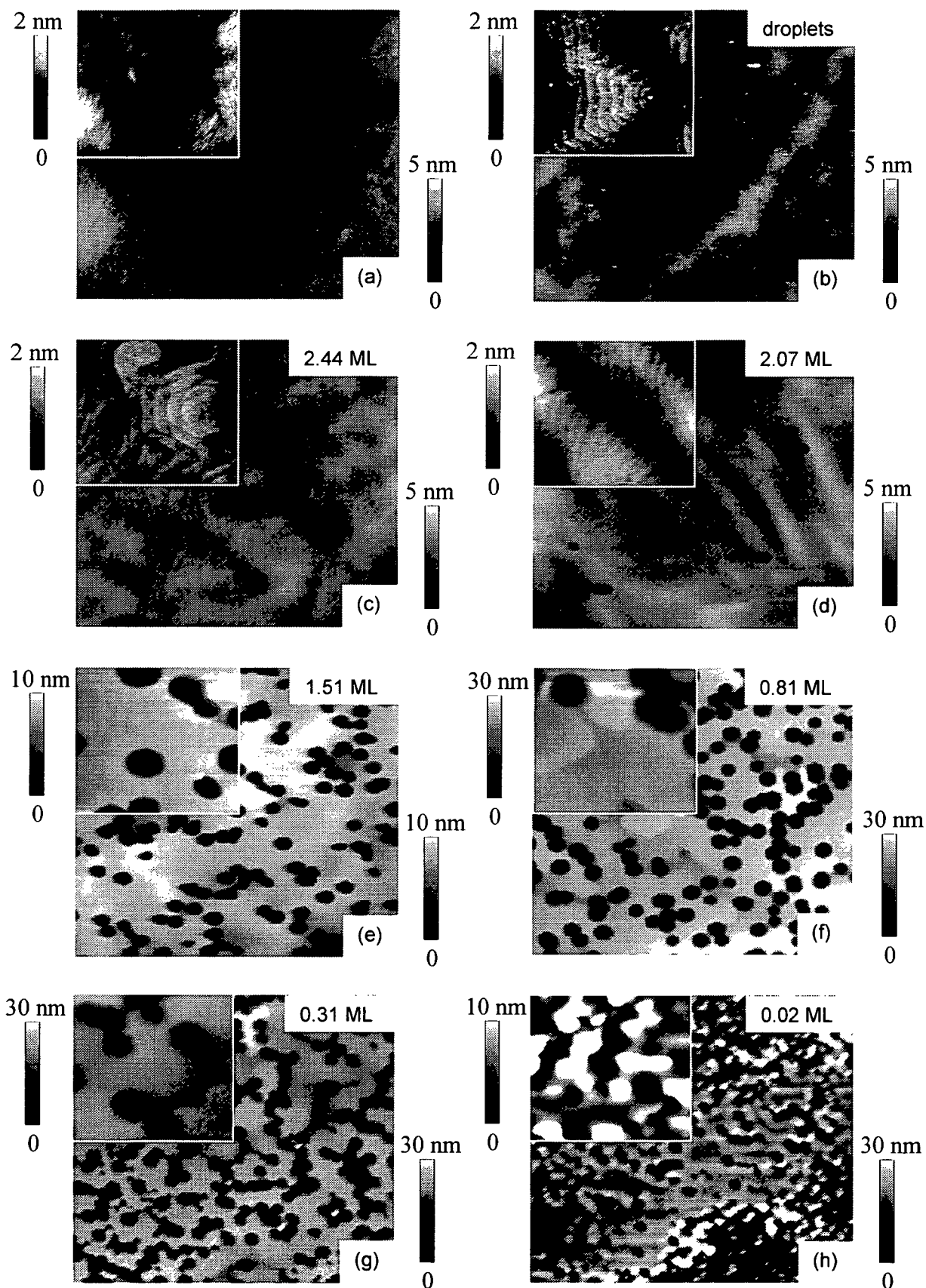
Fig. 6.8. AFM surface images (5×5 μm² and 1×1 μm² for the inserts) of (a) a MOCVD GaN template and (b) – (h) 0.5 μm GaN layers grown on top under different Ga fluxes (0.64 – 0.19 ML/s) at constant N flux and T_S = 710 °C. The bars in the righthand corner of each image give the actual Ga adlayer coverage during growth.

are associated rather to pure edge than mixed–type dislocations, as they appear predominantly within the terraces and not at surface steps.
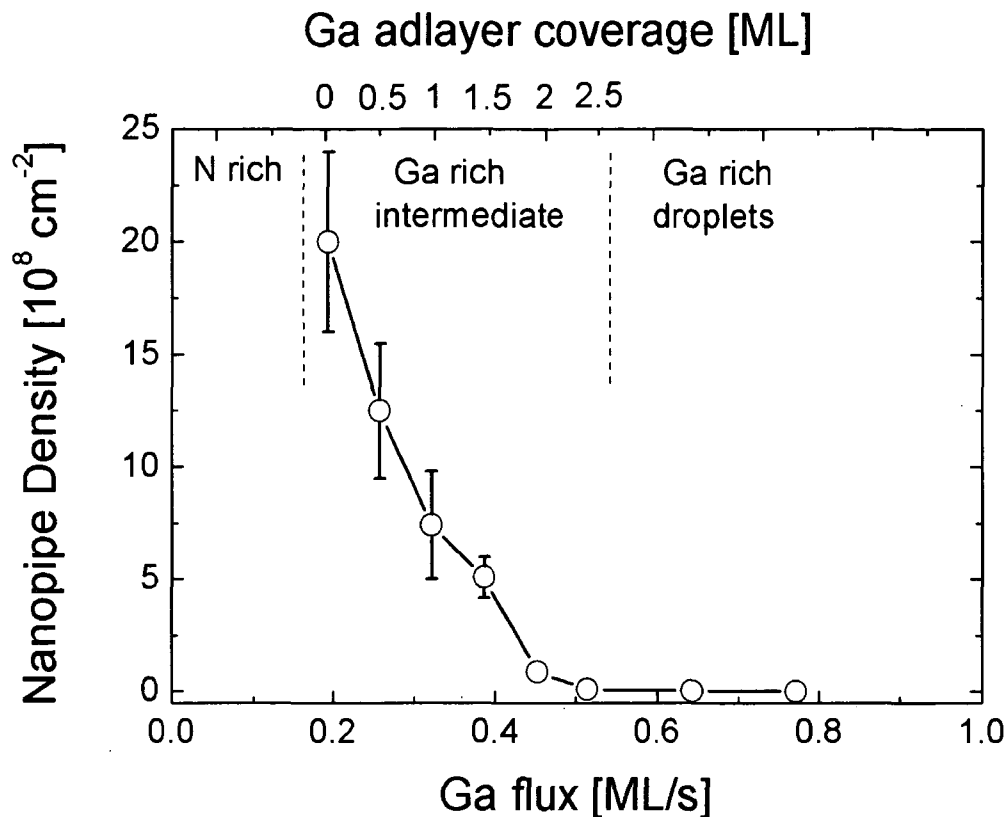

Fig. 6.9. Density of hexagonal nanopipe defects in MBE GaN as a function of Ga flux and Ga adlayer coverage.

However, in previous studies it was suggested that the pit or nanopipe forming mechanism is driven by kinetically controlled processes, particularly by adatom surface diffusion under the different growth conditions [116]. In general, under conditions where the surface adatom mobilities are high, the growth morphology can planarize and reduce the surface free energy. In contrast, at low adatom mobilities the nanopipe defects that form on the surface due to dislocations cannot be filled in and therefore propagate to the surface. The present study corroborates this conception, as it directly proves that the Ga adlayer coverage plays the key role in determining surface diffusion mechanisms and hence the GaN surface properties, i.e. nanopipe densities. Under low Ga adlayer coverages the highest densities of nanopipe defects were found on the surface and they gradually disappear when increasing the adlayer coverage up to a complete laterally contracted bilayer of ~ 2.4 ML. This is consistent with theoretical adatom diffusion calculations, where adatom transport was found the highest when a complete Ga bilayer covers the surface [20]. Particularly, the Ga bilayer allows N adatoms to diffuse rapidly between subsurface sites, which is also referred to as adlayer enhanced lateral diffusion (AELD). Quite large energy barriers to surface migration on the other hand occur on bare GaN surfaces (without a Ga adlayer) for both N and Ga adatoms, which are 1.3 eV and 0.7 eV, respectively [19]. The reduced surface diffusion is then responsible for the formation of the V–shaped hexagonal nanopipes. Most remarkable, the nanopipe defect density scales

with the Ga adlayer coverage when growth is performed in the intermediate growth regime. In fact, there is even a clear difference in nanopipe density between GaN layers grown with a stable Ga bilayer of 2.0 ML and a laterally contracted Ga bilayer of 2.4 ML on top. These results thus evidence a *continuous* evolution in GaN surface morphology with rising Ga adlayer coverage, as opposed to the perception of self regulated discrete Ga adlayer coverages that would yield identical morphologies within a wide growth window [118,151]. All this implicates that the growth kinetics (Ga/N ratio and substrate temperature) have to be kept as close as possible to a fully laterally contracted Ga bilayer coverage just below the Ga droplet border in order to achieve the best GaN surface morphologies.

7. Growth of GaN in the Vicinity of the Ga Droplet Border

7.1. Introduction

The results of the previous section pointed out that the growth of the best GaN surface morphologies can only be achieved under high Ga/N flux ratios close to the border of Ga droplet formation. GaN films grown under much higher Ga/N ratios yielded also uniform, atomically flat surfaces with characteristic spiral hillocks but also Ga droplets, which are detrimental for any device application. The ultimate objective in PAMBE growth of highest–quality GaN (with minimized pit and droplet densities) is therefore to achieve the capability for accurate control of the essential growth parameters, Ga/N flux ratio and growth temperature, in the immediate vicinity of the Ga droplet border.

One conceivable approach to produce GaN surfaces without pits and droplets would be to apply a pulsed growth technique. This could be realized by performing short sequences of GaN growth pulses slightly above the droplet border with growth stops inbetween in order to desorb the accumulated Ga perpetually. In the following, however, it will be shown that such an approach can be bypassed as we find that there seems to exist a narrow growth region above the Ga droplet border where Ga droplets become metastable and decay even during growth. These findings will further be corroborated by a detailed GaN morphology study where clearly GaN surfaces appear without pits and droplets.

7.2. Temperature dependent Ga Desorption

In contrast to the growth series with variable Ga fluxes in Sect. 6, we now conduct a growth series of $\sim 1\mu m$ thick GaN films grown under different temperatures, but constant Ga/N flux ratio (Ga/N=6). Prior to the growth of each of these thick layers, a 100 nm GaN nucleation layer has been grown in the Ga–rich intermediate regime directly on sapphire under constant conditions of Ga/N = 3.91 and T_S = 735 °C. At this point it must be noted that for all of these films the surface polarity is N–polar, meaning that Ga droplet formation is expected to set in after the completion of a 1ML thick Ga adlayer. A schematic illustration of the entire growth series including also the growth conditions for the nucleation layer is shown in Fig. 7.1.

When monitoring the entire GaN growth process by QMS, we can differentiate among three distinct Ga desorption regimes with respect to the substrate temperature, as shown for three exemplary temperatures in Fig. 7.2. For the highest temperature of T_S = 743 °C [Fig. 7.2(a)], the Ga desorption signal rises instantly to a steady–state level when GaN growth is initiated. In this case, the desorbing steady–state Ga flux equals the total Ga flux in excess of the supplied nitrogen flux (i.e. mass balancing), which is indicative of GaN growth in the Ga–rich intermediate growth regime. However, when we lower the growth temperature to T_S =
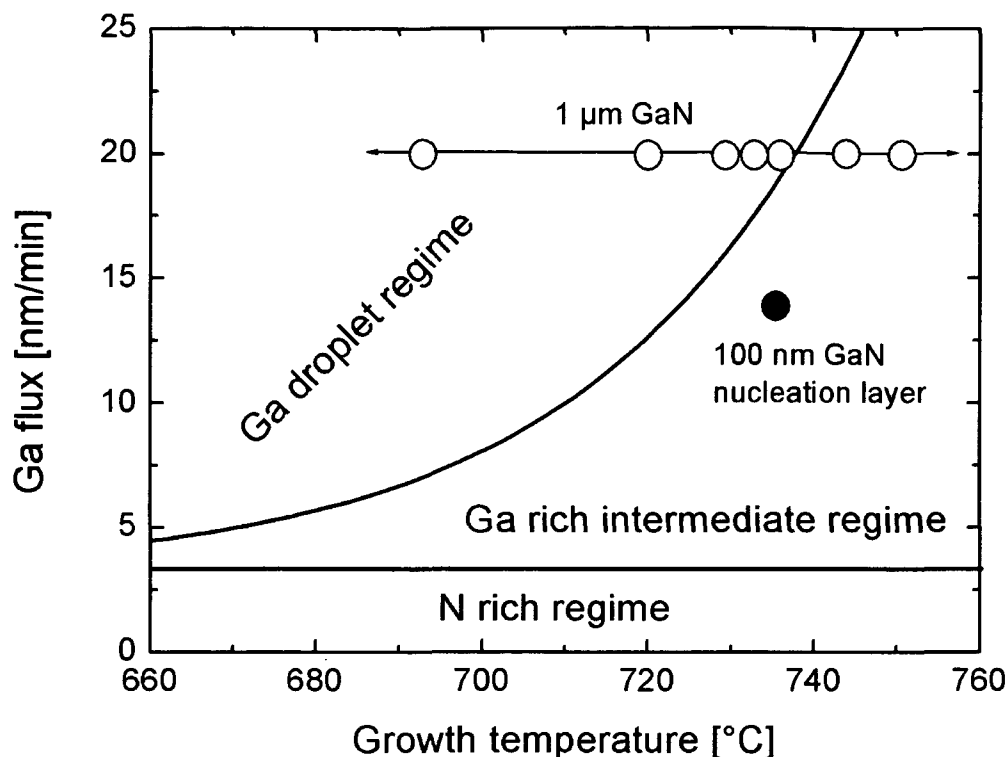
Fig. 7.1. GaN growth phase diagram showing the growth conditions for both the 100 nm thick GaN nucleation layer and the variable temperature series at constant Ga/N ratio for the 1 μm thick GaN layers.

728 °C [Fig. 7.2(b)], we observe an entirely different desorption behavior. At the very beginning of GaN growth the Ga desorption rises to a level that is slightly lower than the steady–state value typical for growth in the intermediate regime. The lower desorption level is a sign of reduced thermal desorption of the excess Ga as it is defined by the border for Ga droplet formation. At this temperature, growth is therefore performed in the Ga droplet regime. In addition, with proceeding growth the Ga desorption rises to a maximum and then levels out at a desorbing Ga flux identical to that found for growth the intermediate regime [compare Fig. 7.2(a)]. The details of this specific desorption behavior are attributed to the nucleation and desorption of metastable Ga droplets and will be discussed in the following sections. Yet, another different situation appears for GaN growth under Ga droplet conditions performed at even lower temperatures of e.g. $T_S = 693$ °C [Fig. 7.2(c)]. Here, as the thermal limit (i.e. droplet border) for the desorption of excess Ga is very low, the Ga desorption starts out at a level that is significantly lower than in the case of Fig. 7.2(b). With continuing growth, the desorbing Ga flux rises gradually to a steady–state level where it remains constant until the end of growth. This level equals exactly the Ga flux that is in excess to the nitrogen flux, meaning that finally all Ga desorbs except the portion that is consumed by the N atoms. The precedent stage of rising Ga desorption, however, can be understood by a process where Ga droplets nucleate, grow in size and where they finally reach a stable equilibrium between adsorption and desorption with the surrounding vapor. In other words, when growth is initiated, the desorbing Ga flux of ~ 3 nm/min corresponds to the droplet border and all additional excess Ga
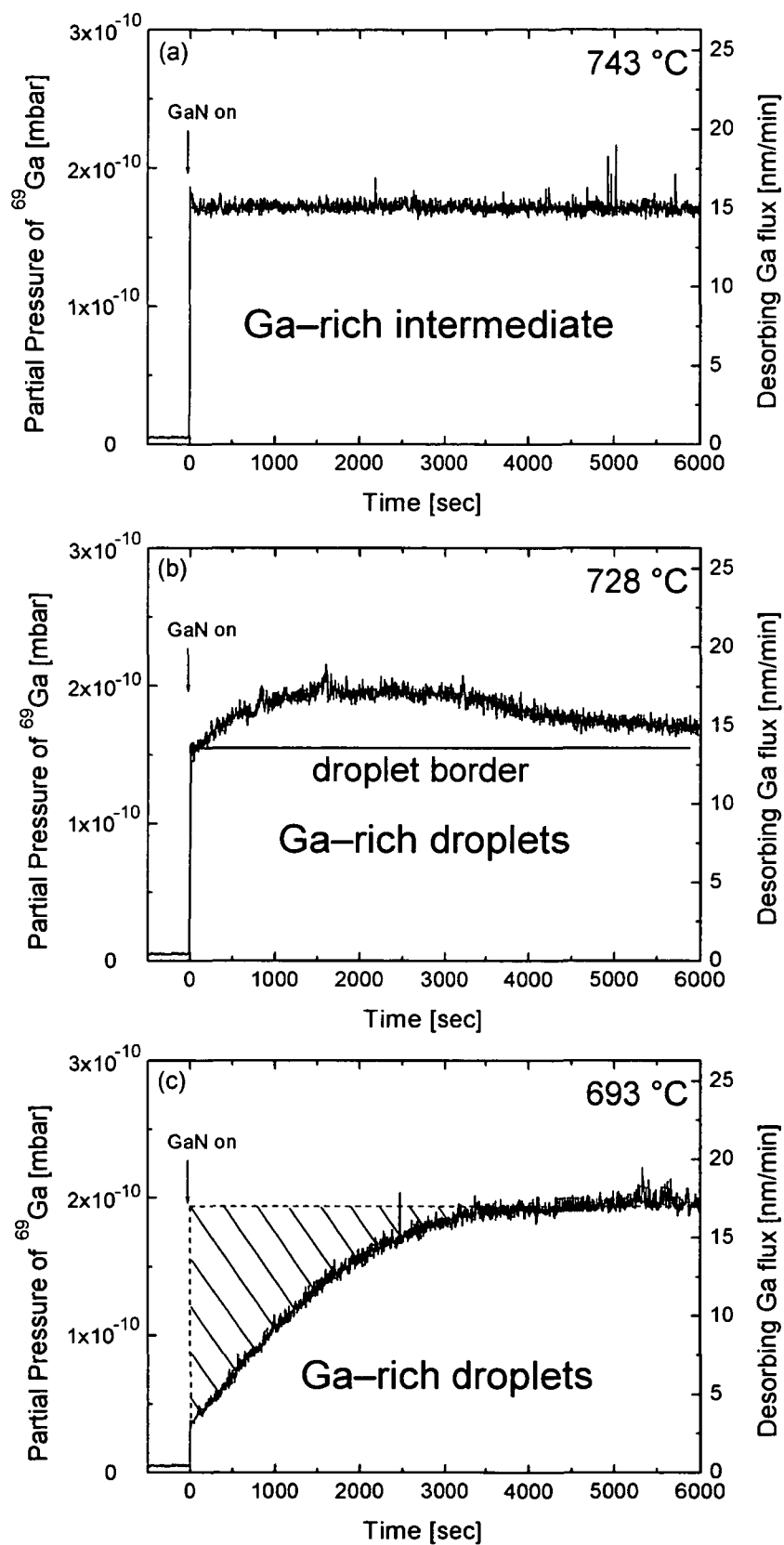
Fig. 7.2. Desorbing Ga flux during GaN (0001) homoepitaxy on a 100 nm GaN nucleation layer deposited on sapphire for three different growth temperatures (a) 743 °C, (b) 728 °C and (c) 693 °C; the hatched area in (c) corresponds to the total amount of Ga contained in droplets.

must be accumulated as droplets. As the droplets grow in size, we suggest that the overall surface area becomes larger, which – in addition to the simultaneous desorption from droplets – causes the Ga desorption to increase as well. At the point where steady–state desorption is reached and all excess Ga desorbs again, the Ga droplets must have acquired a stable equilibrium where no further Ga is incorporated into droplets. To confirm this notion, we have integrated the area between the steady–state level (given by the total excess Ga) and the actual Ga desorption signal, i.e. hatched area in Fig. 7.2(c), and determined an amount of 290 nm equivalent film thickness of Ga contained in droplets. For comparison, *ex situ* measurements by x–ray fluorescence (XRF) were performed to evaluate the total amount of Ga contained in the entire GaN layer (once including the Ga droplets and once without droplets, after they have been etched in a hot HCl solution). The difference between the two measurements equals therefore the total amount of Ga contained in droplets and was found to be 294 nm, which is in excellent agreement with our *in situ* QMS measurement. If Ga was incorporated infinitely into droplets and if no desorption from the droplets occurred, then we would expect the droplets to contain an amount of Ga equal to 1700 nm equivalent film thickness after approximately 1 μm of GaN growth. This major difference, however, to the observed data corroborates our understanding of the tendency of Ga droplets to form a stable equilibrium with the surrounding supersaturated vapor phase.

7.3. Variation of Ga Droplet Size with Temperature

In the following, we place special emphasis on the formation of such stable Ga droplets and their size control as a function of growth temperature. For this purpose, in Fig. 7.3. Ga desorption measurements are presented for GaN growths at two different temperatures (693 °C and 728 °C), but otherwise constant conditions. The QMS spectrum for the lower temperature of 693 °C is identical to that of Fig. 7.2(c), and the Ga desorption for the higher temperature of 720 °C shows a qualitative similar behavior, but differs quantitatively by some aspects. First, the initial level of Ga desorption immediately upon shuttering is much higher compared to the low temperature case, because at the higher temperature the thermal limit for Ga desorption (i.e. border for droplet formation) is increased. Secondly, the Ga desorption saturates much faster, indicated by the time t^{steady} as defined by the onset of steady–state desorption. This means that the stable equilibrium of Ga droplets is reached much earlier and when determining the amount of Ga contained in the droplets we get 140 nm equivalent thickness (compared to 290 nm for the lower temperature case). The different amounts of Ga in droplets are further confirmed by *ex situ* optical microscope imaging of both GaN layers after growth [see Fig. 7.4]. Both images show a comparable droplet density of $\sim 1 \times 10^6$ cm^{-2}, but evidence a significant deviation in droplet size. For growth at the lower temperature (T$_S$ = 693 °C), Ga droplets appear as a pronounced bimodal droplet size distribution with diameters ranging between 5 – 8 μm [Fig. 7.4(a)]. On the other hand, Ga droplet sizes are more homogeneously distributed with much smaller diameters of $\sim 2 - 3$ μm when growth is performed at the higher temperature of T$_S$ = 720 °C [Fig. 7.4(b)]. The different size distributions will be further addressed in the discussion, where the different stages of droplet

growth will be explained by nucleation theories, in particular by first order phase transitions and Ostwald ripening.
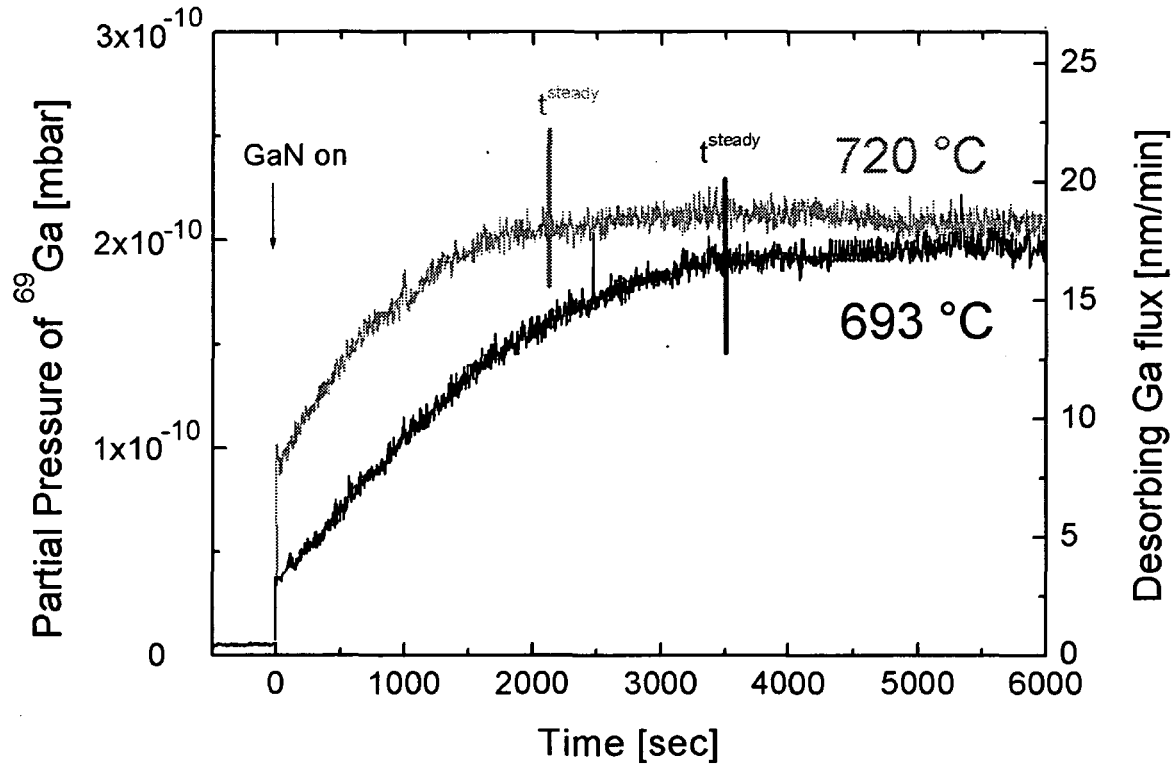

Fig. 7.3. Ga desorption during GaN homoepitaxy in the Ga droplet regime for two different temperatures. The point where steady–state desorption is reached (t^{steady}) corresponds to Ga droplets having formed a stable equilibrium between adsorption and desorption, meaning that they stopped growing in size.
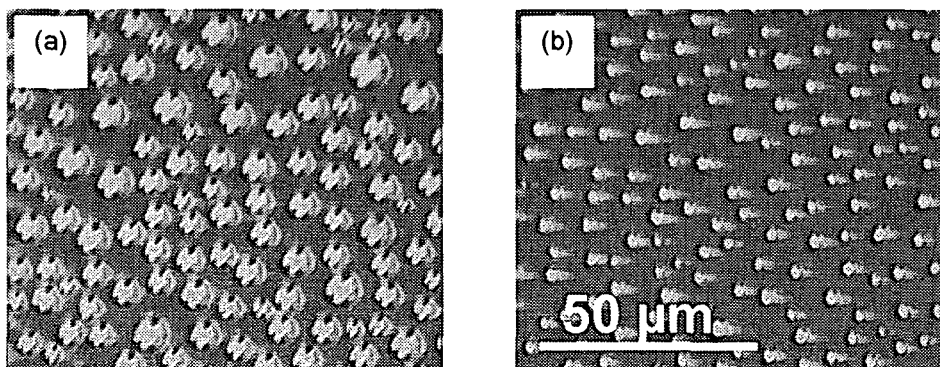

Fig. 7.4. Optical microscopy images of GaN surfaces containing stable Ga droplets of different size distributions due to differences in growth temperature, i.e. (a) T_S = 693 °C and (b) T_S = 720 °C.

7.4. **Region of Metastable Droplet Formation**

To further investigate the complicated Ga desorption behavior found in Sect. 7.2 [i.e. Fig. 7.2(b)], where GaN growth was performed under slightly Ga droplet conditions, a similar growth series was carried out at nearly identical conditions. Specifically, the Ga/N flux ratio was unaltered at 3.91, while T_S was slightly higher at 735 °C. In order to study each single phase during the whole GaN growth process and the consequential surface morphology, the growth time was varied from 60 to 7200 sec. In Fig. 7.5 each of the five different growth durations is presented as an open symbol (A – E) along the Ga desorption signal. Upon each growth stop the sample was immediately quenched to room temperature in order to preserve the eventually accumulated amount of Ga that has adsorbed during growth. The representative drop–off in the Ga desorption at the growth stop is only shown for case E (t = 7200 sec), but is identical for all other growths.
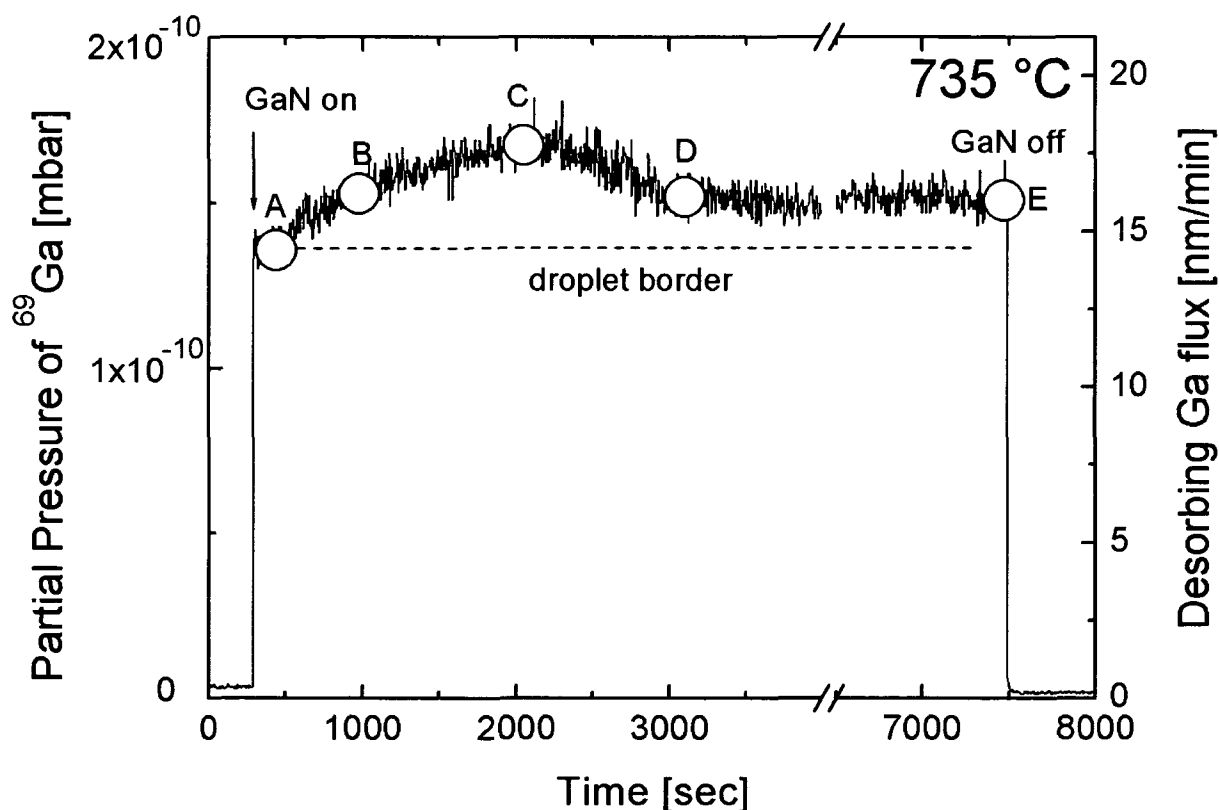

Fig. 7.5. Desorbing Ga flux during GaN (000 $\bar{1}$) homoepitaxy on a 100 nm GaN nucleation layer on sapphire for T_S = 735 °C and Ga/N = 3.91; the evolution of the Ga desorption resembles that earlier found in Fig. 7.2(b).

Note, that the evolution of the Ga desorption resembles that of Fig. 7.2(b), meaning that Ga desorption starts out at a level given by the Ga droplet border, rises to a maximum and decreases thereafter to a steady–state level. The first GaN growth case (A) with a growth time of merely 60 sec shows that the Ga desorption has not significantly risen above the level of the Ga droplet border. The subsequent optical microscope analysis [Fig. 7.6(a)] indicates that

no macroscopic Ga droplets have nucleated during this short growth period, or at least the amount of accumulated Ga was so low that it desorbed entirely during the cool down process after growth. However, when GaN growth is performed for a longer period and stopped during the rising Ga desorption (case B), small Ga droplets with diameters of around 1 μm have clearly formed on the surface [Fig. 7.6(b)]. For GaN growth terminated directly at the maximum of Ga desorption (case C) results also still in Ga droplets with similar diameters [Fig. 7.6(c)], but apparently their density has decreased by a factor of 1.5. This means, that at the maximum level of Ga desorption the amount of initially accumulated Ga droplets must have already decreased by a certain amount. Finally, when GaN growth procedes longer and the desorbing Ga flux reaches steady–state characteristics (cases D and E), the precedent Ga droplets seem to have disappeared completely [Fig. 7.6(d)]. Therefore, the slope of desorption in Fig. 7.5. gives the build–up of Ga droplets to a maximum coverage and its subsequent desorption with no remaining droplets.
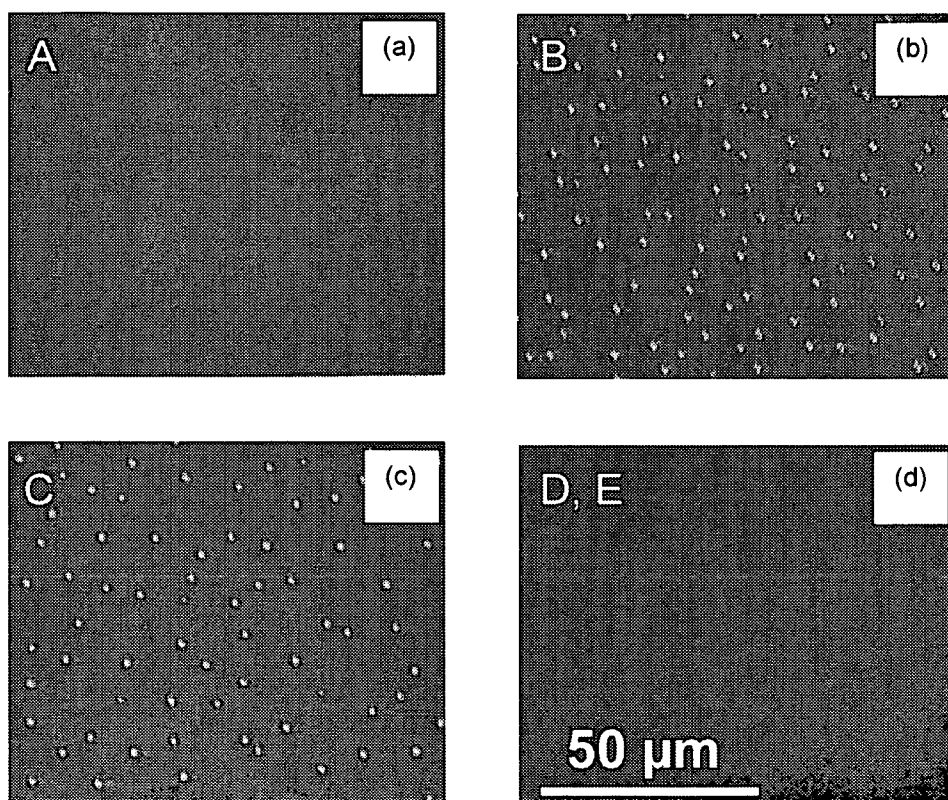

Fig. 7.6. Optical microscopy (OM) images of GaN surfaces established by the different growth periods as indicated by the open sympols in Fig. 7.5: (a) 60 sec, (b) 700 sec, (c) 1750 sec, (d) 2800 sec and 7200 sec, respectively. Note, that Ga droplets disappear for growth periods > 700 sec.

This creates some particular interest for the final atomic–scale suface morphology of such GaN layers grown under the given low droplet conditions. In Fig. 7.7(a) 10×10 μm² and 0.5×0.5 μm² AFM surface scans of the GaN layer grown for 7200 sec (case E) are shown. The surface exhibits an overall smooth morphology with a tendency towards spiral hillocks

consisting of curved atomically flat terraces separated by monolayer (2 – 3 Å) high steps. The mean surface (i.e. rms) roughness over the whole 10×10 µm^2 scale is as low as 0.8 nm. Similar scans performed on even larger scales evidenced that no Ga droplets were on the surface and no hexagonal nanopipe defects (as in Sect. 6.5.) either. Comparatively, also shown in Fig. 7.7(b), is the surface morphology of a GaN layer grown at a slightly higher temperature of T_S = 743 °C, meaning just below the Ga droplet border in the intermediate growth regime. Obviously different to the previous case, occasionally some nanopipe defects occur (typical for GaN growth in the intermediate regime) and the respective rms roughness of 1.2 nm is also higher. The apparent droplet and nanopipe free GaN surface of Fig. 7.7(a) implies the existence of a narrow growth region slightly above the droplet border. It seems that here Ga droplets are not stable throughout the entire growth process, with possible scenarios for their metastability being discussed in the following section.
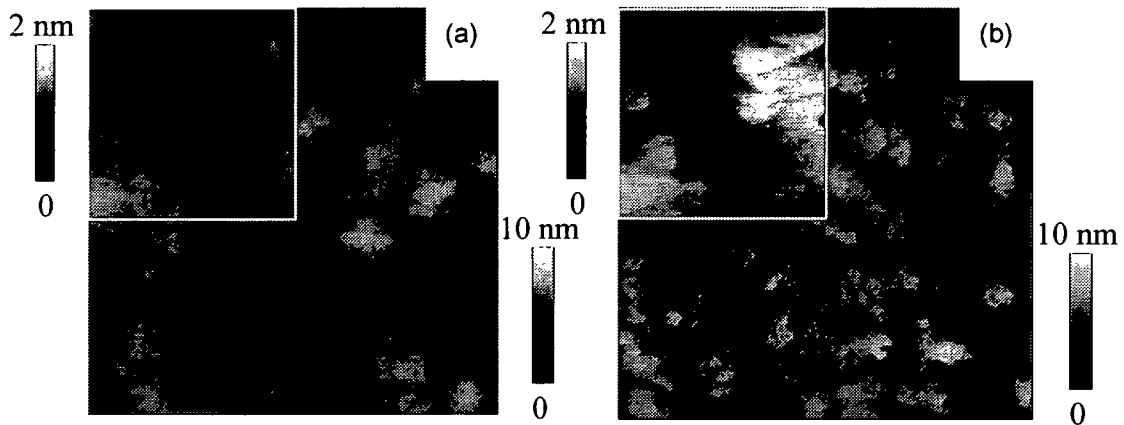

Fig. 7.7. AFM surface images (10×10 µm^2 and 0.5×0.5 µm^2 for the inserts) of GaN layers grown under (a) slightly Ga droplet conditions (T_S = 735 °C) and (b) high Ga–rich intermediate conditions (T_S = 743 °C) with a Ga/N flux ratio of 3.91 for both cases. Most remarkable, no Ga droplets and nanopipe defects appear on the surface in (a).

7.5. Discussion

To give an approach of understanding GaN growth in the vicinity of the Ga droplet border, specifically the issues of droplet formation, their growth and even their metastability within a narrow growth region, it is most convenient to apply classical nucleation theories. The basic ideas of the most simple, i.e. homogenous nucleation theory, as developed by Volmer and Weber [173] and Becker and Döring [174], are based on the *thermodynamic classical droplet model* which presumes an incompressible liquid droplet being at rest. To derive the crucial parameters for droplet formation, the following assumptions have to be made: the surface of such a droplet can be described by the macroscopic flat-film surface tension σ (so–called *capillarity approximation*), and its density is given by the macroscopic liquid density ρ_α. This approach lacks the capability though to extrapolate the macroscopic

density and the surface tension to small droplet sizes. However, the free energy to form a droplet with n atoms comprises of two parts:

$$\Delta F_n = (\mu_\alpha - \mu_\beta)V_n(\rho_\alpha - \rho_\beta) + \sigma A_n \ . \tag{7.1.}$$

The first term on the right hand side is the volume free energy of the droplet and represents the decrease in chemical potential due to the formation of the droplet. The second term is the contribution of the surface free energy that yields an increase in ΔF_n. V_n is the volume of the droplet, A_n its surface, μ_α denotes the chemical potential of the droplet, ρ_α its density, while μ_β stands for the chemical potential of the surrounding vapor and ρ_β for the density of the supersaturated vapor phase. In this classical approximation μ_α and μ_β are assumed to be constant, meaning that a change in the vapor state due to the formation of the drop is not considered. Additionally, assumptions are made that the vapor is ideal, the latent heat released by at the droplet–vapor interface is negligible, and the nucleation is isothermal. For an ideal vapor and an incompressible liquid this yields:

$$\mu_\alpha - \mu_\beta = -k_B T \ln\frac{\rho_\alpha}{\rho'} = -k_B T \ln y \ . \tag{7.2.}$$

The ratio ρ_β/ρ' gives the supersaturation and is constant because of $\rho_\beta = $ const. Neglecting further ρ_β in comparion with ρ_α and assuming a spherical droplet with a radius r, one obtains from Equ. (7.1.)

$$\Delta F_n = -\frac{4\pi}{3}r_n^3 k_B T \ln y + 4\pi\sigma r_n^2 \ . \tag{7.3.}$$
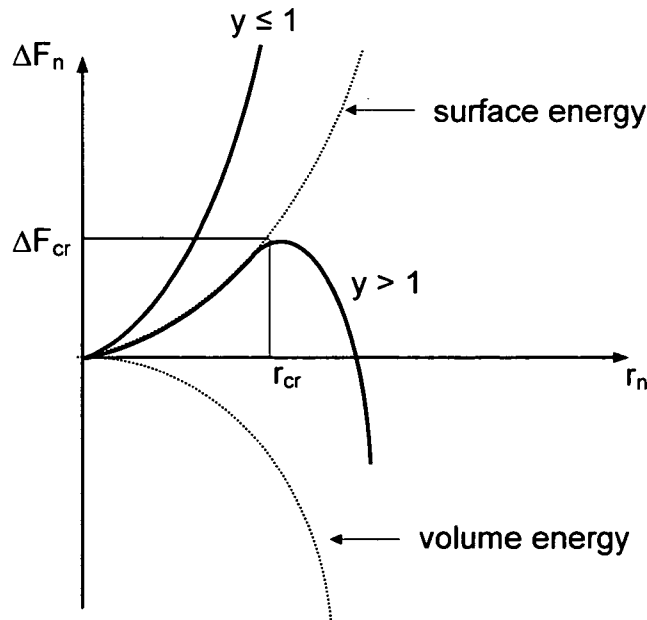

Fig. 7.8. Illustration of the formation energy ΔF_n of droplets versus droplet radius r (y means the supersaturation, r_{cr} the critical droplet radius and ΔF_{cr} the maximum of the free energy).

The free energy of the droplet formation is illustrated in Fig. 7.8 versus the droplet radius. For initial supersaturations y $\leq$1 the free energy is a monotonously increasing function of the radius, which means that the vapor is the absolutely stable phase. For y > 1, however, the free energy decreases continuously, when the droplet has reached an overcritical size $r > r_{cr}$. The critical droplet radius is derived from the extremum condition ($\partial\Delta F_n / \partial r_n$) = 0:

$$r_{cr} = \frac{2\sigma}{\rho_\alpha k_B T \ln y} \,. \qquad (7.4.)$$

Applying this equation to Equ. (7.3.) it yields the maximum of the formation energy, expressed by

$$\Delta F_{cr} = \frac{16\pi\sigma^3}{3(\rho_\alpha k_B T \ln y)^2} \,. \qquad (7.5.)$$

Since ΔF_n has a maximum the equilibrium between the droplet and the surrounded vapor is an instable one. The maximum of ΔF_n is therefore related to a *nucleation barrier* which the droplet must cross over to reach a macroscopic size. Hence, overcritical droplets can grow further, while undercritical droplets have to diminish again in a deterministic sense.

This classical droplet model is a very simple approximation and it creates some serious difficulties when describing real droplet systems. Lothe and Pound [175] argue for instance that translational and rotational energies for the droplet, as it moves through the system, provide significant contributions to the estimation of the formation energy. Moreover though, one of the most substantial assumptions made in the classical theory is that the supersaturation of the gas phase remains constant during droplet growth. This implies an infinite gas phase acting as a reservoir to the nucleating droplets. The result of such an assumption is that once a droplet reaches a critical size catastrophic growth will occur, i.e. the droplet will grow to an infinite size. This is clearly an unphysical result as the droplets must therefore deplete the gas phase, contradicting the original assumption. It also fails to explain droplets apparently existing in equilibrium with a vapor phase as seen commonly in nature, in clouds or fogs. Instead, Pippard [176] states that an enclosed system has a minimum in free energy, implying that a droplet can exist in stable equilibrium with its surrounding vapor. The physical origin of this minimum was described by the decrease in the chemical potential of the gas phase as it is further depleted of atoms, so that there is a driving force for the atoms to desorb from the droplet for sizes greater than the equilibrium size. To relate such an equilibrium droplet radius r_{equ} to the critical radius for droplet formation, it is worth noting that $r_{equ} >> r_{cr}$ holds true.

When recollecting the experiments performed in Sect. 7.3. and 7.4, it seems that the above considerations are directly applicable for the Ga droplets as occurred during MBE GaN growth. For the shortest GaN growth duration (60 sec) under the slight Ga droplet conditions (as shown in Figs. 7.5 and 7.6(a)) no macroscopic Ga droplets have accumulated on the surface. This may be due to the fact that the growth time was not sufficiently long in order to achieve Ga droplets of overcritical size and hence all the subcritical nuclei desorbed. Also, the

supersaturation at the initial stage of droplet nucleation could be too low ($y \leq 1$) for sufficient contribution to the droplet volume energy. For longer growth periods, macroscopic Ga droplets with equilibrium sizes and coverages have appeared under all the investigated droplet conditions. The droplet sizes and coverages scale directly with the growth temperature, meaning that the equilibrium Ga droplets are largest for the lowest temperature ($T_S = 693$ °C, Fig. 7.4(a)), followed by intermediate temperatures ($T_S = 720$ °C, Fig. 7.4(b)) and are smallest in size for high temperatures ($T_S = 735$ °C, Fig. 7.6(b,c)). These differences can similarily be understood by the amount of excess Ga prevalent under the different temperatures, which is highest for low T_S and lowest for high T_S. In any case though, the same mechanism seems to apply to reach the equilibrium or stationary condition for the Ga droplet coverage with the surrounding vapor. Achieving such a stationary condition has also been proclaimed for cases where the surface diffusion coefficient of Ga atoms is large compared to the incoming Ga vapor atoms [177], a typical kinetic factor valid in Ga–rich MBE GaN growth [178].

The present Ga droplet density and size studies correlated with the QMS desorption spectra indicated further that the final and stable Ga droplet configuration deviates strongly from configurations at an earlier stage of growth. As obvious in Figs. 7.6 (b,c), Ga droplets are by a factor of 1.5 more densely distributed on the surface compared a stage prior to the maximum (i.e. stable) Ga desorption (compare with Fig. 7.5), despite similar droplet sizes. This implies directly that the Ga accumulation in droplets per unit time decreases with increasing growth time and comes to a stand at the point of maximum Ga desorption. This reorganization of the Ga droplet density can be described in the realm of first order phase transitions, particularly by the so–called Ostwald ripening. Ostwald ripening is driven by the energetically more favorable condition to form one larger droplet by cannibalizing atoms from other droplets, rather than to retain two similar medium–sized droplets. Therefore the density of Ga droplets decreases with increasing time, by gaining gradually larger droplet sizes. This mechanism is limited by the rate of Ga surface diffusion primarily, but also by the rate of droplet collision. As an example, the image in Fig. 7.4(a) evidences a pronounced difference in Ga droplet size, where it can be visualized that the larger droplets have grown at the expense of the smaller ones.

To completely understand the droplet evolution as found in Sect. 7.4 is quite challenging, since the once nucleated Ga droplets decay again completely, leaving behind perfect GaN surfaces free of any surface depressions and droplets. There are only few reports so far on the metastability of nucleated droplets, which occurs exceptionally in finite–sized vapor phase systems. In this context, semianalytic theoretical calculations based on partition functions done by M. P. Moody et al. [179] investigated the temperature dependence of droplet forming phase. It was found that at low temperatures it was hard to overcome the energy barrier for spontaneous nucleation, but once overcritical droplets have formed the resulting droplets were very stable. In contrast, for high temperatures the activation energy for droplet nucleation is lowest, but the energetic minimum for droplet equilibration is very shallow, allowing the formed droplets to become metastable and desorb eventually. These results reflect the temperature dependent Ga droplet stability as also found in this work. However, it can not be ruled out that other parameters, such as the final supersaturation or even local effects may play a central role in causing this metastability. Regarding this, one other possible explanation could

be that droplets cause locally a latent heat transfer to the surrounding vapor but also to the underlying substrate interface. Such a mechanism could be responsible for a local increase in substrate temperature that might be sufficient to desorb the accumulated droplets or keep them at an undercritical stage. So, at such critical conditions the state of the droplet might rather be determined by its immediate vicinity rather than by the system as a whole.

8. GaN Nucleation on SiC and Sapphire

8.1. Introduction

While the previous sections have dealt exclusively with the surface and growth kinetics on GaN surfaces (*homoepitaxy*), special focus will now be directed towards the *heteroepitaxial* GaN growth issues as prevalent during the nucleation stage on foreign substrates. As widely accepted, the nucleation phase in many heteroepitaxial systems determines the subsequent layer properties and is the critical step in producing high–quality material.

Thin film nucleation is usually divided into several stages, which are adsorption and desorption of arriving atoms, surface diffusion of adatoms, nuclei formation and their further growth, coalescence etc. [180], as also earlier illustrated in Fig.3.6. In conventional nucleation theories (such as the *classical droplet model* in Sect. 7.5), nucleation rates are typically limited by energetic barriers associated with the formation of critical–size nuclei (a *thermodynamic* effect), while the morphology is controlled generally by adatom mobility (a *kinetic* effect) [181]. More significant steps towards enhancing atomistic film nucleation theories were developed by Zinsmeister [182] and Venables [183], who have set up rate equation models depending on a variety of nucleation parameters (supersaturation, temperature, arrival rates, cluster size, etc.). However, once critical–size nuclei are stable, it is generally accepted that their further growth obeys one of three essential growth modes [181]: the much–studied island, or *Volmer–Weber* (VM) growth mode, where small three–dimensional (3D) island form directly on the bare substrate. In the layer, or *Frank–van der Merwe* (FM) mode, it is expected that two–dimensional (2D) clusters will form on each layer. In the layer–plus–island, or *Stranski–Krastanow* (SK) growth mode, the simplest picture is that the 2D intermediate layer forms first, and that the islands grow from two- or three–dimensional clusters on top of the intermediate layer.

Furthermore, when a large lattice mismatch exists between substrate and epilayer (i.e. GaN/6H–SiC: -3.4 % and GaN/Al$_2$O$_3$: -13.9 %), it is known that the high strain energy during the initial growth is generally accomodated by a high density of defects at the growth interface, mainly misfit dislocations.

To date, in heteroepitaxial GaN growth much attention was given to the optimization of the nucleation layer. Due to the large lattice mismatch and chemical dissimilarities, GaN nucleation on sapphire and SiC was found to procede generally by a three–dimensional (3D) island growth mode, leading to high amounts of threading dislocations (TDs) upon coalescence of these islands [184,185]. In a recent attempt, it was demonstrated that 3D GaN growth can partially be suppressed by a two–step growth technique which uses low–temperature AlN [186,187] or GaN nucleation layers [124]. In addition, Narayanan *et al.* have shown that stacking faults and point defects in the nucleation layer likely generate TDs in the bulk GaN material, impairing the growth of high–quality GaN [188]. On the other hand, fewer nucleation TD defects were observed when changing the kinetics (i.e. Ga/N flux ratio) [189], mainly caused by a delay in the coalescence of the 3D islands [190]. Controlling 3D island growth

and the point of coalscence seems therefore one of the key parameters for high–quality GaN growth. But it is inevitably challenging since wetting, critical island nucleation and other effects such as island strain relaxation, thermal decomposition and many more can all contribute to an initially highly non–linear growth rate [191]. This effects also severe problems for many applications, where accurate thickness control is required, such as for the nano–scale nucleation layers in GaN/AlN superlattices. There are ongoing attempts to control the GaN nucleating phase and the growth rate evolution *in situ*, with techniques used such as RHEED [192, 193], real–time x–ray fluorescence and scattering [194-196], and optical reflectance [197].

In the following, it will be demonstrated that the QMS technique provides a unique *in situ* method to quantify the GaN growth rate directly at any stage during nucleation and growth. In particular, GaN growth on both 6H–SiC and sapphire substrates will be investigated and compared with homoepitaxial GaN growth along the N–polar and Ga–polar surface polarities, an extension to previous work done in this group [198]. To correlate the QMS data with post-growth thickness measurements, *ex situ* Rutherford backscattering was employed and compared to the nominally expected thicknesses. Consecutively, the results of highly non–linear GaN nucleation will be shown, leading to a precise determination of the initial wetting problem, i.e. island growth rates and coalescence thicknesses.

8.2. Evolution of Film Thickness

To investigate the film thickness evolution of thin GaN nucleation layers, GaN growths were performed directly on c-plane sapphire and 6H–SiC at a constant temperature of $T_S = 740$ °C and a Ga/N flux ratio of 2.3. The growth time was different for all GaN layers, so that the nominal thickness varied from 2.59 nm (10 ML) to 1000 nm, assuming an entirely linear growth rate according to the growth model presented in Sect. 4.2. Within this model, the N flux is limiting the growth rate and all excess Ga desorbs from the surface, as long as GaN growth is performed in the Ga–rich intermediate growth regime. Postgrowth layer thickness measurements were performed by Rutherford Backscattering Spectroscopy (RBS), where the actual thickness was evaluated from the total Ga coverage within the layer.

These RBS measurements revealed major differences compared to the nominal GaN layer thicknesses, as calculated using the steady state growth rate. While at small layer thicknesses (< 20 nm) the measured thickness is by far smaller than the expected value, at thicker layers (>> 20 nm) both data nearly coincide [evidenced in Fig. 8.1(a)]. Note, that the GaN thickness evolution is identical for both sapphire and 6H–SiC substrates. As an example, if nominally 10 ML of GaN are deposited, the measured GaN thickness results in only 1ML of the calculated value, thus reducing the adsorption efficiency by one order of magnitude for the completion of the first ML. This evidences that growth is not initiated with the maximum growth rate, but that with increasing growth time a steady–state growth rate is approached [Fig. 8.2(b)]. By fitting the slopes to the experimental data one can clearly differentiate between two regimes of growth, initially a highly nonlinear evolution of thickness with time and
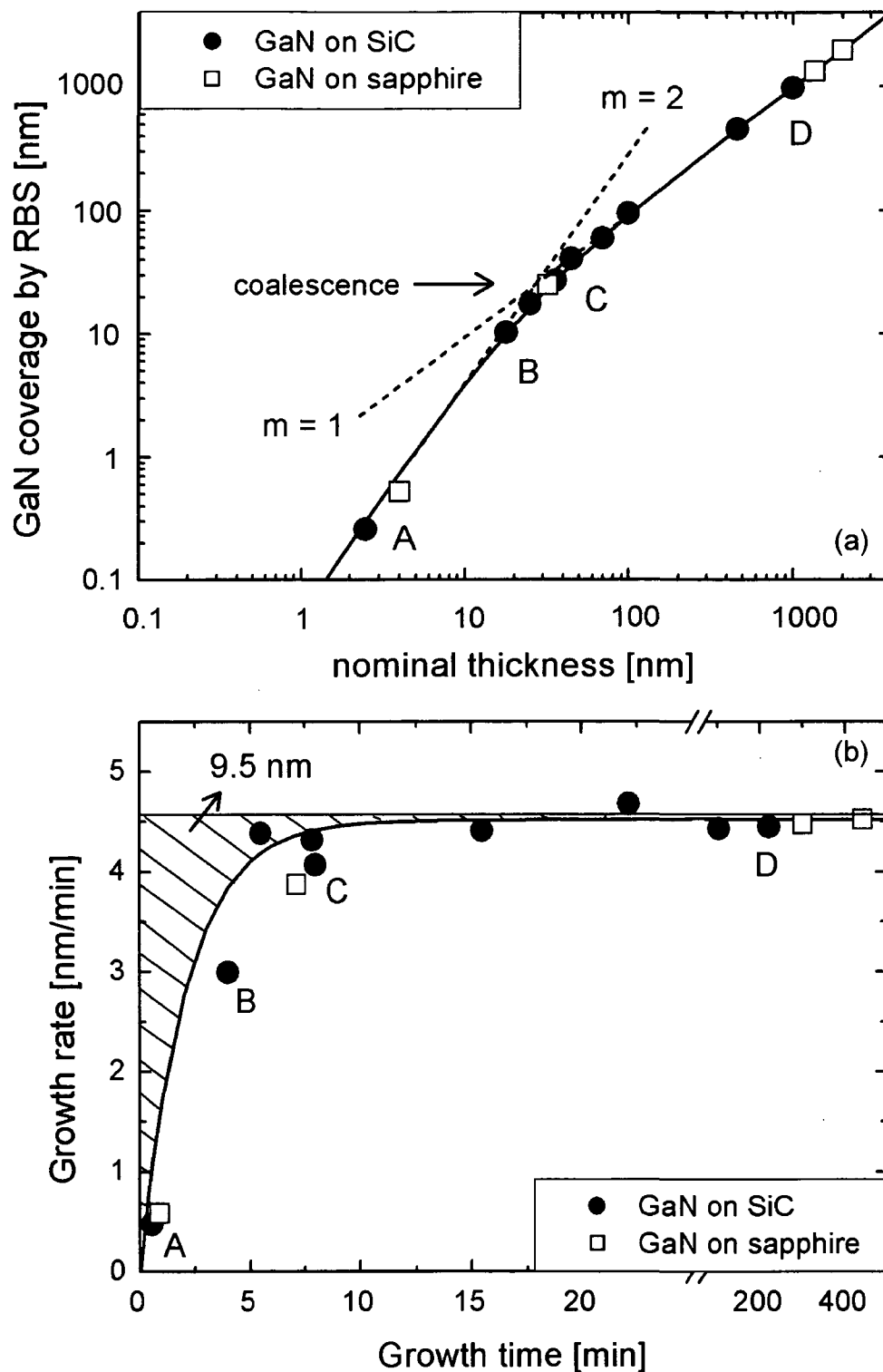
Fig. 8.1. (a) GaN coverage on 6H–SiC and sapphire determined by Rutherford backscattering spectroscopy as a function of the calculated thickness from linear growth. Note, the point where the fitted slopes change from quadratic growth (gradient m = 2) to linear growth (m = 1) corresponds to the island coalescence thickness (b) evolution of the GaN growth rate as a function of time as derived from the data in (a); the hatched area gives the amount of GaN that is not incorporated during the initial stage of growth and is equivalent to 9.5 nm. Datapoints marked from A–D are subjected to AFM scans whaich are shown in Fig. 8.2.

later a constant growth mode. The nonlinear part follows a power–law dependence (quadratic increase), that is typical for island growth before the coalescence stage, as also found by Headrick *et al.* [194,195]. The transition from power–law growth to linear growth is evidenced by the kink at coalescence [Fig. 8.1(a)], indicated by the point where the slope changes form gradient $m = 2$ to $m = 1$. Applying these gradients, the best fits of the growth rate and the layer thickness as a function of growth time are given by the following empirical equations, including both the power–law growth and the linear regime after coalescence:

$$R(t) = R_\infty \left[1 - e^{-(t/t_x)^{m-1}} \right] = R_\infty \left[1 - e^{-(t/t_x)} \right] \quad \text{for } m = 2. \tag{8.1.}$$

and

$$d(t) = R_\infty \left[t + t_x e^{-(t/t_x)} - t_x \right]. \tag{8.2.}$$

The equation (8.2.) for the layer thickness is obtained simply by integrating the equation for the growth rate (8.1.). The crossover time from island nucleation to coalescence is given by t_x and the steady–state growth rate is $R_\infty = 4.5$ nm/min. Both expressions give the desired limits: $R(t) = R_\infty t/t_x$ and $d(t) = R_\infty t^2/2\, t_x$ when $t/t_x \ll 1$, $R(t) = R_\infty$ and $d(t) = R_\infty t$ when $t/t_x \gg 1$. The best fitted curve is obtained for a crossover time of $t_x = 2.1$ min with an error between RBS and fitted data being always below 10 %. As the coalescence thickness can be defined by the point of intersection between the two tangents, one gets $d_{coal} = 2t_x R_\infty = 19$ nm.

When looking at the evolution of the growth rate in Fig. 8.1(b), one can also calculate the difference between the actual growth rate and the steady–state growth rate. Integrating this difference over time represented by the hatched area equals to 9.5 nm and gives exactly the amount of GaN that is not incorporated during the initial nonlinear island nucleation stage.

8.3. GaN Island Shape and Surface Morphology

To confirm the proposed 3D–island growth mode of GaN on sapphire and SiC, AFM surface scans were performed for a variety of samples grown to different thicknesses. In Fig. 8.2 1×1 μm^2 AFM images and RHEED patterns along the $[2\bar{1}\bar{1}0]$ zone axes of GaN layers grown on 6H-SiC are presented with measured thicknesses ranging from 0.25 nm to 985 nm (labeled A–D). There is clear evidence that initially discrete islands of GaN nucleate, which then grow predominantly lateral in size. These growth kinetics are confirmed by additional AFM studies, which found that the lateral nuclear dimensions are roughly 20 times larger than the respective vertical extensions of the islands. However, for thicker GaN layers large coalesced islands appear with trenchlike features at the coalescence boundaries [Fig. 8.2(C)] that grow into a continuous film with increasing growth time [Fig. 8.2(D)].

Also, with increasing GaN coverage the RHEED pattern undergoes a transition from spotty, evidencing surface roughening by 3D-islands, to truncated streaks signifying large terraces with atomically smooth surfaces. Note, that the ~1 μm thick GaN layer [Fig. 8.2(D)] shows a 2×2 surface reconstruction which is characteristic of the achieved Ga-polar (0001) surface.

The morphological transition from initial 3D-islands to coalesced atomically flat mesas is therefore in sound agreement with the RBS data and the acquired model for island coalescence. GaN coverages below the coalescence thickness of ~20 nm (i.e. the point where the slope changes from gradient $m = 2$ to $m = 1$ in Fig. 8.1(a)) are arranged as 3D–islands, and beyond as homogenously coalesced islands.
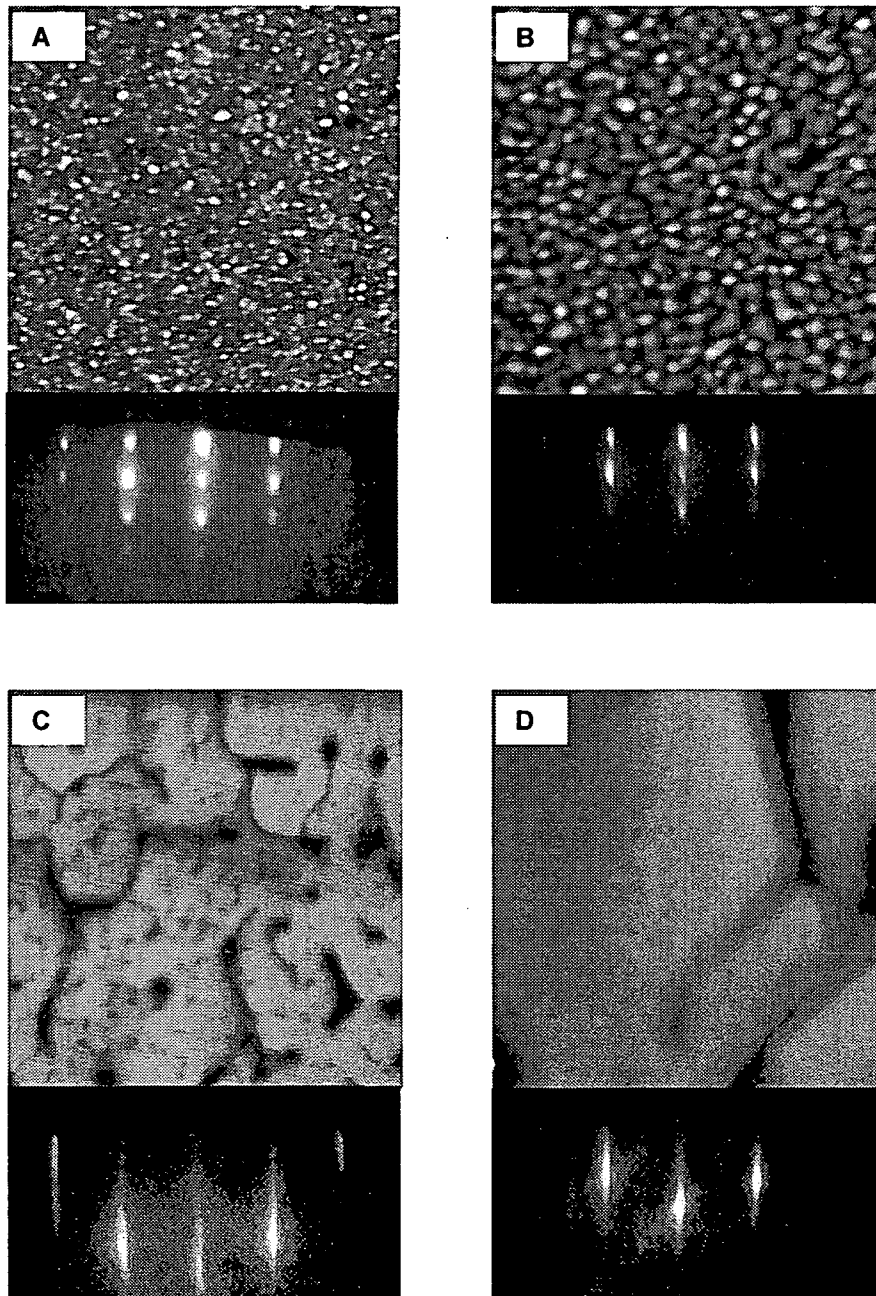

Fig. 8.2. 1×1 μm^2 *AFM images and RHEED patterns along the* $[2\bar{1}\bar{1}0]$ *zone axes of GaN layers on 6H-SiC with measured thicknesses of (A) 0.25 nm, (B) 10 nm, (C) 40 nm and (D) 985 nm; the height scale between black (lowest) and white (highest) areas is 10 nm.*

8.4. Quantification of the Wetting Problem

As a consequence of the nonlinear thickness evolution and the reduced growth rate during the initial stages of GaN growth, it can be suspected that during the nucleation stage a higher reevaporation rate of the impinging atoms must be present. To further investigate the prevailing condensation mechanisms in search for the missing GaN material, the QMS technique was applied to determine the amount of desorbing Ga atoms and hence the growth rate at any time. Prior to each growth event, the Ga cell was stabilized for more than 30 min to guarantee a constant Ga flux during the entire GaN growth procedure. Also, in order to avoid the characteristic transient of the Ga flux occurring immediatley after opening the shutter of the effusion cell, the substrates were annealed in a Ga flux prior to growth for about 15 min at a temperature that allows complete desorption of all impinging Ga atoms. Subsequent GaN growth was established by opening the N shutter. First, as a guideline to all following experiments, homoepitaxial growth of GaN (Ga–polarity) on a GaN template (produced by MOCVD) was investigated. As expected upon opening the N shutter, the desorption signal drops immediately reaches its steady–state value [Fig. 8.3(a)]. The drop of the desorption signal is equivalent to the amount of incorporated Ga atoms and equals the growth rate of 4.5 nm/min given by the N flux. Hence, instant drop in desorption means instant growth.

In contrast to this, heteroepitaxy of GaN on 6H–SiC yields a substantially increased Ga desorption during the initial phase of nucleation that only gradually approaches its steady-state value [also Fig. 8.3(a)]. The time to reach a steady–state desorption rate (i.e steady–state growth rate) takes ~ 12 min under the given growth conditions. During this time lag, integrating the area below the exponentially decreasing desorption curve (i.e. hatched area) leads to the amount of GaN material that is not incorporated during this phase, i.e. 7.5 nm in the present case. Completely identical desorption curves hold also for the growth of N-polarity GaN on sapphire and on MBE-GaN templates [Fig. 8.3(b)]. Several additional mass spectrometric experiments on both SiC and sapphire under identical growth conditions yielded a Ga desorption during the initial stages equivalent to a GaN thickness of 8 ± 1.5 nm. This is in excellent consistency with the 9.5 nm GaN not being incorporated as evaluated from the RBS data of Fig. 8.1(b). Remarkably, nucleation and desorption rates are thus identical for GaN grown either along the (0001) face (Ga polar) or along the ($000\bar{1}$) face (N polar) planes, valid in both homo- and heteroepitaxy.
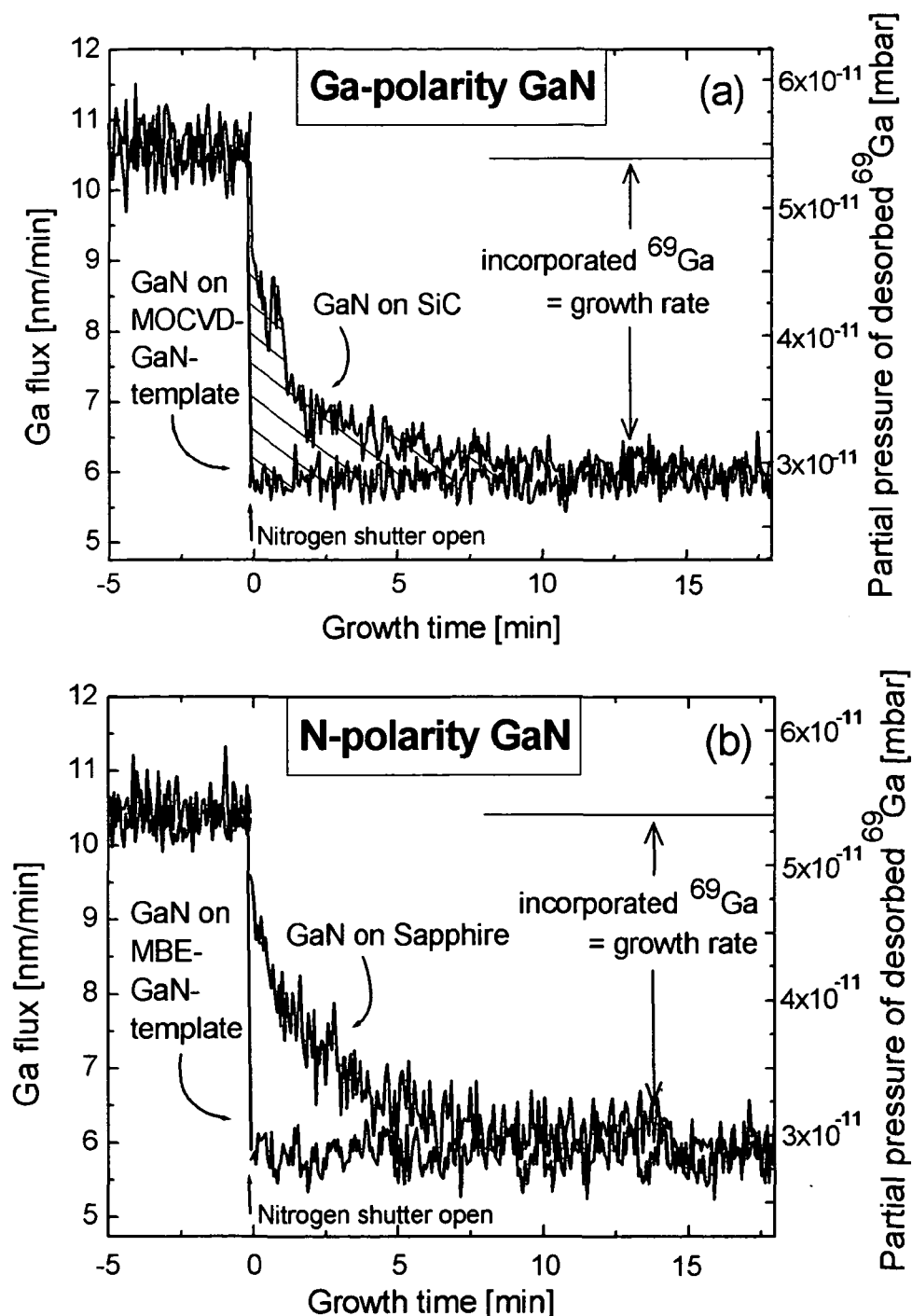
Fig. 8.3. Desorbing Ga flux during the initial phase of (a) Ga-polarity GaN growth on 6H-
SiC and MOCVD GaN-template and (b) N-polarity GaN growth on sapphire and MBE GaN-
template. The decreasing Ga desorption in heteroepitaxial GaN growth corresponds to a
gradual increase in GaN growth rate. Note the deviation between heteroepitaxy and
homoepitaxy, leading to the amount of GaN being not incorporated during the initial stage
(i.e. hatched area), which is 8 ± 1.5 nm, independent of the chosen substrate material.

8.5. Discussion: Energy-barrier induced Nucleation Delay

The presented GaN nucleation studies evidence that at the early stages of film growth the impinging adparticles have a reduced sticking coefficient. This results in a high probability of adatoms escaping before diffusing to an active site and being incorporated into the surface. Such an initial wetting problem can be explained by conventional nucleation theories, with a distinct focus on the formation on critical–sized nuclei. In the thermodynamic *classical droplet approach* of Sect. 7.5, the formation of critical nuclei is strongly governed by the competition of the volume and surface free energies of the forming nuclei. Initially, nuclei develop with an increase in total free energy ΔF_n, which is the sum of volume and surface free energies (Equ. 7.3). During this stage subcritical nuclei can dissolve again, giving a significant contribution to the initially increased Ga desorption. But, when a critical size is reached, growth continues with a decrease in total free energy and the overcritical nuclei grow further. The critical island radius (Equ. 7.4) of the nuclei corresponds directly to an energy barrier (Equ. 7.5), that needs to be overcome for successful nucleation. Such an energy barrier height controlled nucleation behavior was found to lead to a "time lag" (i.e.nucleation delay) problem [199] and nonlinear growth, where the growth rate varies strongly with the size distribution of overcritical nuclei [194,200].

Although the delayed nucleation along with the formation of critical–sized nuclei is one way to describe the observed nucleation phenomenon, surface lifetime limited growth kinetics is another approach to understand the growth of islands. Basically, there are two possible routes for adsorbed atoms to be incorporated into growing islands. The first is direct impingement onto the growing island. The second is by adsorption onto the substrate followed by surface diffusion and capture by a growing island. Accordingly, there are two corresponding categories of island growth morphology [201]: (a) if the islands are hemispherical or cap–shaped, then the growth rate is proportional to the projected surface area. In this case, island growth is dominated by direct impingement, although surface capture might also contribute to growth. (b) If the islands are disk–shaped, they grow rapidaly in two dimensions, then the growth rate varies with their diameter. Such disk–shaped islands grow predominantly by diffusion from the free substrate to the edge of the nuclei. Both cap–shaped and disk–shaped island growth lead to a power–law behavior. Applying the model of the nucleation kinetics by Osipov [202], who introduced the cluster growth index m (varying from 1 – 3), clearer statements regarding the islands growth kinetics can be made. The growth of cap–shaped islands is described by an index of $m = 3$, whereas the growth of disk–shaped islands corresponds to $m = 2$. For the present case of GaN island growth, a growth index of $m = 2$ was found to be most appropriate to describe the power–law evolution by the fits of equations (8.1) and (8.2). Indeed, these growth kinetics were confirmed by AFM studies of various different GaN island samples, where it was found that the lateral island dimension was by a factor of 20 larger than the island height. This relation was nearly constant up to the point of coalescence, but beyond additional lateral growth is prevented. A schematic diagram of the proposed disk–shaped island growth kinetics is presented in Fig. 8.4.
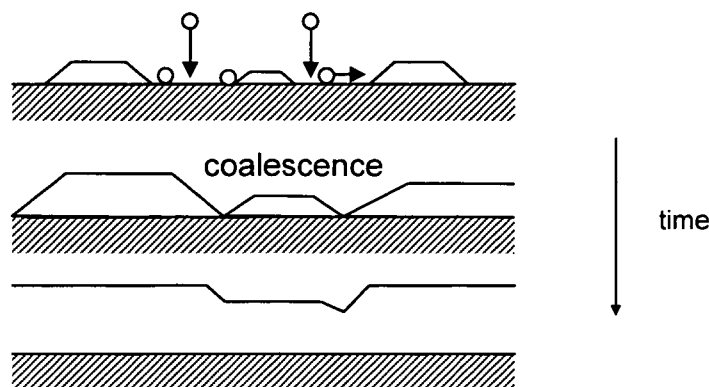
Fig. 8.4. Growth kinetics of disk–shaped islands with a high lateral (2D) growth velocity due to surface diffusion of adatoms and their capture at the islands edges; at coalescence lateral growth seizes and vertical growth bcomes predominant.

What is most remarkable, is the fact that for the constant growth conditions the nucleation rates and island growth modes seem independent of the used substrate materials, SiC and sapphire. In both cases, disk–shaped island growth was found, that could either be formed by incomplete wetting and Volmer–Weber (VW) growth or by Stranski–Krastanow (SK) growth after an initially grown wetting layer. For eventually very thin wetting layers, however, the presented experimental methods do not allow a differentiation between these two growth modes. In this context, *in situ* X–ray reflectivity measurements of the GaN nucleation on sapphire performed in gas–source MBE [195] pointed out that depending on the N species the growth mode can be changed from VW to SK growth. Three–dimensional (3D) VW island growth was found when using thermal ammonia (NH_3), whereas low energy 30 eV NH_x^+ ions resulted in a SK modus. On SiC, on the other hand, the usually poor surface preparation leads to poor interface nucleation, but with a Ga adsorbate layer terminating the SiC surface initial island (VW) nucleation can be prevented and two–dimensional growth promoted [202]. In this case, the Ga adsorbate was believed to enhance the surface mobility of the adatoms, as typical in a surfactant induced step–flow growth mode. In the present case, however, a quasi–two–dimensional island growth mode persists that might be generated by active sites, such as substrate surface steps or kinks, that can alter the nucleation kinetics severely. Also, GaN surface polarity might play a role in the nucleation behavior. The results demonstrate though that, independent of the polar GaN characteristics, nucleation rates remain the same. It is well known, that MBE growth of GaN on the two investigated substrates yields two different surface polarities, N–face surfaces on sapphire [12] and Ga–face surfaces on Si–terminated 6H–SiC [17]. Furthermore, GaN is exposed to two different intrinsic stress fields during growth, high tensile stress if grown on sapphire and lower compressive stress if grown on SiC. It is thus even more remarkable, that despite the two polarity–determining bonding mechansims, i.e. Ga–O bonds in GaN growth on sapphire and Si–N bonds for growth on SiC and the opposite stresses, nucleation rates do not differ between the two types of substrates at all.

9. Nucleation of GaN on AlN and Quantum Dot Growth

9.1. Introduction

Optimizing the performance of state–of–the–art GaN–based devices by aiming at a reduction of the typically high threading dislocation densities generated at the island coalescence stage can be achieved by implementing thin AlN nucleation layers in the grown heterostructures [186,187]. As GaN grown on such AlN nucleation layers presents still a rather large lattice mismatch (about 2.4 %), the issue of strain relaxation in the GaN layer is of particular importance and it may determine its structural and optical properties. However, unlike in direct GaN growth on sapphire or SiC, several studies pointed out that by carefully controlling the growth kinetics, GaN 3D–islanding on AlN can be suppressed and a two–dimensional (2D) growth mode achieved [171,203,204]. In some cases, it was even reported that GaN layers grown on SiC were polycrystalline unless a monocrystalline AlN nucleation layer was deposited first [205]. Regarding the reduced compressive strain in GaN/AlN heterostructures compared to GaN layers grown directly on Al_2O_3 or SiC, strain engineering can be rendered possible by varying the AlN layer thickness as was demonstrated recently in our group [206]. Another practical use of controlling the compressive strain relaxation mechanism in the GaN/-AlN system arises from the misfit accomodation by the Stranski–Krastanow (SK) growth mode under certain growth conditions [207]. Unlike in 2D growth, where the strain relaxes plastically by the formation of misfit dislocations, in the SK case the built–up strain is relieved elastically by the formation of islands after a thin wetting layer (WL) has formed. If these islands can be produced with negligible dislocation propagation and a narrow size distribution, the SK mode is one very appealing approach for the fabrication of GaN semiconductor quantum dots (QDs) in an AlN matrix. With the typically large strain induced piezoelectric polarization in QDs [208] an additional blue–shift of emission wavelengths along with improved lifetime of optoelectronics devices could be achieved.

Several ambitious efforts of studying the influence of the growth kinetics on strain relaxation mechanisms and quantum dot formation during GaN growth on AlN were based on either RHEED analysis [171,207–209], TEM studies [210–212] or high–resolution XRD observations [213]. These methods have been used to also determine the critical thickness for 3D–islanding (i.e. QD formation), but by leaving the involvement of atomistic processes such as adsorption, desorption, surface diffusion etc. rather speculative, accurate control of GaN islands of desired dimensions is somewhat impeded. In the following, with the employment of the QMS desorption monitoring technique, it will be demonstrated that the AlN substrate surface structure, strain and incorportion kinetics (adsorption/desorption) all act in a mutual manner on the GaN growth mode, island formation and morphology. Especially, the current growth rate will be quantified during the SK transition, pinpointing the influence of the kinetically driven differences of strain relaxation on the growth rate. On this basis, the real

critical thickness can be determined more accurately, with the consequence of proposing a procedure for thickness control of GaN islands. Furthermore, the exact Ga adlayer coverage during GaN growth on AlN will be determined, that facilitates either quantum dot growth or entire 2D–growth. As a starting point for these studies, the growth of optimum AlN surfaces will be investigated and a growth phase diagram for AlN will be created, similar to that of GaN (compare Sect. 4).

9.2. AlN Growth

9.2.1. AlN Growth Phase Diagram

Obtaining high quality GaN, from nanostructures to thick layers, relies crucially on the predeposition of very smooth and low defect density AlN buffer layers. The ability to meet these requirements is, in general, determined thermodynamically by the growth mode [177], i. e. two–dimensional versus three–dimensional growth, as well as by the growth kinetics. In the following, a growth diagram will be established giving the conditions for smooth two–dimensional versus rough three–dimensional AlN growth based on an investigation of surface morphologies as a function of Al/N ratio and growth temperature.

The growth of (0001) AlN layers was performed on c-plane sapphire and on on-axis 6H-SiC substrates. All molecular fluxes are given in terms of potential AlN growth rates in units of nm/min. The AlN layers presented here were grown at temperatures ranging from 775 to 820 °C with a constant N flux of 2.9 nm/min unless otherwise noted. The nitrogen flux was adapted from scanning electron microscopical (SEM) thickness measurements from cross sections of thick GaN layers grown under Ga–rich conditions. As noted in Sect. 4.2., under these conditions all excess Ga desorbs from the growing surface at typical growth temperatures and thus the growth rate is limited by the active N flux [115]. Analogously, the Al flux in terms of growth rate was determined from thickness measurements of AlN layers grown under N–rich conditions. Similar to N–rich GaN growth, it is expected that under these conditions the growth rate is limited by the flux of the group–III element.

This behavior was also directly demonstrated in a distinct AlN growth series on sapphire, where the AlN thickness and growth rate were evaluated by determining the Al coverage using Rutherford backscattering spectrometry (RBS). For the droplet–free AlN surfaces the backscattering spectra were evaluated by RUMP simulation code [214,215], basically by exploiting the shape of the Al signal with a well expressed step between the signal from the AlN layer and the sapphire substrate, which is caused by the different Al concentrations and projectile stopping powers in both materials. A similar procedure was used for the quantitative determination of the amount of Al contained in the droplets. Due to the lateral inhomogeneity of the surface in that case, however, an adapted differential evaluation scheme had to be applied to the total Al signal, taking into account its increase with droplet growth, the constant contribution from the AlN layer and the partly counteracting loss of substrate signal as it is shifted out of the considered spectral range. The contribution of the AlN was determined from

the same samples after the Al droplets had been removed by selective wet chemical etching with H_3PO_4.

For this Al coverage study, the AlN layers were grown with a constant N flux of 3.6 nm/min and with Al fluxes varying from 1.8–5.6 nm/min, while the growth temperature was kept constant at 810 °C. In Fig. 9.1 the Al coverage, as determined by RBS, is plotted as a function of the Al flux. It is obvious that for Al fluxes lower than the active N flux, the Al coverage scales linearly with rising Al flux. This clearly confirms the notion that in the N–rich growth regime the Al flux limits the growth rate and excess nitrogen desorbs, resulting in stoichiometric AlN layers. When the Al flux is raised above the N flux, thus entering the Al–rich growth regime, the Al coverage remains constant even up to an Al/N ratio of ~1.1. This proves directly that within this regime the N flux limits the growth rate and all excess Al desorbs from the surface, independent of the amount of excess Al. This self-regulated growth regime corresponds exactly to the intermediate growth regime found for GaN growth in Sect. 4.3. However, a further increase of the Al flux (> 4 nm/min) again leads to an increase in the Al coverage due to the accumulation of Al droplets on the surface. The existence of Al droplets is evidenced
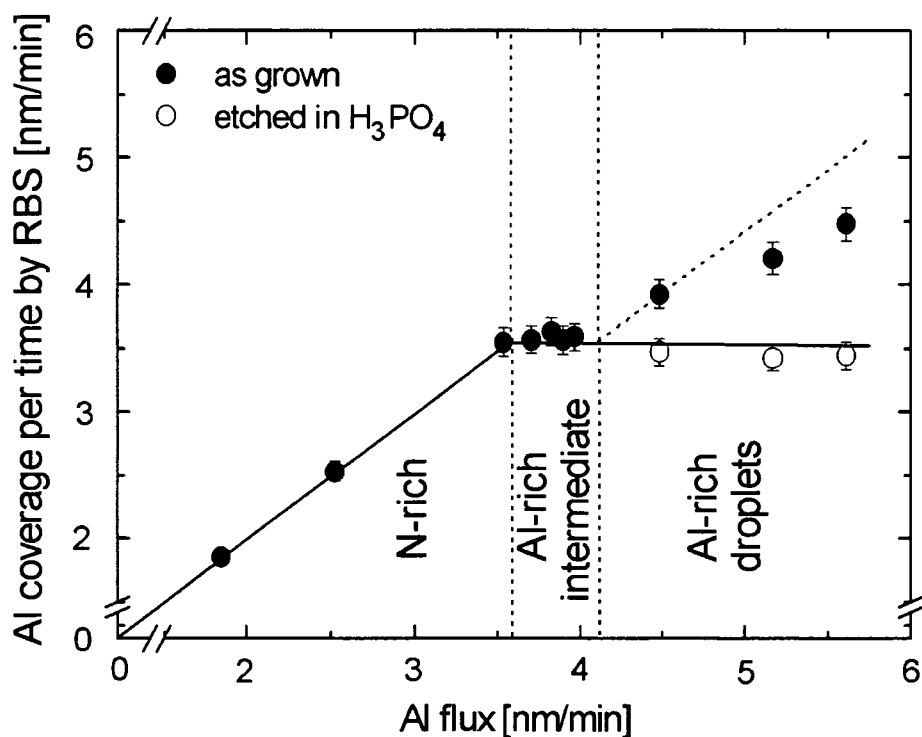

Fig. 9.1. Al coverage (closed circles) by Rutherford backscattering spectrometry as a function of Al flux for a series of AlN layers grown on sapphire at 810 °C and constant N flux of 3.6 nm/min. The Al coverage is found to be constant in the self-regulated intermediate regime, evidencing complete desorption of all excess Al. (Open circles correspond to AlN layers with Al droplets etched in acidic H_3PO_4.)

by the SEM topography of the AlN layer grown with the highest Al flux, as shown in Fig. 9.2. For the two samples with the highest Al flux, the Al coverage deviates slightly from the expected value given by the slope with gradient 1 (dotted line in Fig. 9.1.). This can be

attributed to an additional Al desorption from the droplets, a fact that has also been observed for Ga droplets on GaN (Sect. 7.3.). Etching the three AlN samples with Al droplets in H_3PO_4 selectively removes the Al droplets, affirming that in this regime the growth rate of the underlying AlN layer is limited by the N flux in the same manner as found for the intermediate regime.
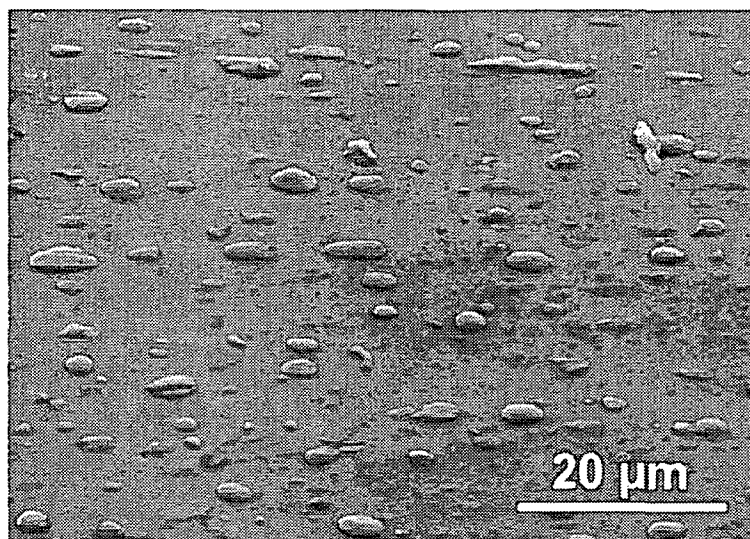

Fig. 9.2. Scanning electron micrograph of an AlN layer showing Al droplets of typical size.

9.2.2. AlN Surface Morphologies

Independently, the three proposed AlN growth regimes were also found by investigating the RHEED patterns and AFM surface morphologies under the various different growth conditions. For Al–deficient growth (Al/N < 1), where the Al flux limits the growth rate (as referred to the N–rich regime), the AlN layers exhibit spotty RHEED patterns [Fig. 9.3(A)], corresponding to diffraction through the surface asperities of the rough surface. When raising the Al flux beyond the N flux (Al/N > 1), a transition of the RHEED pattern to truncated streaks is observed, evidencing a surface with atomically smooth terraces [Fig. 9.3(B,C)]. AlN grown under Al–rich conditions at high temperature and with an intermediate Al flux yielding this type of surface structure, i.e. RHEED pattern, characterizes the intermediate growth regime. The boundary line between the N–rich and Al–rich intermediate regimes is defined by the transition from a spotty to a streaky RHEED pattern at the limit where the Al flux equals the N flux. From additional RBS thickness measurements of several AlN layers it was found that this boundary is independent of the growth temperature in the given temperature range of 775 – 820 °C. Considering thermal decomposition of AlN with a high activation energy of 5.4 eV [216] and a threshold temperature of ~1040°C [217], the observed temperature independence of growth rate can be accounted to a vanishing degree of decomposition in the investigated temperature range. For very high Al fluxes (Al/N >> 1), again excess Al accumulates on the surface during growth in the form of large droplets (with typical diameters of 1 – 10 µm and heights of 0.1 – 0.6 µm) (compare Fig. 9.2.). AlN layers grown in the Al–droplet

regime yield a RHEED pattern of low intensity contrast with hardly visible streaked diffractions due to shadowing effects of the Al droplets [Fig. 9.3(D)].
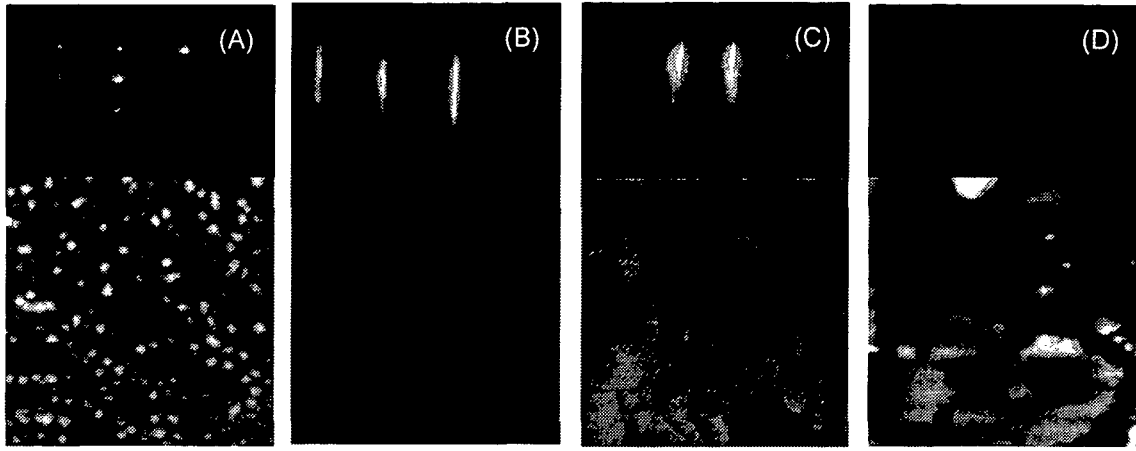

Fig. 9.3. RHEED patterns observed along the $[2\bar{1}\bar{1}0]$ zone axes and respective 1×1 μm^2 AFM images for AlN layers grown on sapphire at ratios of (A) Al/N = 0.9 (N–rich), (B) Al/N = 1.03 (intermediate), (C) Al/N = 1.05 (intermediate) and (D) Al/N = 1.12 (Al–droplet); the height scale between black (lowest) and white (highest) areas is 10 nm. AlN layer thicknesses are 100 nm in (A), (B) and (D) and 1 μm in (C). RHEED patterns and AFM images of AlN layers grown on SiC exhibit the same features.

By carefully distinguishing Al–rich grown AlN layers exhibiting droplets or not (by *ex situ* optical microscopy), a clear temperature dependence is found. In particular, the Al–droplet regime is separated from the intermediate regime by an exponential boundary line [Fig. 9.4(a)]. The Arrhenius plot in Fig. 9.4(b) shows the excess Al flux as a function of inverse growth temperature, which is independent of the growth rate. Data points referring to AlN layers with and without Al droplets are separated by a straight line. For this boundary condition the following equation was fitted to the experimental data

$$\phi^*_{Al} - \phi_N = 2.14 \times 10^{15} nm/min \times \exp\left(\frac{-3.41 \pm 0.13 eV}{kT}\right), \qquad (9.1.)$$

where ϕ^*_{Al} is the flux of Al at the boundary and ϕ_N is the N flux, both in units of nm/min, k is the Boltzmann constant and T is the growth temperature in Kelvin. It is obvious that for low growth temperatures (< 760 °C) excess Al can hardly desorb, thus forming metallic Al droplets on the surface. With increasing temperature much higher Al fluxes can be desorbed and droplet formation is limited to Al fluxes higher than ϕ^*_{Al}. In other words, the margin of the intermediate growth regime is very narrow at low temperatures (< 760 °C) and much broader at higher temperatures (> 800 °C). The slope of the boundary line for droplet formation follows an Arrhenius behavior with an activation energy that was determined to
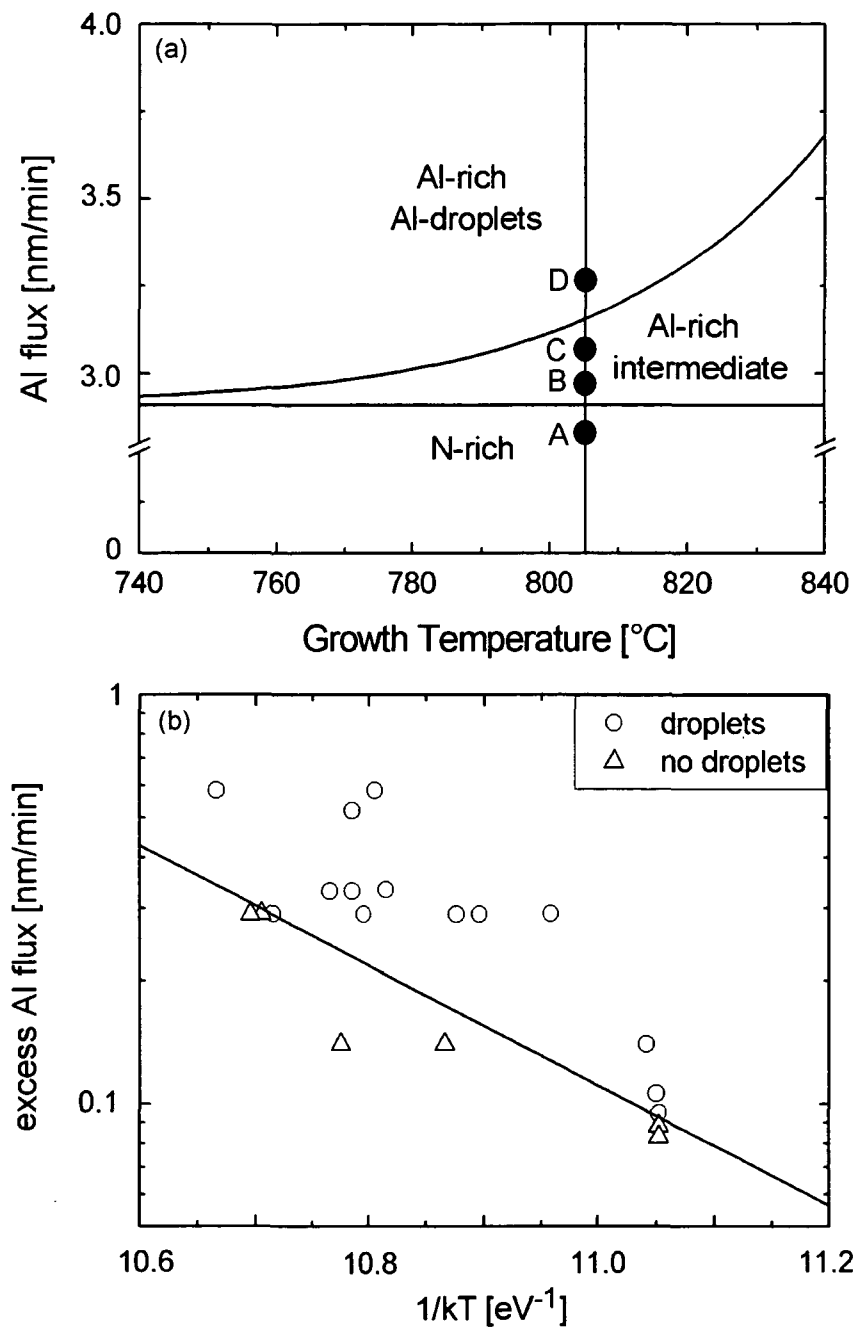
Fig. 9.4. (a) Growth diagram for AlN giving Al–fluxes and growth temperatures for the N–rich, intermediate and Al–droplet regimes at a constant N flux of 2.9 nm/min (circles labeled A–D correspond to the samples shown above in the RHEED patterns and AFM images). (b) Arrhenius plot of excess Al $(\phi^*_{Al} - \phi_N)$ in dependence of growth temperature defining a boundary line between layers exhibiting droplets after growth and those without droplets.

3.4 ± 0.1 eV. Note, that within the growth diagram of Fig. 9.4(a) both boundaries (between N–rich and intermediate regime, and between intermediate and Al–droplet regime) can be shifted along the Al flux axis by varying the N flux.

The AFM surface morphologies of the AlN layers grown in the respective growth regimes exhibit some large differences, as presented Fig. 9.3. The three 100 nm thick AlN layers grown on sapphire labeled A, B and D, are referred to the growth conditions as given in Fig. 9.4(a). The AlN layer grown in the N–rich regime [Fig. 9.3(A)] displays rough three–dimensional (3D) features. In this case, the root mean square (rms) roughness is as high as 1.4 nm over a $1 \times 1 \mu m^2$ scale. In contrast, Al–rich conditions with intermediate Al–fluxes produce an excellent smooth surface morphology with a rms roughness as low as 0.2 nm [Fig. 9.3(B)]. The surface morphology consists of coalesced two-dimensional (2D) platelets. These 2D–platelets are determined to have step heights of about 0.25 nm, which agrees well with the monolayer height of $c/2=0.249$ nm for bulk α-AlN. The surface of the AlN layer grown in the Al-droplet regime consist of a mesalike structure of uniform, atomically flat areas that are separated by pits and trenches [Fig. 9.3(D)]. The large Al droplets have typical diameters of 1-10 μm and distances of 5 – 20 μm and hence do not appear in the presented AFM image. However, miniscule humps (20 - 50 nm in diameter) are visible which could possibly be attributed to seeds of Al droplets. The area free of Al droplets exhibits a rms roughness of 0.9 nm over a $1 \times 1 \mu m^2$ scale. Peak-to-valley heights between pits and the flat mesas are in the range of 10–15 nm. Since the AlN layers analyzed above have a thickness in the order of 100 nm, further a 1 μm thick AlN layer was grown in the intermediate regime with an Al flux very close to the boundary line for droplet formation (Al/N=1.05). The larger film thickness was designated to assess wether definitely no metallic precipitates are formed on the surface in this regime. The resulting surface morphology in Fig. 9.3(C) is free of Al droplets and resembles the pitless 2D-like morphology of the 100 nm thick AlN layer grown in the same regime (sample B). It thus supports the fact that in the intermediate regime all excess Al desorbs and no Al droplets accumulates on the surface, leading to very smooth surfaces even for high thicknesses. Note, that the 1 μm thick AlN layer shows a rms roughness of only 0.3 nm over a $1 \times 1 \mu m^2$ scale.

What is most remarkable is the fact that AlN layers grown on 6H-SiC exhibit identical surface structures, i.e. morphologies and RHEED patterns, to those grown on sapphire when grown in the same regimes. This is not that surprising, considering that on both substrate materials AlN yielded a surface of Al-polarity. The polarity was confirmed by comparing RHEED patterns and polarity selective wet chemical etching behavior in a hydroxide solution of subsequently grown thick GaN layers. For both sapphire and SiC, a 2×2 RHEED recon-struction for GaN grown on AlN was observed, which is characteristic of a Ga-face (0001) surface [12]. Moreover, a Ga-face surface, is also specified by its resistance to wet chemical etching as proposed by Seelmann-Eggebert *et al.*[28]. After a 30 min exposure to a 10-molar KOH solution, no signs of etching were visible as confirmed by subsequent morphology stu-dies using AFM. Since wurtzite GaN proceedes to grow on the c-plane of the wurtzite AlN sublayer with Al atoms only being substituted by Ga atoms, it can be deduced that the Ga-face (0001) surface in GaN thus displays the Al-face (0001) surface of its AlN sublayer [34].

Therefore, the established growth diagram is completely independent of the investigated substrate materials and is only determined by the growth kinetics.

9.2.3. Nitridation of AlN Surfaces

Al droplets are detrimental for the subsequent growth of device layers in that they roughen the interface and may cause metallic precipitates in the layers. Thus, the current aim was to propose an *in situ* method to remove all Al droplets from the AlN surface. Such an objective can be approached for instance by a postgrowth nitridation step. By keeping the N shutter open after growth for ~10 min at a temperature equal to the AlN growth temperature, all metallic Al droplets were transformed into additional AlN, as confirmed by optical microscopy and an increase of the AlN thickness according to RBS measurements. Also, the topmost AlN surface layer undergoes a transition from a low contrast streaky RHEED pattern to a superposition of streaks and Bragg spots [see Fig. 9.5]. In comparison, AlN layers grown in the N-rich and intermediate, near-stoichiometric regimes show no change in the RHEED pattern during this nitridation process due to the lacking metallic Al droplets (therefore not shown here). In consistence with RHEED observations, post-growth nitridation leads to a change in surface morphology for AlN layers grown in the Al-droplet regime, as also demonstrated in the AFM image of Fig. 9.5(b). In this case, the nitridation procedure has an adverse effect on the surface morphology by additional surface roughening due to the transformation of metallic Al into AlN clusters. Note, that by comparing the AFM image of Fig. 9.5(a) with the nitridated surface of Fig. 9.5(b) a major increase in rms roughness up to 3.8 nm was determined over the same lateral scale.
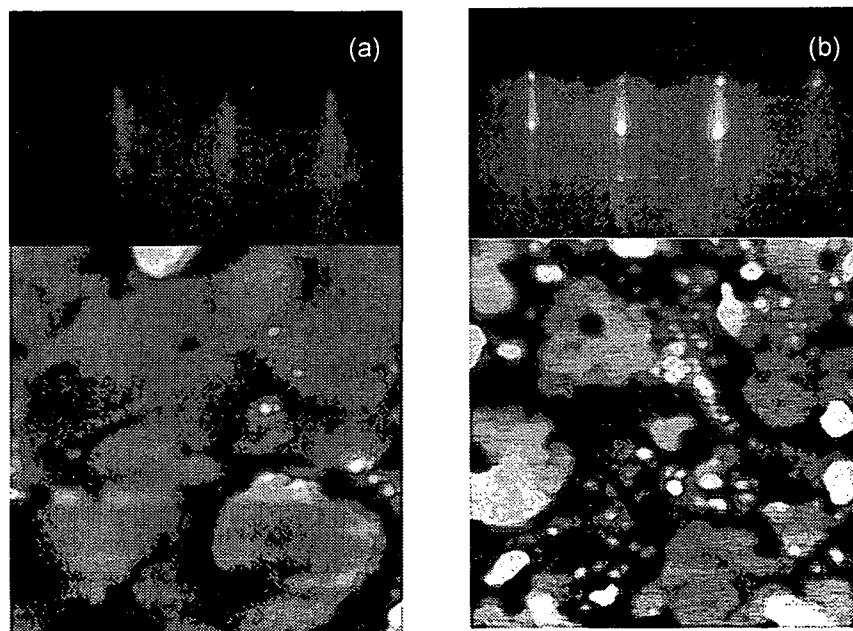

Fig. 9.5. RHEED pattern along the $[2\bar{1}\,\bar{1}\,0]$ zone axes and $1 \times 1\ \mu m^2$ AFM image (height scale is 10 nm) of AlN grown in Al-droplet regime (a) (sample D) and (b) after a 10 min postgrowth nitridation step. Note, the increased rms surface roughness of 3.8 nm by nitridation.

Furthermore, a second *in situ* approach for the removal of Al droplets was investigated by applying post-growth annealing in vacuum at the highest possible substrate temperatures, i.e. at about 830 °C. The practical annealing times of 10-20 min, however, did not appear to desorb the Al droplets effectively, as confirmed by subsequent optical microscopy.

9.2.4. Discussion

The presented results evidence that the growth of AlN by MBE is strongly influenced by the Al/N ratio and the growth temperature, in an equivalent manner as for the growth diagram of GaN (Sect. 4.3.) [116]. Only slight changes of the growth conditions produce distinctive changes in the surface structure. The characteristic surface structures, i.e. RHEED patterns and surface morphologies, for these regimes were reproducible and independent of film thickness. The morphologies were also found to be independent of the chosen substrate material, SiC or sapphire, despite the different strains in AlN originating from differing lattice mismatches (- 1% for SiC and −11.7% for sapphire). From a general perspective, the growth of AlN is qualitatively equivalent with the GaN growth diagram, distinguished merely by a few exceptions: the boundary line of droplet formation shows an activation energy of 3.4 eV, which as expected is significantly higher than the one found for GaN (E_A= 2.83 eV) [116]. In the present AlN study, the value for this activation energy agrees well with the evaporation energy of Al over liquid Al (E_A= 3.27 eV), as derived from equilibrium Al vapor pressure data [117]. It is thus acceptable to describe the activation energy as the maximum group-III flux for desorption from the free metallic group-III element. Therefore, the entity $\phi_{Al}^* - \phi_N$ in equation (9.1.) describes the maximum Al flux desorbing from metallic Al on the AlN surface, which rises exponentially with temperature. Due to the higher activation energy for Al desorption compared to the one for Ga desorption, the boundary line for droplet formation appears much flatter and nearly horizontal for AlN in the temperature range used for GaN growth. This corresponds to the vapor pressure of Al being one order of magnitude lower than the vapor pressure of Ga. Therefore, in order to perform optimum growth of AlN in the intermediate regime, the Al flux is limited to almost near-stoichiometric conditions, since at usual growth temperatures of 775-820 °C and growth rates an Al flux of merely 3-14% in excess of the given N flux already generates Al droplets. The limitation in temperature is particularly stringent when growth of GaN is also involved, i.e. as in GaN/AlN superlattices or GaN/AlN stacked QD structures. In such cases, the growth temperature needs to be even lower, since at temperatures above 760 °C significant decomposition of GaN takes place (> 0.2µm/h), as demonstrated in Sect. 4.5.

Associated with the different growth regimes are distinct morphology transitions from three-dimensional to two-dimensional, as found between N-rich and Al-rich growth. This change in morphology between N-rich and metal-rich growth conditions was only recently observed in the case of AlN by Ferro *et al.*[218], while it has been widely studied and is considered well understood for the case of GaN [25,26,116,219]. As for GaN growth, it can be suggested that also for AlN layers the change in morphology is strongly governed by the varying surface adatom mobilities present under N-rich versus Al-rich conditions. Under N-

rich conditions, the rough three-dimensional surface morphology results from the low Al adatom surface mobility. It is assumed that the Al-polar surface is predominantly terminated by N atoms, with each N atom being bonded to an Al atom leaving three dangling bonds behind [25]. This high density of dangling bonds is believed to limit surface migration of Al adatoms substantially, that could only be promoted by breaking the strong Al-N bonds (binding energy E_b = 2.88 eV [220]).

Based on surface energy calculations for GaN [19], it is likewise speculated that for AlN growth under Al-rich conditions the excess Al adatoms form a saturated surface of about 1-2 monolayers of Al. The chemisorbed adatoms may be bonded via weak, metallic Al-Al bonds forming a metallic film on the growing surface and reducing the energy barrier for surface migration of N atoms. Thus, the N adatoms exploit higher surface diffusion lengths and can move to a preferable incorporation site, resulting in the observed smooth two-dimensional growth morphology, as shown in Fig. 9.3(B-D). However, surface morphologies between the intermediate and Al-droplet regime differ slightly by the density of forming pits. AlN films grown in the intermediate regime exhibit no pits at all, while a finite density of pits occurs for growth in the Al-droplet regime. It is important to note, that pit formation in AlN is at odds with the observations for GaN (Sect. 6.5), where the pit density decreased at the transition from the intermediate to the Ga-droplet regime by planarizing all pits. Further investigations will be needed to address the mechanisms responsible for these contrary morphology features.

The post-growth nitridation process introduced, in order to remove detrimental Al droplets from the AlN surface, was found to change the surface morphology adversely. To address the formation of the AlN clusters from Al droplets during nitridation and the resulting surface roughening, it is suggested that this type of morphology is a consequence of the reduced surface mobility present under the N-rich like conditions during nitridation. In general, AlN is known to be a very stable material due to the strong Al-N bonds, which affirms the notion that any surface rearrangement during nitridation in the given temperature range (< 830 °C) can only be attributed to the fact that elemental Al is turned into AlN. In this context, it was shown by *ex situ* annealing experiments of AlN that only at temperatures above 1050 °C the structural and morphological properties were effected, which is in consistence with results reported by Vaillant et al. [221] and George *et al.* [222].

Moreover, the attempt to remove Al droplets by an *in situ* post-growth annealing step was not successful. This is a consequence of the low Al vapor presssure that impedes desorption by large extent as compared to the more readily desorbable Ga at identical temperatures. It can be also assumed that the Al desorption rate from Al droplets is enormously decreased as compared to the steady state value during growth. After growth the metallic Al adlayer of ~1-2 ML might be flashed off quickly, restricting the effective area, from which Al can desorb, to the surface of the remaining droplets. From Fig. 9.2 this fraction of the total surface can be estimated to about 1/10, that would increase the desorption time to basically impractical duration.

9.3. Initial Stages of GaN Growth on AlN

9.3.1. GaN Nucleation dependent on AlN Surface Termination

In the following, the influence of the AlN surface termination will be further investigated, particularly with respect to the nucleation and growth of GaN on top. As evaluated in Sect. 9.2, there are three distinct AlN surface terminations, (a) a rough and Al adlayer–free surface achieved under N–rich conditions, (b) an Al adlayer–stable smooth surface produced under slightly Al–rich conditions, and (c) an AlN surface with macroscopic Al droplets as a consequence of very Al–rich growth. GaN growths on these three characteristic AlN surfaces were performed under identical conditons of T_S = 730 °C, a N flux of 2.5 nm/min and a flux ratio of Ga/N=1.4, yielding slightly Ga–rich intermediate growth conditions. Prior to each growth, the AlN surfaces were annealed in the Ga flux only, in order to avoid the characteristic transient of the Ga flux after opening (similar to the heteroepitaxial GaN nucleation experiments performed on 6H–SiC and Al_2O_3 in Sect. 8.4). The annealing temperature was identical to the subsequent growth temperature (i.e. 730 °C) and the annealing time was set to about 22 min, long enough for the Ga flux to stabilize. Subsequent GaN growth was established by opening the N shutter.
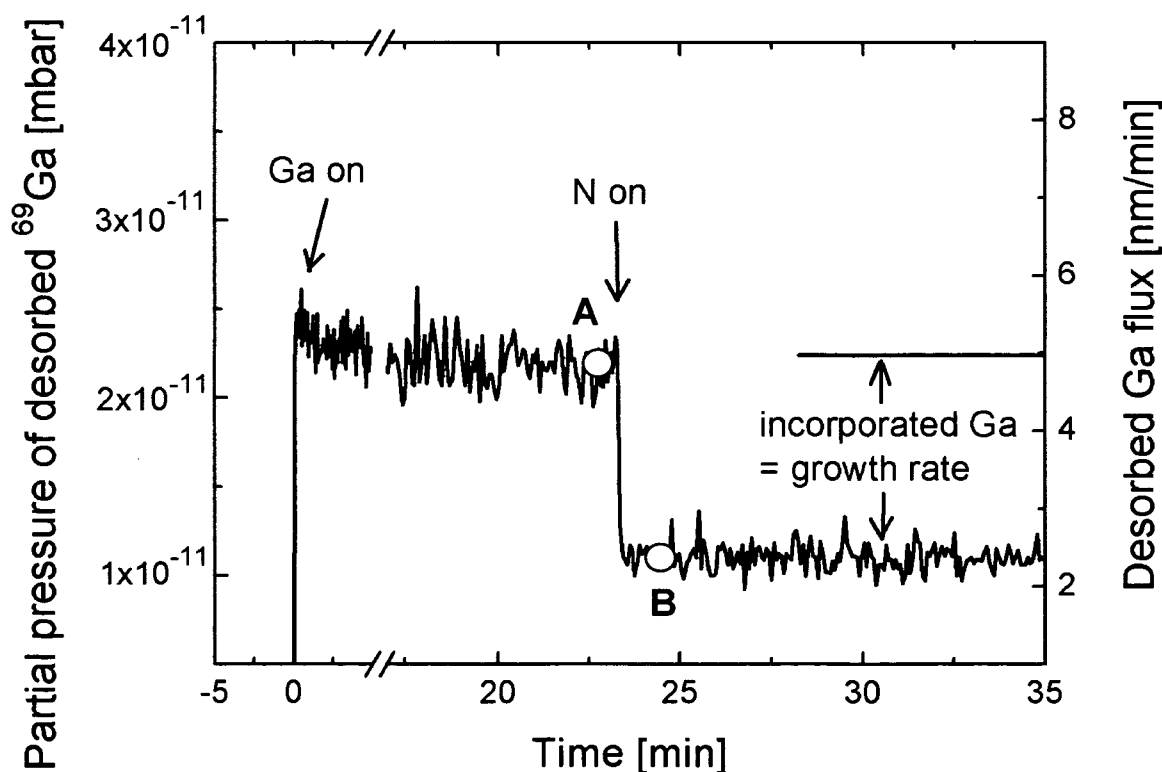

Fig. 9.6. Desorbing Ga flux during the Ga annealing step and the initial GaN growth phase (N shutter open) on AlN grown at Al/N = 0.9. The difference between the two levels of Ga desorption during Ga annealing and GaN growth represents the actual growth rate. The labels A and B are referred to the surface morphologies presented in Fig. 9.7, in correlation to the QMS experiment.

First, the GaN nucleation behavior is investigated on an AlN template grown on sapphire under a flux ratio of Al/N = 0.9. When opening the shutter, one observes initially an abrupt increase in the Ga desorption signal to a level where all the impinging Ga atoms (Ga flux = 5 nm/min) desorb again [Fig. 9.6].

After this annealing step, GaN nucleates immediately, evidenced by the sharp drop in Ga desorption upon opening of the N shutter, resembling strongly the behavior observed for the case of GaN homoepitaxy (Sect. 8.4). This means that the full GaN growth rate is reached right at the beginning of growth and no nucleation delay is observed. One can understand this instant nucleation behavior easily, when considering the high number of dangling bonds per N atom (i.e. 3) that terminate the AlN surface and the high density of AlN step edges. Both can be made responsible for the high incorporation rate of Ga atoms at the initial stage of GaN growth. In this first case, the AlN layer exhibits a clear 3D morphology as shown by the AFM image and RHEED pattern in Fig. 9.7(a). This morphology along with the spotty RHEED pattern prevails when nominally 4 ML of GaN are grown on such a surface [Fig. 9.7(b)], meaning that GaN nucleates in a 3D–island (Volmer–Weber) mode.
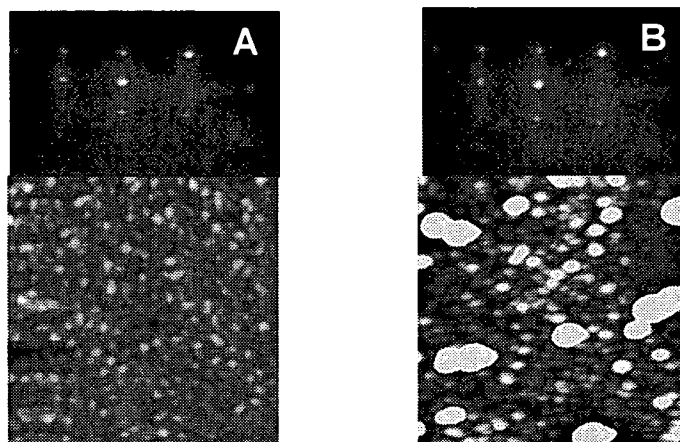

Fig. 9.7. RHEED patterns along the $[2\bar{1}\bar{1}0]$ zone axes and $1 \times 1\,\mu m^2$ AFM images (height scale is 10 nm) of (A) the starting AlN layer grown at Al/N = 0.9 (N–rich regime) and (B) 4 ML of GaN grown on top, which nucleates instantly in the form of 3D–islands.

A quite different situation occurs when GaN nucleates on an AlN template grown on sapphire under slightly Al–rich conditions of Al/N = 1.03. Whereas the Ga desorption during the Ga annealing step remains the same [Fig. 9.8] compared to the previous case, the actual nucleation of GaN follows a two–step process. First, the Ga desorption decreases (i.e. the growth rate increases) linearly to approximately 2/3 of the final steady–state value, and then at nominally 2.5 ML it changes to an exponential decline.
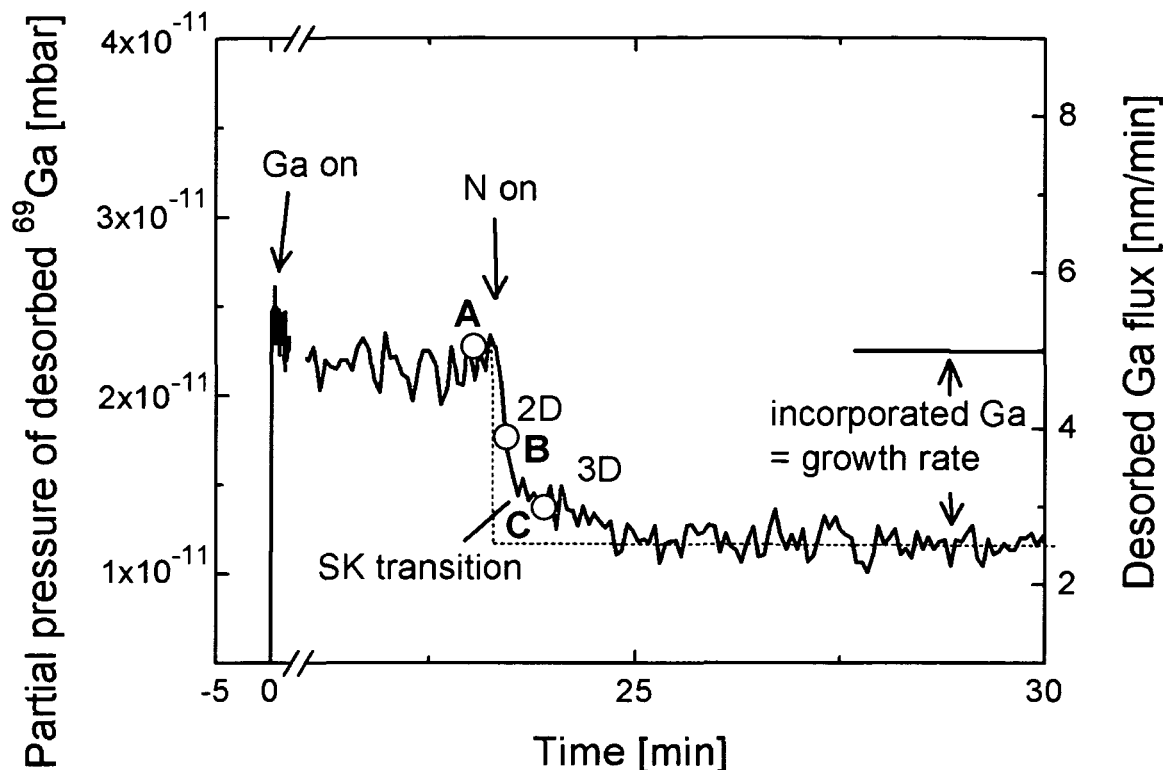
Fig. 9.8. Desorbing Ga flux during Ga annealing and the GaN nucleation stage (N shutter open) on AlN grown at Al/N = 1.03. The drop of the Ga desorption during GaN growth represents the actual growth rate and changes from linear to exponential during the Stranski–Krastanow (SK) transition. The labels A, B and C are referred to the surface morphologies presented in Fig. 9.9.

The point where the growth rate changes from linear to exponential coincides also with a morphology transition from 2D-to-3D growth, evidenced by the AFM images and the streaky-to-spotty RHEED transition in Fig. 9.9. The growth of GaN on an initially flat 2D AlN surface [Fig. 9.9(A)] results first in a 2D-islandlike structure with monolayer step heights which coalesce into a coherent 2D layer [Fig. 9.9(B)]. By passing over to the exponential regime, distinct 3D-islands appear [Fig. 9.9(C)]. In detail, this growth mechansim represents the Stranki–Krastanow (SK) mode, meaning that initially a highly strained 2D wetting layer builds up, which beyond a critical thickness relaxes elastically by the formation of 3D islands, i.e. quantum dots (QDs).

When integrating the desorbing Ga flux (i.e. 1/growth rate) over time (equal to the area below the desorbed signal and the dotted lines in Fig. 9.8), there is a loss in film thickness that totals 0.9 nm. It is worth noting that this material loss during nucleation is much smaller than in the case of GaN growth on SiC or sapphire (d_{loss} = 8 ± 1.5 nm). By this evaluation, also the actual critical thickness for GaN on AlN is therefore lower than nominally expected, being only 1.6 ML instead of 2.5 ML. The loss in film thickness has also been confirmed by subsequent RBS measurements of the GaN coverage, analogous to the procedure in Sect. 8.2. The increased Ga desorption during the linear 2D growth regime can be explained by a less pronounced form of incomplete wetting caused by an energy barrier for nucleation, as proposed for the

cases of GaN growth on sapphire an SiC. However, the exponential regime occurs at a stage where the surface is already covered by a coherent layer of GaN, and should therefore rather resemble the case of homoepitaxy (see Sect. 8.4). The only obvious reason for the growth rate to differ from the final steady–state value is the different strain state in the 3D–islands, which will be investigated closer in the next section.
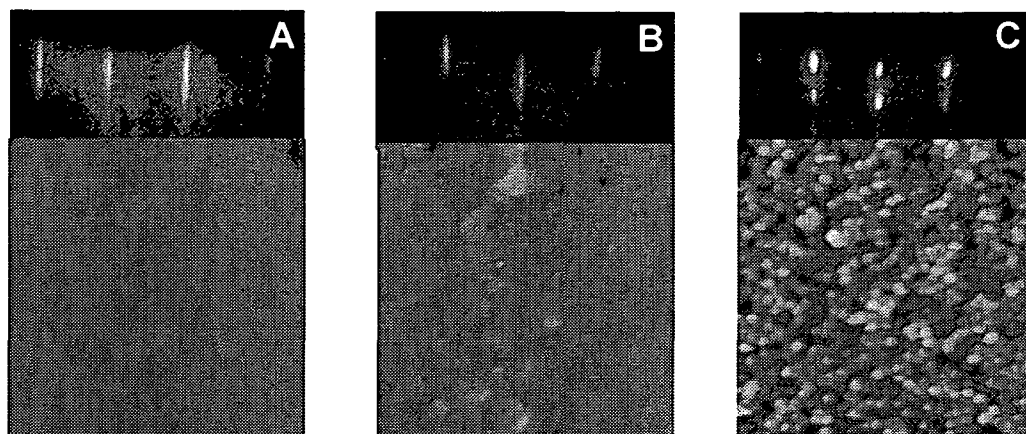

Fig. 9.9. RHEED patterns along the [2$\overline{1}$ $\overline{1}$0] _zone axes and_ $1 \times 1\,\mu m^2$ _AFM images (height scale is 10 nm) of (A) the starting AlN layer grown at Al/N = 1.03 (Al–rich intermediate regime), (B) 1 ML of GaN grown on top, which nucleates as a 2D layer and (C) 4 ML of GaN transformed into distint 3D–islands._

In the third case, where GaN nucleates on an AlN template grown under Al–droplet conditions of Al/N = 1.12, the Ga desorption underlies a very complicated behavior [Fig. 9.10]. In close detail, when the Ga shutter is opened in order to anneal the AlN template, the Ga desorption does not rise instantly to the level corresponding to full desorption of the impinging Ga atoms, as characteristic for the two previous cases. Instead, the Ga desorption increases only gradually to the full steady–state desorption level. Another substantial difference arises when GaN growth is initiated by opening of the N shutter. Here, the Ga desorption does not drop as observed earlier, but it remains constant for a short period. Subsequently, the Ga desorption even rises and goes through a maximum, before finally decreasing to the steady–state level that represents the final GaN growth rate. In fact, this indicates a very long nucleation delay for actual GaN growth, which was also determined from postgrowth thickness measurements. For GaN growth stopped for instance at label B [see respective morphology in Fig. 9.11 (B)], the actual GaN coverage was determined to 1.6 nm (= 6 ML) by RBS, in contrast to nominally 17 nm, calculated by assuming entirely linear growth from the point where the N shutter was opened. The RHEED and AFM images in Fig. 9.11 point out, that even on an AlN layer with Al droplets covering the surface, an initial 2D growth mode of GaN leads to a Stranski–Krastanow (SK) mode and 3D islands (QDs), though with a huge delay time. The SK (streaky–to–spotty RHEED) transition for this specific case has occurred when the Ga desorption was past the maximum and below the steady–state level typical during Ga annealing (indicated by the grey circle). It is also important to note, that the final GaN island surface is free of any Al droplets that terminated the surface before growth.
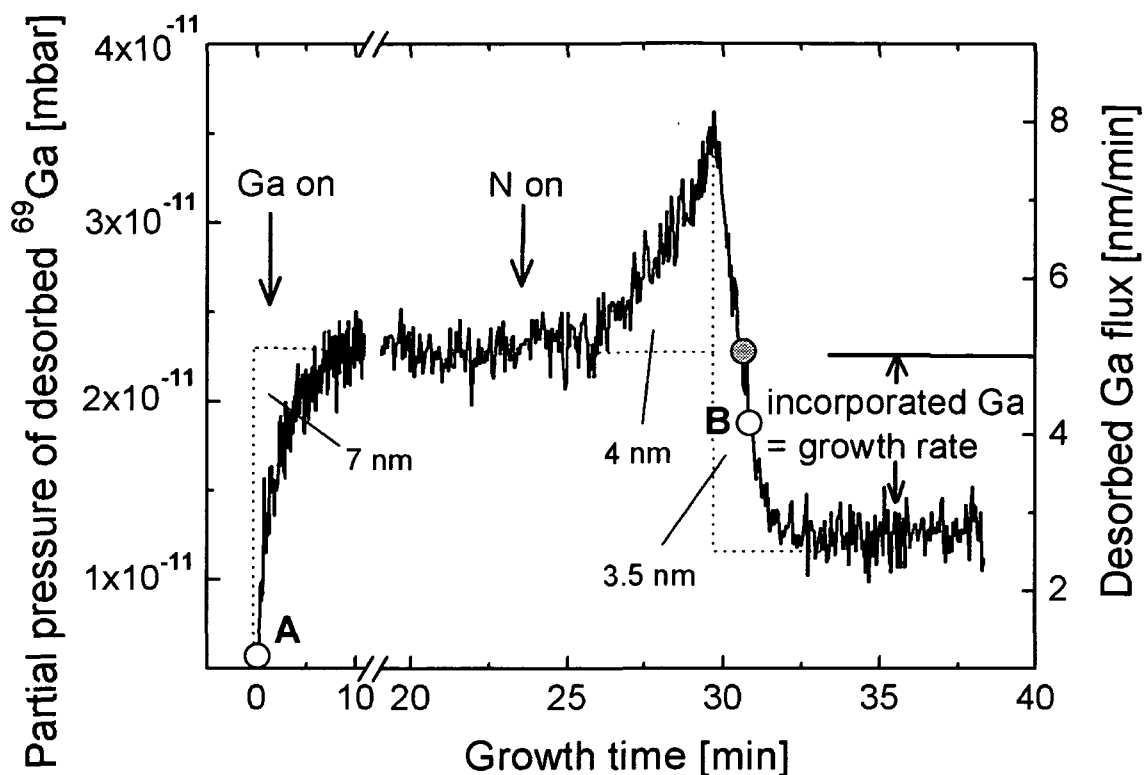
Fig. 9.10. Desorbing Ga flux during Ga annealing and GaN growth on AlN grown at Al/N = 1.12. GaN nucleation is extremely delayed, indicated by the grey point where Ga desorption is past the maximum and starts to drop below the initial steady–state desorption level. The labels A and B are referred to the surface morphologies presented in Fig. 9.11.
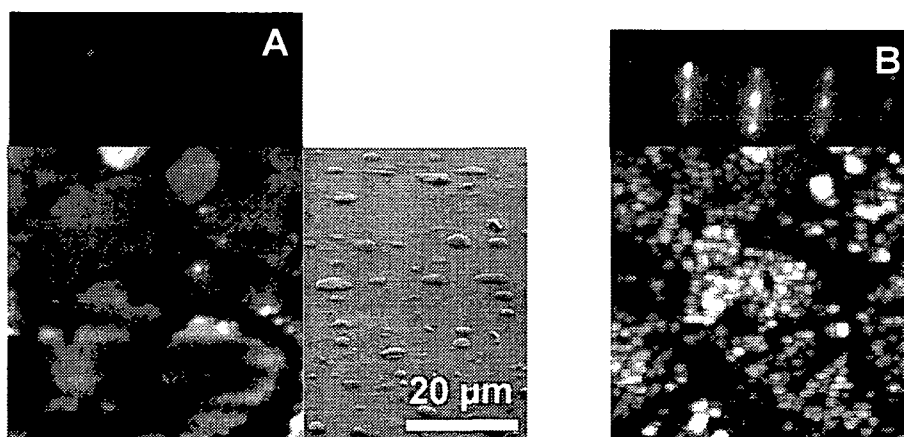

Fig. 9.11. RHEED patterns along the [2$\bar{1}$$\bar{1}$0] zone axes and $1 \times 1\,\mu m^2$ AFM images (height scale is 10 nm) of (A) the starting AlN layer grown at Al/N = 1.12 (Al–rich droplet regime) showing also a SEM surface covered by Al droplets (to the right), (B) 6 ML of GaN grown on top, which nucleates by an SK mode as 3D islands and a huge time delay.

To explain the huge delay time for GaN nucleation and the complicated Ga desorption features of Fig. 9.10, the following model was set up to depict the fundamental mechanisms in an atomistic view [Fig. 9.12]. The starting point is represented by an AlN surface covered with Al droplets [Fig. 9.12(a)]. When Ga is supplied to the surface during the annealing step, initially a reduced Ga desorption was observed, that can be attributed to an enhanced dissolution of Ga atoms in the Al droplets [Fig. 9.12(b)]. However, when a critical dissolution of the Al/Ga alloy is reached, all arriving Ga atoms desorb again, yielding an adsorption/desorption equilibrium [Fig. 9.12(c)], as characteristic during the entire Ga annealing step in the cases where the AlN surface was grown under N–rich and intermediate growth conditions. When the N shutter is opened, instead of a drop in the Ga desorption the Ga adsorption/desorption equilibrium persists. Since the Al–N bond (11.67 eV/atom pair) is much stronger than the Ga–N bond (9.06 eV/atom pair), it can be assumed that N is preferentially bonded to Al from the Al droplet reservoir [Fig. 9.12(d)] and no Ga is incorporated yet. This means that additional AlN is grown by consumption of the Al droplets, which was also confirmed by RBS thickness measurements of Al droplets containing AlN layers grown with GaN on top. The growth of additional AlN is indicated by the hatched area, that increases in thickness from Fig. 9.12(d) to (f), in accordance with the continuous depletion of the Al droplet reservoir. The depletion of Al droplets enables the dissolved Ga to desorb, which is indicated by the gradual rise desorption in Fig. 9.10. Ga desorption reaches a maximum at the
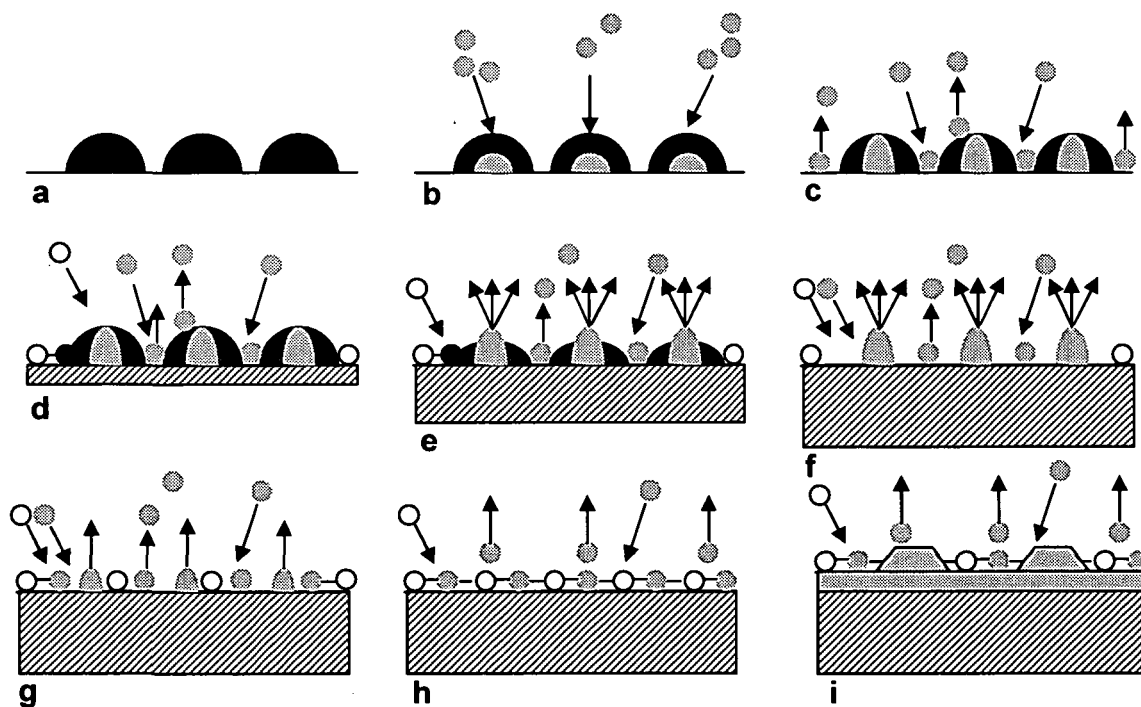

Fig. 9.12. Atomistic model of Ga adsorption and desorption processes during Ga annealing and GaN nucleation on an AlN surface covered with Al droplets. Al droplets and atoms are indicated in black, Ga in light grey, N atoms are white, and the additional AlN layer grwon from Al droplets is presented by the hatched area, while the GaN material grown is shown in grey.

point where no Al droplets are left on the surface, as there is no more energy barrier for the previously dissolved Ga atoms to overcome [Fig. 9.12(f)]. Since no Al is left on the surface, the N atoms can now be consumed by the arriving Ga atoms [Fig. 9.12(g),(h)], allowing the Ga desorption to decrease (compare Fig. 9.10). Finally, GaN growth procedes by a SK growth mode, meaning that an initally 2D wetting layer transforms into 3D–islands [Fig. 9.12(i)] as also observed by RHEED. The time that passed from the opening of the N shutter to the actual decrease in Ga desorption equals the delay time for GaN nucleation which is therefore a direct function of the amount of Al droplets covering the initial surface. When performing careful mass balancing (i.e. integrating the areas of adsorbed and desorbed Ga atoms during the annealing step and the GaN nucleation phase), as indicated by the dotted lines in Fig. 9.10, it is astounding that the initial amount of Ga stored in the Al droplets is completely desorbed again once the Al droplet reservoir is depleted. In detail, initially a Ga amount of 7 nm equivalent film thickness is dissolved in the Al droplets, which matches exactly the desorbed amounts of 4 nm (until maximum Ga desorption) plus the 3.5 nm during decreasing Ga desorption until the steady–state GaN growth rate is reached. Along with the *ex situ* RBS measurements of the additionally grown AlN layer from the Al droplet reservoir, the mass balanced Ga desorption features support strongly the proposed atomistic model, yielding also an estimate of the Al/Ga alloy ratio of approximately 1:1.

9.3.2. GaN Nucleation as a Function of the Growth Kinetics

9.3.2.1. Strain Relaxation induced Growth Rate Changes

In the previous section it was demonstrated that under certain growth conditions a Stranski–Krastanow (SK) growth mode can be achieved, that is accompanied by a change in growth rate at the critical thickness, where a compressively strained 2D wetting layer is transformed into relaxed 3D–islands. To evaluate the growth window where such a SK transition of GaN on AlN can occur (i.e. depicting the conditions for GaN QD growth), in the following a series of GaN growths was performed as a function of the growth kinetics. According to the GaN growth diagram of Fig. 9.13, the Ga/N flux ratio was set to constant 1.4 at a N flux of ~ 2.5 nm/min, whereas the growth temperature was varied from 670 to 740 °C. The ~0.3 μm thick AlN templates were grown under near–stoichiometric conditions on sapphire, yielding the typically smooth surface morphologies as found in Sect. 9.2.2. Thus, optimum prerequisites regarding the AlN template and further GaN growth are guaranteed, and the other two special cases found in Sect. 9.3.1 (N–rich grown and Al–droplet AlN) are not treated here.

In Fig. 9.14 the desorbing Ga flux and hence the initial growth rate during the nucleation stage of GaN is shown for growths performed directly on the AlN templates at four different growth temperatures (in the range of 670 – 740 °C). Prior to the nucleation of GaN the AlN templates were annealed in a Ga flux (not shown in the viewgraphs), similar to the procedure in Fig. 9.8 of Sect. 9.3.1. When the N shutter is opened and GaN starts to nucleate, in all cases one observes an immediate drop in the Ga desorption. This means that GaN
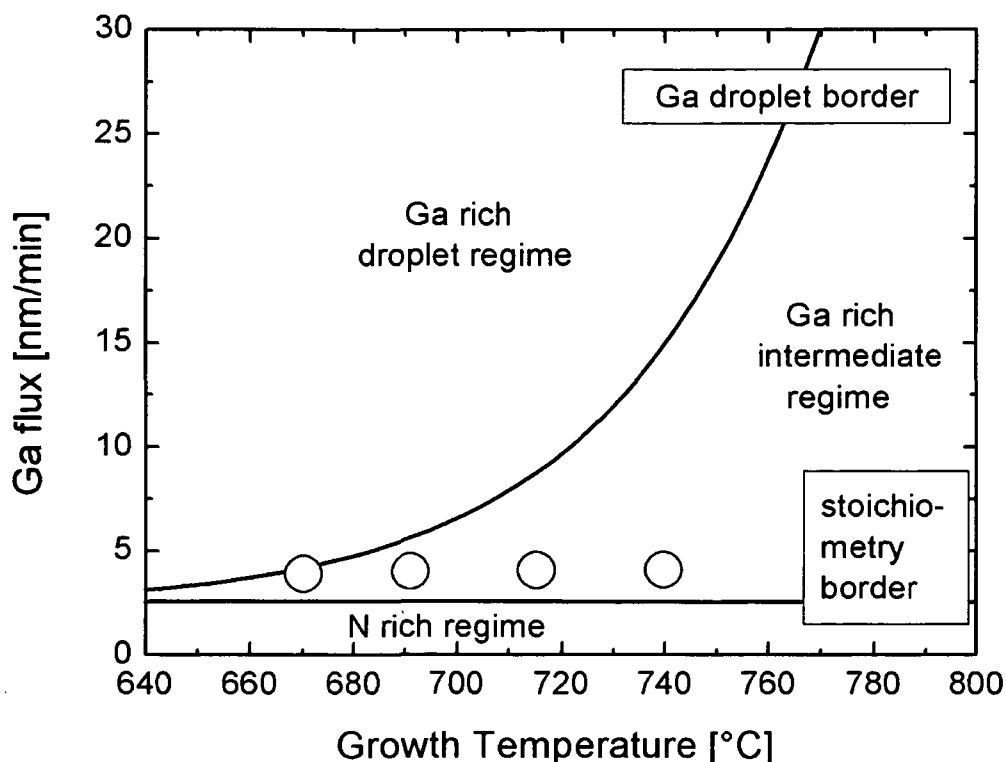
Fig. 9.13. GaN growth phase diagram showing the four selected growth temperatures (670 °C, 690 °C, 715 °C, 740 °C) and otherwise constant conditions of Ga/N ratio = 1.4 and N flux = 2.5 nm/min.

nucleation happens instantly and as expected no delay occurs as there are no metallic Al precipitates or droplets on the AlN surface. However, depending on the chosen growth temperature, there are some distinct GaN nucleation features, which will be investigated in more detail. At the highest temperature of T_S = 740 °C [Fig. 9.14(a)], the Ga desorption and the growth rate reach the final steady–state value at about 2 ML of nominal GaN growth, corresponding to typical values for the critical thickness (2.0–2.7 ML) for the SK transition in the GaN/AlN system [207,223]. When the growth temperature is lowered to T_S = 715 °C and T_S = 690 °C respectively, a linear–to–exponential growth rate transition is obtained at the critical thickness of ~ 2ML of GaN, as was also found in the previous section. For both these selected temperatures the final GaN growth rate is approached only gradually at about 16 ML of nominal GaN growth. It is important to note, that the increased Ga desorption during the exponential growth regime indicates a significant impeded GaN incorporation, in contrast to the previous high–temperature case, where the exponential regime does not occur and GaN incorporation is more enhanced. Finally, for the lowest temperature of T_S = 670 °C, where the growth conditions are close to the Ga droplet border, GaN nucleates even faster and reaches the steady–state growth rate almost instantly.
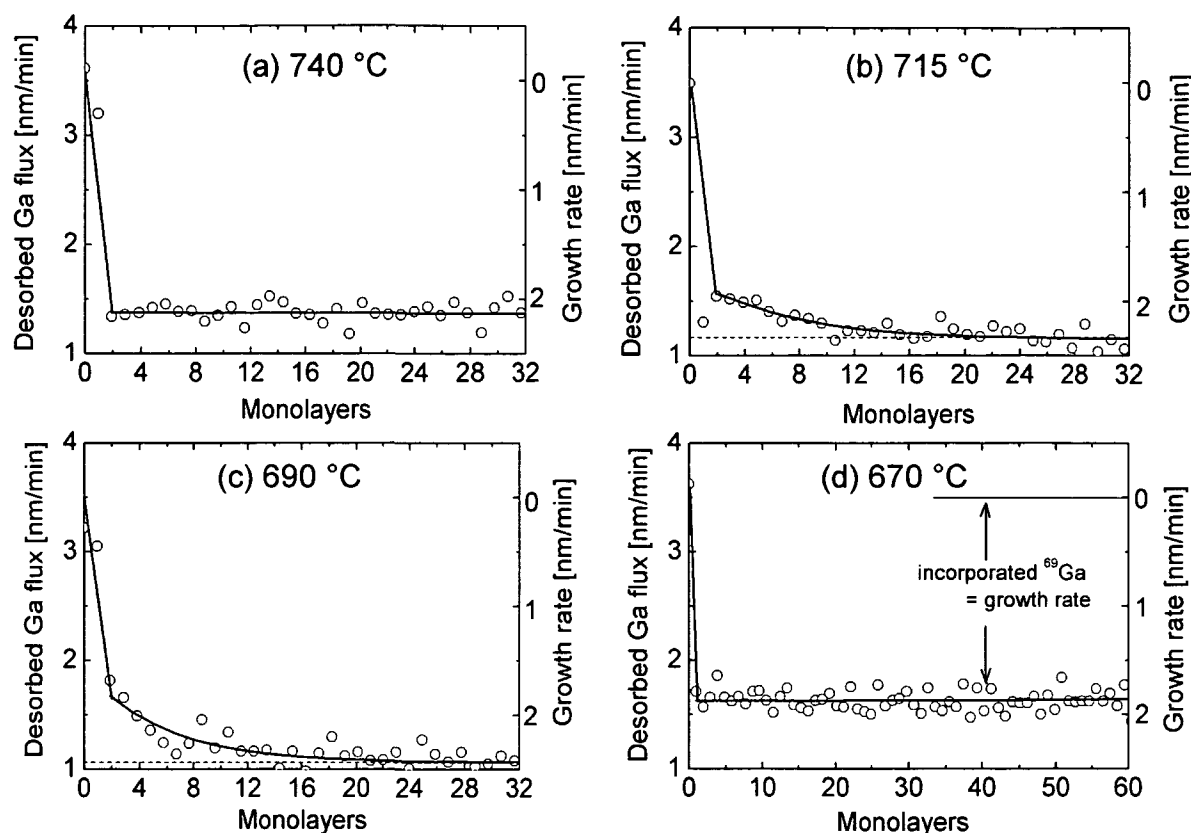
Fig. 9.14. Ga desorption and growth rate during the initial stages of GaN growth on optimized AlN at constant Ga/N = 1.4 and four different growth temperatures (a) 740 °C, (b) 715 °C, (c) 690 °C and (d) 670 °C. Note, at intermediate temperatures the growth rate follows a linear–to–exponential transition, symptomatic for the 2D-to-3D morphology transition during the Stranski–Krastanow growth mode as also found in Figs. 9.8 and 9.9.

To correlate the observed growth rate evolution with the degree of strain relaxation during the SK transition, for all the above experiments the in-plane lattice parameter a was simultaneously recorded *in situ* by measuring the RHEED lattice spacing between two adjacent streaks. The results are shown in Fig. 9.15, where the a lattice parameter can vary from a pseudomorphic GaN layer (i.e. fully strained to the lattice of the underlying AlN, $a =$ 3.12 Å) to a fully relaxed GaN layer with its native lattice constant of $a = 3.19$ Å. The difference between the two lattice parameters (pseudomorphic and relaxed) give exactly the literature value for the lattice mismatch for the GaN/AlN system $\Delta a/a = 2.4\%$, as also obvious on the right hand axis of Fig. 9.15. As is clearly observable, for the highest temperature ($T_S =$ 740 °C) the a lattice parameter of GaN remains identical to that of AlN ($a = 3.12$ Å) during the first 2 ML of GaN growth, meaning that a fully strained wetting layer builds up. The strained wetting layer has a 2D morphology, as evidenced by the streaky RHEED pattern of Fig. 9.16. When exceeding the critical thickness of approximately 2ML of GaN, instant elastic relaxation occurs (SK transition) and the value for the fully relaxed a lattice parameter of GaN is reached. Simultaneously, the RHEED pattern transforms from a streaky to spotty pattern
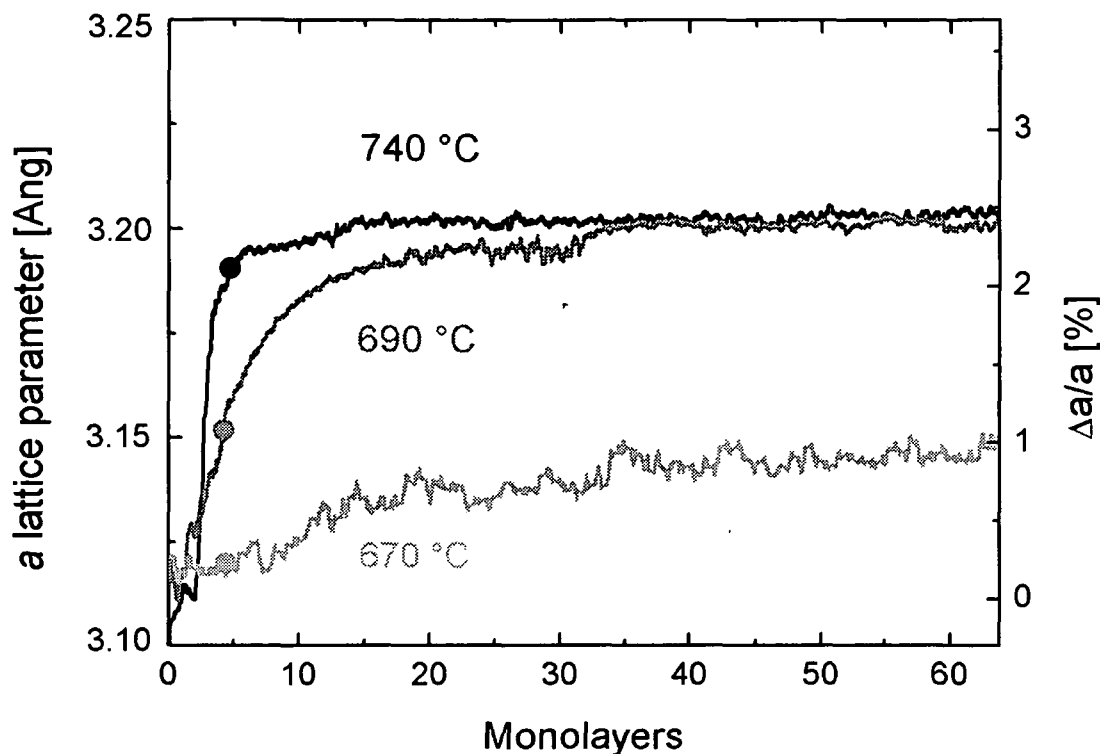
Fig. 9.15. In plane a lattice parameter variation observed by RHEED during the growth of GaN on AlN as a function of GaN coverage and growth temperature. A GaN lattice parameter of a = 3.12 Å indicates a fully strained layer, whereas a = 3.19 Å is typical for a completely relaxed layer. For temperatures above 690 °C, elastic relaxation beyond 2ML of GaN is governed by the SK growth mode, but for temperatures below 670°C the SK mode is inhibited and relaxation occurs plastically. The labels (light grey, grey and black) at 4ML of GaN coverage are referred to the RHEED patterns in Fig. 9.16.

[Fig.9.16(a)], indicating 3D-islanding and the formation of QDs. Note, that the time evolution of elastic strain relaxation matches exactly the growth rate evolution for this specific case. For the intermediate growth temperature of T_S = 690 °C, the in plane strain in the GaN layer starts to relax also after a 2 ML thick wetting layer has formed, but full relaxation (2.4%) is reached only gradually. Again, the spotty RHEED pattern at 4 ML of GaN [Fig. 9.16(b)] implies the elastic relaxation mechanism by the formation of coherent 3D islands through the SK growth mode. When comparing the amount of GaN coverage needed to achieve full relaxation (in Fig. 9.15) with the time needed for the growth rate to gain its full steady-state value [Fig. 9.14(c)], there is a sound consistency between the two observations. This points strongly to the fact that the evolution of growth rate and GaN incorporation are directly linked to the degree of elastic strain relaxation in 3D islands.

At the very low temperature of T_S = 670 °C the strain relaxation mechanism deviates drastically from the two former cases. First, the RHEED pattern remains streaky throughout the whole growth process [Fig. 9.16(c)], indicating a smooth growth front, and secondly full relaxation is not achieved even after approximately 60 ML of GaN growth. Since no elastic

relaxation by 3D islanding occurs, it can be suggested that the mismatch strain is relaxed plastically through the formation of misfit dislocations in the GaN layer.
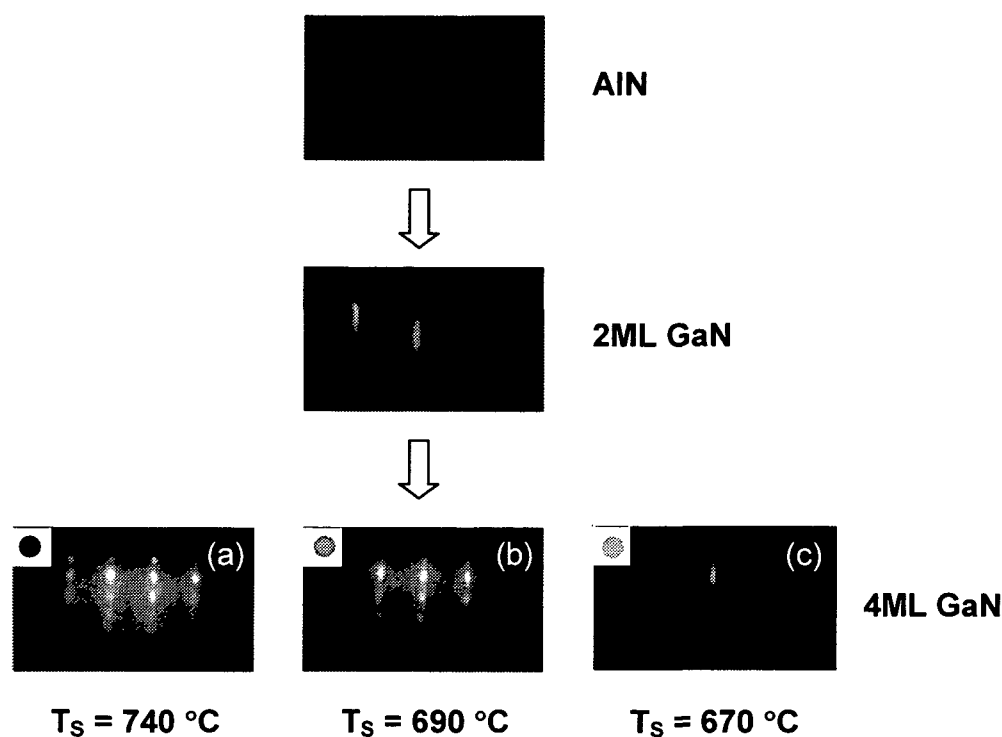

Fig. 9.16. Evolution of the RHEED pattern during the deposition of GaN on AlN; the streaky pattern in the top image represents the smooth AlN template and the intermediate pattern is indicative of an initially highly strained 2D wetting layer of GaN grown on top (valid for all growth temperatures). The spotty images at nominally 4 ML of GaN in (a) for T_S = 740 °C and (b) for T_S = 690 °C pinpoint to the formation of 3D islands by the SK mode. In contrast, at T_S = 670 °C (c), the RHEED pattern remains streaky and no SK transition occurs.

Since the strain relaxation mechanism influences directly the GaN incorporation rate, differences in the morphology of 3D islands can be expected, when grown under different growth temperatures. For a nominal amount of 4 ML of GaN grown at the highest temperature of T_S = 740 °C, the strain according to Fig. 9.15 is elastically completely relaxed. Likewise, at 4 ML of growth the GaN incorporation rate is at its maximum, since the full growth rate is achieved after 2 ML at this temperature [see Fig. 9.14(a)]. This means that beyond the critical thickness for the SK transition, the attachment of Ga and N atoms to the emerging islands is not counteracted by desorption processes and all arriving species get either incorporated immediately or diffuse efficiently to an active site of an island's edge. The resulting GaN island morphology in Fig. 9.17(a) shows densely packed islands, which have grown already to such a large size that they have coalesced. Much smaller and higher density islands appear when the same nominal GaN amount is deposited at the lower temperature of T_S = 690 °C [Fig. 9.17(b)]. Actually, two distinct island sizes are obtained, leading to a strong bimodal size distribution, as also observed lately by C. Adelmann et. al. for such high coverages [224]. Here, the overall QD density is about 4×10^{10} cm^{-2}, with partial densities for the two size modes of 0.6×10^{10} cm^{-2} and 3.4×10^{10} cm^{-2} respectively, in good agreement with densities re-

ported in the literature [212,224]. It is tempting to determine the island sizes, but the dimensions of the surface corrugations measured by AFM are influenced by the finite size of the probe tip, so the measured topopraphy is a convolution of the real surface and the tip shape. Anyway, the reduced island sizes can be understood by the fact that at nominally 4 ML of GaN growth at this temperature the GaN incorporation is not fully accomplished, as evident by the increased Ga desorption during the exponential regime after the SK transition in Fig. 9.14(c). Also, for this low temperature case at 4 ML of GaN growth the strain is not fully relaxed yet and a residual elastic strain component exists in the islands [indicated by the grey label in Fig. 9.15]. It can therefore be assumed that the strong strain field around these partially strained distinct islands influences the attachment and detachment rates of arriving atoms, which will be discussed more in detail in the following section.

Island formation is completely suppressed when growth is performed at the lowest temperature of T_S = 670 °C. Consistent with the entirely smooth RHEED pattern of Fig. 9.16(c), the respective AFM surface morphology in Fig. 9.17(c) exhibits a very smooth coherent GaN layer (surface rms roughness of 0.6 nm) that is separated by occasional pits or trenches. The reason for the inhibition of the SK transition can be attributed to the presence of a coherent Ga adlayer on the surface, which acts as an autosurfactant during growth, as will be shown in a precise study in the next section.
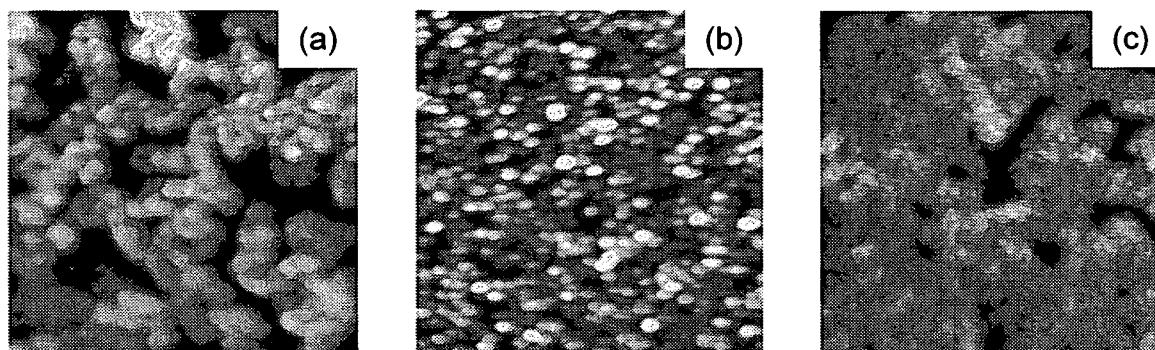

Fig. 9.17. 1×1 µm² AFM images of GaN on AlN grown to nominally (a) 4ML at T_S = 740 °C, (b) 4ML at T_S = 690 °C and (c) 60 ML at 670 °C. The height scale between black (low areas) and white (high areas) is 5 nm.

9.3.2.2. Effect of Ga Adlayer on Quantum Dot Growth

The previous results highlighted clearly that the growth of GaN QDs, their relaxation mechanisms and even their sizes can be kinetically controlled by slight changes of the growth temperature. As pointed out in elaborate detail in Sect. 6, another critical parameter governing the growth kinetics is given by the Ga/N flux ratio, or the absolute supplied Ga flux. It is therefore particularly interesting in which way the Ga flux, and as a consequence the Ga adlayer on top of the growing GaN layer, influences the formation of GaN QDs on AlN. To investigate this, a series of nominally 3ML thick GaN layers was grown in a stack embedded

in 25 nm thick AlN interlayers, all deposited on a 150 nm thick AlN template grown on 6H-SiC. The detailed growth conditions along with the grown GaN/AlN structure are shown schematically in Fig. 9.18. All AlN layers were grown at constant 800 °C under stoichiometric conditions, including a 120 sec nitridation step after each layer was completed. The post-growth nitridation was a precautious measure to remove any eventual Al accumulated on the surface. For the GaN growth cycles, the Ga flux was varied from 15 nm/min (Ga droplet conditions) to 3 nm/min (stoichiometric conditions) at a constant N flux of 2.5 nm/min (i.e. 0.158 ML/sec) and constant T_S = 705 °C. Therefore, as the GaN growth conditions pass through the entire Ga-rich intermediate growth regime, and by consideration of the Ga-face GaN polarity on an AlN/6H-SiC template, the Ga adlayer is expected to change from 0 ML to 2.5 ML (see Sect. 6). After each GaN layer grown, a 300 sec long pause was inserted before the subsequent AlN cap layer growth, in order to allow the accumulated Ga droplets or adlayer to desorb completely.
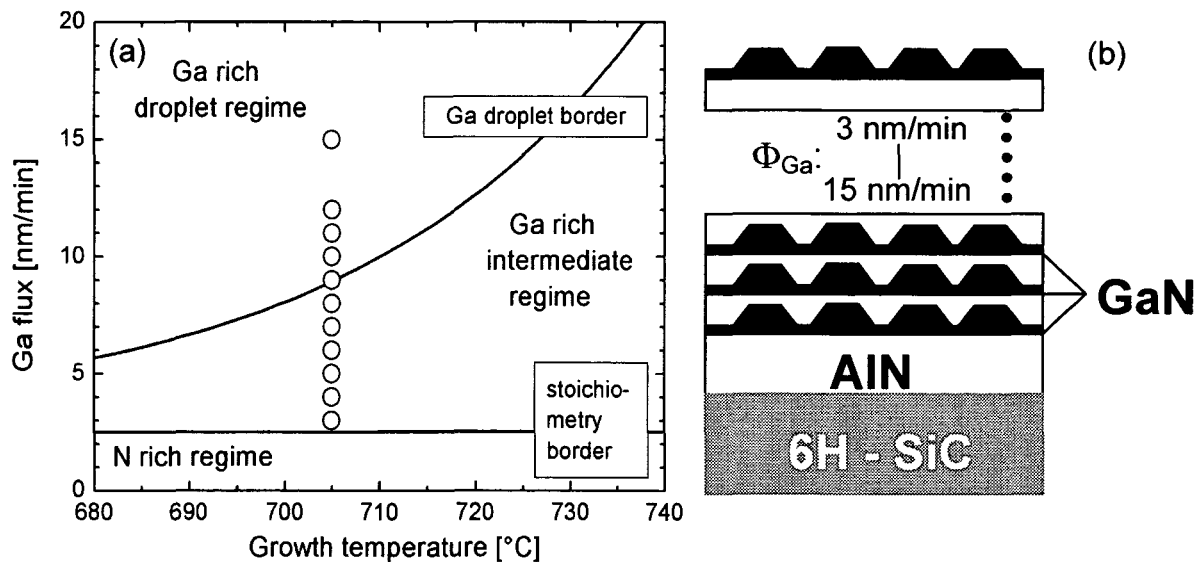

Fig. 9.18. (a) GaN growth phase diagram depicting the conditions (variable Ga flux, constant N flux = 2.5 nm/min and T_S = 705 °C) for (b) stacks of 3ML thick GaN layers embedded in a matrix of 25 nm thick AlN interlayers grown on an AlN/6H-SiC template. The Ga flux from the first to the last GaN layer varies from 15 nm/min to 3nm/min.

In order to correlate the GaN growth and strain relaxation mechanism with the Ga surface coverage under the different Ga flux conditions, both RHEED and QMS were used as complementary _in situ_ techniques. In RHEED the evolution of the strain relaxation (i.e. SK transition) during the 3 ML GaN growth on AlN was determined by lattice spacing analysis giving a measure for the variation of the in-plane lattice parameter a. Simultaneous Ga desorption measurements by QMS were used to determine the amount of Ga surface coverage responsible for changes in the a lattice parameter, i.e. evaluate the critical Ga coverage for the SK transition. Depending strongly on the selected Ga flux, the correlated lattice parameter and Ga surface coverage point to two very distinct growth mechanisms, shown in Fig. 9.19: For instance, depicted in Fig. 9.19(a), a Ga flux of 5 nm/min leads to a transformation from a

streak-to-spotty RHEED pattern and an onset for elastic strain relaxation (SK transition) after 9 sec (i.e. 1.5 ML) of GaN growth (gray curve). At approximately 12 sec of growth the emerged GaN QDs are fully relaxed, indicating no change in the *a* lattice parameter during further growth and even after the growth stop at 19 sec. Integrating the area below the simultaneously recorded Ga desorption (black curve) after the growth stop, which is indicated by the hatched area, gives exactly the amount of Ga that has accumulated on the surface during the entire 3 ML GaN growth. The Ga adlayer coverage was thus determined to 0.55 ML. For other very low Ga fluxes (ranging from 3 - 6 nm/min) in the near-stoichiometric growth regime, the SK transition was found to occur similarly at typical critical thicknesses of approximately 1.5 - 2.0 ML, and the respective Ga adlayer coverages do not to exceed 1 ML. This is
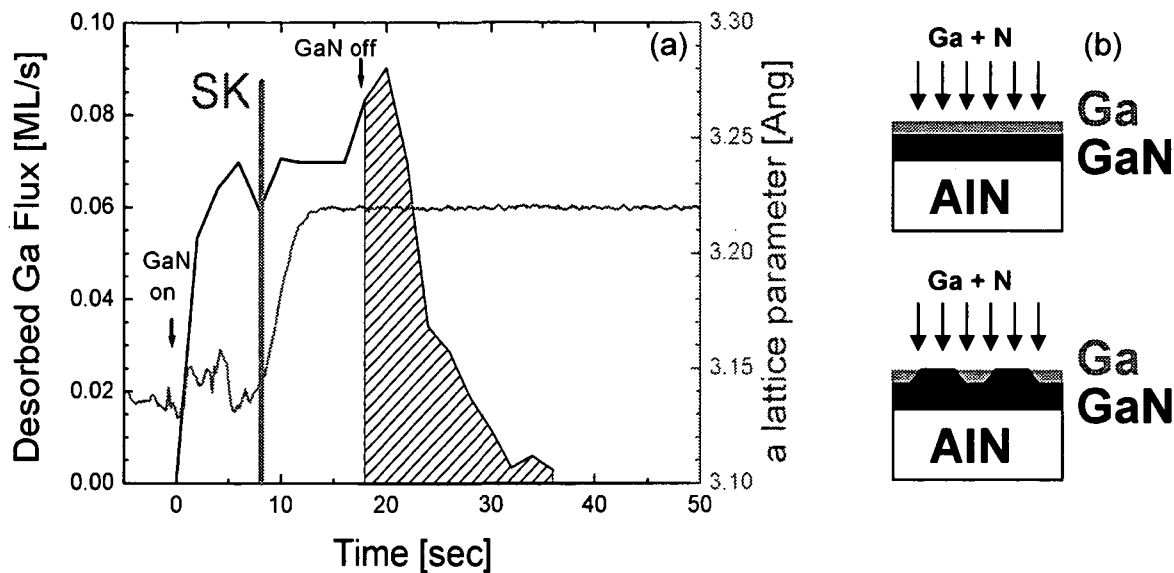

Fig. 9.19. The conventional Stranski-Krastanow (cSK) growth mode: (a) In-plane lattice parameter variation measured by RHEED (gray curve) and desorbing Ga flux by QMS (black curve) during the growth of 3 ML of GaN on (0001) AlN at a Ga flux of 5 nm/min, N flux of 2.5 nm/min (i.e. growth rate = 0.158ML/sec) and T_S = 705 °C. The hatched area is equivalent to a Ga surface coverage of 0.55 ML that has accumulated during growth and desorbed after the growth stop. Note, that the cSK transition occurs at a typical critical thickness of 1.5 ML. (b) Schematics for the cSK growth mode showing the transformation from a 2D wetting layer to 3D islands for a critical Ga surface coverage (gray layer) not exceeding 1ML.

referred to the *conventional Stranski-Krastanow* (cSK) growth mode, as also performed in earlier experiments in Sect. 9.3.2.1. The QD formation mechanism for this mode is illustrated schematically in Fig. 9.19(b), showing also the supplied Ga and N fluxes and the Ga adlayer. Comparatively, an extreme delay of the SK transition occurs for higher Ga fluxes and consequently higher Ga surface coverages. Illustrated in Fig. 9.20(a) for a Ga flux of 8 nm/min, QD formation by the streaky-to-spotty RHEED transition and the elastic strain relaxation sets in only at a certain time after the completion of the 3ML of GaN, i.e. at approximately 23 sec. Actually, it is obvious that some of the accumulated Ga surface coverage needs to desorb for the SK transition to occur. To evaluate the critical amount of Ga that is left on the surface at

the onset of the SK transition, integration of the Ga desorption signal beyond this point yielded exactly 1ML. The mechanism for QD formation in this case is thus very different from the former case, and it is referred to the so-called *modified Stranski-Krastanow* (mSK) growth mode, as also found independently by Refs.[Adelmann, Brown]. The schematics in Fig. 9.20(b) illustrate this, by showing first the suppression of the SK transition through a thick enough Ga adlayer prevalent under very Ga-rich conditions. Similar to the observations for GaN growth on GaN-templates in Sect. 6, it can be assumed that the Ga adlayer (at least 1ML thick) acts as an autosurfactant [Mula] and promotes therefore 2D growth, even beyond the
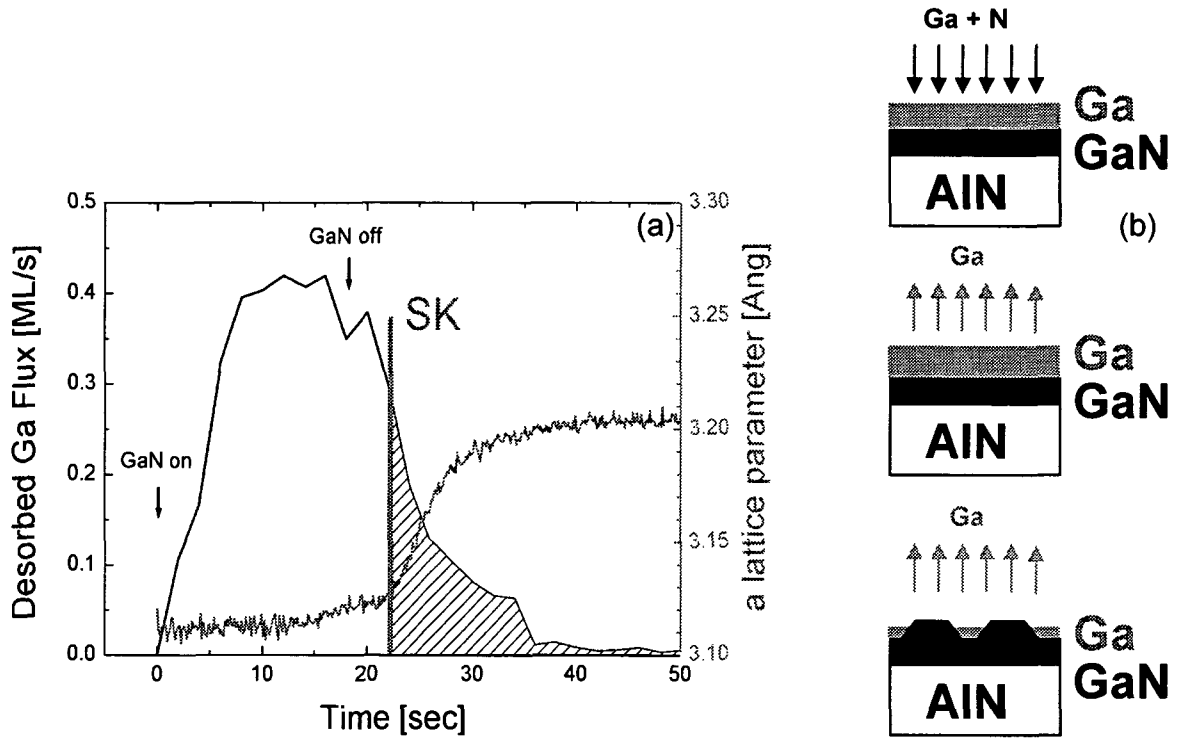

Fig. 9.20. The modified Stranski-Krastanow (mSK) growth mode: (a) In-plane lattice parameter variation (gray curve) and desorbing Ga flux (black curve) during the growth of 3 ML of GaN on (0001) AlN at a Ga flux of 8 nm/min, and otherwise constant conditions as noted in Fig. 9.19. The hatched area gives the critical residual Ga surface coverage of 1 ML, that determines the mSK transition with a certain time delay after the growth stop. (b) Schematics for the mSK growth mode illustrating the transition from a coherent 2D wetting layer to 3D islands appearing only after the growth stop when the Ga adlayer (gray layer) has partially desorbed to a residual coverage of below 1ML.

typical critical thickness for GaN on AlN. Secondly, when the Ga adlayer has desorbed to some critical coverage below 1ML, the 2D GaN layer is facilitated to spontaneously transform into 3D islands (QDs).

When determining the remaining Ga surface coverage at the point of the SK transition and at the point of the growth stop for each single GaN growth experiment, Fig. 9.21 is obtained as a function of the impinging Ga fluxes in the range of 3 - 15 nm/min. Plotting the accumulated Ga coverage evaluated at the point of the growth stop gives a gradual rise with increasing Ga flux, as shown by the open circles. This reflects exactly the behavior found earlier for Ga-

polar GaN growth, where the accumulated Ga adlayer evolves continuously from 0 ML at the stoichiometry border to 2.5 ML at the Ga droplet border and resulted in Ga droplets for higher Ga fluxes (compare Fig.6.2). On the other hand, when the actual Ga coverage is determined at the SK transition, i.e. the onset for QD formation, the repective datapoints marked by full circles break off and remain constant at 1ML Ga coverage for Ga fluxes above 6 nm/min. Accordingly, this means that for Ga adlayer coverages above 1 ML the mSK growth mode is
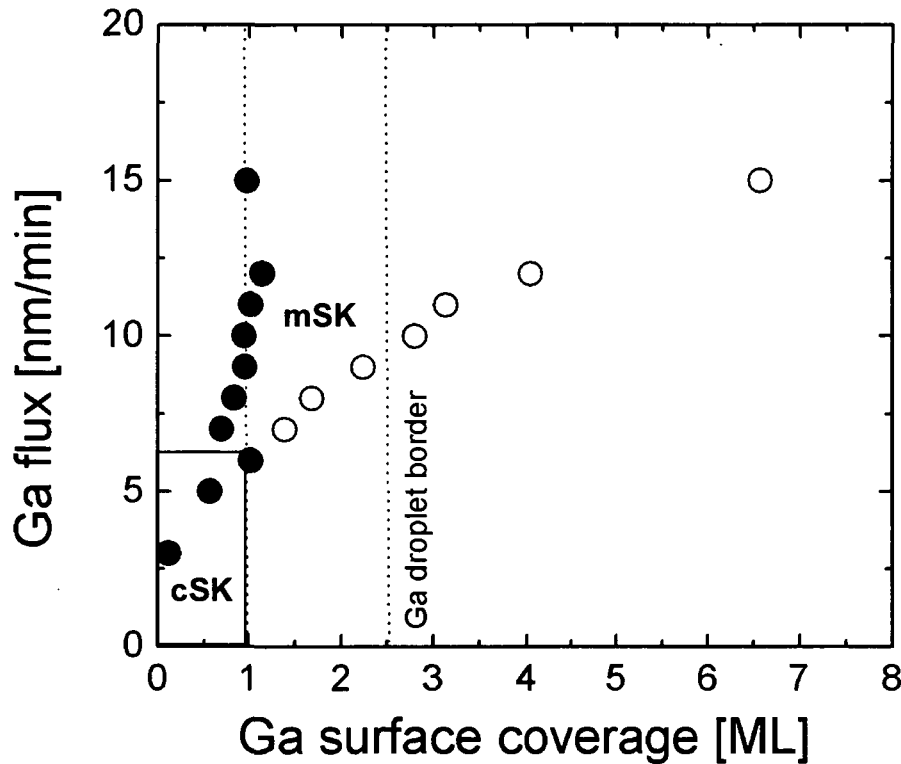

Fig. 9.21. Ga surface coverage in dependence of the impinging Ga flux determined from the integrated Ga desorption signal after the growth of 3ML of GaN QDs on AlN at T_S = 705 °C. The evaluation scheme is directly exemplified by the hatched areas in Figs. 9.19 and 9.20. Full circles give the remaining Ga surface coverage present at the Stranski-Krastanow (SK) transition, while open circles stand for the entire Ga surface coverage accumulated at the point of growth stop. Thus, the cSK mode is only favored in a narrow region below a Ga flux of 6nm/min where less than 1 ML of Ga coverage accumulates during growth, while all Ga fluxes above yield a mSK mode.

necessary, while for Ga coverages below 1ML GaN QD formation obeys the cSK mode at the typical critical thickness. In other words, assuming that GaN growth is not interrupted at nominally 3 ML but procedes to larger thicknesses, 3D-islanding can only be facilitated under submonolayer Ga coverages, whereas QD formation is completely suppressed under conditions where more than 1 ML of Ga terminates the GaN surface. In this case 2D growth prevails, and similar to the lowest temperature case in Sect. 9.3.2.1. the strain relaxes plastically by the introduction of misfit dislocations. Thus, 1 ML of Ga adlayer coverage can be seen as a critical measure for the differentiation between SK growth and QD formation on the one hand and pure 2D growth on the other hand, as illustrated schematically in Fig. 9.22.
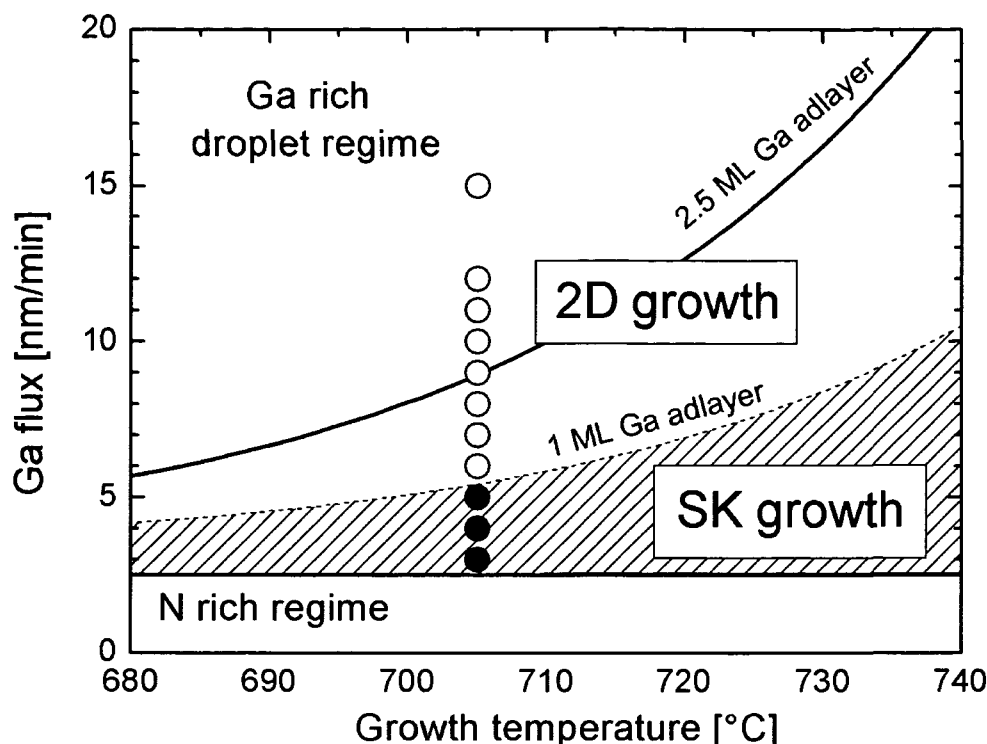
Fig. 9.22. Growth diagram for Ga-polar GaN growth on (0001) AlN differentiating between conventional SK growth and pure 2D-growth. The boundary between the two growth modes is given by the critical Ga adlayer coverage of 1ML.

9.3.2.3. Discussion

Concerning the observed promotion or suppression of the 2D-3D or Stranski-Krasta-now transition, the Ga adlayer forming under the excess Ga conditions is found to be directly responsible for this. To recall, under growth conditions where less than 1 ML of Ga covers the GaN surface, 3D-islanding occurs at the expected critical thickness of about 2 ML of GaN, which was referred to the cSK mode. Under higher Ga adlayer coverages (> 1ML), the GaN layer remains 2D, though when growth is interrupted and the adlayer desorbs, a rapid transformation of the GaN layer into 3D facetted islands occurs (denoted as mSK mode). The inhibition of island formation by a metallic adlayer, also called *surfactant*, is of major relevance for high–quality crystal growth and has also been shown for many other semiconductor material systems. By definition, a surfactant has a strong tendency to segregate and float on the growing surface without being incorporated and it has the effect of reducing the surface free energy. The surfactant effect (i.e. fostering 2D growth) was successfully applied to e.g. the Ge/Si system, where As and Sb act as surfactants [225,226], as well as Te in the InAs/-GaAs system [227]. In those cases the surfactant action was attributed to both kinetic and energetic mechanisms.

In the *kinetic* view, surfactant–mediated growth is characteristic of enhanced incorporation of the growth species, and as a consequence, reduced diffusion [228]. Thus, the lower free

energy surfactant–terminated surfaces provide generally a strong tendency for an exchange of the adatoms of the growth species with the surfactant adatoms. This promotes rapid incorporation of the growth species at subsurfaces sites, leading to limited diffusion on top of the surface which prevents 3D–islanding. However, in the case of GaN the observed surface structures and reconstructions are essentially different to those of all other III–V semicondutors. Especially, calculations based on density functional theory proposed that for GaN the Ga–rich surface has a lower surface free energy than the N reconstructed surface [150]. As a consequence, the surfactant action by the Ga adlayer in GaN growth is unique, as further adatom diffusion calculations have suggested not only a fast exchange between growth species and surfactant atoms, but also a very efficient lateral subsurface diffusion of N adatoms [20]. In conventional surfactant theory this would imply that due to the high N diffusion 3D–islanding should be favored over 2D–growth, which is in contradiction with the experimental results. Therefore the adatom diffusion considerations can be partially discarded for the surfactant effect of Ga and the inhibition of 3D–islanding in GaN growth.

A more proper explanation can be derived from _energetic_ considerations of the Ga surfactant mechansim. In particular, it can be suggested that due to the Ga surfactant adlayer the total surface strain energy of the GaN layer beneath is modified in a way that 3D–islanding can be suppressed. As proposed in the Ga bilayer model of Sect. 5.4, the bottom Ga adlayer (1 ML) is coherent to the adjacent GaN layer underneath. This Ga adlayer should thus be under large tensile strain, since the equilibrium lattice parameter of Ga is about 15 % smaller than that of GaN [150]. Considering also the coherency between GaN and the AlN sublayer, then the GaN layer is compressively strained by −2.4 % and the Ga adlayer is tensilely strained by + 12.5 %. When relaxation of the compressively strained GaN layer occurs, an additional increase of tensile strain in the Ga adlayer should result, meaning that the energy gain by GaN relaxation might be balanced by the increase in elastic energy in the Ga adlayer. The effect of the elastic energy of the Ga adlayer acting on the GaN layer was recently investigated in elaborate efforts by Mula et al. [171]. It was found that when depositing a Ga adlayer on top of relaxing GaN 3D–islands, the a lattice parameter in GaN decreased by 0.7%, suggesting a partial reversibility of the 2D/3D transition.

However, _ab initio_ calculations have demonstrated that the Ga adlayer decreases the overall surface energy from 100 meV/Å^2 (for the bare (0001) GaN surface) to 25 meV/ Å^2 [150]. If the surface energy is isotropic then the lower surface energy under excess Ga conditions would still promote 3D–islanding. This problem can partially be solved by assuming anisotropic distributions of the surface energies, as has been successfully done by Zhang et al. for the Si/Ge system [229]. To discuss the discrepancy between the apparent theoretical surface energies and the experimental results for the GaN/AlN system, Gogneau et al. [230] have introduced a facet energy for pyramidal 3D–islands that contributes critically to the energy balance between surface and elastic energy. Depending on the value of the facet energy (21 meV/Å^2 < $\gamma_{1\text{-}103}$ < 83 meV/Å^2), it was found possible that the 2D/3D transition can be suppressed.

An issue accompanied with the differentiation between SK growth and pure 2D growth is the mechanism of strain relaxation and the determination of the critical thickness. There are several controversies regarding the critical thickness of GaN on AlN and they seem

to be dependent on the chosen growth method, with reported values ranging from ~ 2 ML to 20 ML [207, 223,231–234]. The wide scatter may be due to a non–distinct differentiation between the critical thickness related to *elastic* and the other related to *plastic* relaxation. In the present case, the nominal critical thickness for elastic relaxation, as derived from the changes of the in–plane lattice parameter during the SK transition by RHEED, was found to be always at 2 ± 0.5 ML, consistent with the values at the low end as noted above. The increased Ga desorption and reduced growth rate before the SK transition, however, point out for the first time that the actual critical thickness is lower at typical values around 1.6 ML. On the other hand, the present RHEED observations allow no clear assertion of the critical thickness for plastic relaxation and detailed analysis of misfit dislocation generation by TEM needs to be performed.

One of the most significant findings in the previous experiments is the intimate correlation between surface structure, the degree of strain relaxation, i.e. residual strain in 3D islands, and actual growth rate. To recollect the results of Sect. 9.3.2.1., it was found that at a high growth temperature the strain in the GaN layer relaxes abruptly by the formation of immediately relaxed 3D–islands which grow at a faster rate. In contrast, the strain built–up in the GaN layer at its critical thickness in the low temperature case results in a slow elastic relaxation process and a much slower 3D–island growth rate. To understand the mechanisms leading to these differences in strained island growth, several concepts need to be considered. First, from an atomistic viewpoint and in disregard of strain, island growth is strongly steered by the competition between surface migration of adatoms and attachment to existing islands and the nucleation of new islands. At higher temperatures the adatom mobility and surface diffusion are very high, so the attachment of adatoms to existing islands is more favorable than the nucleation of new islands. At lower temperature the nucleation of islands is the dominant process, as the adatom mobility is lower. Thus, one observes many small islands for low temperatures in contrast to larger islands at high temperatures. In fact, this behavior was demonstrated by kinetic Monte Carlo simulations of self–organized QD growth, showing that the proposed island size distribution can be kinetically controlled [235].

In the case of a SK growth mode, however, the strains in the growing GaN layer and 3D–islands need to be considered correctly. At the initial stage of SK epitaxy, the sum of the surface and interface energies is first reduced by the growth of a wetting layer up to a few MLs (~ 2 ML for the GaN/AlN system). During this wetting layer growth, strain energy is built into the layer in order to fit its lattice with the lattice–mismatched substrate. As the strain energy is relieved by the formation of coherent (dislocation free) islands, the substrate is elastically deformed to relieve some of the mismatch. In general, it was found that coherently strained islands are energetically favored over dislocated islands for islands smaller than some critical size [236]. In terms of growth rate, early studies of the Ge/Si system showed that coherent islands grow more slowly than dislocated islands of the same size, with a strong acceleration of the growth rate upon misfit dislocation formation [237]. This seems to hold also for the present study, where the island growth rate was found to be higher for immediately relaxed (incoherent) GaN islands at high T_S, compared to the slow growth rate of partially elastically strained islands at low T_S. This can be mainly attributed to the high strain energy at the island edges, where the generation of misfit dislocations occurs as found for various

material systems [238–240]. To give a general idea of the strain energy density distribution over the lateral extension of a coherently strained 3D island, the illustration in Fig. 9.23 is quite useful. The strain energy distribution for this case was calculated for Ge islands on Si [241], but is qualitatively also applicable for the present GaN/AlN system. Considering the high strain energy at an island's edge, it is conceivable that there is an increased strain–induced detachment of atoms at their perimeter, reducing the net incorporation and thus the island's growth rate. This is related to an energy barrier for adatoms hindering the attachment to a strained island, which was calculated independently by Refs. [241] and [242] to decrease by ~$1/d$ with increasing distance d from the island's edge. Thus, the growth rate of a strained island is determined by two terms, first by the incorporation of adatoms directly deposited on the island surface (direct impingment) and secondly by the adatoms deposited on the substrate surface diffusing to the island (energy barrier limited growth). Only adatoms arriving within a critical distance from the island's edge are thus believed to overcome the strain–induced energy barrier for attachment and incorporate at an island. All others desorb or nucleate new islands. An increase in substrate temperature allows adatoms then to overcome the energy barrier more easily, which consequently yields higher island growth rates, as qualitatively consistent with the experimental observations.
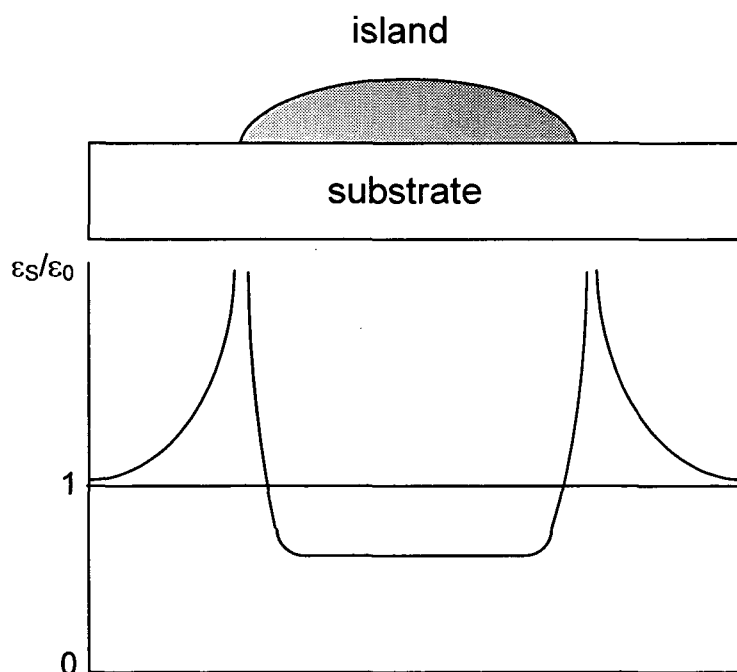

Fig. 9.23. Strain energy distribution of a strained island on a mismatched substrate. The variation in surface strain along the system surface ε_S in relation to the lattice mismatch ε_0 is highest at the island edges. The strain energy presented here was derived for Ge islands on Si [241], but is equally applicable to the GaN/AlN system.

However, as islands grow in size their strain energy at their edges increases as well, leading to additional detachment of atoms. Also, elastic interaction between islands can facilitate the detachment of atoms from their perimeter [243]. This has the much sought advantageous effect that smaller islands grow at the cost of larger islands (conversely to Ostwald ripening),

which finally leads to a generally homogenous island size distributions, as has been observed experimentally in a few cases [238,244,245]. But, as strained islands relax by the formation of misfit dislocations, it becomes energetically very favorable for adatoms to attach to these out–of–lattice positions and the increased growth rate of such incoherent islands leads then to generally much larger island sizes. As the GaN strain relaxation mechanism happens very fast for the high temperature case (Fig. 9.15), it can be assumed that along with the fast island growth rate misfit dislocation generation may occur at a very early stage of island growth. In contrast, GaN islands grown at a low temperature that underlie a much slower relaxation process, might appear free of dislocations. Though, according to the bimodal island size distribution in Fig. 9.17(b), the large island size mode might show a tendency of plastic relaxation and dislocations whereas the small island size mode features presumably a predominant elastic strain component and negligible dislocations. The theoretical notion of a homogenous island size distribution with increasing island size and additional strain–induced island detachment cannot be retraced in the present GaN island studies. This would require that GaN island growth is controlled in such a way that the islands become large enough to exhibit a sufficiently large elastic strain component at their edges, but do not surpass the critical size for plastic relaxation and dislocation generation. This makes the competition between the two strain components challenging and recent attempts to avoid such a bimodal island size distribution found that nominal GaN coverages of typically below 2.8 ML are most promising [224].

Conclusions

As some of the fundamental issues of nitride growth are still not well understood, the goal of the present work was to study the nucleation and growth kinetics with a strong focus on the related surface physics during the plasma–assisted molecular beam epitaxial (PAMBE) growth of {0001} GaN thin films. This much desired knowledge is seen as an essential step towards improving the comparatively low GaN material quality and an enhanced implementation of the PAMBE grown films into device applications. A conventional analytical tool for investigating and controlling the MBE growth of GaN *in situ* is realized typically by reflection high–electron energy diffraction (RHEED), which gives the crystallography and microstructure of surfaces, but allows merely qualitative statements of the surface kinetic processes taking place during thin film growth. For atomistic and fully quantitative *in situ* studies of the growing GaN surface, a novel technique had to be developed. With a quadrupole mass spectrometer (QMS) attached to a source flange of the MBE chamber and directed in line–of–sight to the GaN surface, several intimate insights into the relevant atomistic processes, such as adsorption, surface reactivity, incorporation etc. were gained by measuring the desorbing Ga species during the entire growth procedure.

One initial issue investigated was concerned with the metastability of the MBE growth of GaN, in the sense that there exists a strong competition between the forward reaction, i.e. GaN formation depending on the arrival rate of the nitrogen species on the surface, and the reverse reaction, given by GaN thermal decomposition. In detail, for the technologically most relevant (0001) GaN surface the decomposition rates were determined by QMS measurements of the Ga desorption into the MBE vacuum environment over a wide temperature range. It was found that GaN decomposition becomes significant at temperatures above 740 °C and reaches rates of approximately 1 μm/hour at ~ 800 °C, thus in the order of typical GaN growth rates. Also, the decomposition rate obeys a characteristic Arrhenius behavior with a very high activation energy of 3.9 eV, which reflects the exceptionally high Ga–N bond strength. So, in order to keep GaN thermal decomposition and its related surface roughening negligible, optimum (0001) GaN growth with complete nitrogen incorporation is therefore limited to temperatures lower than ~ 740 °C.

In PAMBE growth of GaN, the growth mechanism and resulting surface structures are crucially sensitive to the growth kinetics, meaning Ga/N flux ratio and temperature. In particular, under Ga–rich growth conditions, the GaN growth front is stabilized by an adsorbed metallic Ga adlayer, a feature totally different to the predominant group–V termination in all other III–V semiconductors. The role of the Ga surface adlayer is thus a major point of interest as, according to theoretical calculations, it directly effects surface diffusion mechanisms and consequently the overall material properties. With the employment of the QMS technique, it was achieved for the first time that the Ga adlayer coverage is quantified by direct analyis on both polar wurtzite (0001) and ($000\overline{1}$) GaN surfaces. In particular, the Ga adlayer coverage was found to deviate strongly between the two orientations. While on a ($000\overline{1}$) GaN surface preferentially 1.1 ML of Ga can be stabilized, the Ga adlayer coverage in equilibrium on

a (0001) GaN surface corresponds to a 2.5 ML bilayer in terms of GaN atomic density, both being independent of the substrate temperature. These values agree excellent with recent predictions based on first principles theory. From the desorption behavior of the Ga adlayer, typical surface residence lifetimes of the Ga adatoms could be derived, which change with substrate temperature and also differ drastically between the two surface polarities. Long Ga adatoms lifetimes are typical on (0001) surfaces and at lower temperatures compared to shorter lifetimes on ($000\bar{1}$) surfaces and at higher temperatures. With the different activation energies for the desorption of Ga adatoms (3.7 – 4.9 eV) it can be stated the Ga adlayer is more strongly bound to a (0001) GaN surface than to a ($000\bar{1}$) surface. Despite of these differences in Ga adlayer coverage and surface kinetics, both polar GaN surfaces exhibit a second stable phase forming on top of the Ga adlayer. The Ga adatoms within this phase occur in a rather weakly adsorbed state and tend to accumulate in the form of Ga droplets under very Ga–rich conditions. The lower activation energy (~3.1 eV) for the desorption of Ga adatoms from the droplet phase resembles strongly the evaporation characteristics of liquid bulk Ga. The two stable Ga surface phases (adlayer and droplets) have been more closely investigated for the (0001) GaN surface as a function of both Ga/N flux ratio and temperature. In particular, three distinct growth regimes were derived depending on the actual Ga surface coverage: a N–rich regime (Ga/N < 1) where no free Ga atoms occur on the surface, and two Ga–rich regimes denoted as intermediate (i.e. Ga adlayer, Ga/N > 1) and Ga–droplet regime (Ga/N >> 1). The borderline between the intermediate regime and the droplet regime depends strongly on the growth temperature and the Ga adlayer was found to increase _continuously_ with rising Ga flux from 0 at the stoichiometry border (Ga/N =1) to a 2.5 ML contracted bilayer at the Ga droplet boundary. This finding is at odds with the latest perception of a stepwise increase in adlayer coverage, because the adlayer underlies no constant desorption rate but follows a complicated three–stage decay process as modelled by differential rate equations.

The importance of the Ga adlayer evolution with changing growth conditions is directy reflected in the GaN material properties. The surface morphologies of PAMBE GaN layers grown on MOCVD–(0001) GaN templates under low Ga adlayer coverages (i.e. near–stoichiometric conditions) are generally rough and exhibit a high density of hexagonally inverted pyramidal (HIP) surface defects. With increasing Ga adlayer coverage the density of the HIP defects decreases continually and disappears when a complete 2.5 ML thick Ga bilayer covers the surface. At the droplet boundary, the resulting GaN surfaces are very smooth with characteristic spiral growth hillock features, an indication of a step–flow growth mode. The change in these surface features (surface defects versus spiral hillocks) depends on the kinetic surface processes, especially the adatom diffusion under different Ga adlayer coverages. Under high Ga adlayer coverages, surface adatom mobilities are high, as calculated theoretically, so the growth morphology can planarize and reduce the surface free energy. On the other hand, low adatom mobilities exist under low Ga adlayer coverages and the HIP defects forming as a consequence of dislocations cannot be filled in and propagate to the surface. When GaN growth is performed in the Ga droplet regime, the surface morphology consists also of atomically flat terraces arranged as spiral hillocks but exhibit also Ga droplets which are detrimental for device application. However, under conditions with a Ga flux only in slight excess above the droplet border, Ga droplets were found to be metastable,

as they desorb completely during the growth procedure, leaving behind a smooth surface without any HIP surface defects. The metastability of Ga droplets is to date not clear, and vague assumptions were made on its origin, being either an energy barrier to nucleation, or local effects such as heat transfer between droplets and substrate surface. The latter may increase the substrate temperature and enhance significant droplet desorption.

Another critical issue determining the final GaN material properties is the initial growth or nucleation stage, as the majority of deleterious crystal defects, especially dislocations, are generated during this phase. In order to understand the leading mechanisms of GaN nucleation on foreign substrates such as sapphire and 6H–SiC, a quantitative analysis was performed focusing on the wetting behavior of GaN, the island growth mode, coalescence features and growth rate evolution. As in many other heteroepitaxial systems, GaN growth on sapphire and SiC faces thermodynamical limits, especially a large energy barrier to nucleation (similar as in droplet growth), which results in a severe wetting problem, a huge nucleation delay and consequently in an initally reduced growth rate. Once adatoms have surpassed the energy barrier and overcritical nuclei have formed, a strong correlation between island shape and the prevailing growth mechanism was found. As confirmed by surface morphology studies, initially GaN nucleates as disk–shaped islands, that grow predominantely in two dimensions (with a lateral growth velocity being 20 times higher than the vertical velocity) and give rise to distinct non–linear growth kinetics. It has been calculated and also confirmed by the GaN coverage measurements, that initially a power–law (i.e. quadratic) island growth prevails, but when the islands coalesce linear growth continues and the final nominal steady–state growth rate is reached. For both chosen substrate materials the point of coalescence occurs at a thickness of approximately 20 nm and the amount of GaN material lossduring the initial wetting problem is equivalent to a thickness of 8 ± 1.5 nm. The quantitatively identical nucleation behavior of GaN on sapphire and 6H–SiC is surprising, considering the different GaN surface polarities and lattice mismatches (i.e. strain states) between the two heteroepitaxial systems.

If controlled properly, the island growth of GaN offers some potential for appealing and novel device applications. When GaN islands can be fabricated free of dislocations and with such low dimensions that quantum confinement effects come into play, they act as quantum dots (QDs) and allow improved performance of optical devices. One way to achieve such small–sized coherent GaN islands, was demonstrated by the Stranski–Krastanow (SK) growth mode on AlN substrates. Here, the GaN islands are formed from a thin compressively strained GaN wetting layer as this layer relaxes through the surface corrugation instead of generating misfit dislocations. In the present work, special emphasis was directed to investigations on the influence of the atomic–scale adatom processes on the QD growth and relaxation mechanisms. Initial studies of the effect of the AlN surface structure on the GaN nucleation behavior revealed that the AlN surface needs to be free of any metallic Al, as it tends to alloy with the arriving Ga atoms and inhibits GaN formation by forming rather additional AlN due the stronger Al–N bond strength. The fabrication of AlN layers with no metallic Al accumulation is challenging, since the PAMBE growth window is very small and precise control of the Al/N flux ratio and temperature are mandatory. However, on optimized AlN templates grown at stoichiometric flux conditions the GaN growth mechanism was found to depend severely on

the growth kinetics, i.e. Ga/N flux ratio, temperature and consecutively Ga adlayer coverage. In particular, the Ga adlayer coverage defines critically if the 2D–3D or SK growth mode is promoted or suppressed. Growth conditions yielding less than 1 ML of Ga coverage on the GaN surface results in 3D–islanding at a critical thickness of about 2 ML of GaN, which was referred to the conventional SK mode. Under higher Ga adlayer coverages (> 1 ML), the GaN layer remains 2D, even if the critical thickness is exceeded. But, when growth is interrupted and the adlayer desorbs, a rapid transformation of the GaN layer into 3D facetted islands occurs, which was referred to as modified SK mode. However, if GaN growth procedes to larger film thicknesses the built–up strain is accomodated plastically by the formation of misfit dislocations. The inhibition of island formation by a metallic adlayer of a thickness greater than 1 ML can be attributed to a _surfactant effect_, but more properly to a change in the surface strain energy at the Ga/GaN interface. Moreover, the adsorbed Ga adlayer acts directly on the degree of strain relaxation and on the actual growth rate of the GaN islands. At high growth temperatures and small Ga adlayer coverages, a fast elastic relaxation of the GaN wetting layer occurs, forming immediately fully relaxed 3D–islands with a high growth rate. In contrast, at low temperatures and higher Ga adlayer coverages (but still below 1ML), elastic relaxation happens much slower and the residual strain in 3D–islands was found to cause a significant impediment to adatom attachment and thus slower island growth rates. Thus, equal GaN coverages deposited at different temperatures yield substantial deviations in island size. The consideration of the interplay between strain relaxation and the atomistic surface processes during the SK island growth facilitates thus a more accurate control of the GaN QD formation and of well–defined island sizes and distributions.

References

[1]   K. H. Ploog, O. Brandt, H. Yang, B. Yang, and A. Trampert, J. Vac. Sci. Technol. B **16**, 2229 (1998).

[2]   H. Okumura, S. Yoshida, and T. Okahisa, Appl. Phys. Lett. **64**, 2997 (1994).

[3]   J. Wu, H. Yaguchi, K. Onabe, Y. Shiraki, and R. Ito, Jpn. J. Appl. Phys., Part 1 **37**, 1440 (1998).

[4]   R. C. Powell, N. E. Lee, Y. W. Kim, and J. E. Greene, J. Appl. Phys. **73**, 189 (1993).

[5]   C. Y. Yeh, Z. W. Lu, S. Froyen, and A. Zunger, Phys. Rev. B **46**, 10086 (1992).

[6]   M. Levinshtein, S. L. Rumyantsev, and M. S. Shur, *Properties of Advanced Semiconductor Materials (GaN, AlN, InN, BN, SiC, SiGe),* Wiley-Interscience (2001).

[7]   T. L. Tansley and C. P. Foley, J. Appl. Phys. **59**, 3241 (1986).

[8]   V. Yu. Davydov, A. A. Klochikhin, V. V. Emtsev, D. A. Kurdyukov, S. V. Ivanov, V. A. Vekshin, F. Bechstedt, J. Furthmüller, J. Aderhold, J. Graul, A. V. Mudryi, H. Harima, A. Hashimoto, A. Yamamoto, and E. E. Haller, phys. stat. sol. (b) **234**, 787 (2002).

[9]   C. Stampfl and C. G. Van de Walle, Phys. Rev. B **59**, 5521 (1999).

[10]   J. Furthmüller, J. Hafner and G. Kresse, Europhys. Lett. **28** (1994) 659.

[11]   F. A. Ponce, D. P. Bour, W. T. Young, M. Saunders, and J. W. Steeds, Appl. Phys. Lett. **69**, 337 (1996).

[12]   A. R. Smith, R. M. Feenstra, D. W. Greve, J. Neugebauer, and J. E. Northrup, Appl. Phys. Lett. **72**, 2114 (1998).

[13]   A. R. Smith, R. M. Feenstra, D. W. Greve, J. Neugebauer, and J. E. Northrup, Phys. Rev. Lett. **79**, 3934 (1997).

[14]   A. Kazimirov, G. Scherb, J. Zegenhagen, T. L. Lee, M. J. Bedzyk, M. K. Kelly, H. Angerer, and O. Ambacher, Appl. Phys. Lett. **84**, 1703 (1998).

[15]   F. Semond, P. Lorenzini, N. Grandjean, and J. Massies, Appl. Phys. Lett. **78**, 335 (2001).

[16]   L. Zhao, H. Marchand, P. Fini, S. DenBaars, U. Mishra, and J. S. Speck, MRS Internet J. Nitride Semicond. Res. **5S1**, W3.3 (2000).

[17]   J. N. Stirman, F. A. Ponce, A. Pavlovska, I. S. T. Tsong, and D. J. Smith, Apll. Phys. Lett. **76**, 822 (2000).

[18]   J. T. Torvik, C. Qiu, M. Leksono, J. I. Pankove, B. Van Zeghbroeck, H. M. Ng, and T. D. Moustakas, Appl. Phys. Lett. **72**, 1371 (1998).

[19]   T. Zywietz, J. Neugebauer, and M. Scheffler, Appl. Phys. Lett. **73**, 487 (1998).

[20]   J. Neugebauer, T. Zywietz, M. Scheffler, J. E. Northrup, H. Chen, and R. M. Feenstra, Phys. Rev. Lett. **90**, 056101 (2003).

[21]   L. K. Li, M. J. Jurkovic, W. I. Wang, J. M. VanHove, and P. P. Chow, Appl. Phys. Lett. **76**, 1740 (2000).

[22]   M. Sumiya, K. Yoshimura, K. Ohtsuka, and S. Fuke, Appl. Phys. Lett. **76**, 2098 (2000).

[23]   H. M. Ng, D. Doppalapudi, T. D. Moustakas, N. G. Weimann, and L. F. Eastman,

Appl. Phys. Lett. **73**, 821 (1998).

[24]   K. Wook, A. E. Botohkarev, H. Morkoc, Z. Q. Fang, D. C. Look, and D. J. Smith, J. Appl. Phys. **84**, 6680 (1998).

[25]   E. J. Tarsa, B. Heying, X. H. Wu, P. Fini, S. P. DenBaars, and J. S. Speck, J. Appl. Phys. **82**, 5472 (1997).

[26]   B. Heying, I. Smorchkova, C. Poblenz, C. Elsass, P. Fini, S. P. DenBaars, U. Mishra, and J. S. Speck, Appl. Phys. Lett. **77**, 2885 (2000).

[27]   Z. Lilienthal–Weber, C. Kisielowski, S. Ruvimov, Y. Chen, J. Washburn, I. Grzegory, M. Bockowski, J. Jun, and S. Porowski, J. Electron. Mater. **25**, 1545 (1996).

[28]   M. Seelmann-Eggebert, J. L. Weyher, H. Obloh, H. Zimmermann, A. Rar, and S. Porowski, Appl. Phys. Lett. **71**, 2635 (1997).

[29]   B. J. Rodriguez, A. Gruverman, A. I. Kingon, R. J. Nemanich, and O. Ambacher, Appl. Phys. Lett. **80**, 4166 (2002).

[30]   A. Zoroddu, F. Bernardini, P. Ruggerone, and V. Fiorentini, Phys. Rev. B **64**, 045208 (2001).

[31]   T. Takeuchi, C. Wetzel, S. Yamaguchi, H. Sakai, H. Amano, I. Akasaki, Y. Kaneko, S. Nakagawa, Y. Yamaoka, and N. Yamada, Appl. Phys. Lett. **73**, 1691 (1998).

[32]   C. Wetzel, T. Takeuchi, H. Amano, and I. Akasaki, J. Appl. Phys. **85**, 3786 (1999).

[33]   A. Hangleiter, J. S. Im, H. Kollmer, S. Heppel, J. Off, and F. Scholz, MRS Internet J. Nitride Semicond. Res. **33**, 15 (1998).

[34]   O. Ambacher, J. Smart, J. R. Shealy, N. G. Weimann, K. Chu, M. Murphy, W. J. Schaff, L. F. Eastman, R. Dimitrov, L. Wittmer, M. Stutzmann, W. Rieger, and J. Hilsenbeck, J. Appl. Phys. **85**, 3222 (1999).

[35]   R. Langer, J. Simson, V. Oritz, N. T. Pelekanos, A. Barski, R. Andre, and M. Godlewski, Appl. Phys. Lett. **74**, 3827 (1999).

[36]   M. Leroux, N. Grandjean, J. Massies, B. Gil, P. Lefebvre, and P. Bigenwald, Phys. Rev. B **60**, 1496 (1999).

[37]   I. Grzegory, S. Krukowski, M. Leszczynski, P. Perlin, T. Suski, and S. Porowski, *High Pressure Crystallization of GaN in Nitride Semiconductors, Handbook on Materials and Devices,* edited by P. Ruterana, M. Albrecht, and J. Neugebauer, Wiley, Weinheim (2003).

[38]   J. A. Van Vechten, Phys. Rev. B **7**, 1479 (1973).

[39]   S. Porowski and I. Grzegory, J. Cryst. Growth **178**, 174 (1997).

[40]   D. W. Pashley, Adv. Phys. **14**, 327 (1965).

[41]   A. K. Green, J. Dancy, and E. Bauer, J. Vac. Sci. Technol. **7**, 159 (1970).

[42]   S. Strite and H. Morkoc, J. Vac. Sci. Technol. B **10**, 1237 (1992).

[43]   J. Narayan, P. Tiwari, X. Chen, R. Chowdhury, and T. Zheleva, Appl. Phys. Lett. **61**, 1290 (1990).

[44]   T. Kehagias, P. Komninou, G. Nouet, P. Ruterana, and T. Karakostas, Phys. Rev. B **64**, 195329 (2001).

[45]   C. C. Kim, J. H. Je, M. S. Yi, D. Y. Noh, and P. Ruterana, J. Appl. Phys. **90**, 2191 (2001).

[46]   I. Jin Seo, H. Kollmer, J. Off, A. Sohmer, F. Scholz, and A. Hangleiter, Phys. Rev. B **57**, R9435 (1998).

[47]   P. Lefebvre, J. Allegre, B. Gil, H. Mathieu, N. Grandjean, M. Leroux, J. Massies, and P. Bigenwald, Phys. Rev. B **59**, 15363 (1999).

[48]   P. Lefebvre, A. Morel, M. Gallart, T. Taliercio, J. Allegre, B. Gil, H. Mathieu, B. Damilano, N. Grandjean, and J. Massies, Appl. Phys. Lett. **78**, 1252 (2001).

[49]   M. D. Craven, S. H. Lim, F. Wu, J. S. Speck, and S. P. DenBaars, Appl. Phys. Lett. **81**, 469 (2002).

[50]   V. Darakchieva, P. P. Paskov, T. Paskova, E. Valcheva, B. Monemar, and M. Heuken, Appl. Phys. Lett. **82**, 703 (2003).

[51]   T. Matsuoka, and E. Hagiwara, phys. stat. sol. **188**, 485 (2001).

[52]   T. Matsuoka, T. Sakai, and A. Katsui, Optoelectron. Devices Technol. **5**, 53 (1990).

[53]   T. Kato, H. Ohsato, T. Okuda, P. Kung, A. Saxler, C. Sun, and M. Razeghi, J. Cryst. Growth **173**, 244 (1997).

[54]   B. A. Haskell, F. Wu, M. D. Craven, S. Matsuda, P. T. Fini, T. Fujii, K. Fujito, S. P. DenBaars, J. S. Speck, and S. Nakamura, Appl. Phys. Lett. **83**, 644 (2003).

[55]   M. D. Craven, S. H. Lim, F. Wu, J. S. Speck, and S. P. DenBaars, Appl. Phys. Lett. **81**, 1201 (2002).

[56]   D. L. Barrett, J. P. McHugh, H. M. Hobgood, R. H. Hopkins, P. G. McMullin, R. C. Clarke, and W. J. Choyke, J. Cryst. Growth **128**, 358 (1993).

[57]   H. M. Hobgood, D. L. Barrett, J. P. McHugh, R. C. Clarke, S. Sriram, A. A. Burk, J. Reggi, C. D. Brandt, R. H. Hopkins, and W. J. Choyke, J. Cryst. Growth **137**, 181 (1994).

[58]   J. Giocordi, G. S. Rohrer, M. Skowronski, V. Balakrishna, C. Augustine, H. M. Hobgood, and R. H. Hopkins, J. Cryst. Growth **181**, 351 (1997).

[59]   S. Mahajan, Appl. Phys. Lett. **80**, 4321 (2002).

[60]   P. M. Dryburgh, J. Mat. Sci, Mat. in Electronics **9**, 237 (1998).

[61]   G. Pensl and R. Helbig, *Silicon Carbide (SiC) – recent results in physics and technology*, in: Festkörperprobleme/Advances in Solid State Physics, Vol. **30**, p.133, Ed. U. Rössler (Vieweg, Braunschweig, 1990).

[62]   K. Brack, J. Appl. Phys. **36**, 3560 (1965).

[63]   U. Starke, J. Schardt, P. R. Steiner, W. Hartner, S. Müller, L. Hammer, K. Heinz, and K. Müller, in: Proc. Symp. Surface Science 3S' 95, p.11, Ed. P. Varga and F. Aumayr, Inst. f. Allg. Physik, TU Wien (1995).

[64]   U. Starke, C. Bram, P. R. Steiner, W. Hartner, S. Müller, L. Hammer, K. Heinz, and K. Müller, Appl. Surf. Sci. **89**, 175 (1995).

[65]   R. Kaplan and T. M. Parrill, Surf. Sci. Lett. **165**, L45 (1986).

[66]   L. Muehlhoff, M. J. Bozack, W. J. Choyke, and J. T. Yates, J. Appl. Phys. **60**, 2558 (1986).

[67]   A. J. Van Bommel, J. E. Crombeen, and A. Van Tooren, Surf. Sci. **48**, 463 (1975).

[68]   F. Owman, C. Hallin, P. Mårtensson, E. Janzen, J. Cryst. Growth **167**, 391 (1996).

[69]   P. Mårtensson, F. Owman, L. I. Johannson, phys. stat. sol. (b) **202**, 501 (1997).

[70]   V. Ramachandran, M. F. Brady, A. R. Smith, R. F. Feenstra, and D. W. Greve, J.

Electr. Mat. **27**, 308 (1998).

[71]   Q. Xue, Q. K. Xue, Y. Hasegawa, I. S. T. Tsong, and T. Sakurai, Appl. Phys. Lett. **74**, 2468 (1999).

[72]   A. Kawasuso, K. Kojima, M. Yoshikawa, H. Itoh, K. Narumi, Appl. Phys. Lett. **76**, 1119 (2000).

[73]   R. F. Davis, T. W. Weeks, Jr., M. D. Bremser, S. Tanaka, R. S. Kern, Z. Sitar, K. S. Aliey, W. G. Perry, and C. Wang, Mater. Res. Soc. Symp. Proc. **395**, 3 (1996).

[74]   R. L. Headrick, S. Kycia, Y. K. Park, A. R. Woll, and J. D. Brock, Phys. Rev. B **54**, 14686 (1996).

[75]   S. H. Cheung, L. X. Zheng, M. H. Xie, S. Y. Tong, and N. Ohtani, Phys. Rev. B **64**, 033304 (2001).

[76]   J. Lu, L. Haworth, D. I. Westwood, and J. E. Macdonald, Appl. Phys. Lett. **78**, 1080 (2001).

[77]   Z. Liliental-Weber, H. Sohn, N. Newman, and J. Washburn, J. Vac. Sci. Technol. B **13**, 1578 (1995).

[78]   M. D. Craven, F. Wu, A. Chakraborty, B. Imer, U. K. Mishra, S. P. DenBaars, and J.S. Speck, Appl. Phys. Lett. **84**, 1281 (2001).

[79]   Y. Kumagai, A. Koukitu, and H. Seki, Jpn. J. Appl. Phys. **39**, 149 (2000).

[80]   S. Strite, J. Ruan, Z. Li, A. Salvador, H. Chen, D. J. Smith, W. J. Choyke, and J. Morkoc, J. Vac. Sci. Technol. B **9**, 1924 (1991).

[81]   H. Okumura, S. Misawa, and. S. Yoshida, Appl. Phys. Lett. **59**, 1058 (1991).

[82]   R. C. Powell, N. E. Lee, Y. W. Kim, and J. E. Greene, J. Appl. Phys. **73**, 189 (1993).

[83]   A. Dadgar, J. Bläsing, A. Diez, A. Alam, M. Heuken, and A. Krost, Jpn. J. Appl. Phys. **39**, 1183 (2000).

[84]   O. Contreras, F. A. Ponce, J. Christen, A. Dadgar, and A. Krost, Appl. Phys. Lett. **81**, 4712 (2002).

[85]   A. Dadgar, M. Poschenrieder, O. Contreras, J. Christen, K. Fehse, J. Bläsing, A. Diez, F. Schulze, T. Riemann, F. A. Ponce, and A. Krost, phys. stat. sol. A **192**, 308 (2002).

[86]   A. Kuramata, K. Horino, K. Domen, K. Shinohara, and T. Tanahashi, Appl. Phys. Lett. **67**, 2521 (1995).

[87]   T. George, E. Jacobsohn, W. T. Pike, P. Chang-Chien, M. A. Khan, J. W. Yang, and S. Mahajan, Appl. Phys. Lett. **68**, 337 (1996).

[88]   C. J. Sun, J. W. Yang, Q. Chen, M. S. Khan, T. George, P. Chang-Chien, and S. Mahajan, Appl. Phys. Lett. **68**, 1129 (1996).

[89]   C. D. Lee, R. M. Feenstra, J. E. Northrup, L. Lymperakis, and J. Neugebauer, Appl. Phys. Lett. **82**, 1793 (2003).

[90]   X. Gu, M. A. Reshchikov, A. Teke, D. Johnstone, H. Morkoc, B. Nemeth, and J. Nause, Appl. Phys. Lett. **84**, 2268 (2004).

[91]   R. R. Vanfleet, J. A. Simmons, H. P. Maruska, D. W. Hill, M. M. C. Chou, and B. H. Chai, Appl. Phys. Lett. **83**, 1139 (2003).

[92]   P. Waltereit, O. Brandt, A. Trampert, H. T. Grahn, J. Menniger, M. Ramsteiner, M. Reiche, and K. H. Ploog, Nature (London) **406**, 865 (2000).

[93]   H. Kinoshita, S. Otani, S. Kamiyama, h. Amano, I. Akasaki, J. Suda, and H.

Matsunami, Jpn. J. Appl. Phys. **40**, 1280 (2001).

[94] J. Suda and H. Matsunami, J. Cryst. Growth **237 – 239**, 1114 (2002).

[95] R. Liu, A. Bell, F. A. Ponce, S. Kamiyama, H. Amano, and I. Akasaki, Appl. Phys. Lett. **81**, 3182 (2002).

[96] S. Nakamura, T. Mukai, and M. Senoh, Appl. Phys. Lett. **64**, 1687 (1994).

[97] H. Sakai, T. Kiode, H. Suzuki, M. Yamaguchi, S. Yamasaki, M. Kioke, H. Amano, and I. Akasaki, Jpn. J. Appl. Phys. **34**, 1429 (1995).

[98] H. Tews, R. Averbeck, A. Graber, and H. Riechert, Electron. Lett. **32**, 2004 (1996).

[99] R. P. Vaudo, I. D. Goepfert, T. D. Moustakas, D. M. Beyea, T. J. Frey, and K. Meehan, J. Appl. Phys. **79**, 2779 (1996).

[100] M. A. L. Johnson, S. Fujita, W. H. Rowland, W. C. Hughes, Y. W. He, N. A. El-Masry, J. W. Cook, J. F. Schetzina, J. Ren, and J. A. Edmond, J. Electron. Meter. **25**, 793 (1996).

[101] F. Semond, P. Lorenzini, N. Grandjean, and J. Massies, Appl. Phys. Lett. **78**, 335 (2001).

[102] P. Waltereit, H. Sato, C. Poblenz, D. S. Green, J. S. Brown, M. McLaurin, T. Katona, S. P. DenBaars, J. S. Speck, J. H. Liang, M. Kato, H. Tamura, S. Omori, and C. Funaoka, Appl. Phys. Lett. 84, 2748 (2004).

[103] B. Heying, E. J. Tarsa, C. R. Elsass, P. Fini, S. P. DenBaars, and J. S. Speck, J. Appl. Phys. **85**, 6470 (1999).

[104] M. A. Herman and H. Sitter, *Molecular Beam Epitaxy*, Springer Berlin (1989).

[105] W. C. Hughes, W. H. Rowland, M. A. L. Johnson, S. Fujita, J. W. Cook, J. F. Schetzina, J. Ren, and J. A. Edmond, J. Vac. Sci. Technol. B **13**, 1571 (1995).

[106] A. Kritschl, H. Witte, M. Lisker, J. Christen, U. Birkle, S. Einfeldt, and D. Hommel, Appl. Phys. Lett. **74**, 2032 (1999).

[107] V. Kirchner, H. Heinke, U. Birkle, S. Einfeldt, D. Hommel, H. Selke, and P. L. Ryder, Phys. Rev. B **8**, 15749 (1998).

[108] S.-H. Cho, H. Okumura, and K. Akimoto, Appl. Phys. Lett. **76**, 3861 (2000).

[109] A. V. Blant, O. H. Hughes, T. S. Cheng, S. V. Novikov, and C. T. Foxon, Plasma Sources Sci. Technol. **9**, 12 (2000).

[110] A. J. Ptak, M. R. Millecchia, T. H. Myers, K. S. Ziemer, and C. D. Stinespring, Appl. Phys. Lett. **74**, 3836 (1999).

[111] R. P. Vaudo, J. W. Kook, and J. F. Schetzina, J. Vac. Sci. Technol. B **12**, 1232 (1994).

[112] S. Schöffberger, Diplomarbeit FH Munich (2001).

[113] A. Georgakilas, H. M. Ng, and P. Komninou, *Plasma–Assisted Molecular Beam Epitaxy of III–V Nitrides in Nitride Semiconductors, Handbook on Materials and Devices,* edited by P. Ruterana, M. Albrecht, and J. Neugebauer, Wiley, Weinheim (2003).

[114] N. Newman, J. Cryst. Growth **178**, 102 (1997).

[115] R. Averbeck, and H. Riechert, phys. stat. sol. **176**, 301 (1999).

[116] B. Heying, R. Averbeck, L. F. Chen, E. Haus, H. Riechert, and J. Speck, J. Appl. Phys. **88**, 1855 (2000).

[117] I. Barin, *Thermodynamical Data of Pure Substances* (VHC, Weinheim, 1993).

[118] C. Adelmann, J. Brault, D. Jalabert, P. Gentile, H. Mariette, G. Mula, and B. Daudin, J. Appl. Phys. **91**, 9638 (2002).

[119] E. Monroy, E. Sarigiannidou, F. Fossard, N. Gogneau, E. Bellet-Amalric, J.-L. Rouviere, S. Monnoye, H. Mank and B. Daudin, Appl. Phys. Lett. **84**, 3684 (2004).

[120] S. Nakamura, T. Mukai, M. Senoh, and N. Iwasa, Jpn. J. Appl. Phys. **31**, L139 (1992).

[121] H. W. Choi, J. Chua, A. Ramam, J. S. Pan, and A. T. S. Wee, Appl. Phys. Lett. **77**, 1795 (2000).

[122] A. P. Zhang, B. Luo, J. W. Johnson, F. Ren, J. Han, and S. J. Pearton, Appl. Phys. Lett. **79**, 3636 (2001).

[123] S. J. Pearton, J. C. Zolper, R. J. Shul, and F. Ren, J. Appl. Phys. Lett. **86**, 1 (1999).

[124] S. Nakamura, Jpn. J. Appl. Phys. **30**, L1705 (1991).

[125] C. F. Lin, G. C. Chi, M. S. Feng, J. D. Guo, J. S. Tsang, and J. M: Hong, Appl. Phys. Lett. **68**, 3758 (1996).

[126] L. Sugiura, K. Itaya, J. Hishio, H. Fujimoto, and Y. Kokubun, J. Appl. Phys. **82**, 4877 (1997).

[127] D. D. Koleske, M. E. Coltrin, A. A. Allerman, K.C. Cross, C. C. Mitchell, and J. J. Figiel, Appl. Phys. Lett. **82**, 1170 (2003).

[128] H. W. Choi, M. G. Cheong, M. A. Rana, S. J. Chua, T. Osipowicz, and J. S. Pan, J. Vac. Sci. Technol. B **21**, 1080 (2003).

[129] D. D. Koleske, A. E. Wickenden, R. L. Henry, J. C. Culbertson, and M. E. Twigg, J. Cryst. Growth **223**, 466 (2001).

[130] R. C. Schoonmaker, A. Buhl, and J. Lemley, J. Phys. Chem. **69**, 3455 (1965).

[131] A. S. Bolgar, S. P. Gordienko, E. A. Ryklis, and V. V. Fesenko, in *Chemistry and Physics of the Nitrides*, edited by G. V. Samsonov (Naukova, Dumka, Kiev 1968), p. 151; also, see I. G. Pichugin and D. A. Yas'kov, Izv. Akad. Nauk SSSR, Neorg. Mater. **6**, 1973 (1970).

[132] M. Mayumi, F. Satoh, Y. Kumagai, K. Takemoto, and A. Koukitu, Proceedings of the International Workshop on Nitride Semiconductors, Japan, 2000, pp. 38–41.

[133] D. D. Koleske, A. E. Wickenden, R. L. Henry, M.E. Twigg, J. C. Culbertson, and R. J. Gorman, MRS Internet J. Nitride Semicond. Res. **4S1**, G3.70 (1999).

[134] Z. A. Munir and A. W. searcy, J. Chem. Phys. **42**, 4223 (1965).

[135] R. Groh, G. Gerey, L. Bartha, and J. I. Pankove, Phys. Stat. Solidi **26**, 353 (1974).

[136] R. Held, D. E. Crawford, A. M. Johnston, A. M. Dabiran, and P. I. Cohen, Surf. Rev. Lett. **5**, 913 (1998).

[137] N. Grandjean, J. Massies, F. Semond, S. Yu. Karpov, and R. A. Talalaev, Appl. Phys. Lett. **74**, 1854 (1999).

[138] A. N. Alexeev, B. A. Borisov, V. P. Chaly, D. M. Demidov, A. L. Dudin, D. M. Krasovitsky, Yu. V. Pogorelsky, A. P. Shkurko, I. A. Sokolov, M. V. Stepanov, and A. L. Ter-Martirosyan, MRS Internet J. Nitride Semicond. Res. **4**, 6 (1999).

[139] C. J. Sun, P. Kung, A. Saxler, H. Ohsato, E. Bigan, M. Razeghi, and D. K. Gaskill, J. Appl. Phys. **76**, 236 (1994).

[140] O. Ambacher, M. S. Brandt, R. Dimitrov, T. Metzger, M. Stutzmann, R. A. Fischer, A. Miehr, A. Bergmaier, and G. Dollinger, J. Vac. Sci. Technol. B **14**, 3532 (1996).

[141] S. Guha, N. A. Bojarczuk, and D. W. Kisker, Appl. Phys. Lett. **69**, 2879 (1996).

[142] M. Kuball, F. Demangeot, J. Frandon, M. A. Renucci, J. Massies, N. Grandjean, R. L. Aulombard, and O. Briot, Appl. Phys. Lett. **73**, 960 (1998).

[143] H. Nienhaus, C. Schepers, S. P. Grabowski, and W. Mönch, Appl. Phys. Lett. **77**, 403 (2000).

[144] S. D. Lester, F. A. Ponce, M. G. Craford, and D. A. Steigerwald, Appl. Phys. Lett. **66**, 1249 (1994).

[145] A. R. Smith, V. Ramachandran, R. M. Feenstra, D. W. Greve, M.-S. Shin, M. Skowronski, J. Neugebauer, and J. E. Northrup, J. Vac. Sci. Technol. A **16**, 1641 (1998).

[146] R. M. Feenstra, H. Chen, V. Ramachandran, A. R. Smith, and D. W. Greve, Appl. Surf. Sci. **166**, 165 (2000).

[147] A. R. Smith, R. M. Feenstra, D. W. Greve, M. S. Shin, M. Skowronski, J. Neugebauer, and J. E. Northrup, Surf. Sci. **423**, 70 (1999).

[148] A. R. Smith, R. M. Feenstra, D. W. Greve, M. S. Shin, M. Skowronski, J. Neugebauer, and J. E. Northrup, J. Vac. Sci. Technol. B **16**, 2242 (1998).

[149] H. Chen, R. M. Feenstra, J. E. Northrup, T. Zywietz, J. Neugebauer, and D. W. Greve, J. Vac. Sci. Technol. B **18**, 2284(2000).

[150] J. E. Northrup, J. Neugebauer, R. M. Feenstra, and A. R. Smith, Phys. Rev. B **61**, 9932 (2000).

[151] C. Adelmann, J. Brault, G. Mula, B. Daudin, L. Lymperakis, and J. Neugebauer, Phys. Rev. B **67**, 165419 (2003).

[152] E. Monroy, E. Sarigiannidou, F. Fossard, N. Gogneau, E. Bellet-Amalric, J.-L. Rouviere, S. Monnoye, H. Mank, and B. Daudin, Appl. Phys.Lett. **84**, 3684 (2004).

[153] M. Zinke-Allmang, L. C. Feldmanm and M. H. Grabow, Surf. Sci. Rep. **16**, 377 (1992).

[155] G. Koblmüller, R. Averbeck, L. Geelhaar, H. Riechert, W. Hösler, and P. Pongratz, J. Appl. Phys. **93**, 9591 (2003).

[156] J. R. Arthur, J. Appl. Phys. **39**, 4032 (1968).

[157] P. Hacke, G. Feuillet, H. Okumura, and S. Yoshida, Appl. Phys. Lett. **69**, 2507 (1996).

[158] L. X. Zheng, M. H. Xie, and S. Y. Tong, Phys. Rev. B **61**, 4890 (2000).

[159] P. I. Cohen, G. S. Petrich, P. R. Pukite, G. J. Whaley, and A. S. Arrott, Surf. Sci. **216**, 222 (1989).

[160] B. Daudin, J. L. Rouviere, and M. Arlery, Appl. Phys. Lett. **69**, 2480 (1996).

[161] J. L. Rouviere, J. L. Weyher, M. Seelmann-Eggebert, and S. Porowski, Appl. Phys. Lett. **73**, 668 (1998).

[162] L. K. Li, M. J. Jurkovic, W. I. Wang, J. M. Van Hove, and P. P. Chow, Appl. Phys. Lett. **76**, 1740 (2000).

[163] M. Sumiya, K. Yoshimura, K. Ohtsuka, and S. Fuke, Appl. Phys. Lett. **76**, 2098 (2000).

[164] D. E. Crawford, R. Held, A. M. Johntson, A. M. Dabiran, and P. I. Cohen, MRS Internet J. Nitride Semicon. Res. **1**, 12 (1996).

[165] K. R. Evans, T. Lei, and C. R. Jones, Solid State Electron. **41**, 339 (1997).

[166] J. Speck (private communication).

[167] H.Riechert, R. Averbeck, A. Graber, M. Schienle, U. Strauß and H. Tews, Mat. Res. Soc. Symp. Proc. **449**, 149 (1997).

[168] S. Einfeldt, U. Birkle, C. Thomas, M. Fehrer, H. Heinke, and D. Hommel, Mat. Sci. Eng. **B 50**, 12 (1997).

[169] V. Ramachandran, C. D. Lee, R. M. Feenstra, A. R. Smith, J. E. Northrup, and D. E. Greve, J. Cryst. Growth **209**, 355 (2000).

[170] C. R. Elsass, C. Poblenz, B. Heying, P. Fini, P. M. Petroff, S. P. DenBaars, U. K. Mishra, and J. S. Speck, J. Cryst. Growth **233**, 709 (2001).

[171] G. Mula, C. Adelmann, S. Moehl, J. Oullier, and B. Daudin, Phys. Rev. B **64**, 195406 (2001).

[172] F. C. Frank, Acta Crystallogr. **4**, 497 (1951).

[173] M. Volmer and A. Weber, Z. Phys. Chem. **119**, 277 (1926).

[174] R. Becker and W. Döring, Ann. Physik **24**, 719 (1935).

[175] J. Lothe and G. M. Pound, J. Chem. Phys. **36**, 2080 (1962).

[176] A. B. Pippard, *Elements of Classical Thermodynamics for Advanced Students of Physics* (Cambridge University Press, London, 1957).

[177] J. A. Venables, G. D. Spiller, and M. Hanbücken, Rep. Prog. Phys. **47**, 399 (1984).

[178] B. Daudin, G. Mula, and P. Peyla, Phys. Rev. B **61**, 10330 (2000).

[179] M. P. Moody and P. Attard, J. Chem Phys. **117**, 6705 (2002).

[180] B. Lewis and J. C. Anderson, *Nucleation and Growth of Thin Films* (Academic Press, New York, 1978).

[181] J. A. Venables, and G. L. Price, in *Epitaxial Growth*, edited by J. W. Matthew (Acedemic Press, New York, 1975).

[182] G. Zinsmeister, Thin Solid Films **2**, 497 (1968).

[183] J. A. Venables, Philos. Mag. **27**, 697 (1973).

[184] X. H. Wu, P. Fini, E. J. Tarsa, B. Heying, S. Keller, U. K. Mishra, S. P. DenBaars, and J. S. Speck, J. Cryst. Growth **189/190**, 231 (1998).

[185] F. Degave, P. Ruterana, G. Nouet, J. H. Je, and C. C. Kim, J. Phys.: Condens. Matter **14**, 13019 (2002).

[186] H. Amano, N. Sawaki, I. Akasaki, and Y. Toyoda, Appl. Phys. Lett. **48**, 353 (1986).

[187] T. Sasaki and T. Matsuoka, J. Appl. Phys. **77**, 192 (1995).

[188] V. Narayanan, K. Lorenz, W. Kim, and S. Mahajan, Philos. Mag. A **82**, 885 (2002).

[189] T. Yang, K. Uchida, T. Mishima, J. Kasai, and J. Gotoh, phys. stat. sol. (a) **180**, 45 (2000).

[190] S. Figge, T. Böttcher, S. Einfeldt, and D. Hommel, J. Cryst. Growth **221**, 262 (2000).

[191] A. R. Woll, R. L. Headrick, S. Kycia, and J. D. Brook, Phys. Rev. Lett. **83**, 4349 (1999).

[192] N. Grandjean and J. Massies, Appl. Phys. Lett. **71**, 1816 (1997).

[193] Y. Moriyasu, H. Goto, N. Kuze and M. Matsui, J. Cryst. Growth **150**, 916 (1995).

[194] R. L. Headrick, S. Kycia and Y. K. Park, Phys. Rev. B **54**, 14686 (1996).

[195] R. L. Headrick, S. Kycia, A. R. Woll, J. D. Brock and M. V. R. Murty, Phys. Rev. B **58**, 4818 (1998).

[196] G. B. Stephenson, J. A. Eastman, C. Thompson, O. Auciello, P. H. Fuoss, A. Munkholm, P. Fini, S. P. DenBaars, and J. S. Speck, MRS Bulletin **01**, 21 (1999).

[197] D. D. Koleske, A. J. Fischer, A. A. Allerman, C. C. Mitchell, K. C. Cross, S. R. Kurtz, J. J. Figiel, K. W. Fullmer, and W. G. Breiland, Appl. Phys. Lett. **81**, 1940 (2002).

[198] G. Koblmüller, *Molecular Beam Epitaxy of Group–III Nitrides on Silicon Carbide* (Diploma Thesis, TU Wien, 2001).

[199] I. L. Maksimov, M. Sanada, and K. Nishioka, J. Chem Phys. **113**, 3323 (2000).

[200] F. Family and J. G. Amar, Mater. Sci. Eng. B **30**, 149 (1995).

[201] D. P. Adams, L. L. Tedder, T. M. Mayer, B. S: Swartzentruber, and E. Chason, Phys. Rev. Lett. **74**, 5088 (1959).

[202] K. Jeganathan, M. Shimizu, and H. Okumura, J. Appl. Phys. **95**, 3761 (2004).

[203] B. Daudin and F. Widmann, J. Cryst. Growth **182**, 1 (1997).

[204] C. Adelmann, J. Brault, J.-L- Rouviere, H. Mariette, G. Mula, and B. Daudin, J. Appl. Phys. **91**, 5498 (2002).

[205] T. W. Weeks Jr., M. D. Bremser, S. Ailey, E. Carlson, W. G. Perry and R. F. Davis, Appl. Phys. Lett. **67**, 401 (1995).

[206] J. Keckes, G. Koblmüller, and R. Averbeck, J. Cryst. Growth **246**, 73 (2002).

[207] B. Daudin, F. Widmann, G. Feuillet, Y. Samson, M. Arlery, and J. L. Rouviere, Phys. Rev. B **56**, 7069 (1997).

[208] F. Widmann, J. Simon, B. Daudin, G. Feuillet, J. L. Rouviere, N. T. Pelekanos, and G. Fishman, Phys. Rev. B **58**, 15989 (1998).

[209] E. Martinez-Guerrero, F. Chabuel, B. Daudin, J. L. Rouviere, and H. Mariette, Appl. Phys. Lett. **81**, 5117 (2002).

[210] M. Arlery, J. L. Rouviere, F. Widmann, B. Daudin, G. Feuillet, and H. Mariette, Appl. Phys. Lett. **74**, 3287 (1999).

[211] A. Bourret., C. Adelmann, B. Daudin, J. L. Rouviere, G. Feuillet, and G. Mula, Phys. Rev. B **63**, 245307 (2001).

[212] J. Brown, F. Wu, P. M. Petroff, and J. S. Speck, Appl. Phys. Lett. **84**, 690 (2004).

[213] E. Bellet-Amalric, C. Adelmann, E. Sarigiannidou, J. L. Rouviere, G. Feuillet, E. Monroy, and B. Daudin, J. Appl. Phys. **95**, 1127 (2004).

[214] L. R. Doolittle, Nucl. Inst. Meth. **B9**, 344 (1985).

[215] L. R. Doolittle, Nucl. Inst. Meth. **B15**, 227 (1986).

[216] Z. Y. Fan and N. Newman, Mater. Sci. Eng. **87**, 244 (2001).

[217] O. Ambacher, M. S. Brandt, R. Dimitrov, T. Metzger, M. Stutzmann, R. A. Fischer, A. Miehr, A. Bergmaier, and G. Dollinger, J. Vac. Sci. Technol. B **14**, 3532 (1996).

[218] G. Ferro, H. Okumura, and S. Yoshida, J. Cryst. Growth **209**, 415 (2000).

[219] A. Botchkarev, A. Salvador, B. Sverdlov, J. Myoung and H. Morkoc, J. Appl. Phys. **77**, 4455 (1995).

[220] Landolt-Börnstein: *Numerical Data and Functional Relationships in Science and Technology, New Series, Group III: Crystal and Solid State Physics* **17**, *Semiconductors*, Springer, New York (1982).

[221] Y.-M. Le Vaillant, R. Bisaro, J. Olivier, O. Durand, J.-Y. Duboz, S. Ruffenbach-Clur, O. Briot, B. Gil, and R.-L. Aulombard, J. Cryst. Growth **189/190**, 282 (1998).

[222] T. George, W. T. Pike, M. A. Khan, J. N. Kuznia and P. Chang-Chien, L. Electron. Mater. **24**, 241 (1995).

[223] C. Adelmann, N. Gogneau, E. Sarigiannidou, J.-L. Rouviere, and B. Daudin, Appl. Phys. Lett. **81**, 3064 (2002).

[224] C. Adelmann, B. Daudin , R. A. Oliver, G. A. D. Briggs, and R. E. Rudd, Phys. Rev. B **70**, 125427 (2004).

[225] M. Copel, M. C. Reuter, E. Kaxiras, and R. M. Tromp, Phys. Rev. Lett. **63**, 632 (1989).

[226] J. R. Power, K. Hinrichs, S. Peters, K. Haberland, N. Esser, and W. Richter, Phys. Rev. B **62**, 7378 (2000).

[227] N. Grandjean, J. Massies, and V. H. Etgens, Phys. Rev. Lett. **69**, 796 (1992).

[228] M. Copel, M. C. Reuter, M. Horn-von Hoegen, and R. M. Tromp, Phys. Rev. B **42**, 11682 (1990).

[229] Y. W. Zhang, Phys. Rev. B **61**, 10388 (2000).

[230] N. Gogneau, D. Jalabert, E. Monroy, T. Shibata, M. Tanaka, and B. Daudin, J. Appl. Phys. **94**, 2254 (2003).

[231] C. Kim, I. K. Robinson, J. Myoung, K.-H. Shim, and K. Kim, J. Appl. Phys. **85**, 4040 (1999).

[232] Z. Sitar, M. J. Paisley, B. Yan, J. Ruan, W. J. Choyke, and R. F. Davis, J. Vac. Sci. Technol. B **8**, 316 (1990).

[233] A.D. Bykhovski, B. L. Gelmont, and M. S. Shur, J. Appl. Phys. **81**, 6332 (1997).

[234] B. Damilano, N. Grandjean, F. Semond, J. Massies, and M. Leroux, Appl. Phys. Lett. **75**, 962 (1999).

[235] M. Meixner, E. Schöll, V. A. Shchukin, and D. Bimberg, Phys. Rev. Lett. **87**, 236101 (2001).

[236] W. A. Jesser and D. Kuhlmann-Wilsdorff, Phys. Stat. Sol. **19**, 95 (1967).

[237] M. Krishnamurthy, J. S. Drucker, and J. A. Venables, J. Appl. Phys. **69**, 6461 (1991).

[238] F. K. LeGoues, M. C. Reuter, J. Tersoff, M. Hammar, and R. M. Tromp, Phys. Rev. Lett. **73**, 300 (1994).

[239] S. Guha, A. Madhukar, and K. C. Rajkumar, Appl. Phys. Lett. **57**, 2110 (1990).

[240] Y. Chen, X. W. Lin, Z. Lilienthal-Weber, J. Washburn, J. Klem, and J. Y. Tsao, Appl. Phys. Lett. **68**, 111 (1996).

[241] Y. Chen and J. Washburn, Phys. Rev. Lett. **19**, 4046 (1996).

[242] H. T. Dobbs, D. D. Vvedensky, A. Zangwill, J. Johansson, N. Carlsson, and W. Seiffert, Phys. Rev. Lett. **79**, 897 (1997).

[243] H. M. Koduvely and A. Zangwill, Phys. Rev. B **60**, 2204 (1999).

[244] B. Voigtländer and A. Zinner, Appl. Phys. Lett. **63**, 3055 (1993).

[245] D. Leonard, K. Pond, and P. M. Petroff, Phys. Rev. B **50**, 11687 (1994).

Publications

G. Koblmüller, R. Averbeck, H. Riechert, and P. Pongratz: *Delayed Nucleation during Molecular–Beam Epitaxial Growth of GaN observed by Line–of–Sight Quadrupole Mass Spectrometry*, **Applied Physics Letters** 80, 2281 (2002).

G. Koblmüller, R. Averbeck, H. Riechert, and P. Pongratz: *GaN Nucleation by Line–of– Sight Quadrupole Mass Spectrometry*, **International Workshop on Nitride Semiconductors (IWN)** Aachen, Germany 2002.

R. Averbeck, G. Koblmüller, H. Riechert, and P. Pongratz: *Nucleation and Growth of GaN observed by Line–of–Sight Quadruploe Mass Spectrometry*, **International Conference on Molecular Beam Epitaxy**, San Fransisco, USA (2002).

G. Koblmüller, R. Averbeck, H. Riechert, and P. Pongratz: *Nucleation Phenomena during Molecular Beam Epitaxy of GaN observed by Line–of–Sight Quadrupole Mass Spectrometry*, **Physica Status Solidi** (a) 194, 515 (2002).

J. Keckes, G. Koblmüller, and R. Averbeck: Temperature Dependence of Stresses in GaN/AlN/6H–SiC (0001) Structures: *Correlation between AlN Buffer Thickness and Intrinsic Stresses in GaN*, **Journal of Crystal Growth** 246, 73 (2002).

G. Koblmüller, R. Averbeck, H. Riechert, and P. Pongratz: *GaN Growth Modes during Molecular Beam Epitaxy on AlN observed by In Situ Line–of–Sight Quadrupole Mass Spectrometry*, **12th European MBE Workshop** Bad Hofgastein, Austria (2003).

R. Averbeck, G. Koblmüller, H. Riechert, and P. Pongratz: *Nucleation and Growth of GaN observed by Line–of–Sight Quadruploe Mass Spectrometry*, **Journal of Crystal Growth** 251, 505 (2003).

G. Koblmüller, R. Averbeck, H. Riechert, and P. Pongratz: *MBE looks to New Applications*, in **Compound Semiconductors**, edited by R. Campion June (2003).

G. Koblmüller, R. Averbeck, L. Geelhaar, H. Riechert, W. Hösler and P. Pongratz: *Growth Diagram and Morphologies of AlN Thin Films Grown by Molecular Beam Epitaxy*, **Journal of Applied Physics** 93, 9591 (2003).

G. Koblmüller, R. Averbeck, H. Riechert, and P. Pongratz: *Growth Diagram for Molecular Beam Epitaxy of AlN Thin Films*, **12th European Workshop on Heterostructure Technology**, San Rafael, Spain (2003).

G. Koblmüller, R. Averbeck, H. Riechert, and P. Pongratz: *Direct Observation of Different Equilibrium Ga Adlayer Coverages and their Desorption Kinetics on GaN (0001) and (000-1) Surfaces,* **Physical Review B** 69, 035325 (2004).

G. Koblmüller, J. Brown, R. Averbeck, H. Riechert, P. Pongratz, and J. S. Speck: *Quantification of Ga Surface Coverages and their Desorption Kinetics on GaN (0001) and (000-1) Surfaces,* **International Workshop on Nitride Semiconductors (IWN)** Pittsburgh, USA 2004.

R. Averbeck, G. Koblmüller, J. Brown, H. Riechert, P. Pongratz and J. S. Speck: *Ga Adlayer Coverage during Molecular Beam Epitaxy of GaN,* **International Conference on Molecular Beam Epitaxy,** Edinburgh, Scotland (2004).

G. Koblmüller, J. Brown, R. Averbeck, H. Riechert, P. Pongratz, and J. S. Speck: *Quantification of Ga Surface Coverages and their Desorption Kinetics on GaN (0001) and (000-1) Surfaces,* submitted to **Physica Status Solidi** (c) (2004).

G. Koblmüller, J. Brown, R. Averbeck, H. Riechert, P. Pongratz, and J. S. Speck: *Continuous Evolution of Ga Adlayer Coverages during Plasma Assisted Molecular Beam Epitaxy of GaN (0001),* submitted to **Applied Physics Letters** (2004).

Acknowledgements